Microsystems and Nanosystems

Wonhee Lee
Peter Tseng
Dino Di Carlo *Editors*

Microtechnology for Cell Manipulation and Sorting

Springer

Microsystems and Nanosystems

More information about this series at http://www.springer.com/series/11483

Wonhee Lee · Peter Tseng · Dino Di Carlo
Editors

Microtechnology for Cell Manipulation and Sorting

Springer

Editors
Wonhee Lee
Korea Advanced Institute of Science and Technology
Daejeon
South Korea

Dino Di Carlo
University of California, Los Angeles
Los Angeles, CA
USA

Peter Tseng
Tufts University
Medford, MA
USA

ISSN 2198-0063 ISSN 2198-0071 (electronic)
Microsystems and Nanosystems
ISBN 978-3-319-44137-5 ISBN 978-3-319-44139-9 (eBook)
DOI 10.1007/978-3-319-44139-9

Library of Congress Control Number: 2016947772

Printed on acid-free paper

This Springer imprint is published by Springer Nature
The registered company is Springer International Publishing AG Switzerland

We would like to dedicate the volume to the micro and nanotechnology research community which has created numerous innovative devices to interface at the scale of biology. We appreciate how this community is extremely open and helpful as exemplified in the collaborative atmosphere at the yearly international meeting for miniaturization in life sciences and chemistry (MicroTAS). We also would like to recognize the many young researchers who have trained at the Microfluidic Biotechnology lab at UCLA, who have explored many fruitful branches of how microscale systems can interface at the cellular scale and achieve a positive impact on our health.

Preface

Innovation in the biomedical field is often seen as a critical driver of scientific progress, and a cornerstone of developing modern technology. This has been reflected in the early twenty-first century, as technological developments in biomedicine and biomedical devices have become increasingly prevalent in our hospitals and medical treatments. With the advent of personalized biologics and biomedicine, these advancements are presumed to change our healthcare system entirely. An important aspect of many of these innovations is microfluidic technology, where such devices possess the same size as structures being assayed. Critically, engineers can now create microfluidic devices that possess the precision control required to handle, manipulate, and sort complex biological fluids.

This book contains a collection of chapters intended to highlight, explain, and review the dominant mechanisms that have emerged to manipulate and sort biological structures. Chapter "Microfluidic cell sorting and separation technology" will provide an overview of the state of the microfluidics field in medicine by highlighting conventional cell sorting techniques, the principles of microfluidics (and establish terminologies and metrics that will be used in the book to assay the performance of devices), and give perspective on future directions for microfluidic devices. The following chapters will cover the dominant mechanisms utilized by microfluidic devices to handle biological samples, including Chapter "Magnetic Cell Manipulation and Sorting": magnetism, Chapter "Electrical Manipulation and Sorting": electrical, Chapter "Optical Manipulation of Cells": optical, Chapter "Acoustic cell manipulation": acoustic, Chapter "Gravity-Driven Fluid Pumping and Cell Manipulation": gravity/sedimentation, Chapter "Inertial Microfluidic Cell Separation": inertial, Chapter "Microfluidic technologies for deformability based cell sorting": deformability, and Chapter "Microfluidic Aqueous Two-Phase Systems": aqueous two-phase systems. All chapters thoroughly explain the physics of the mechanism at work, review common geometries and devices utilized by engineers/scientists and their accompanying devices, and highlight the benefits and drawbacks of each technique.

This book is intended for use by both graduate-level biomedical engineering and analytical chemistry students as well as engineers/scientists in the biotechnology industry. By organizing the book around dominant physical mechanisms,

explaining these in detail, and covering the state of the art in each respective field, we hope that this book can be a resource for engineers and scientists of all levels. An important theme will be the metrics and capabilities accompanying each technique. For example, one approach may be passive and possess no external driving power, but possess low-throughput and sorting capability. Only by understanding these benefits and drawbacks can engineers decide the type and style of device required for a respective application. The authors believe microfluidics and microtechnologies will continue to play a critical role in biomedicine, and we hope that this book will continue to serve as a resource for this developing field.

We finally thank all the authors for their time and effort in writing their respective chapters.

Daejeon, South Korea — Wonhee Lee
Medford, MA, USA — Peter Tseng
Los Angeles, CA, USA — Dino Di Carlo

Contents

Microfluidic Cell Sorting and Separation Technology

Wonhee Lee, Peter Tseng and Dino Di Carlo

Abstract Cell sorting and separation is widely used as a critical first step for research and clinical applications where it is needed to isolate individual cell types from a heterogeneous biological sample. In this introductory chapter, we review conventional cell sorting and separation techniques and their applications. To meet the complex and diversifying needs for cell sorting, many microfluidic techniques based on diverse sorting criteria have been developed recently. Microfluidics has many advantages including variety of sorting principles, precise cell manipulation capability, and combination with downstream analysis. We highlight microfluidic cell sorting and separation techniques and their principles, and establish terminologies and metrics used in their analysis. Lastly, we provide perspective of potential future applications or directions for microtechnologies.

Keywords Cell sorting · Cell separation · Microfluidics · Magnetophoresis · Dielectrophoresis · Optical sorting · Acoustic sorting · Gravity-driven cell manipulation · Inertial microfluidics · Aqueous two-phase system · FACS · MACS · Centrifugation · Filtration · Terminology

W. Lee (✉)
Graduate School of Nanoscience and Technology, Korea Advanced Institute of Science and Technology, 291 Daehak-ro, Yuseong-Gu, Daejeon 34141, Korea
e-mail: whlee153@kaist.ac.kr

P. Tseng (✉)
Tufts University, 200 Boston Ave, Medford, MA 02155, USA
e-mail: pctseng@gmail.com

D. Di Carlo (✉)
Department of Bioengineering, California NanoSystems Institute, Jonsson Comprehensive Cancer Center, University of California, Los Angeles, 420 Westwood Plaza, Los Angeles, CA 90095, USA
e-mail: dicarlo@ucla.edu

W. Lee et al. (eds.), *Microtechnology for Cell Manipulation and Sorting*, Microsystems and Nanosystems, DOI 10.1007/978-3-319-44139-9_1

1 Introduction

Manipulation and sorting of biological cells has seen ever increasing widespread use in medicine, biotechnology, and cellular biology. Extracted biofluids are often heterogenous in composition, and depending on their source of origin can possess a mixture of cell types (white blood cells, red blood cells, circulating progenitor cells, malignant cells), and biomolecules (plasma, proteins, antibodies). Cell manipulation and sorting are often a critical first step to either separate samples into constituent cell populations/components, or to isolate a desired cell type from a complex biofluid. Traditionally, this task is accomplished with fluorescent-activated cell sorting (FACS), or magnetic-activated cell sorting (MACS). However, these traditional methods are hampered by several limitations including large, unwieldy instrumentation, low sample throughput, cell death, limited quantitation capability, or high costs.

Limitations of existing traditional techniques, alongside the advent of personalized medicine (either for personalized diagnostics or developing patient-specific cell therapies/treatments) has generated tremendous need for modernized devices and systems that either possess reduced costs, higher throughput, improved specificity, or portability.

Microtechnologies/microdevices are looked toward as the solution to these issues. Operating at scales similar to biological structures, these devices possess inherent scalability and low cost due to microfabrication techniques, inherent portability due to operating at the size limit of biology, while potentially possessing higher throughputs due to parallelized designs or unique parallel physical manipulation methodologies.

In this introductory chapter, we will highlight conventional cell sorting and separation techniques (including label-free and antibody-based approaches) and their applications, microfluidic techniques and principles (and establish terminologies and metrics used in their analysis), and provide perspective of potential future applications or directions for microtechnologies in biological sample handling.

2 Conventional Cell Sorting and Separation Techniques

Biological samples, such as blood, bone marrow, and tissues consist of different types and lineages of cells. As a result, studies with such heterogeneous samples require a sample preparation step that can yield a purified cell population to avoid biased or erroneous results. Conventional cell separation and sorting techniques allow classification and separation of cells based on characteristics of cells including size, density, and cell contents, such as proteins and DNA (Orfao and Ruiz-Argüelles 1996; Almeida et al. 2014). Advances in monoclonal antibodies led to a dramatic increase in the use of immunologic methods to identify cell contents, while label-free methods such as centrifugation and filtration are also widely used as a preparatory step for analysis or further sorting and separation. Here summarized are frequently used conventional cell separation and sorting techniques (Table 1).

Table 1 Comparison of conventional cell sorting techniques

	Technique	Principle	Pros	Cons
Label-free	Filter	Size	Simple process Low cost High-throughput	Low purity Low yield
	Centrifugation	Density		
	Adherence	Adherence		
	Culture	Growth		
Antibody-based	Panning	Antibody	High purity High yield	Complexity of labeling High cost Labeling may change cell function
	FACS	Antibody		
	MACS	Antibody		

2.1 Label-Free Techniques

Label-free cell separation techniques separate cells based on physical properties of cells, such as size, deformability, electrical polarizability, adhesion, and density. Widely used label-free techniques include filtration, centrifugation (and sedimentation), cell adherence-based separation, and cell culture. These techniques allow the separation of large numbers of desired cells in relatively simple ways. More importantly, cells separated using label-free techniques are readily available for subsequent analysis and even for therapeutic purposes. However, the separation is achieved in a qualitative way rather than a quantitative way and the separation purity is generally low.

Cell separation by *filtration* is a simple and inexpensive method to separate cells by size and/or deformability using filters with uniform microscale meshes or pores. Filtration is typically used as a pre-enrichment step for further cell purification, and it is especially useful in preparing single cell suspensions by removal of cell aggregates and large particles. The cell separation filters traditionally are made of cotton wool columns or copper filters, and recently polymer meshes, for example, made with nylon and polyethylene terephthalate (PET) are replacing them. A notable disadvantage of filtration is the significant amount of cell loss during the process. Filtration is also used to concentrate and retain larger cells for sample preparation prior to cytological analysis (e.g., ThinPrep®).

Centrifugation (or *sedimentation*) separates cells by their differences in density. Centrifugation is an extensively used cell separation technique because it is suitable for separation of large numbers of cells in a relatively simple and inexpensive way. Although it is not as significant as in filtration, centrifugation also has problems associated with low purity and loss of target cells. The low purity can be overcome by repeated centrifugations using different conditions (density of medium, and angular velocity). Alternatively, density gradient centrifugation can provide more efficient and practical cell separation results (Carmignac 2002). For this purpose, Percoll or other gradient media (e.g., polysaccharides, iodinated gradient media) are prepared to create isopycnic density gradients. Cells with different densities settle to their isopycnic points via centrifugation. Rosetting is also

a widely used separation technique based on density to deplete a cell population, which is a combination of antibody binding and centrifugation (Strelkauskas et al. 1975; Slaper-Cortenbach et al. 1999). Antibody-enabled binding with a linker between nontarget cells and erythrocytes leads to formation of aggregates or immuno-rosettes, which are denser than the other cell types of interest cells and can be removed by centrifugation.

Cell adherence to a substrate and cell culture can also be used as separation techniques. Cell adherence-based separation enriches desired cells by removing cells that do not attach onto a cell substrate. The method relies on a cell's adhesion capacity (without specific target binding), which is often shared by many different cell types. Therefore, adherence-based separation is used only when high purity is not required or depletion of a specific cell type is needed. The separation is performed typically on a tissue culture plastic dish but more refined methods use glass beads grafted with polymer brushes (Nagase et al. 2012) or micro/nanostructured surfaces (Didar and Tabrizian 2010). An important cell type that was first isolated using such an approach from bone marrow aspirates are mesenchymal stem cells, also called marrow stromal cells (MSCs). These cells spread and adhere strongly to these rigid plastic surfaces.

Cell culture using media that stimulates or inhibits the growth of certain cell types can be used as a cell separation technique. For example in the process of bone marrow transplants, long-term bone marrow culture in controlled media can be used to selectively expand hematopoietic stem cells (Devine et al. 2003). These methods can provide a relatively homogeneous cell population; however, the resulting sample is not the original cells but expanded cells.

2.2 Techniques Based on Antibody Binding

High purity cell separation and sorting can be achieved by the use of a monoclonal antibody that binds to a cellular component. Typically, an antibody is selected to identify a single (or a few) cell surface markers and the antibody is conjugated with fluorescent molecules or attached to microparticles to separate target cells. Owing to high specificity of antibody—antigen binding, antibody-based separation and sorting techniques can provide much higher purity compared to label-free techniques. However, antibody-based techniques have some disadvantages related with labeling. First, labeling with fluorescent molecules and antibodies may affect cell fate and functions, which affects downstream analysis and efficacy of therapeutics. Second, a labeling process is often time-consuming and labor-intensive, which adds difficulty and cost. Lastly, for a practical separation and sorting application the choice of antibodies is limited within a pool of commercially available antibodies, which in turn limits the separation targets to those cells with specific markers. Widely used antibody-based cell separation techniques include cell panning, MACS, and FACS.

With the *cell panning* technique, cells having specific antigens can be selectively attached on an antibody-coated surface. Typically, antibodies are adsorbed to a plastic surface, such as petri dishes or polymer microparticles. Cell panning can provide high purity but high cell loss is unavoidable, and quantitative separation based on surface expression is not achievable, yielding only a binary separation. Compared to other antibody-based techniques, it is easier to release cells and the separated cells can be used for further analysis or therapeutics.

MACS employs antibody-conjugated magnetic beads to target the specific marker on the cell surface. Cells labeled with magnetic beads can be selectively collected under a magnetic field produced by a permanent magnet. MACS is hugely benefited by the well-established technology for magnetic particles. Magnetic particles are commercially available with diversity not only in size and material but also with surface modification or antibody conjugation. MACS allows significantly higher throughput but lower purity then FACS, because cells with a few bound magnetic particles compared to many particles are both concentrated in the magnetic field. That is, like panning, the separation cannot quantify the amount of surface antigen on a cell. Another notable limitation is the difficulty of detachment and removal of the beads after separation.

FACS is one of the most powerful cell sorting techniques that is based on flow cytometry. A flow cytometer allows the analysis and classification of individual cells by multiparameter optical measurements. Cells are hydrodynamically focused to a narrow stream and pass optical interrogation points one by one where laser beams illuminate individual cells. At this point scattered light and fluorescent signals are generated and detected by multiple detectors. Sorting decisions are made based on these signals, which provide quantitative information on the size of the cells and the amount of the fluorescent-labeled antibodies bound to cell membrane and/or internal structures of the cells. Modern flow cytometers can offer throughput in the range of 10,000 cells/s, which is fairly high but lower than bulk sorting techniques like MACS or centrifugation. To sort the individual cells, the cell stream is ejected into air and broken up into droplets containing no more than one cell per droplet. The droplet formation can be influenced by many parameters including orifice size and temperature. The droplets are electrically charged depending on the sort decision and then the droplets are diverted into separate containers based on their charge by using an electrostatic deflection system. While FACS provides high purity quantitative sorting decisions throughput is not sufficient for sorting of therapeutic cells, and cells are often damaged during the sorting process. Limited throughput also prevents FACS from use in certain applications such as rare cell sorting. High equipment cost (typically >$100,000), in addition to high operation and material costs, is one other notable limitation. The process of droplet formation also produces aerosols, which is a potential biohazard to a user and appropriate safety measures should be taken.

2.3 Applications

By enabling the study of individual cell types isolated from a heterogeneous population, cell separation, and sorting is widely used for research in cell biology and many other fields including molecular genetics and proteomics (Orfao and RuizArguelles 1996; Mattanovich and Borth 2006; Gossett et al. 2010; Autebert et al. 2012; Almeida et al. 2014; Shields et al. 2015). Especially, in the field of cancer, stem cells and immunology rare cell separation and sorting receives increasing attention. In clinical fields, preparation of homogeneous, purified cell populations is essential for immunology, oncology, hematology, tissue engineering, and regenerative medicine.

Cell sorting and separation has been extensively used for blood because it is a necessary step not only to collect cell-free plasma, but also to sort the different types of RBCs and WBCs. Blood is extremely rich in information about the physiological state of the body, which can be extracted from the genetic material, protein disease markers, and cellular components within blood. Especially, blood cells, which represent ~45 % of blood volume (~10^9 RBCs and ~10^6 WBCs in 1 mL blood), are often used for hematological tests, diagnosis of disease, gene expression profiling, and therapeutics. Despite the importance, the separation of pure cell populations from blood is still a challenging task due to blood cell diversity and susceptibility to alteration during the handling procedures. Centrifugation and FACS or MACS have been generally used for blood separation but recent studies suggest lab-on-a-chip microscale or microfluidic approaches can address many challenges (Toner and Irimia 2005).

Cell-based therapy is one of the fields that can be most benefited from advanced cell sorting techniques because infusion of high purity cells can increase therapeutic efficacy. In case of bone marrow transplants, patients have received transplants of whole human leukocyte antigen (HLA)-identical bone marrow to avoid the risk of graft versus host disease with the finding of hematopoietic stem cells, transplantation of purified CD34+ cells from bone marrow has been performed (Beaujean 1997). Recently, peripheral stem cell transplantation of MSCs has also became a more common procedure due to its less invasive nature (Handgretinger et al. 1998; Despres et al. 2000), and regulatory approval for use in treatment of a variety of diseases. More recently, cell immunotherapies, including engineered T-cell receptor and chimeric antigen receptor T-cells have shown significant promise in programming one's own immune system to attack cancer. In the normal process of cell isolation and further upon transduction with engineered receptors and expanding cell clones, separation approaches are used.

As can be seen from an example of bone marrow transplantation, while traditional applications of cell sorting focused on the enrichment of larger populations of desired cells, recent focus has expanded to sorting of rare cells, which include circulating tumor cells (CTCs), circulating endothelial cells (CECs), and endothelial progenitor cells (EPCs), stem cells, fetal cells, infected cells, and bacteria.

CTCs, for example, are related to cancer metastasis and can be found in blood at very low abundance (1–100 cells/mL). Not only are CTCs extremely rare compared to a large population of RBCs and WBCs, their heterogeneity complicates the sorting; antibody-based sorting has relied on binding to epithelial markers (EpCAM), however, tumor cells can undergo epithelial–mesenchymal transition and may not express EpCAM (Thiery 2002; Kalluri and Weinberg 2009). Instead of antibodies, physical properties such as size and deformability could be used for CTC enrichment (Cima et al. 2013; Jin et al. 2014; Low and Abas 2015). Rare cell separation requires high-throughput while maintaining high purity and yield (low loss). MACS provides very high-throughput but it does not allow labeling based on multiple markers and detachment of collected cells is difficult. FACS can analyze multiple signals yet its throughput is still a limiting factor for rare cells.

3 Microfluidic Cell Sorting Technology

Advances in genomics and cell biology have significantly increased the complexity of sorting criteria and previously known-to-be homogeneous cell populations may be further classified into different subgroups using new sorting criteria. As a result, conventional techniques based on a few sorting principles would be insufficient to deliver proper sorting strategies. On the other hand, microfluidic technology is expected to provide better solutions with its unique advantages (Pamme 2007; Chen et al. 2008; Didar and Tabrizian 2010; Gossett et al. 2010; Lenshof and Laurell 2010; Autebert et al. 2012; Gao et al. 2013; Sajeesh and Sen 2014; Shields et al. 2015). Several noteworthy advantages of microfluidics for cell sorting and separation applications are: (1) The laminar nature of fluid flow at these scales allows confinement of cells within a narrow controlled stream line. (2) The flow field can have velocity gradients over the scale of cells which allows separation mechanisms that are not possible in the macroscale (e.g., hydrodynamic separations). (3) Small device dimensions allows the generation of strong electric or magnetic fields and their gradient. (4) High surface to volume ratio increase the chance of surface binding of cells. (5) Multiple microfluidic devices can be integrated to perform separation and downstream analysis of cells seamlessly. In addition, general advantages of microfluidic techniques apply, such as easy multiplexing for higher throughput, rapid, and low cost operation, and reduced requirements for a skilled user with automation.

3.1 Terminology for Cell Manipulation

Microfluidic technology enables diverse cell handling techniques, which include physical and biochemical analysis, cell patterning, cell culture, and cell manipulation. Among these, the focus of this book is on cell manipulation techniques,

especially on cell sorting and separation. Cell manipulation refers to general operations that involve physical methods to control a cell's position, orientation, or shape. Cell sorting conventionally refers to a procedure that can separate, isolate, or enrich a specific cell type. The usage of the term cell separation has increased with development of diverse microfluidic-based cell sorting techniques. Although sorting and separation have been often used with the same meaning, it is more common to use them in different situations within the microfluidics community. Cell sorting can be defined as a process to separate cells based on their properties. In the sorting process, for each of the cells, an identification is made and a decision is followed whether to sort or not. For example, FACS can identify cells by optical properties and following this a sorting action is performed according to the predetermined sorting gates. In contrast to cell sorting, cell separation usually refers to a process that does not involve a sort decision, that is, a passive process. In a separation process, a physical property of the cell itself serves as the basis for a cell being accumulated or not. For example, filtration of cells involve the process that cells larger than a pore size get trapped, where identification of cell size that is trapping take places at the same time at the filter. Since there is no individual active decision-making process, one cannot choose cells to sort.

3.2 Performance Metrics

Different sorting and separation techniques have different capabilities, which may lead to trade-offs in performance for varying applications. Here, we summarize definitions of these performance metrics to help in comparing different techniques and the trade-offs between performance throughout the many techniques described in the following chapters.

Purity is the **ratio between the number of target cells and the number of total sorted cells**. In case the sorted cell population contains unwanted cells, purity will have a low value. When a sorting technique reports high purity near 100 %, collected cells may be still mixed with unwanted cell populations if the characteristic that is used as the basis of the sorting decision or separation is shared by multiple types of cells. Therefore, a value of purity may vary significantly depending on how one defines "target cells." Without knowing the exact definition of target cells and samples used, it would be difficult to make a fair comparison between different techniques.

Yield or *recovery* is the **ratio between the number of target cells collected and the number of target cells in the original sample**. Yield usually is less than unity not only because sorting capabilities are not perfect but also target cells in the original sample may be lost by lysis, adhesion to device surfaces, and retention within the device or tubing. Yield can be an especially important parameter in case of rare cell sorting.

Enrichment or *enrichment ratio* can be defined as the **ratio between the number of target cells at the inlet divided by total cells and the number of target**

cells at the outlet divided by total cells. Enrichment can be larger than 1 for enrichment and smaller than 1 for depletion. While 'yield' focuses on the description of loss of target cells, 'enrichment' focuses on concentration of the specific cells compared to the other cells. Therefore, *enrichment ratio* is often used to emphasize the separation capability.

Efficiency can be defined as the **ratio between the number of sorted target cells and the number of target cells identified to sort**. Efficiency can be defined for cell sorting where sorting and identification are separate processes. In case of cell separation, efficiency is often used to indicate the same meaning as yield.

Throughput of cell separation is typically expressed as **the number of processed cells per second**. The unit of throughput can vary depending on the application. For a continuous separation technique, a volumetric flow rate and a cell concentration can be given. There is typically trade-offs between throughput and other performance. For example, high cell concentration can cause errors in sorting decisions, which leads to lower purity and yield. For microfluidic devices, throughput per foot print (device area) may provide basis for fair comparisons, because throughput of many microfluidic devices can be easily multiplied by use of parallel channels.

3.3 Principles of Microfluidic Cell Manipulation

When a cell suspension is first introduced into a microfluidic channel, the position of the cells in the cross-section are intrinsically random. The goal of cell manipulation using microfluidics is mainly to control the cell positions relative to the fluid or other cells through a variety of means: Cells can be trapped, focused, moved into different solutions (washing and solution exchange), separated, and sorted (enrichment). Other manipulation operations can include deformation (shape change such as stretching), mechanical lysis, and rotation. To achieve cell manipulation, one needs to apply a force on cells against the drag force from the surrounding fluid that is either stagnant or flowing. The methods that generate forces on cells can be categorized into three groups: (1) use of direct contact with device structures, (2) use of force fields such as gravity, electric fields, or magnetic fields, and (3) use of hydrodynamic drag and lift forces. Microstructures such as filters, or pillars can exert direct mechanical force onto cells by contact, which allows trapping of cells or shifting cells to different streamlines. The use of external force fields such as electromagnetic fields can also provide efficient methods to manipulate cells. For example, an optical tweezer has long been used to trap and move suspended cells and gravitational force acting on cells results in sedimentation of cells. Another important method to manipulate cells in microfluidic systems is to use the secondary flows that are flowing orthogonal to the main fluid flow along the channel. Combined with the laminar nature of microfluidic flows, hydrodynamic methods are very efficient cell manipulation methods in microfluidic systems because the viscous drag becomes significantly larger than other forces at

small scales. Fluid flows can exert a drag force along the flow direction and a lift force orthogonal to the flow direction. Inertial lift forces can be used to manipulate cells at finite Reynolds number flow conditions ($Re > 1$), where Reynolds number (Re) describes the ratio of inertial to viscous forces in the flow.

Similar to conventional sorting techniques, microfluidic sorting techniques also can be categorized into label-free techniques and antibody-binding-based techniques. Because the use of antibodies provides high purity separation and important sorting criteria, there have been many studies of microfluidic-based cell sorting and separation involving antibodies (Du et al. 2007; Nagrath et al. 2007; Didar and Tabrizian 2010). Microfluidic systems combined with optical sensing or imaging capabilities can sort fluorescent-labeled cells by switching flow paths to multiple outlets (Kruger et al. 2002; Johansson et al. 2009). Unlike FACS, microfluidic cell sorting devices are closed systems and contamination and safety issues are less of a concern. Antibody-coated micro or nano particles are also widely used (Inglis et al. 2004; Xia et al. 2006; Adams et al. 2008). Diverse microfluidic techniques are utilized to guide cells bound with the particles. Alternatively cells can be collected in microchannels with immobilized antibodies (Nagrath et al. 2007). In this case the large surface-area-to-volume ratio of microfluidic structures can significantly enhance the capture efficiency.

Microfluidic separation techniques are mostly focused on label-free techniques, by which one can utilize a variety of physical principles to manipulate cells. Label-free techniques can be grouped into (1) *passive manipulation* and (2) *active manipulation* depending on their physical principles (Table 2). Passive manipulation techniques uses microfluidic devices predesigned to perform a specific manipulation operation. For example, a deterministic lateral displacement (DLD) device separates cells based on their size; with cell-to-wall interactions and the laminar nature of flow, cells larger, and smaller than a critical diameter follow a different

Table 2 Comparison of microfluidic cell separation and sorting techniques

	Separation technique	Mode of separation	Separation criteria
Passive	Mechanical Filter	Size exclusion	Size, deformability
	Hydrodynamic	Streamline manipulation	Size, shape
	DLD	Migration in micropost array	Size, shape
	Microstructure	Microstructure perturbation of cell flow	Size, density, deformability
	ATPS	Differential affinity	Surface property and net charge
	Inertial	Lift force and secondary flow	Size, shape, deformability
Active	Electric	Dielectrophoresis	Polarizability, size
	Magnetic	Differential magnetic mobility	Intrinsic magnetic susceptibility
	Acoustic	Acoustic radiation force	Size, density, compressibility
	Optical	Optical lattice	Refractive index, size
	Gravity	Sedimentation difference	Size, density

flow stream line. As the name suggests the particle motion is deterministic, and the operation is *passive*. On the other hand, active manipulation involves a force field that can be *actively* controlled by the operator. For example, cells with different polarizability experience different forces within a nonuniform AC electric field. Using this property cells can be separated by dielectrophoresis (DEP).

4 Future Directions and Outlook

As you will see throughout the following chapters, microfluidic systems and microscale devices using a variety of active and passive approaches have been shown to have unique advantages for cell manipulation, sorting, and separation. Future work must now apply these techniques to applications with significant unmet needs, integrate with analysis approaches to achieve clinically actionable information, and scale through parallelization to throughputs of importance in developing cell therapies. Some of these activities are now well-suited for industry to tackle, and along these lines, we see increasing investment into companies focused on cell sorting and manipulation, which will in the end lead to the translation and use of these technologies.

One future direction is in connecting advantages of microscale manipulation to suitable research or clinical needs. In the research setting, it is becoming clear that populations of cells once thought to be homogenous have significant heterogeneity. Using techniques such as single cell RNA-sequencing of individual cells, or mass flow cytometry (CyTOF) in the last few years has led to uncovering of a range of subpopulations of cells, however, these processes are destructive to cells. One goal would be to develop microscale tools to probe a variety of molecular or phenotypic markers in parallel to better classify cells in a method compatible with downstream separation. One could imagine multiparameter panning or sampling and analysis of small amounts of intracellular components in a nondestructive manner. Drop-based compartmentalization may also allow sampling after disruption of cell membranes for significant periods of time without cell death, because cellular components remain at relatively high concentration in the droplet until the membrane seals. Sorting and separation of nonmammalian cells is also becoming an important area, whether for studying algae that produce biofuels or concentrating bacteria to identify blood stream infections. Sorting is in essence a process of selection, and we anticipate continuous sorting or separation systems combined with culture and mutagenesis can be developed in the future to select and evolve cellular traits of interest for scientific research and clinical production of cell therapies.

Integration of separation with downstream analyses is also an important direction to yield complete clinical solutions. For example, for CTCs, which can provide information about a patient's tumors to direct therapy, separation alone does not provide information, but requires downstream analysis, e.g., enumeration, or measurement of mutations in the genome to provide clinically actionable

information. Techniques that can combine separation seamlessly with downstream workflows should be enabled by microfluidic systems and will be extremely valuable in the future.

Throughput for most single-device microfluidic systems is relatively low, which is not compatible with separations that are needed for emerging cell therapy technologies where tens of millions to billions of cells should be purified. This is particularly difficult for technologies that rely on cell surface antigens, which are most likely to be relevant for cell therapy-based purification. New ways of parallelizing active sorting decisions or developing more quantitative MACS-type approaches which already possess high-throughput should be investigated.

Because of the many exciting developments, microscale cell manipulation technologies have garnered significant commercial investment. This is helping bring research-grade proof-of-concepts to real products that are being used and developed for a range of assays. A range of new companies are being well funded in this space, such as Berkeley Lights, which is commercializing optoelectronic tweezer technology, as well as a number of companies focused on the problem of isolating CTCs, including Vortex Biosciences, which is developing vortex trapping microfluidic cartridges for CTC isolation, Clearbridge Biomedics, commercializing inertial microfluidic-based CTC separation chips, and ApoCell, developing a DEP-based enrichment technique. Commercial successes may then drive future investment into this field, especially targeting the important problem of reducing the cost of cell therapies—from stem cell to immunotherapies. Indeed, the future in cell separation is looking *small*!

References

Adams JD, Kim U, Soh HT (2008) Multitarget magnetic activated cell sorter. Proc Natl Acad Sci USA 105(47):18165–18170

Almeida M, Garcia-Montero AC, Orfao A (2014) Cell purification: a new challenge for biobanks. Pathobiology 81(5–6):261–275

Autebert J, Coudert B, Bidard F-C, Pierga J-Y, Descroix S, Malaquin L, Viovy J-L (2012) Microfluidic: an innovative tool for efficient cell sorting. Methods 57(3):297–307

Beaujean F (1997) Methods of CD34+ cell separation: comparative analysis. Transfus Sci 18(2):251–261

Carmignac DF (2002) Biological centrifugation J. Graham, BIOS Scientific Publishers Ltd., 201 pp., £21-99, ISBN 1 85996 037 5 (2001). Cell Biochem Funct 20(4):357

Chen P, Feng XJ, Du W, Liu BF (2008) Microfluidic chips for cell sorting. Front Biosci Landmark 13:2464–2483

Cima I, Yee CW, Iliescu FS, Phyo WM, Lim KH, Iliescu C, Tan MH (2013) Label-free isolation of circulating tumor cells in microfluidic devices: current research and perspectives. Biomicrofluidics 7(1):16

Despres D, Flohr T, Uppenkamp M, Baldus M, Hoffmann M, Huber C, Derigs HG (2000) CD34(+) cell enrichment for autologous peripheral blood stem cell transplantation by use of the CliniMACS device. J Hematother Stem Cell Res 9(4):557–564

Devine SM, Lazarus HM, Emerson SG (2003) Clinical application of hematopoietic progenitor cell expansion: current status and future prospects. Bone Marrow Transplant 31(4):241–252

Didar TF, Tabrizian M (2010) Adhesion based detection, sorting and enrichment of cells in microfluidic Lab-on-Chip devices. Lab Chip 10(22):3043–3053

Du Z, Cheng KH, Vaughn MW, Collie NL, Gollahon LS (2007) Recognition and capture of breast cancer cells using an antibody-based platform in a microelectromechanical systems device. Biomed Microdev 9(1):35–42

Gao Y, Li WJ, Pappas D (2013) Recent advances in microfluidic cell separations. Analyst 138(17):4714–4721

Gossett DR, Weaver WM, Mach AJ, Hur SC, Tse HTK, Lee W, Amini H, Di Carlo D (2010) Label-free cell separation and sorting in microfluidic systems. Anal Bioanal Chem 397(8):3249–3267

Handgretinger R, Lang P, Schumm M, Taylor G, Neu S, Koscielnak E, Niethammer D, Klingebiel T (1998) Isolation and transplantation of autologous peripheral CD34(+) progenitor cells highly purified by magnetic-activated cell sorting. Bone Marrow Transplant 21(10):987–993

Inglis DW, Riehn R, Austin RH, Sturm JC (2004) Continuous microfluidic immunomagnetic cell separation. Appl Phys Lett 85(21):5093–5095

Jin C, McFaul SM, Duffy SP, Deng XY, Tavassoli P, Black PC, Ma HS (2014) Technologies for label-free separation of circulating tumor cells: from historical foundations to recent developments. Lab Chip 14(1):32–44

Johansson L, Nikolajeff F, Johansson S, Thorslund S (2009) On-chip fluorescence-activated cell sorting by an integrated miniaturized ultrasonic transducer. Anal Chem 81(13):5188–5196

Kalluri R, Weinberg RA (2009) The basics of epithelial–mesenchymal transition. J Clin Investig 119(6):1420–1428

Kruger J, Singh K, O'Neill A, Jackson C, Morrison A, O'Brien P (2002) Development of a microfluidic device for fluorescence activated cell sorting. J Micromech Microeng 12(4):486–494

Lenshof A, Laurell T (2010) Continuous separation of cells and particles in microfluidic systems. Chem Soc Rev 39(3):1203–1217

Low WS, Abas WAW (2015) Benchtop technologies for circulating tumor cells separation based on biophysical properties. Biomed Res Int 2015: Article ID 239362

Mattanovich D, Borth N (2006) Applications of cell sorting in biotechnology. Microb Cell Fact 5:11

Nagase K, Kimura A, Shimizu T, Matsuura K, Yamato M, Takeda N, Okano T (2012) Dynamically cell separating thermo-functional biointerfaces with densely packed polymer brushes. J Mater Chem 22(37):19514–19522

Nagrath S, Sequist LV, Maheswaran S, Bell DW, Irimia D, Ulkus L, Smith MR, Kwak EL, Digumarthy S, Muzikansky A, Ryan P, Balis UJ, Tompkins RG, Haber DA, Toner M (2007) Isolation of rare circulating tumour cells in cancer patients by microchip technology. Nature 450(7173):U1235–U1210

Orfao A, Ruiz-Argüelles A (1996) General concepts about cell sorting techniques. Clin Biochem 29(1):5–9

Pamme N (2007) Continuous flow separations in microfluidic devices. Lab Chip 7(12):1644–1659

Sajeesh P, Sen AK (2014) Particle separation and sorting in microfluidic devices: a review. Microfluid Nanofluid 17(1):1–52

Shields CW, Reyes CD, Lopez GP (2015) Microfluidic cell sorting: a review of the advances in the separation of cells from debulking to rare cell isolation. Lab Chip 15(5):1230–1249

Slaper-Cortenbach ICM, Wijngaarden-du Bois M, de Vries-van Rossen A, Borst HPE, van der Lelie H, van Heugten HG, Verdonck LF, Wulffraat NM, Hoogerbrugge PM (1999) The depletion of T cells from haematopoietic stem cell transplants. Rheumatology 38(8):751–754

Strelkauskas AJ, Teodorescu M, Dray S (1975) Enumeration and isolation of human T-lymphocytes and B-lymphocytes by rosette formation with antibody-coated erythrocytes. Clin Exp Immunol 22(1):62–71

Thiery JP (2002) Epithelial–mesenchymal transitions in tumour progression. Nat Rev Cancer 2(6):442–454

Toner M, Irimia D (2005) Blood-on-a-chip. Annu Rev Biomed Eng 7:77–103

Xia N, Hunt TP, Mayers BT, Alsberg E, Whitesides GM, Westervelt RM, Ingber DE (2006) Combined microfluidic–micromagnetic separation of living cells in continuous flow. Biomed Microdev 8(4):299–308

Magnetic Cell Manipulation and Sorting

Maciej Zborowski, Jeffrey J. Chalmers and William G. Lowrie

Abstract Cell manipulation is one of the fastest growing segments of biotechnology engineering, and magnetic cell separation plays a large part in its development. Because of low magnetic permeability of biological materials, the magnetostatic forces can be made to operate highly selectively on cells tagged with magnetic nanoparticles, with no interference from the physiological electrolyte solutions used for cell suspension and from other cells. The increasing availability of inexpensive permanent magnet blocks capable of generating fields in excess of 1 tesla (T) and gradients up to 1000 T/m combined with a large selection of targeting antibodies against nearly all cell surface markers of interest in clinical and laboratory applications, together with high-quality superparamagnetic iron oxide nanoparticles, makes magnetic separation an appealing alternative to other cell separation methods, including centrifugation and fluorescence-activated cell sorting. This chapter provides a brief overview of the underlying physical principles and a number of examples selected from a large body of scientific literature published on the subject.

M. Zborowski
Department of Biomedical Engineering, Lerner Research Institute,
Cleveland Clinic, Cleveland, OH, USA
e-mail: zborowm@ccf.org

J.J. Chalmers (✉) · W.G. Lowrie
Department of Chemical and Biomedical Engineering,
Analytical Cytometry Shared Resource, Comprehensive Cancer Center,
The Ohio State University, Columbus, OH, USA
e-mail: chalmers.1@osu.edu

W. Lee et al. (eds.), *Microtechnology for Cell Manipulation and Sorting*,
Microsystems and Nanosystems, DOI 10.1007/978-3-319-44139-9_2

Keywords Magnetophoresis · Magnetophoretic mobility · Magnetophoretic fractionation · Magnetic separation · Diamagnetic separation · Immunomagnetic separation · High gradient magnetic separator, HGMS · Magnetic field-flow fractionation · Particle tracking velocimetry · Cell tracking velocimetry · Biomagnetism · Biogenic magnetism · Cell magnetic susceptibility · Erythrocyte magnetic susceptibility · Intracellular paramagnetic species · Superparamagnetic iron oxide nanoparticles, SPIONs · Magnetic susceptibility-modified solutions · Magnetic nanoconveyors · Permanent magnet · Magnetic levitation

1 Introduction

Rapidly growing demands for better cell separation methods in cell biology and clinical laboratories propelled magnetic cell separation to the forefront of laboratory preparative separation techniques (Yavuz et al. 2009; Zborowski and Chalmers 2008; Pamme and Manz 2004). Its advantages include relative simplicity of operation, low capital investment, and rapidly expanding selection of targeting antibodies and magnetic tagging nanoparticles (Grützkau and Radbruch 2010). It has become one of the principal cell separation methods, alongside with centrifugation and fluorescence-activated cell sorting (FACS) (Gijs et al. 2010). Notable examples include its application to detection of rare, circulating tumor cells (CTCs) as a prognostic biomarker of cancer treatment approved by the U.S. Food and Drug Administration (FDA) for detection of metastatic breast, prostate, and colorectal CTCs (de Wit et al. 2015). Progress in the chemistry of superparamagnetic iron oxide nanoparticles (SPIONs) and their conjugation with monoclonal antibodies made it possible to sort cells in high throughput bioassays (Vyas et al. 2012). Notable recent examples include ligand-independent magnetic cell sorting by field-induced cell motion (magnetophoresis) instead of capture on a solid substrate (Karabacak et al. 2014). This, plus a rapid progress in microelectromechanical systems (MEMS), optical detection and separation technologies brought about much improved understanding of CTC biology. The remarkable increase in the strength of permanent magnets over the past two decades makes it possible to consider building a practical system strong enough to sort cells based on their weakly paramagnetic moment, without labeling by SPIONs (Knowlton et al. 2015; Sumari et al. 2016; Melnik et al. 2007). This chapter provides a brief review of underlying physical principles of magnetic cell separation and selected examples that only partially cover the rapidly expanding field.

2 Elements of Magnetostatics in Application to Cell Separation

The unique feature of magnetic cell separation is that it is performed in a continuous phase (aqueous electrolyte solutions) that is similar in its characteristic physical properties to those of the dispersed phase (cells) because of the cells' high water content (approximately 70 % volume by volume, v/v). This is unlike magnetic separation in typical industrial applications, such as separation of iron contaminants from dry mass or iron particles from environmental water, or use of magnetic forces in particle physics requiring high vacuum (Ramsey 1990; Sun 1980). The similarity between the continuous and dispersed phases poses challenges in magnetic cell separation but is also a source of opportunities that continue to be explored in many laboratories. Therefore, a brief overview of the magnetic forces and their effect on cell motion in the viscous media is provided here.

2.1 Magnetic Ponderomotive Force in Two-Phase Media

The application of the magnetic field to an aqueous cell suspension leads to the magnetic polarization (magnetization) of both the dispersed phase (cells) and the continuous phase (aqueous electrolyte solution). The resulting local field causing the cell magnetization is modified by the magnetization of the continuous phase, resulting in the expression for the force similar to that describing the effect of the dielectric polarization on the local electric field, known as Clausius–Mossotti relation (Schwinger et al. 1998). Thus assuming a small, spherical, magnetically polarizable particle of radius R and magnetic permeability μ_p free to translate and rotate in magnetically polarizable solution of magnetic permeability μ_s, the magnetic force acting on the particle is

$$\mathbf{F}_m = 4\pi R^3 \frac{\mu_p - \mu_s}{\mu_p + 2\mu_s} \mu_s H \nabla B, \tag{1}$$

where H is the local magnetic field strength (in ampere/m, A/m) and ∇B is the gradient of the magnetic field induction B (in tesla, T) measured in the absence of the magnetically polarizable media. Here the dimensionless, relative magnetic permeabilities are used, expressed with respect to the magnetic permeability of free space, $\mu_o = 4\pi \times 10^{-7}$ T m/A. For a freely suspended particle, the magnetic force vector is thus aligned with the vector of the local field gradient. It vanishes in the absence of the local field gradient. For separation of small, weakly magnetizable particles, high magnetic field gradients are necessary.

Related to the molecular properties of the magnetically polarizable materials, their relative magnetic permeability differs from slightly less than unity (diamagnetic matter, such as water) to more than unity (paramagnetic matter) to several orders of magnitude higher than unity (ferromagnetic materials). This has

interesting implications for the direction of the magnetic force vector relative to that of the local field gradient as that direction depends on the sign of magnetic permeability difference, $\mu_p - \mu_s$. Thus, six combinations are possible:

1. Paramagnetic particle in weakly paramagnetic solution, $1 < \mu_s < \mu_p \rightarrow \mu_p - \mu_s > 0$ resulting in the magnetic force being parallel to the local field gradient (attractive force).
2. Weakly paramagnetic particle in a (relatively) strongly paramagnetic solution, $1 < \mu_p < \mu_s \rightarrow \mu_p - \mu_s < 0$ resulting in the magnetic force being antiparallel to the local field gradient (repulsive force).
3. Paramagnetic particle in diamagnetic solution, $0 < \mu_s < 1 < \mu_p \rightarrow \mu_p - \mu_s > 0$ (attractive force).
4. Diamagnetic particle in paramagnetic solution, $0 < \mu_p < 1 < \mu_s \rightarrow \mu_p - \mu_s < 0$ (repulsive force).
5. Diamagnetic particle in a relatively weaker diamagnetic solution, $0 < \mu_p < \mu_s < 1 \rightarrow \mu_p - \mu_s < 0$ (repulsive force).
6. Diamagnetic particle in a relatively stronger diamagnetic solution, $0 < \mu_s < \mu_p < 1 \rightarrow \mu_p - \mu_s > 0$ (attractive force).

All six instances of the attractive and repulsive magnetic forces have been described in the literature on magnetic cell separation, leading to interesting observations of the fundamental and practical nature. One of them was an apparent contradiction with the fundamental tenet of magnetostatics that the magnetostatic forces alone (or in combination with conservative forces, such as gravity) could not lead to a stable equilibrium (the Earnshaw theorem applied to magnetostatics). A vivid illustration is an everyday life experience of impossibility of suspending a steel ball in the air using permanent magnets only. Yet such a stable configuration has been realized by replacing air with a ferrofluid of a higher magnetic permeability than that of the steel ball (which would make it an example of the type no. 2 in the above list, with the paramagnetic matter replaced by the ferromagnetic one) (Rosensweig 1997). Practical examples of type 4 in the list include addition of soluble paramagnetic ions (rare earth) to separate dispersed phase (such as cells) by magnetic repulsion (Zimmels and Yaniv 1976; Watarai and Namba 2001; Moore et al. 2004; Peyman et al. 2009; Hwang et al. 1984). Other examples include magnetic attraction of deoxygenated erythrocytes as a type 6 mechanism, and magnetic repulsion of oxygenated erythrocytes as type 5 mechanism (albeit very weak in typical laboratory applications) (Zborowski et al. 2003).

Most magnetic permeabilities encountered in the biological magnetic separations are small, with their relative permeabilities very nearly equal to unity, and therefore their magnetic properties are more conveniently described by the volume magnetic susceptibility, $\chi = \mu - 1$. From the foregoing, $\chi > 0$ for paramagnetic and ferromagnetic materials, and $\chi < 0$ for diamagnetic materials. With the substitution of $\mu = \chi + 1$ in Eq. (1), one obtains:

$$\mathbf{F}_m = 4\pi R^3 \frac{\chi_p - \chi_s}{\chi_p + 2\chi_s + 3}(\chi_s + 1) H \nabla B \quad \overset{\chi_p \ll 1,\, \chi_s \ll 1}{\longrightarrow} \quad \frac{4}{3}\pi R^3 \left(\chi_p - \chi_s\right) \tag{2}$$

The limiting case for $\chi_p \ll 1$, $\chi_s \ll 1$ shown on the right approximates well most if not all the magnetic cell separation situations, where the volume magnetic susceptibility of the particle (cell) and the aqueous electrolyte solution is orders of magnitude smaller than unity (the volume magnetic susceptibility of water is $\chi_{H_2O} = -9.05 \times 10^{-6}$). Further simplification is obtained if one assumes that the direction of the magnetic field gradient, ∇B changes little along the particle (cell) trajectory, in which case only the force in the direction of the dominant component of the field gradient is considered, here along the $0x$ axis:

$$F_m = \frac{4}{3}\pi R^3 (\chi_p - \chi_s) H \frac{dB}{dx}. \tag{3}$$

The above formula is the one most frequently encountered in the literature on magnetic cell separation for the good reason of providing a satisfactory, quantitative measure of the magnetic force on the cell based on the material properties of the cell and the continuous phase, and the imposed, local magnetic field and gradient (unperturbed by the media). There are other forms of the same equation of the magnetic force on a cell whose usefulness depends on the context. One particular variant often encountered in the literature makes an explicit use of the cell volume, $V = \frac{4}{3}\pi R^3$ and the fact that the magnetic permeability of the media is practically equal to that of the free space, so that $H = \frac{B}{\mu_0}$ and therefore $H\frac{dB}{dx} = \frac{d}{dx}\left(\frac{B^2}{2\mu_0}\right)$ leading to the expression:

$$F_m = V(\chi_p - \chi_s)\frac{d}{dx}\left(\frac{B^2}{2\mu_0}\right) \tag{4}$$

which emphasizes the fact that the magnetic force is proportional to the gradient of square of the local field magnitude, for materials whose magnetization is a linear function of the applied field (diamagnetic and paramagnetic). The importance of the field variable $\frac{B^2}{2\mu_0}$ (where μ_0 is a constant) is that it has a dimension of the magnetostatic energy density (in J/m^3) which allows a direct comparison of magnetic force generation by permanent magnets, such as used for magnetic separation, typically characterized by the (external) field energy product given in units of megagauss × oersted, MGOe, equivalent to 7957.75 J/m^3 in the SI system. Thus the neodymium–iron–boron (NdFeB) magnet rated at the energy product of 50 MGOe (3.98×10^5 J/m^5) has a capability of exerting a force on paramagnetic or superparamagnetic substance that is up to 100 times higher than that of an Alnico magnet rated at five MGOe (assuming the same geometrical magnet configuration and no demagnetization effects). Another important property of the field variable $\frac{B^2}{2\mu_0}$ is that it has a dimension of pressure (in pascals) and as such plays an important role in magnetohydrodynamics and ferrohydrodynamics, where it is referred to as the magnetic field pressure (Rosensweig 1997). Thus Eq. (4) provides a link between the magnetohydrodynamics and a special case of the magnetic force on discrete particles (cells) in continuous media.

2.2 Note on the Magnetic Susceptibility

There are a bewildering number of definitions of the magnetic susceptibility encountered in the scientific literature, reflecting the depth and width of research and applications of the electromagnetic phenomena, and a nearly 200 year history of rigorous, quantitative materials' property determinations. The task of recalculating one type of magnetic susceptibility to another could be quite daunting, especially to a novice to the magnetic cell separation literature, yet necessary for any meaningful comparison between various magnetic separation systems. A brief summary of the most frequently used formulas is provided below. The problem is compounded by different systems of units used in the literature, which further complicates an effective communication in such an interdisciplinary field that is magnetic cell separation. The comparison between the two most relevant systems of unit important for the magnetic separation topic, electromagnetic Gauss system of units (centimeter–gram–second–coulomb, EM CGS), and the International System of units (meter–kg–second–ampere, MKSA, or SI) is illustrated in Table 1. The SI system of units is used in this chapter.

2.2.1 Volume Magnetic Susceptibility

The susceptibility χ used in Eq. (3) is the volume magnetic susceptibility. It has the desirable feature of being a dimensionless quantity and a simple physical interpretation as a ratio of the magnetization of matter (more on magnetization below), M, to the imposed magnetic field in the absence of matter, H:

$$\chi = \frac{M}{H}. \tag{5}$$

Both M and H are in the units of Å/m. The volume magnetic susceptibility is the standard magnetic susceptibility in the physics literature and is occasionally referred to simply as the magnetic susceptibility.

Table 1 Magnetic susceptibility conversion factors

Susceptibility designation	Symbol	χ (EMU CGS units)	χ (SI units)	To obtain value in SI units, multiply value in EMU CGS units by
Volume	χ	1	1	4π
Mass	χ_g	$\frac{cm^3}{g}$	$\frac{m^3}{kg}$	$\frac{4\pi}{1000}$
Specific	χ_g	$\frac{cm^3}{g}$	$\frac{m^3}{kg}$	$\frac{4\pi}{1000}$
Molar	χ_N	$\frac{cm^3}{mol}$	$\frac{m^3}{mol}$ or $\frac{m^3}{kmol}$	$\frac{4\pi}{10^6}$ or $\frac{4\pi}{1000}$, respectively
One-gram-formula-weight	χ'_N	$\frac{cm^3}{mol}$	$\frac{m^3}{mol}$ or $\frac{m^3}{kmol}$	$\frac{4\pi}{10^6}$ or $\frac{4\pi}{1000}$, respectively

2.2.2 Mass (or Specific) Magnetic Susceptibility

The mass magnetic susceptibility, χ_g, arises when the volume of substance is replaced by its mass in Eq. (1), as is the case in many practical applications for which it is easier to determine the mass (by way of the weight) than the volume of substance, such as for dry matter. The conversion of the mass magnetic susceptibility to volume magnetic susceptibility requires determination of the mass density, ρ of the substance:

$$\chi = \chi_g \rho \tag{6}$$

The unit of the mass (or specific) magnetic susceptibility is the inverse of the mass density, $[\chi_g] = \mathrm{m}^3/\mathrm{kg}$.

2.2.3 Molar Magnetic Susceptibility

The molar magnetic susceptibility, χ_N arises from measurements of known molar amounts of the substance, and in order to recalculate it to the standard volume magnetic susceptibility, a known molar concentration, c_N (molarity, in units of mol/L) is required:

$$\chi = \chi_N c_N \times 1000, \tag{7}$$

where the factor 1000 accounts for the conversion of the molarity, c_N, to mol/m^3. The unit of the molar magnetic susceptibility typically encountered in the literature is L/mol, and in the proper SI units it is $[\chi_N] = \mathrm{m}^3/\mathrm{mol}$.

2.2.4 One-Gram-Formula-Weight Magnetic Susceptibility

The one-gram-formula-weight susceptibility, χ'_N also arises from measurements of known molar amounts, but unlike the molar magnetic susceptibility, the mass and the volume of the substance are required to recalculate it to the standard volume magnetic susceptibility. For known mass density, ρ and the molecular weight, M_w of the substance, one obtains:

$$\chi = \chi'_N \frac{\rho}{M_w} \tag{8}$$

Again, care is required to express ρ and M_w in the SI units (kg/m^3 and kg/mol) rather than the customary CGS units (g/cm^3 and g/mol). The units of the one-gram-formula-weight magnetic susceptibility are the same as the molar susceptibility, $[\chi'_N] = \mathrm{m}^3/\mathrm{mol}$. The significance of this type of magnetic susceptibility is that it is occasionally used in the reference books in physics and chemistry, a carryover from older literature.

2.2.5 Magnetic Susceptibility of a Mixture (or Bulk Magnetic Susceptibility)

For a compound substance, the volume magnetic susceptibility is the weighted sum of the component susceptibilities, with the volume fraction as the weighting factor:

$$\chi = \sum_{i=1}^{N} \phi_i \chi_i, \tag{9}$$

where χ_i is the volume magnetic susceptibility of the ith component with the fractional volume of $\phi_i = V_i/V$, $i = 1 \ldots, N$ and V is the total volume of the sample.

2.2.6 Magnetic Susceptibility Conversion Factor Between the CGS and SI System of Units

For the properly defined volume magnetic susceptibilities in the two units systems, the conversion factor is 4π, so that the susceptibility in the SI units is 4π-times larger than that in the CGS units. For instance, water volume susceptibility (CGS) is -0.72×10^{-6}, that in the SI system of units (SI) is -9.04×10^{-6}.

3 Basic Magnetic Properties of Matter

The introduction of matter in the magnetic field modifies the field and the difference between the field measured in the matter, **B** and the field in free space, **H** is the matter magnetization:

$$\mathbf{M} = \frac{\mathbf{B}}{\mu_0} - \mathbf{H} \tag{10}$$

Here again the constant μ_0 is the unit conversion factor. In the absence of matter (in free space) or for very weakly magnetized substances ($|M| \approx 1$ A/m) typical of air, water and applications in biology, magnetization vanishes or is assumed negligible and the B field equals the H field, $\mathbf{B} = \mu_0 \mathbf{H}$. For strongly magnetic materials, the magnetization may far exceed the applied field H, often by several orders of magnitude (iron). Because of the difference in the response to the applied magnetic field, the materials are classified as (1) diamagnetic, weakly magnetized in the opposite direction to the applied field, (2) paramagnetic, moderately magnetized in the direction of the applied field, and (3) ferromagnetic, strongly magnetized in the direction of the applied field. The magnetic properties of matter are directly related to its molecular composition and the topic far exceeds the scope of this chapter. There are many excellent introductory tests and advanced textbooks covering various aspects of the magnetic properties of matter (Jiles 2016).

Suffices to say that magnetic materials are at the heart of the key technologies of modern life, including information technology (hard disk drives and mass information storage), microwave ovens (based on magnetron), reusable energy technology (wind turbines), electric cars, and small electric helicopters (drones) just to name the few. Closer to the topic of this chapter, the rapid progress in the synthesis and characterization of magnetic microparticles and nanoparticles made it possible to design and implement new, high sensitivity diagnostic tests, MRI contrast agent, targeted hyperthermia for localized tumor treatment, and the magnetic cell separation (Jiles 2016; Krishnan 2016). Therefore, the topic of material magnetization will be treated here only briefly, focusing on the aspects important for magnetic cell separation.

3.1 Linearly Magnetizable Matter

A linear relationship between the magnetization and the applied field is characteristic of diamagnetic and paramagnetic substances, with the volume magnetic susceptibility as a proportionality constant, χ (Eq. 5). The diamagnetic substances are repulsed by the magnetic field and the paramagnetic substance is attracted by it, as already mentioned above. Illustrative examples are discussed below.

3.1.1 Diamagnetic Matter

The diamagnetism is present in all types of substances because it is related to subatomic properties of matter. For relatively weak magnetic fields, its presence is negligible and in the presence of paramagnetic and ferromagnetic effects, it is usually masked by them because it is the weakest of the three. Nevertheless, for accurate susceptibility determination, the diamagnetic contributions from the sample constituents cannot be neglected, especially if those constituents take up a significant volume fraction of the sample (Eq. 8), such as water in the cell (70 % v/v or higher). For sufficiently high magnetic fields and gradients, the diamagnetic effects become appreciable and have been proposed for use in practical applications, such as diamagnetic separation (Peyman et al. 2009; Hirota et al. 2004; Mirica et al. 2009, 2010; Vojtisek et al. 2012). To estimate the magnitude of the magnetic field and gradient necessary to suspend a water droplet in the air, one compares the magnetic force (Eq. 4) to the weight ($\rho V g$) of the droplet:

$$\frac{F_\mathrm{g}}{F_\mathrm{m}} = \frac{\rho V g}{\chi^V \frac{\mathrm{d}}{\mathrm{d}x}\left(\frac{B^2}{2\mu_0}\right)} = \frac{\rho}{\chi} \cdot \frac{2\mu_0 g}{\frac{\mathrm{d}B^2}{\mathrm{d}x}} \quad \overset{F_\mathrm{m}=F_\mathrm{g}}{\longrightarrow} \quad \frac{\mathrm{d}B^2}{\mathrm{d}x} = 2\mu_0 g \frac{\rho}{\chi}, \tag{11}$$

where $\rho = 1000\ \mathrm{kg/m^3}$ is the water mass density, $g = 9.81\ \mathrm{m/s^2}$ is the standard gravitational acceleration, $\chi = -9.05 \times 10^{-6}$ and $\mu_0 = 4\pi \times 10^{-7}\ \mathrm{T\,m/A}$. Note that the volume V of droplet dropped out of the equation. No correction for the

air density and air magnetic susceptibility was made in Eq. (11). The resulting field energy density gradient required to suspend the water droplet in the air is 2720 T^2/m, which could be achieved, for instance, in a configuration of field gradient of 272 T/m and field magnitude of 10 T. This has been experimentally demonstrated using superconducting magnets (Hirota et al. 2004) and is within the reach of permanent magnets and microdroplets, for which the field gradients could be made much higher to compensate for the lower available magnetic field, for instance 1500 T/m and field of 1.82 T.

The majority of biological material is diamagnetic with a few important exceptions, such as hemoglobin and its derivatives (Zborowski et al. 2003), ferritin (Zborowski et al. 1995), magnetosomes in magnetotactic bacteria (Posfai et al. 2013), and endospores of *Bacillus thuringiensis* (Melnik et al. 2007). The bulk magnetic susceptibility of eukaryotic organisms is diamagnetic as demonstrated by magnetic levitation of whole organisms, notably frogs and strawberries (Simon and Geim 2000).

3.1.2 Paramagnetic Matter

Unlike diamagnetic matter, paramagnetic matter consists of atomic or molecular permanent magnetic dipoles whose magnitude does not depend on the applied magnetic field, in particular, they do not vanish in the absence of the magnetic field. Rather, their spatial orientation depends on the magnetic field—the higher the field, the higher the degree of alignment with the local field vector. The unit atomic dipole moment is Bohr magneton, $\mu_B = 9.274 \times 10^{-24}$ J/tesla (J/T). A good first approximation of the net magnetization of a mole of paramagnetic material per unit of the applied magnetic field is that of an ideal gas of elementary magnetic dipoles, μ_A at the absolute temperature T, due to Paul Langevin (Bozorth 1993). In the limit of low field, the molar magnetic susceptibility does not depend on the applied field and is a quadratic function of the elementary magnetic dipole moment, μ_A and an inverse function of the temperature:

$$\chi_N = \frac{N_A \mu_0 \mu_A^2}{3kT}, \tag{12}$$

where $k = 1.38 \times 10^{-23}$ J/kelvin (J/K) is the Boltzmann constant and $N_A = 6.022 \times 10^{23}$ is the Avogadro number. With increasing applied field the molar magnetization departs from linearity and it becomes a (Langevin) function of the applied field, reaching saturation at high fields. Further refinements include correction to temperature T by replacing it by $T - T_C$, where T_C is the Curie temperature below which the elementary dipole moments become frozen in space, important in the description of ferromagnetic materials (see below). Quantum mechanical effects are introduced by replacing Boltzmann statistics of the elementary dipole moment distribution by quantized states statistics limiting the number of allowable dipole orientations relative to the applied field vector (due to Brillouin) (Bozorth 1993). This was used by Pauling and Coryell (1936) to

demonstrate consistency of the quantum mechanical model of chemical bond with experimental measurements of the magnetic susceptibility using hemoglobin and its derivatives as an example.

Examples of paramagnetic substances include certain lanthanides and their aqueous solutions. For instance, gadolinium has the fourth highest magnetic moment of all the elements (7.95 Bohr magnetons), significantly higher than elemental iron (2.2 Bohr magnetons) (Bozorth 1993). Correspondingly, the molar susceptibility of Gd^{3+} is 0.34 in room temperature. The high magnetic moment, plus the extreme stability of the Gd–DTPA complex, made it a contrast agent of choice for MRI applications. Commercial preparations of chelated gadolinium, such as Magnevist (Berlex Labs, Richmond, CA, USA) and Optimark (Mallinckrodt Inc., St. Louis, MO, USA) were used but had to be withdrawn from the market because of kidney toxicity. The strictly paramagnetic behavior of lanthanide solutions is important for calibration of the instruments used for measuring cell magnetophoresis by cell tracking velocimetry (CTV) (Moore et al. 2004; Zhang et al. 2005). Paramagnetic solutions of erbium have been evaluated for use as the cell magnetization reagents for magnetic cell separation (Russell et al. 1987; Zborowski et al. 1992).

Another example of paramagnetic compound important in the context of magnetic cell separation is hemoglobin, the oxygen-carrying protein in red blood cells. The paramagnetic contribution comes from the heme group but not from the globin part, and only when the hemoglobin is dissociated from the oxygen molecule (deoxyhemoglobin). The effective magnetic moment of the deoxy heme group is 5.46 Bohr magnetons, and the total paramagnetic contribution of the heme increases to four times that value because of the presence of four heme groups in the hemoglobin molecule. With the binding of the oxygen molecule, the electronic structure of the heme group changes so that its magnetic dipole moment vanishes (Pauling and Coryell 1936). The paramagnetic forces acting on deoxygenated erythrocytes are sufficiently high to observe their motion in the magnetic field (Zborowski et al. 2003).

3.2 Superparamagnetic Microparticles

The atomic structure of certain metals, notably iron, favors coordination of elemental magnetic dipole moments below Curie temperature over the distances of hundreds of atom diameters. The effect is known as the ferromagnetism (Jiles 2016; Bozorth 1993). This gives rise to a strong magnetization of the volume of such coordinated magnetic moments, known as the magnetic domain (Jakubovics 1994). The magnetic properties of ferromagnets depend, among other things, on their size. In particular, if the size of a ferromagnetic material is equal to or smaller than that of a magnetic domain, typically on the order of 10 nm, then such materials are extremely hard to demagnetize and behave like single but large magnetic dipoles (Krishnan 2010). The magnetic moment of such magnetic domain

dipoles can reach 10^5 Bohr magnetons (Gider et al. 1995). The collective behavior of such nanoparticles, including the volume magnetization of their liquid suspension, is similar to that of paramagnetic solutions except that it is much stronger (Rosensweig 1997). In particular, the magnetization curve of a superparamagnetic colloid does not depend on previous history of magnetization (no hysteresis) and ideally crosses zero. For that reason such a dispersed phase came to be known as "superparamagnetic". Superparamagnetic particles have many interesting properties and are a subject of active research and applications. In particular, because of their small size and high magnetic moment, and in the case of iron, relatively low toxicity, they are an ideal component of magnetic cell separation schemes. That particular class of magnetic particles is often referred to as "superparamagnetic iron oxide nanoparticles", or SPIONs, in the magnetic cell separation literature (Thanh 2012). All commercial magnetic cell separation systems operate on the basis of selective attachment of superparamagnetic particle to target cells and their removal from suspension by the applied magnetic field. From Eqs. (4), (7), (9), and (12), and for known composition and physical properties of SPIONs one calculates that it takes only a few SPIONs to convert the average volume magnetic susceptibility of the cell–SPION complex from diamagnetic to paramagnetic and thus isolate it magnetically from an aqueous suspension of unlabeled cells. The high specificity of SPIONs to a particular cell type is achieved by conjugating it to a ligand such as a monoclonal antibody that has high specificity to that particular cell type (Grützkau and Radbruch 2010). SPION suspensions have other biomedical uses, such MRI contrast agents, replacing chelated gadolinium solutions because of their lower toxicity. They have been considered for applications to tumor-targeted hyperthermia although their mechanism of action is unclear because they lack hysteresis and therefore do not dissipate demagnetization energy. They gave rise to a new body imaging technique, termed "Magnetic Particle Imaging" (MPI) that provides information about SPION distribution in the body similar to the information provided by an MRI contrast agent but at a much lower cost of the capital equipment as no large, superconducting MRI magnets are required but only a set of Helmholtz coils for the imaging (Krishnan 2016). The preparation of magnetic particles for biomedical applications, including cell separation has to take into account not only the magnetic properties of the particle, but also its biological activity, including toxicity and biocompatibility (Hafeli et al. 2008).

3.3 Ferromagnetism and Permanent Magnets

Large, multi-domain structures in the order of centimeters form permanent magnets that have been known since antiquity. They gave the name to the science of magnetic phenomena, thought to be derived from an ancient site of the magnetic mineral mining in Turkey's Aegean Region. The mineral, magnetite, consists of a mixture of iron oxides at different oxidation states, 2+ and 3+, with the chemical

formula designated as Fe_3O_4. The synthesis and characterization of permanent magnet materials is a very active part of materials science and engineering, and the magnetic field intensity generated by the permanent magnet has grown exponentially since 1940s. Because their magnetic properties are qualitatively comparable to those of the natural magnetic mineral consisting of iron oxide, they are classified as "ferromagnets" and the associated phenomena as "ferromagnetism". Pure metallic iron, Fe is ferromagnetic up to its Curie temperature of 770 °C, above which it becomes paramagnetic (Bozorth 1993). In addition to iron, cobalt and nickel also exhibit ferromagnetic properties, and are used in combination with iron, as alloys, for permanent magnet production (Al–Ni–Co, or Alnico). The current, widely used commercial magnets are alloys of iron with a rare earth element, neodymium, and boron, $Nd_2Fe_{14}B$, capable of generating at their surface the magnetic fields in excess of 1 T. They combine the desirable features of high magnetization (high remanence, up to 1.3 T), resistance to demagnetization (high coercivity, equivalent to more than 1 T), reasonably high Curie temperature (in excess of 300 °C, although their magnetization starts to degrade at much lower temperature, at around 150 °C), and a relatively low price (at around USD 100 per kilogram). Permanent magnets become indispensable for green energy technology development because they are a critical part of wind turbine generator (three metric tons of NdFeB magnets per megawatt) and became an important element of electric cars (in excess of 2 kg NdFeB per car). The NdFeB magnets are also a key part of a rapidly growing industry of unmanned aerial vehicles (UAVs) or drones. The predicted growth in the global use of the permanent magnets leads to concerns about the limited supply of rare earth metals and their becoming an element of strategic importance, leading to renewed interest in research and development of new permanent magnet materials not relying on rare earth metals.

The magnetization of the ferromagnetic materials is determined by the applied magnetic field and their magnetization history (hysteresis) (Fig. 1). In particular, pure metallic iron exhibits the highest saturation magnetization of all permanent magnet materials, $M_s = 2.17$ T. The corresponding effective magnetic dipole moment of iron atom in the elemental iron sample is 2.2 Bohr magnetons. Pure metallic iron is characterized by low saturating field, 15 mT, but also by a low coercivity, 4 mT, which makes it a "soft" magnetic material (easy to demagnetize, unsuitable for magnetic field generation in magnetic structures). It is a good conductor of magnetic flux (high magnetic permeability, $\mu \approx 10^6$) and as such it is a principal component of magnet pole pieces. In contrast, the permanent magnets such as NdFeB are designed for high coercivity (that makes them a "hard" magnetic material) as well as for high remanence, $M_s = 1.3$ T, and as such they are used to generate magnetic field in magnetic structures. The permanent magnet structures are often a combination of soft and hard magnetic materials engineered for optimal generation and conduction of magnetic fluxes, in analogy to Kirchhoff's electric circuit laws.

The second quadrant of the magnetization hysteresis curve is important in describing the properties of permanent magnets. A desirable feature of a

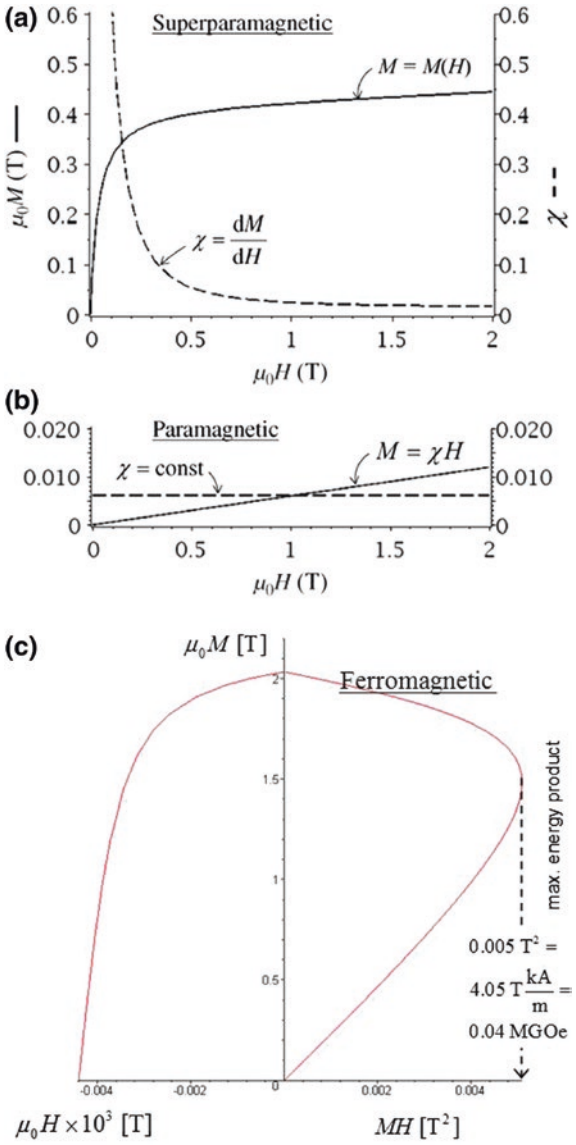

Fig. 1 Magnetization of paramagnetic and ferromagnetic materials. Note lack of hysteresis for paramagnetic materials and superparamagnetic iron oxide nanoparticles, SPIONs. **a** Magnetization M, and volume magnetic susceptibility, χ of the superparamagnetic particles (*top panel*) and **b** a paramagnetic compound (gadolinium chloride) as a function of the applied field H. The free space magnetic permeability constant μ_0 is used to convert units of M to tesla (T). Note differences in ordinate scales (same units as in panel a) and the differences in functional dependence on H between paramagnetic and superparamagnetic particles. **c** Second quadrant of the magnetic hysteresis loop (the demagnetization *curve*) and the corresponding plot of the magnetic energy product, $\mu_0 MH$, showing the maximum energy product of 0.04 MGOe used as a figure of merit for magnet comparison (adapted from Zborowski and Chalmers 2008, 2015, with permission)

permanent magnet is its high remanent magnetization, M_r, and high coercive force, H_c. A plot of the energy product, $\mu_0 M \times H$, for the second quadrant of the magnetization hysteresis loop (Fig. 1c) is used to determine the maximum energy product, a figure of merit when comparing different permanent magnet materials. It is approximately equal to 10 MGOe (mega–gauss–oersted, or 10^6 G × Oe) for Alnico magnets and over 50 MGOe for NdFeB magnets (Hatch and Stelter 2001).

The area enclosed by the hysteresis loop on the *M–B* plot is equal to work expended on the material magnetization, to increase the boundaries of magnetic domains aligned with the field at the cost of contracting boundaries of the magnetic domains that are not, and to realign the atomic dipole moments. The work is dissipated in the form of heat. The large hysteresis of hard magnets, such as ferromagnetic micro- and nanoparticles, makes them an ideal material for application to local thermotherapy using oscillating magnetic field (Krishnan 2010).

The commercial availability of inexpensive, permanent magnets of different shapes and magnetization directions, protected from corrosion by nickel plating, provides unique opportunities for magnetic cell separation. They could be arranged in various configurations for high field [4 T, (Furlani 2001)] and high gradient (Osman et al. 2012) at microscale that makes them an ideal source of the magnetic field for cell separation purposes. Selected examples of such permanent magnet configurations are shown in Fig. 2.

4 Magnetophoresis

Magnetophoresis is a phenomenon of particle motion in viscous media induced by the applied magnetic field. It underlies magnetic cell separation processes relying on differential binding of magnetic label particles to cells. Because it involves motion of cells in aqueous suspensions, it belongs to a part of fluid dynamics that deals with the particle suspensions exposed to external forces, together with gravitational and electrical forces. It is governed by a balance between the local magnetic body forces and viscous stresses on a cell-magnetic label complex that determine the velocity of the labeled cells in suspension and thus the efficiency of magnetic cell separation. The typical approach to describing such particle dynamics is to consider pertinent time constants and characteristic dimensionless numbers entering the equations of motion cell–label complex.

4.1 Cell Reynolds Number

The Reynolds number is a measure of inertial forces with respect to viscous forces and for a spherical cell in a fluid it is:

$$Re = \frac{\rho v D}{\eta}, \tag{13}$$

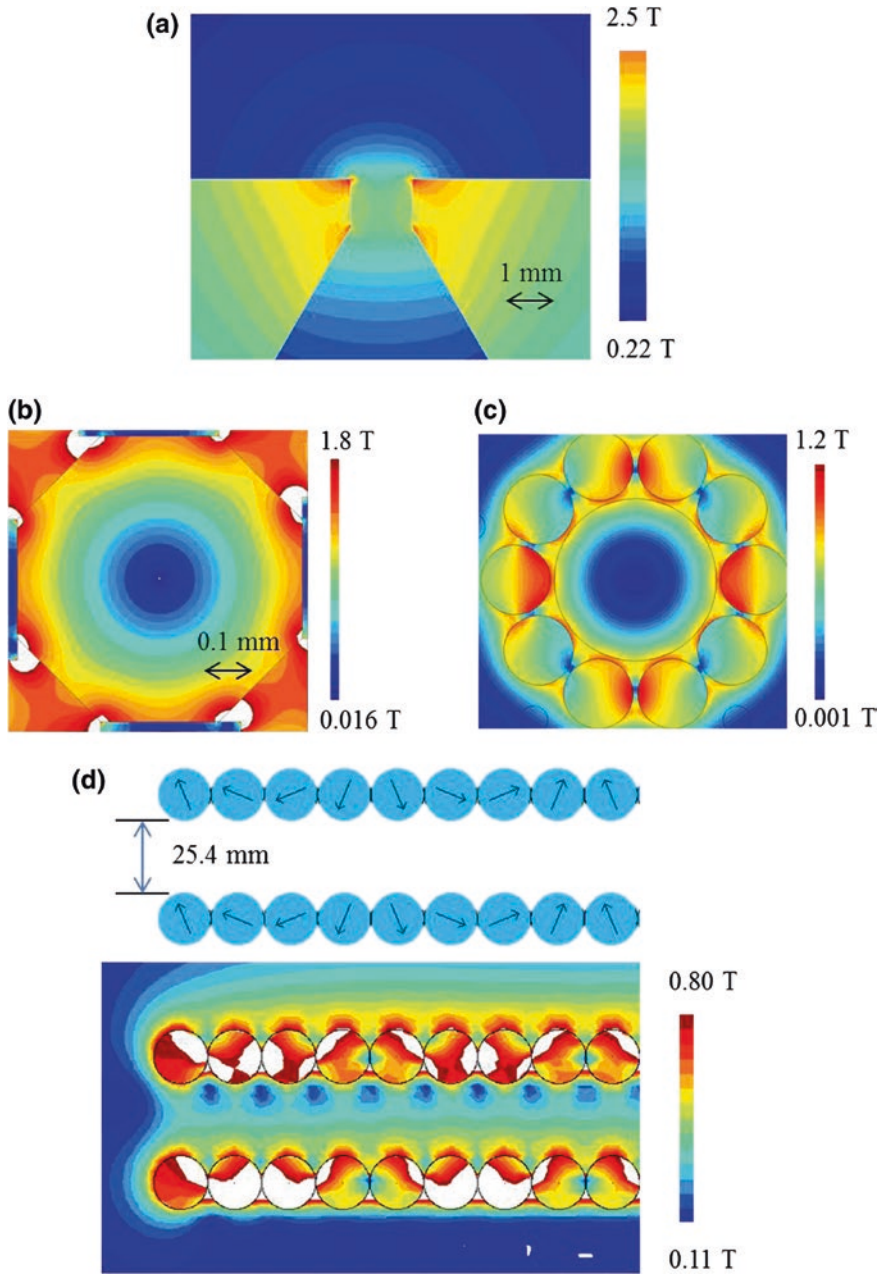

Fig. 2 Examples of permanent magnet configurations for generating high-field gradients. *Arrows* indicated magnetization direction. **a** Interpolar gap between two pentagons, **b** nearly quadrupole field between four rectangles, **c** circular Halbach array of cylindrical magnets magnetized diametrically in quadrupole configuration and **d** two linear Halbach arrays

where ρ is the fluid density, v is the cell velocity relative the bulk of the fluid, D is the cell diameter, and η is the fluid (dynamic) viscosity. For a white blood cell sedimentation in standard laboratory conditions, the representative values are $\rho \approx 1000\ \mathrm{kg/m^3}$, $D = 10\ \mu\mathrm{m} = 10^{-5}\ \mathrm{m}$, $v = 10^{-5}\ \mathrm{m/s}$ (one cell diameter per second), and $\eta = 10^{-3}\ \mathrm{Pa\ s}$ (at nearly 20 °C) resulting in the cell Reynolds number $Re = 10^{-4}$ and showing that the cell inertia is negligible in the description of cell sedimentation. For a (rigid) sphere the value of a critical Reynolds number above which the assumptions about the laminar fluid flow around the sphere do not apply is $Re = 10$. For a viscoelastic body, such as a cell, the onset of flow instabilities is at lower velocity and so critical $Re \approx 1$. Nevertheless, for typical cell diameters (<30 μm) considered in the magnetic cell separation, the cell Re numbers are well within the laminar flow model constraints, even for high cell velocities exceeding 1000 cell diameters per second (up to 30 mm/s). Such high velocities at microscale are possible with the use of SPIONs attached to cells and high magnetic field gradients, although the stress concentration at the point of the SPION attachment to the cell is likely to destroy it before it is reaching such high terminal velocities. In summary, the cell–SPION complex motion analysis under the influence of the applied magnetic field is based on assumptions of laminar flow conditions for typical separation conditions. The laminar flow assumptions apply to cell velocities in the range of several orders of magnitude.

4.2 Inertial Relaxation Time

The negligible inertial force relative to viscous force acting on cells in motion in aqueous media greatly simplify the equations of motion by reducing them to first-order differential equations of cell coordinates as a function of time. The length of time during which the inertial effects play a role is negligibly small and therefore can be omitted in the cell motion analysis:

$$\tau_\mathrm{p} = \frac{m_\mathrm{p}}{f} = \frac{\frac{\pi}{6}D^3\rho_\mathrm{p}}{3\pi\eta D} = \frac{\rho_\mathrm{p}D^2}{18\eta}, \tag{14}$$

where τ_p is the cell inertial relaxation time, m_p is the cell mass, $f = 3\pi\eta D$ is the Stokes friction coefficient, ρ_p is the cell density, D is the cell diameter, and η is the fluid (dynamic) viscosity. Thus for the cell density comparable to that of the aqueous media, $\rho_\mathrm{p} \approx 1000\ \mathrm{kg/m^3}$ and the other parameters as quoted above, $\tau_\mathrm{p} = 5.6\ \mu\mathrm{s}$, which is orders of magnitude shorter than characteristic times involved in the magnetic cell separation, typically tens to hundreds of seconds.

4.3 Stokes Flow

For the cell laminar motion, the viscous drag exerted on a spherical cell is directly proportional to its velocity relative to the bulk fluid:

$$F_{\mathrm{d}} = fv = 3\pi\eta D v, \tag{15}$$

where as before, f is the Stokes friction coefficient, η is the fluid (dynamic) viscosity, D is the cell diameter, and v is the cell velocity relative the bulk of the fluid. The viscous drag is the local reaction force of the viscous media (fluid) to the cell motion imposed by the applied field. Again, taking cell sedimentation as the simplest example of such a motion, the applied field is the difference between the cell weight and its buoyancy:

$$F_{\mathrm{g}} = \frac{\pi}{6} D^3 \left(\rho_{\mathrm{p}} - \rho_{\mathrm{s}}\right) g, \tag{16}$$

where D is the cell diameter, ρ_{p} and ρ_{s} are the cell and the fluid densities, respectively, and $g = 9.81\ \mathrm{m/s^2}$ is the standard gravitational acceleration. Due to the low cell *Re* number and the negligible effect of cell inertia on its sedimentation, Newton's second law of motion takes the form:

$$0 = F_{\mathrm{g}} - F_{\mathrm{d}}, \tag{17}$$

where the minus sign indicates that the drag force is opposed to the applied force, F_{g}. Combining Eqs. (14)–(16) one obtains the cell sedimentation velocity:

$$v = \frac{D^2}{18} \frac{\left(\rho_{\mathrm{p}} - \rho_{\mathrm{s}}\right)}{\eta} g \tag{18}$$

For the white blood cell density of $\rho_{\mathrm{p}} \approx 1050\ \mathrm{kg/m^3}$ the difference in the cell density and that of the aqueous media is $\Delta\rho = \rho_{\mathrm{p}} - \rho_{\mathrm{s}} = 50\ \mathrm{kg/m^3}$ resulting in the sedimentation velocity of $v = 2.7\ \mu\mathrm{m/s}$ or less than one third of the cell diameter per second.

4.4 Cell Sedimentation Coefficient

The ratio of the cell sedimentation terminal velocity to the field acceleration (gravitational or centrifugal) is the cell sedimentation coefficient:

$$s = \frac{v_g}{g} = \frac{D^2\left(\rho_{\mathrm{p}} - \rho_{\mathrm{s}}\right)}{18\eta} \tag{19}$$

which has the dimension of time (compare with Eq. 14). For the centrifugal acceleration fields, the parameter g in the equation above and in Eq. (18) is substituted

by the multiples of the standard gravitational acceleration ("number of g's"). For macromolecular centrifugal separations, the sedimentation coefficient is often quoted in the units of svedbergs, or S, where $1\ S = 10^{-13}$ s. For a representative white blood cell parameters, quoted above, the cell sedimentation coefficient is $s = 0.28\ \mu s$, or $2.8 \times 10^6\ S$. The sedimentation coefficient normalizes the sedimentation velocity of a cell by the acceleration applied to it. It is not dependent on the acceleration but only on the properties of the cell and the media.

4.5 Magnetophoretic Mobility

If the same fluid dynamic model as described above is applied to the cell motion in the magnetic field, then in the absence of gravitational effects, the magnetic field-induced cell velocity is obtained by substituting F_m, Eq. (3), for F_g in Eq. (17), leading to a magnetic analogue of Eq. (18):

$$v_m = \frac{D^2}{18} = \frac{(\chi_p - \chi_s)}{\eta} H \frac{dB}{dx} \tag{20}$$

where the densities of the cell and the fluid were replaced by their volume magnetic susceptibilities, χ_p and χ_s, respectively, and the gravitational field acceleration, g, was replaced by the magnetic field energy density gradient, $H\frac{dB}{dx}$. For the labeled cell–particle complex, the mean magnetic susceptibility of such a complex is much higher than that of the suspending media, which is unlike that for their respective densities, whose difference is small. The resulting magnetic field-induced velocities could be quite high, tens to hundreds cell diameter per second. Such high magnetic field-induced velocities are comparable to cell sedimentation velocities in high centrifugal fields of hundreds of g's.

The magnetophoretic mobility of a cell is its field-induced velocity normalized to the magnetic energy density gradient applied to it:

$$m = \frac{v_m}{H\frac{dB}{dx}} = \frac{D^2}{18} \frac{(\chi_p - \chi_s)}{\eta} \tag{21}$$

For linearly magnetizable media, the magnetophoretic mobility is not dependent on the magnetic field but only on the properties of the cell and the media (similar to the property of the sedimentation coefficient). Unlike the sedimentation coefficient, however, the magnetophoretic mobility is dependent on the field for nonlinear magnetic media, such as superparamagnetic particles and ferrofluids, for which the volume magnetic susceptibility is strongly dependent on the applied field, $\chi = \chi(H)$ (Fig. 1).

A particularly instructive way of characterizing the cell magnetophoresis is by normalizing the magnetic field-induced velocity, v_m, to the sedimentation velocity:

$$\frac{v_{\mathrm{m}}}{v_{\mathrm{g}}} = \frac{\chi_{\mathrm{p}} - \chi_{\mathrm{s}}}{\rho_{\mathrm{p}} - \rho_{\mathrm{s}}} \frac{H\frac{\mathrm{d}B}{\mathrm{d}x}}{g} \equiv \frac{\chi_{\mathrm{p}} - \chi_{\mathrm{s}}}{\rho_{\mathrm{p}} - \rho_{\mathrm{s}}} \frac{S_{\mathrm{m}}}{g} \tag{22}$$

where the symbol $S_m \equiv H\frac{\mathrm{d}B}{\mathrm{d}x}$ is introduced to simplify notation. Thus the dimensionless parameter $v_{\mathrm{m}}/v_{\mathrm{g}}$ describes the effect of the magnetic field on the field-induced cell velocity as a product of two factors: one dependent on the material properties of the cell and the fluid media only, $\frac{\chi_{\mathrm{p}}-\chi_{\mathrm{s}}}{\rho_{\mathrm{p}}-\rho_{\mathrm{s}}}$ and the other dependent on the applied field only, $\frac{S_{\mathrm{m}}}{g}$. For linearly magnetizable materials such separation of variables is exact but not for ferromagnetic and superparamagnetic materials whose magnetization saturates with the applied magnetic field and consequently, the magnetic susceptibility strongly depends on the applied field.

The use of Eq. (22) is illustrated here by comparing the magnetic cell separation to the centrifugal cell separation, a standard separation technique in biology laboratory. For practical purposes, centrifugal acceleration in laboratory centrifuges is quoted in multiples of the standard gravitational acceleration, or "number of g's". In typical laboratory applications, such as red blood cell (RBC) separation from whole blood, the centrifugal field is from 300 to 400 g applied for 15 and 5 min, respectively. Given that one measures the effectiveness of a separation technology by the time of separation, itself being inversely proportional to the field-induced velocity, inspection of Eq. (22) allows one to directly compare the effectiveness of magnetic separation with that of the centrifugal separation. For example, the density difference between a RBC and typical suspending buffer is $\rho_{\mathrm{p}} - \rho_{\mathrm{s}} = 84\ \mathrm{kg/m^3}$, whereas the difference in the volume magnetic susceptibility between a deoxygenated RBC and suspending buffer is on the order of $\chi_{\mathrm{p}} - \chi_{\mathrm{s}} = 5 \times 10^{-6}$ resulting in $\frac{\chi_{\mathrm{p}}-\chi_{\mathrm{s}}}{\rho_{\mathrm{p}}-\rho_{\mathrm{s}}} \approx 6 \times 10^{-8}\ \mathrm{m^3/kg}$. This indicates that in order to produce the magnetic field-induced velocity of the RBC comparable to its sedimentation velocity, $\frac{v_{\mathrm{m}}}{v_{\mathrm{g}}} \approx 1$ the magnetic field gradient to the gravity ($g = 9.81\ \mathrm{m/s^2}$) ratio should be $S_{\mathrm{m}}/g \approx 1.7 \times 10^7\ \mathrm{kg/m^3}$ or $S_{\mathrm{m}} \approx 1.7 \times 10^8\ \mathrm{N/m^3} = 1.7 \times 10^8\ \mathrm{A\,T/m^2}$, equivalent to $207\ \mathrm{T^2/m}$ (because $1\ \mathrm{T} = 1/\mu_0\ \mathrm{A/m} = 1/4\pi \times 10^7\ \mathrm{A/m}$). Considering that $S_{\mathrm{m}} = H\frac{\mathrm{d}B}{\mathrm{d}x} = \frac{1}{2\mu_0}\frac{\mathrm{d}B^2}{\mathrm{d}x}$, the required field gradient in the units of tesla is $2 \times 207\ \mathrm{T^2/m} = 417\ \mathrm{T^2/m}$. The advanced permanent magnet designs used for cell separation are capable of generating $S_{\mathrm{m}} \approx 10^9\ \mathrm{T\,A/m^2}$ (equivalent to $2500\ \mathrm{T^2/m}$) and therefore capable of producing RBC velocity up to six times its sedimentation velocity, thus equivalent to "6 g". This is obviously much lower than the centrifugal acceleration in laboratory centrifuges, by a factor of ~60. The resulting time of the RBC separation would be that much longer if performed over the separation distance equal to the height of the centrifuge tube (10 cm) and therefore quite unrealistic for such applications. Magnetic RBC separation is feasible in thin microfluidics channels, however, where the RBC separation travel distance (typically 250 μm) and thus the separation time can be substantially shortened (by a factor as high as 400) and made comparable to that of the RBC centrifugation.

Binding of SPIONs to cells greatly increases the cell–label magnetic susceptibility contrast relative to the fluid media, $\chi_{\mathrm{p}} - \chi_{\mathrm{s}}$ by up to several order of magnitudes. This results in high magnetic field-induced velocities, equivalent to "300 g" for even moderate field gradients. The limiting factor is the volume of the magnetic field available for the separation.

5 Single Cell Measurement of Magnetophoretic Mobility, Cell Tracking Velocimetry, CTV

The previous discussions have established a theoretical basis for magnetophoresis, and have further extended this introduction to magnetophoresis by normalizing magnetophoresis with sedimentation velocity (Eq. 22). Equation (22) strictly applies to cases of linearly magnetizable materials and as written, would only apply to the intrinsic magnetic susceptibility of a cell or particle, χ_p. Alternatively, cells targeted for separation are routinely labeled with an antibody conjugate to a SPION (i.e., an anti-CD3 antibody conjugated to a MACS® particle). If a submicron SPION is conjugated to a supramicron particle, even if on the order of 10,000 binding events occur, the change in the labeled cell diameter and density is such that Eq. (22) still holds except that the typically very high magnetic susceptibility of the SPION, relative to a cell, would require that the value of χ_p is governed by the relatively small volume of the SPIONs. However, in contrast, when micron sized magnetic microbeads are attached to cells through antibodies, the size and density of the cell microbead conjugate are more closely dictated by the properties of the microbead (e.g., an anti-CD3 antibody conjugated to a Dynabead®) (Zhang et al. 2005).

As with most biological systems, a distribution exists with respect to many cellular properties, be they cell size, magnetic susceptibility, or the number of cell surface markers targeted with antibody–SPION conjugate. Further, the affinity of an antibody for a cell/surface marker can vary from cell to cell as well as antibody clone to antibody clone. To optimize the magnetic manipulation and sorting of cells, it highly desirable to optimize, and characterize the intrinsic magnetic susceptibility of a cell or the magnetic susceptibility imparted to the cell through an antibody–SPION conjugate.

When a cell is labeled with a SPION, mathematically the magnetophoretic mobility has shown to be characterized by

$$m = \frac{\phi_p \beta \, \mathrm{ABC}}{3\pi \eta D_{\mathrm{cell}}} + m_{\mathrm{cell}}, \tag{23}$$

where

$$\phi_p = \left(\chi_p - \chi_f\right) V_p, \quad B < B_{\mathrm{sat}} \tag{24}$$

or

$$\phi_p = \left(\frac{\mu_0 M_{\mathrm{sat}}}{B} - \chi_f\right) V_p, \quad B \geq B_{\mathrm{sat}}, \tag{25}$$

where m_{cell} is the magnetophoretic mobility of the unlabeled cell ϕ_p is the particle–field interaction parameter (equivalent to the particle magnetic polarization), ABC is the antibody binding capacity of a cell, and β is the number of magnetic particles per ABC. As presented in Eqs. (24) and (25), the value of ϕ_p is dependent on whether the SPION becomes saturated (Chalmers et al. 2010).

A number of magnetometer devices exist to measure the magnetic susceptibility of materials, including a Gouy and Faraday balance, vibrating magnetometer, and the superconducting quantum interference device (SQUID). While accurate, these devices only provide bulk measurements of materials and particles, and reflecting this bulk average, are typically reported on a per mass basis. In contrast, Eqs. (22)–(23) are written with respect to a single cell or particle.

To exploit this characteristic, an instrument was developed, Cell Tracking Velocimetry, CTV, which tracks the movement of individual cells in a constant magnetic energy gradient, S_m. Figure 3 presents a schematic diagram of the system. Using digital imaging technology and particle tracking software, it is possible to track on the order of 100–1000 cells at a time and obtain the vertical (sedimentation) and horizontal (magnetic) velocity components of the tracked cells velocity, which correspond to v_m and v_g in Eq. (22). Figure 4 presents a computer screen shoot from an analysis using the CTV to measure the sedimentation and magnetically induced velocity of oxygenated and deoxygenated red blood cells, Fig. 4a, b, respectively. The while lines are computer generated, and correspond to the trajectory the specifically tracked cell has taken over a number of individual frames. The difference between the vertical line in Fig. 4a and the diagonal line in panel (b) corresponds to the constant magnetic energy gradient, S_m, which is operating on the cells in the horizontal, right to left direction. The ratio of these

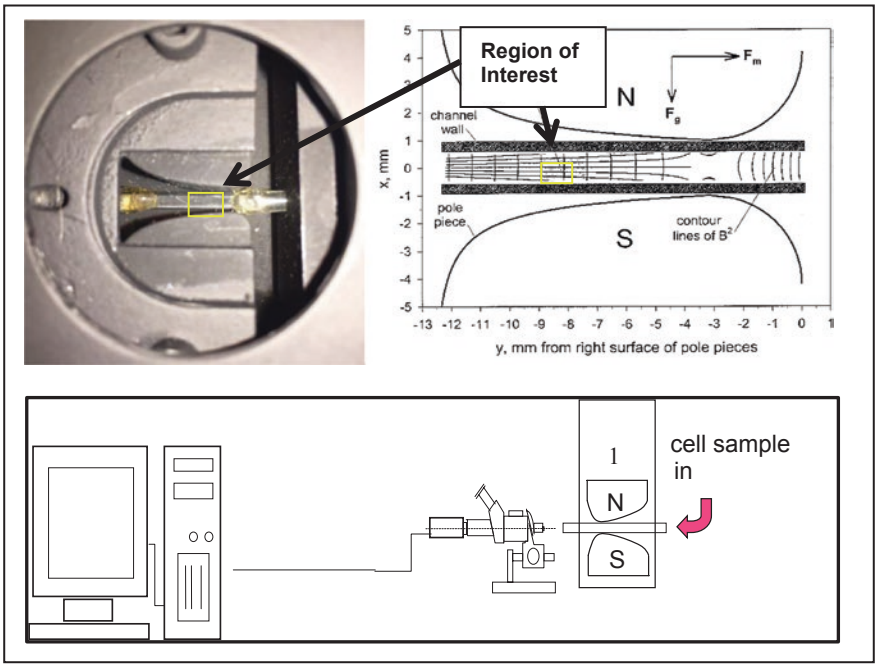

Fig. 3 Schematic diagram of cell tracking velocimetry (CTV) for measuring single-cell magnetophoretic mobility distribution in cell suspensions

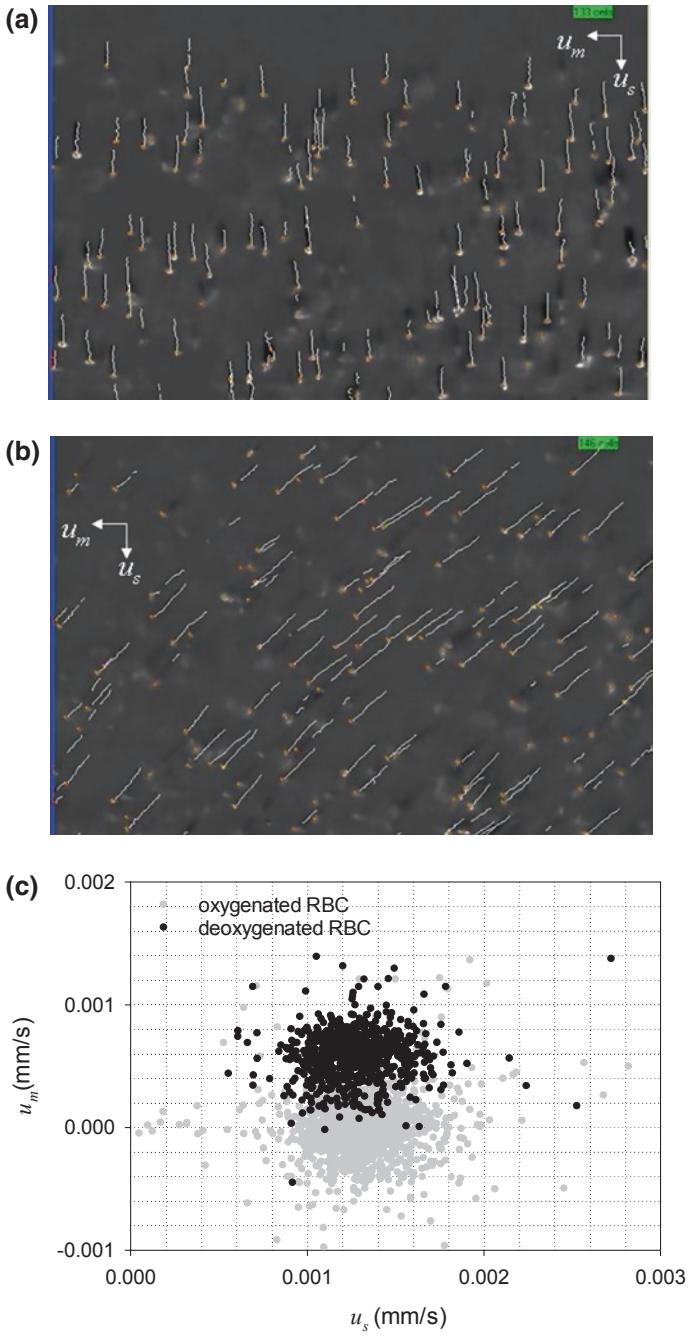

Fig. 4 Screenshots of CTC algorithm of tracked cells. The *white lines* are computer-derived trajectories of the cell as it moves from frame to frame. Panel **a** corresponds to oxygenated human RBCs, while panel **b** corresponds to the same donor deoxygenated, RBCs. Panel **c** is *dot plot* of the oxygenated and deoxygenated RBCs plotting magnetic versus settling velocity

Table 2 Mean volume magnetic susceptibility ($\chi = \mu_0 M/B$, at $B \approx 1$ T) and magnetic polarization (field–particle interaction parameter, $\phi = \chi V = \chi \pi D^3/6$) for selected commercial magnetic beads used for cell tagging (Zhang et al. 2005)

Magnetic beads	Lot nos.	$M_{s,nano\sim 0}/B$ (SI unit system)	Mean diameter (nm)	ϕ ($\times 10^{-25}$ m^3)
Streptavidin-MACS	5,020,305,031	$1.1 \pm 0.3 \times 10^{-3}$	116	8.8 ± 2.1
	5,030,918,049	$1.4 \pm 0.4 \times 10^{-3}$	67.2	2.3 ± 0.6
BD lmag	44,023	$1.4 \pm 0.3 \times 10^{-3}$	231	91 ± 20
Captivate	71 Al-1	$3.8 \pm 1.0 \times 10^{-4}$	136	5.1 ± 1.4
EasySep	2L226593	$3.5 \pm 1.2 \times 10^{-4}$	142	5.4 ± 2.0
	3A317176	$5.5 \pm 1.8 \times 10^{-5}$	160	12 ± 4

horizontal to vertical velocities corresponds directly to the ratio of velocities presented in Eq. (22). Figure 4c presents dot plots of the magnetically induced velocity versus the settling velocity of the oxygenated (gray dots) and the deoxygenated (black dots) of the RBCs presented in Fig. 4a, b.

Beyond measuring the intrinsic magnetization of RBCs, as presented above and in Fig. 4, the CTV system has been extensively used to measure the field interaction parameter, ϕ of a number of commercial SPIONS, (Table 2) as well as the magnetophoretic mobility of a number of different cell types labeled with commercial SPIONs. Figure 5 presents one example in which both the magnetophoretic mobility (and corresponding number of SPIONS) of labeled and unlabeled human lymphocytes when the CD3 surface marker is targeted.

6 Experimental and Theoretical Range of Magnetophoretic Mobility

Tracking the movement of cells, or particles as a result of the imparting of a magnetic force is surprising sensitive. Chalmers et al. (2010) reported that on the order of several hundred commercial SPIONs, nonspecifically bound to a cell can be measured. They further estimated that since a single cell can be tracked with the CTV system, and estimates can be made on the Fe content per SPION, the CTV system has sensitivity on the order of 4.6×10^{-15} g/mL. This compares favorably to an inductively coupled plasma mass spectrometer (ICP-MS), which has typical sensitivity for Fe on the order of 10^{-8} g/mL.

The operational scope of the CTV instrument, including physical and equipment constraints, such as Brownian motion, creeping flow, the diffraction barrier of microscope, wall effect of channel, and software restraints have been previously discussed (Xue 2016) and are summarized in Fig. 6.

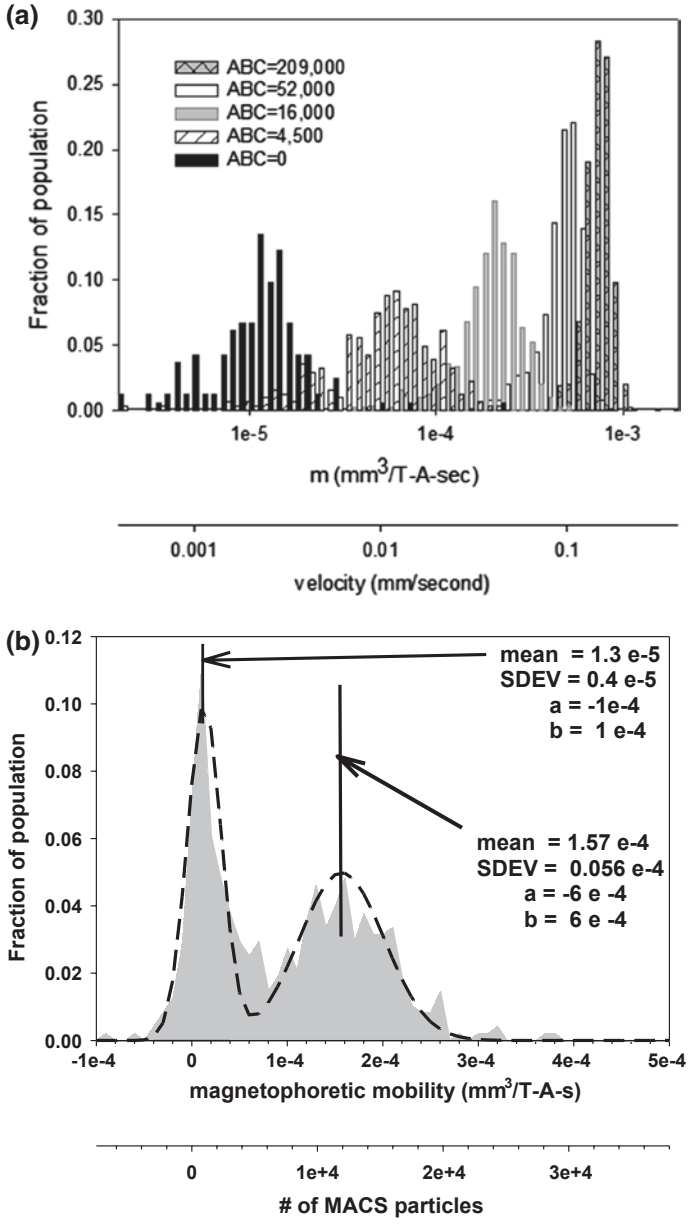

Fig. 5 **a** Histogram of the magnetophoretic mobility as a function of ABC for quantum simply cellular microbeads. These beads were labeled with MACS® Beads (McCloskey et al. 2000). **b** Magnetophoretic mobility of human peripheral blood leukocytes (PBL) labeled with anti-CD3-PE and anti-PE MACS particles. The labeling concentration was 40 μL for the anti-CD3-PE and five times the company recommended value for the anti-PE MACS (Lara et al. 2006)

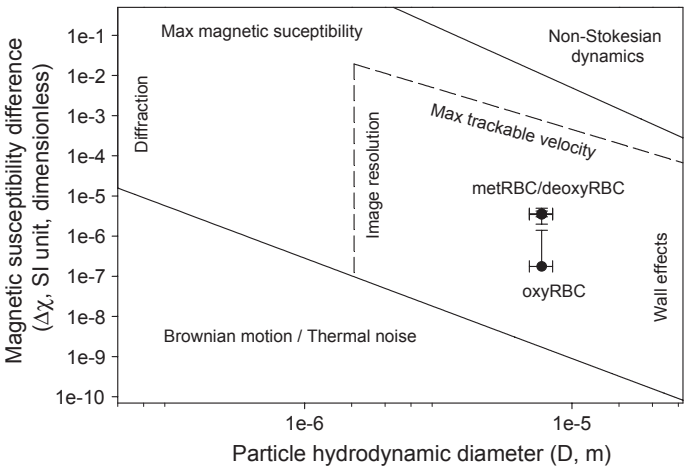

Fig. 6 Operational scope of the CTV approach. *Solid line* corresponds to physical limitation for the method and the *dashed line* presents the limitation for current setup. The result for oxygenated RBCs (oxyRBC), methemoglobin RBCs (metRBC) and deoxygenated RBCs (deoxy) are also shown (*error bar* as standard deviation). The metRBC and deoxyRBC results, which are essentially different, overlap in the figure due to the scale *vertical axis*. The oxyRBC magnetic susceptibility difference only shows upper error, due to the limitation of logarithmic scale of *vertical axis* (Xue 2016)

7 Examples of Various Geometries of Magnetostatic Energy Gradients in Application to Magnetic Cell Separation

7.1 High Gradient Magnetic Separator (HGMS)

The term and the abbreviation "HGMS" in the magnetic cell separation literature is typically limited to secondary effects of the magnetic field on ferromagnetic materials that induce high magnetic field gradients on small surface features of such materials (such as wires) (Watson 1973). Notable early applications include removal of weakly paramagnetic, iron oxide impurities from kaolin clays for high quality porcelain and paper production (Beharrell 2012) and for environmental water treatment, requiring high-field gradients for capture of weakly magnetic contaminants (Nishijima and Takeda 2006). They are particularly well suited for small-scale separation in biology. A primary example is MACS® separation system is based on disposable HGMS columns magnetized by insertion between pole pieces of a permanent magnet, and colloidal magnetic particles for cell labeling (Miltenyi et al. 1990). The columns are filled with a matrix of soft magnetic material in the shape of submillimeter diameter wires or spheres that generate high magnetic field gradient on their surfaces in the presence of the external magnetic field. The permanent magnet field approaches 1 T and the gradients up to 1000 T/m in the submillimeter

interstitial spaces of the magnetized matrix (Kantor et al. 1998). The matrix provides a highly developed surface for magnetic cell capture in the small volume of the column. Upon removal from the magnet, the matrix is demagnetized allowing release of the captured cellular material from the column. The MiniMACS® columns are only 7 mm in diameter and 50 mm long but are capable of separating up 10^6 labeled cells from a mixture of up to 10^7 cells in a volume of 1 mL in a matter of several minutes. The system has been developed over 25 years ago (Miltenyi Biotec GmbH, Bergisch Gladbach, Germany) and has diversified since into many different column and magnet sizes, selection of magnetic reagents and modes of operation, including an automated capture-and-release system (Grützkau and Radbruch 2010). The company provides a wide selection of the magnetic labeling reagents, including mouse monoclonal antibodies against major human cell clusters of differentiation (CD) and anti-mouse antibodies conjugated to magnetic beads for added versatility by the indirect magnetic labeling. It provides such staples of immunocytochemistry as avidin–biotin labeling reagents and fluorescence labeling reagents adapted to magnetic cell labeling (http://www.miltenyibiotec.com). The simplicity of operation and compatibility with the immunocytochemistry protocols contributed to its wide adoption in biology research and laboratory medicine. It has established the magnetic cell separation as one of the standard laboratory techniques, alongside centrifugation and fluorescence-activated cell sorting (FACS).

7.2 Open Gradient Magnetic Separator (OGMS)

The term describes a direct effect of the applied magnetic field on the separands not requiring ferromagnetic matrix inserts for separation and is occasionally used to differentiate it better from the HGMS principle of operation (Fukui et al. 2002). The advantages include independence of specialized, dedicated HGMS columns and thus greater flexibility in the choice of separation vessels and lower cost (Caralla et al. 2013; Joshi et al. 2015; http://www.easysep.com). The disadvantage is a relatively low magnetic field gradient, typically two orders of magnitude smaller than what is possible inside the HGMS column, which for the cell separation applications necessitates the use of more magnetic beads to achieve the same magnetic ponderomotive force acting on the cell–label complex. Such higher magnetic moment per bead is most readily achieved by increasing the magnetic bead size, as the magnetic moment increases with the third power of the bead diameter (with the other bead parameters held constant). The prime example of such a highly magnetic bead is Dynabead® manufactured in the range of diameters from 1 (MyOne™) to 4.5 μm (M450). Its high magnetic moment offers flexibility in the design of the magnetic separators which makes it a popular choice in applications to clinical diagnostic tests (Gijs et al. 2010; Ugelstad et al. 1993; https://www.thermofisher.com/us/en/home/brands/product-brand/dynal.html). Its relatively large surface area (as compared to the colloidal magnetic beads) makes it a suitable solid substrate for the molecular biology applications.

Apart from Dynabead brand, there is a large selection of superparamagnetic microbeads available on the market that are tailored to almost any specialized magnetic separation application of the OGMS type. They are often, but not always, sold together with dedicated magnet systems that are compatible with all typical biology laboratory containers, such as centrifuge tubes, multiwell plates, flasks, etc. (Gutierrez et al. 2015). Examples of the OGMS separators and dedicated magnetic microbeads include StemCell system (http://www.easysep.com) built around a multipole magnet in a cylindrical structure that fits 15 mL conical tubes and Becton Dickinson Immunosciences magnet rack (https://m.bdbiosciences.com/us/reagents/research/magnetic-cell-separation/other-species-cell-separation-reagents/cell-separation-magnet/p/55 2311) that fits six such tubes simultaneously.

7.3 Equilibrium Versus Steady-State Magnetic Separation

The majority of HGMS and OGMS systems described above operate in an equilibrium mode, in which the magnetic fraction is precipitated from the suspension on a suitable substrate surface and held there while the unseparated (nonmagnetic) fraction is removed and replaced with a clear solution. For a typical HGMS application (such as using Miltenyi MACS® system) the volumetric flow rate of the cell suspension through the HGMS column matches residence time necessary for the cell to reach the ferromagnetic matrix surface from the bulk suspension. For typical OGMS applications, the same is accomplished by letting the stationary cell suspension remain in the magnetic field for a sufficient length of time for all the magnetically labeled cells to travel to the vessel wall. Providing that the magnetic microbead saturation magnetization matches the available magnetic field and gradient, and the volume of the cell mixture is fully exposed to the magnetic field, such separations are accomplished quickly and with minimum intervention from the user. They are well suited for typical biological research laboratory protocols requiring small batches of cell suspensions (5–10 mL) and relatively small cell numbers (on the order of 10^8). For well-defined cell surface markers (such found in the CD library) and matching monoclonal antibodies (often available as ready-made cell labeling reagents from commercial companies) they are highly competitive in terms of specificity, cell viability, processing time, labor and equipment cost compared to alternative methods, such as sorting by flow cytometry (FACS).

The equilibrium mode operation of the HGMS and OGMS systems is dependent on the volume of cell batches required for separation, which is a limiting factor for large-scale cell separation, such as in application to cellular therapy. Such mode of operation is prone to the breakthrough effects due to the HGMS column overloading with the magnetically labeled cells, or the labeled cell losses in the wash fluid due to the limited cell access to the container wall surface inside the OGMS magnet. A solution is to either increase the physical dimensions of the

HGMS columns (Grützkau and Radbruch 2010) or the OGMS magnets (http://www.sepmag.eu/), or operate them in an intermittent fashion consisting of fill-capture-evacuate-wash cycles. An alternative approach is to redesign the system for a continuous flow operation with the magnetic cell fraction forming a continuous stream, split from the nonmagnetic fraction at the flow outlet (Pamme and Manz 2004; Hoyos et al. 2011). The first two approaches rely on the equilibrium mode separation and are basis of operation of large HGMS columns, automated HGMS systems for clinical applications [CliniMACS® line of products (http://www.miltenyibiotec.com)] and large OGMS flask systems (http://www.sepmag.eu/).

The continuous flow operation requires maintaining a dynamic equilibrium, or a steady state between the magnetic body forces and the viscous stress forces of the carrier solution acting on the cell–label complex in order to keep the magnetic cell complex in suspension, which brings additional elements of complexity to the system but also new opportunities of better separation (Takayasu et al. 2000). The general principle is described by the theory of field-flow fractionation (FFF) and its variant, split-flow thin (SPLITT) fractionation first developed in application to macromolecular separations using centrifugal, electric, and thermophoretic fields and subsequently extended to particulate suspension separations, including cell separation, by Giddings (1985) and Giddings et al. (Hoyos et al. 2011; Williams et al. 2010). The configuration of recent microfluidic channels is similar to that of a Hele–Shaw cell so that the separation dynamics can be reduced to a two-dimensional problem, whereby the applied magnetic forces are perpendicular to the advection forces resulting in spreading of the magnetically susceptible cell–label complexes across the flow width and their separation between multiple channel outflow ports (Lenshof and Laurell 2010).

The steady-state magnetic cell sorting in flowing suspensions include cell magnetophoretic fractionation according to the level of cell surface marker expression (Fig. 7) when used in combination with the colloidal magnetic labeling reagents (Schneider et al. 2010; Leigh et al. 2005; Adams et al. 2008), cell fractionation using magnetic repulsion in the magnetic susceptibility-modified carrier solutions (Watarai and Namba 2001; Moore et al. 2004; Peyman et al. 2009; Hwang et al. 1984; Tasoglu et al. 2015; Hahn and Park 2011) and a combination of magnetic and fluid dynamics inertial forces (Karabacak et al. 2014; Karle et al. 2010). The addition of fluid forces to the separation mechanism creates new opportunities for innovative design of magnetic elements (Adams et al. 2008; Gao et al. 2015) and a creative design of chemical reaction sequences on a cell–label complex crossing laminar streams of substrate solutions (Pamme 2012). The steady-state magnetic separation combined with a continuous flow operation offers the advantages of a large-scale separation (Doctor et al. 1986; Williams et al. 1999) without the added cost of the equipment scale-up and process automation, inherent to the equilibrium separation. The new opportunities of a better flow control in the microfluidics channels and matching magnetic field designs are being realized in numerous, innovative laboratory prototypes and commercial separators (Sahore and Fritsch 2014; Weston et al. 2010).

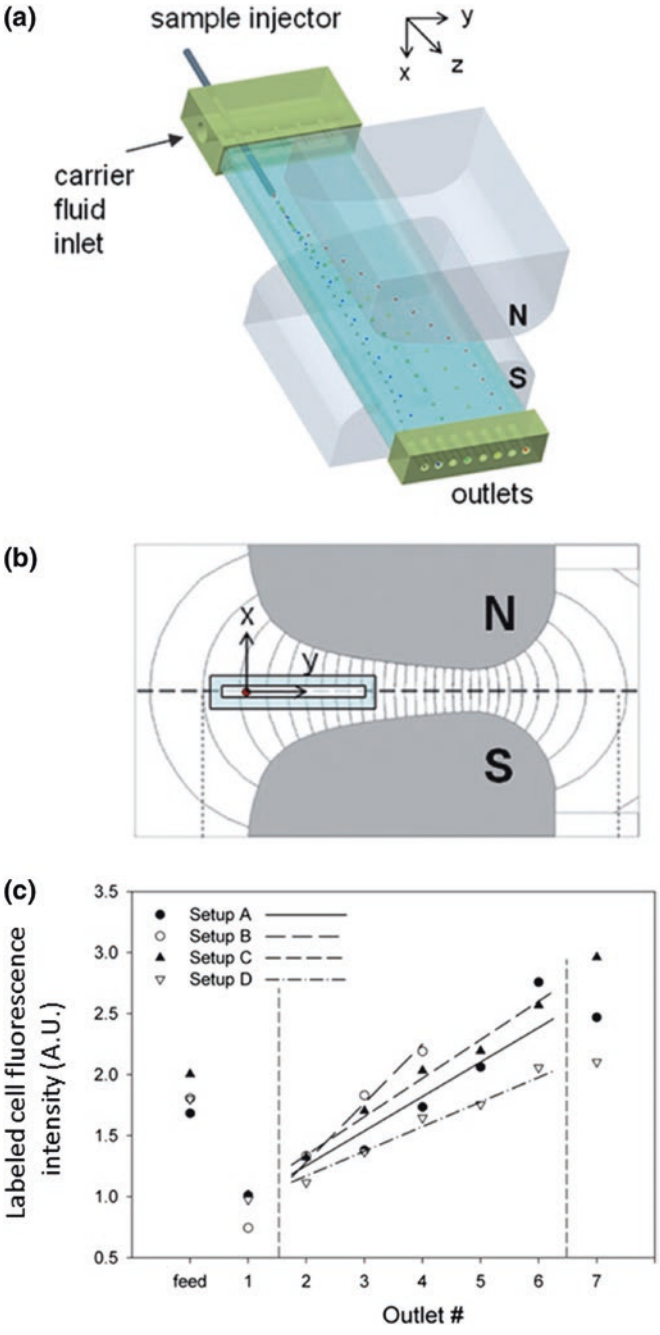
(a)
sample injector
y
x
z
carrier
fluid
inlet
N
S
outlets
(b)
N
X
y
S
(c)
Setup A
Setup B
Setup C
Setup D
Labeled cell fluorescence intensity (A.U.)
3.5
3.0
2.5
2.0
1.5
1.0
0.5
feed
1
2
3
4
5
6
7
Outlet #

◀ **Fig. 7** **a** Principle of the dipole magnetic fractionator. The feed (cell suspension) is continuously injected into a carrier fluid flow inside a rectangular glass channel. The sample flows downward (z = direction) in the channel and is deflected from its flow path by an interaction with the magnetic field (y = direction) generated by a dipole magnet (not to scale). The sample is fractionated based on the strength of interaction with the magnetic field and collected in eight different outlet fractions. **b** Magnetic field lines inside the interpolar gap. **c** Labeled cell fluorescence intensity in arbitrary units (A.U.) for different cell fractions and different transport lamina distribution (for different outlet flow distribution setups *A–D*). Note the increase in the mean number of PE/cell with increasing outlet number as expected from the calculated values based on the cell surface marker expression and MM distribution in the unsorted sample in feed (adapted from Schneider et al. 2010, with permission)

8 Discrete Cell Manipulation, Label-Free Magnetic Separation and Other

Micromanipulation of cell-magnetic bead complexes using electric currents and microcoils fabricated using microelectromechnical systems (MEMS) techniques has been demonstrated (Shen et al. 2012; Ramadan et al. 2006). Innovative use of Halbach magnet arrays has been proposed for scale-up of connective tissue progenitor separation from bone marrow in applications to bone defect repair (Joshi et al. 2015) and to fractionation of disperse magnetic microbead suspensions (Ijiri et al. 2013).

Localization of high magnetic field gradients at the edges of small ferromagnetic features (such as wires) provides an opportunity for an exact control over cell-magnetic bead complex position and displacement at the microscale. This has been accomplished by micropatterning of thin layers of ferromagnetic material (such as nickel alloys) on silica substrates and application of external magnetic field. The ferromagnetic layer pattern provides means of creating a barrier to advection of magnetic bead–cell complexes in a fluid flow inside small channels and separation of such complexes from unlabeled cells (Fig. 8). Various combinations of ferromagnetic micropatterns and flow configurations have been proposed (Adams et al. 2008; Hu et al. 2015). Unlike separation in the HGMS columns (described above) the highly regular micropattern of the ferromagnetic layer and a well-defined, laminar flow in microchannels provide means of a better control over the cell-magnetic bead separation process. Innovative use of susceptibility-modified solutions for mass density difference-based separation and real-time imaging and analysis using smart phone has been demonstrated (Knowlton et al. 2015) (Fig. 9). The technology is particularly appealing in resource-poor settings. The application of magnetic separation for detection of malaria in asymptomatic children has been also demonstrated (Sumari et al. 2016) (Fig. 10).

Control over the domain magnetization of the ferromagnetic single-domain micropatterns provides additional level of precision in the magnetic bead positioning and translation. Because such domains behave like hard magnets and therefore their magnetization is independent of the applied field, this creates an opportunity for using both the attractive and repulsive forces between the single-domain and a

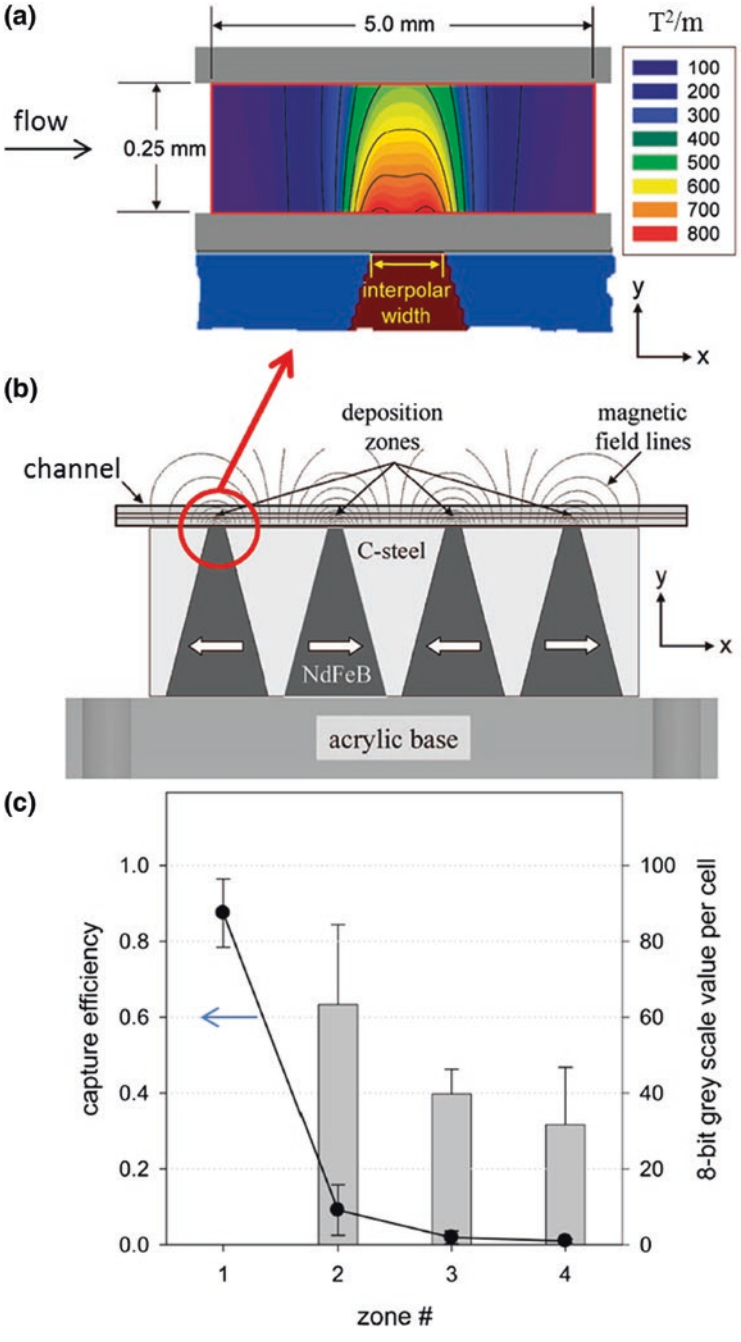
(a)
5.0 mm
T²/m
100
200
300
400
500
600
700
800
flow
0.25 mm
interpolar
width
y
x
(b)
deposition
zones
magnetic
field lines
channel
C-steel
NdFeB
acrylic base
y
x
(c)
capture efficiency
8-bit grey scale value per cell
1.0
0.8
0.6
0.4
0.2
0.0
100
80
60
40
20
0
1
2
3
4
zone #

◀ **Fig. 8** **a** Interpolar gap of a permanent magnet designed for an efficient capture of cell–label complex from a flowing suspension. The contour bands illustrate the magnitude of the *vertical* gradient component of magnetostatic potential energy (proportional to tesla^2/m, T^2/m). The gap width is 1 mm, channel height is exaggerated for clarity. **b** Four such interpolar gaps assembled together. The dimensional relationship between the parts is to scale. **c** Capture efficiency and fluorescence intensity (on a 8-bit gray scale) measured as a function of zone number. The *error bars* show one standard deviation from the mean for three experiments. Note capture of more fluorescent (and more magnetic) cells upstream from the channel outlet (adapted from Nath et al. 2009, with permission)

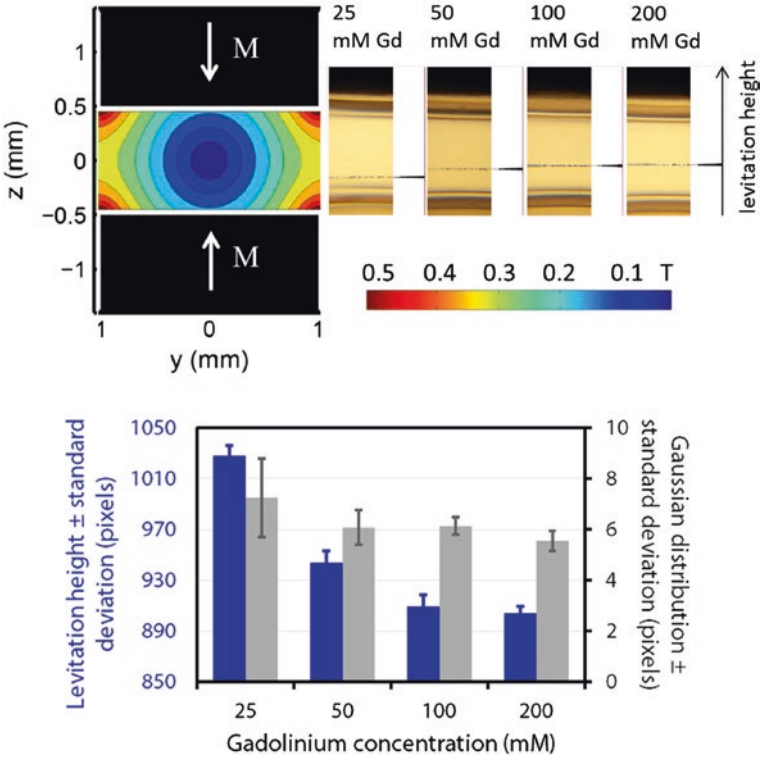

Fig. 9 Contour plot of the magnetic field between two, oppositely polarized permanent magnets. Images of levitating microspheres are acquired by the user with a smartphone fixed to the magnet and flow channel assembly and processed to determine the levitation height and confinement width of the microspheres in the sample stream, at different gadolinium concentration. (adapted from Knowlton et al. 2015, with permission)

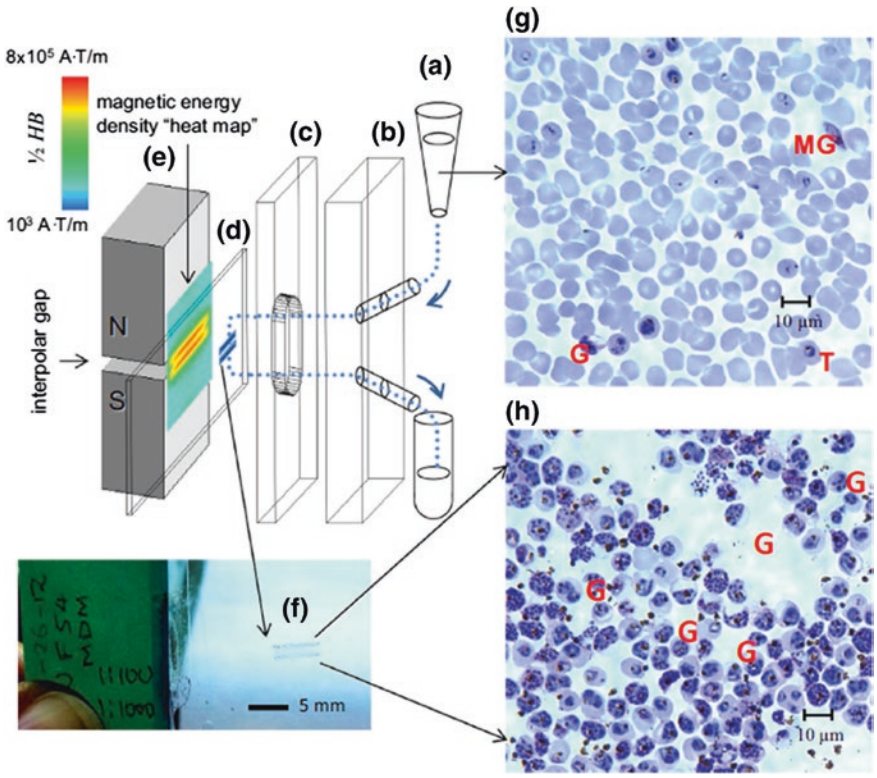

Fig. 10 Magnetic capture of malaria parasite infected red blood cells (RBCs) from RBC culture suspension. The cell suspension **a** is pumped through a channel comprising manifold platen with inlet and outlet ports (**b**), channel cutout spacer (**c**) and a transparent deposition slide (**d**), as indicated by *curved arrows*. The flow channel assembly **b**–**d** is pressed against the interpolar gap of a permanent magnet, **e** generating magnetic force on the magnetically susceptible cells due to a highly nonuniform fringing field, as indicated by the magnetic energy density map (*H* field in amperes per m, Å/m, and *B* field in tesla, T). The captured cells form a deposit **f** amenable to staining and microscopic analysis. **g** Shows approximately ×10 enrichment compared to the original sample, **h** NF54 strain, ×40 oil magnification) where *G* indicates gametocyte, *MG* male gametocyte, *T* trophozoite (adapted from Sumari et al. 2016, with permission)

superparamagnetic bead (type of a soft magnet) depending on the direction of the applied field. This has been demonstrated by superparamagnetic bead propulsion on a square grid of single-domain dots in a rotating magnetic field whereby the rotation of the induced magnetic dipole of the bead causes it to be sequentially pushed and pulled between the neighboring single-domain dots in synchrony with the rotating applied field vector (Hu et al. 2015; Chen et al. 2013). Increased bead capture rate is provided by generation of high-field gradients at the boundaries of magnetic domains (Fig. 11).

There are known, naturally occurring paramagnetic components of the cell that may become important for the label-free magnetic cell manipulation and

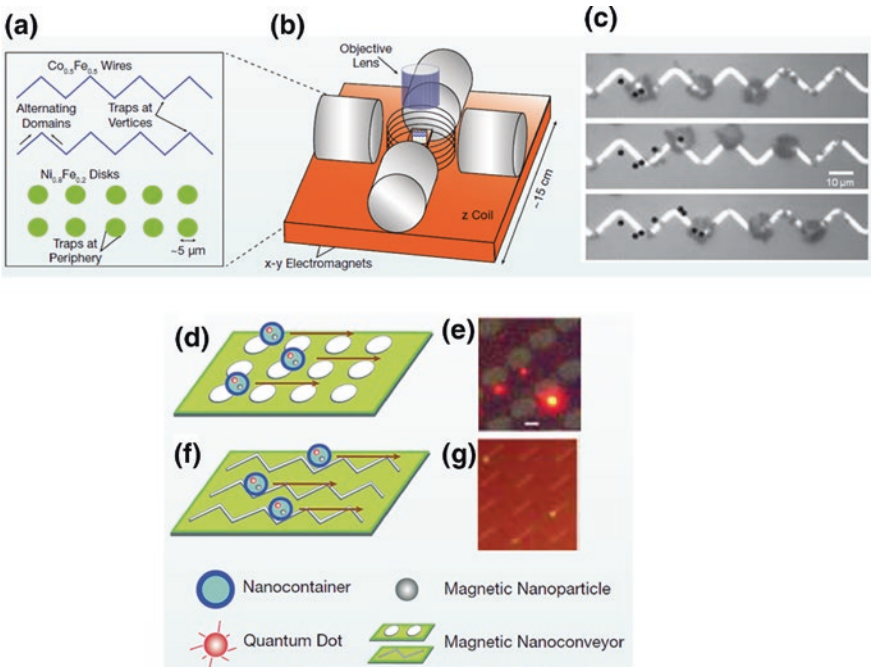

Fig. 11 The magnetic nanoconveyors shown in this schematic **a** are $Co_{0.5}Fe_{0.5}$ zigzag wires and $Ni_{0.2}Fe_{0.2}$ disks. *Points* on the periphery of a magnetized disk act as magnetic particle traps, whereas alternating magnetic domains in zigzag wires give rise to regions of high fields and field gradients at wire vertices. These regions act as traps for magnetic nanoparticles. The entire system, **b** including the external electromagnets and coil required to apply magnetic fields, can be mounted on an optical fluorescence microscope. Application of fields can strengthen, weaken, or move traps, allowing for manipulation of trapped entities along directed pathways. **c** T lymphocyte cells labeled with anti CD3 conjugated 1 µm magnetic particles are propagated along wires. **d** Nanoconveyor technology can be used to transport multiple individual nanocontainers, such as these that encapsulate fluorescent quantum dots for optical tracking and magnetic nanoparticles for controlled transport. **d**, **f** are schematics of nanocontainer transport on microfabricated disks and wire array conveyors, respectively. **e**, **g** Are superimposed differential interference contrast (DIC)/fluorescence images of fluorescent magnetic nanoparticle trapped on micropatterned disks (EF) and zigzag wire conveyors (**g**) (adapted from Mahajan et al. 2012, with permission)

separation given the increasing sophistication of the magnet and fluidics designs. An interesting example are magnetotactic bacteria that contain specialized organelles, magnetosomes, comprising magnetite crystals whose response to the vertical component of the geomagnetic field provide the sense of up-down direction, important for finding nutrients. This has been used to control the direction of a self-propelled motion of the magnetotactic bacteria using the magnetic field in laboratory conditions. A similar function of finding direction is attributed to the presence magnetite inclusions found in homing pigeons.

Other examples are related to the role of paramagnetic iron and manganese in cell biology, in particular as related to their being a part of a large family of

proteins collectively known as metalloproteins. These include an oxygen-carrying protein, hemoglobin, an iron storage protein, ferritin, electron transfer proteins, cytochromes, and superoxide dismutases (manganese). The interconversion between low-spin to high-spin hemoglobin during the binding and release of molecular oxygen has been studied by Pauling and Coryell (1936) as a part of the program of elucidating the nature of chemical bond by quantum mechanics. The increasing hemoglobin concentration in the course of red blood cell maturation was tested for mature erythrocytes enrichment from hematopoietic cell cultures (Jin et al. 2012). The feasibility of erythrocyte depletion from whole blood preparations as a type of a "magnetic centrifuge" was tested (Moore et al. 2013) and considered for application to depletion of aging erythrocytes from stored blood for blood banking purposes (Jin et al. 2011). The theory of magnetophoresis links the field-induced cell motion to the underlying molecular mechanisms (Zborowski et al. 2003; Jin et al. 2008). The feasibility of label-free magnetic cell separation in applications to intraerythrocytic malaria detection has been demonstrated in the laboratory (Hackett et al. 2009; Zimmerman et al. 2006) and tested in field studies (Sumari et al. 2016; Karl et al. 2008). The separation of bacterial spores rich in paramagnetic element manganese (Mn) has been demonstrated and their magnetophoretic mobility analyzed quantitatively (Melnik et al. 2007; Sun et al. 2011). The separation of green algae genetically modified for elevated expression of ferritin was compared with that of the wild type (Buck et al. 2015). A practical system using permanent magnets for field operation for detecting paramagnetic contaminants in food or environmental water has been proposed and tested (Mirica et al. 2010).

9 Conclusions

The field of the magnetic cell separation and manipulation is highly dynamic in response to rapid advances in single cell analysis and molecular biology assays, in nanomedicine and in microanalytical systems and lab-on-a-chip applications, as well as new opportunities created by microfluidics and nanofluidics. The increasing availability of strong permanent magnets and access to superconducting magnets and separators, combined with better understanding and control of fluid dynamical forces in microchannels open new directions for the future magnetic cell separation approaches, such as label-free magnetic separation based on differences in the paramagnetic contribution from natural components of the cell (metalloproteins) and diamagnetic cell separation. This chapter is just a snapshot of a rapidly evolving field and the reader is well advised to consult the latest information, also available online, if this presentation was successful in providing motivation for further study.

References

Adams JD, Kim U, Soh HT (2008) Multitarget magnetic activated cell sorter. Proc Natl Acad Sci USA 105(47):18165–18170. doi:10.1073/pnas.0809795105

Beharrell PA (2012) Applications of superconducting magnetic separation. Quantum Design, Inc., San Diego. http://www.qdusa.com/sitedocs/productBrochures/Applications_of_Superconducting_Magnetic_Separation_2012.pdf. Date Accessed 15 Mar 2016

Bozorth RM (1993) Ferromagnetism. Wiley-IEEE Press, London

Buck A, Moore LR, Lane CD, Kumar A, Stroff C, White N, Xue W, Chalmers JJ, Zborowski M (2015) Magnetic separation of algae genetically modified for increased intracellular iron uptake. J Magn Magn Mater 380:201–204. doi:10.1016/j.jmmm.2014.09.008

Caralla T, Joshi P, Fleury S, Luangphakdy V, Shinohara K, Pan H, Boehm C, Vasanji A, Hefferan TE, Walker E, Yaszemski M, Hascall V, Zborowski M, Muschler GF (2013) In vivo transplantation of autogenous marrow-derived cells following rapid intraoperative magnetic separation based on hyaluronan to augment bone regeneration. Tissue Eng Part A 19(1–2):125–134. doi:10.1089/ten.tea.2011.0622

Chalmers JJ, Xiong Y, Jin X, Shao M, Tong X, Farag S, Zborowski M (2010) Quantification of non-specific binding of magnetic micro- and nanoparticles using cell tracking velocimetry: implication for magnetic cell separation and detection. Biotechnol Bioeng 105(6):1078–1093. doi:10.1002/bit.22635

Chen A, Byvank T, Chang WJ, Bharde A, Vieira G, Miller BL, Chalmers JJ, Bashir R, Sooryakumar R (2013) On-chip magnetic separation and encapsulation of cells in droplets. Lab Chip 13(6):1172–1181. doi:10.1039/c2lc41201b

de Wit S, van Dalum G, Lenferink AT, Tibbe AG, Hiltermann TJ, Groen HJ, van Rijn CJ, Terstappen LW (2015) The detection of EpCAM(+) and EpCAM(−) circulating tumor cells. Sci Rep 5:12270. doi:10.1038/srep12270

Doctor RD, Panchal CB, Swietlik CE (1986) A model of open-gradient magnetic separation for coal cleaning using a superconducting quadrupole field. AIChE Symp Ser 82:154–168

Fukui S, Nakajima H, Ozone A, Hayatsu M, Yamaguchi M, Sato T, Imaizumi H, Nishijima S, Watanabe T (2002) Study on open gradient magnetic separation using multiple magnetic field sources. IEEE Trans Appl Supercond 12(1):959–962. doi:10.1109/TASC.2002.1018559

Furlani EP (2001) Permanent magnet and electromechanical devices: materials, analysis, and applications. Academic Press, San Diego

Gao L, Ct Wyatt Shields, Johnson LM, Graves SW, Yellen BB, Lopez GP (2015) Two-dimensional spatial manipulation of microparticles in continuous flows in acoustofluidic systems. Biomicrofluidics 9(1):014105. doi:10.1063/1.4905875

Giddings JC (1985) Optimized field-flow fractionation system based on dual stream splitters. Anal Chem 57(4):945–947

Gider S, Awschalom DD, Douglas T, Mann S, Chaparala M (1995) Classical and quantum magnetic phenomena in natural and artificial ferritin proteins. Science 268(5207):77–80

Gijs MA, Lacharme F, Lehmann U (2010) Microfluidic applications of magnetic particles for biological analysis and catalysis. Chem Rev 110(3):1518–1563. doi:10.1021/cr9001929

Grützkau A, Radbruch A (2010) Small but mighty: how the MACS®-technology based on nanosized superparamagnetic particles has helped to analyze the immune system within the last 20 years. Cytometry Part A 77A(7):643–647. doi:10.1002/cyto.a.20918

Gutierrez L, Costo R, Gruttner C, Westphal F, Gehrke N, Heinke D, Fornara A, Pankhurst QA, Johansson C, Veintemillas-Verdaguer S, Morales MP (2015) Synthesis methods to prepare single- and multi-core iron oxide nanoparticles for biomedical applications. Dalton Trans 44(7):2943–2952. doi:10.1039/c4dt03013c

Hackett S, Hamzah J, Davis TM, St Pierre TG (2009) Magnetic susceptibility of iron in malaria-infected red blood cells. Biochim Biophys Acta 1792(2):93–99

Hafeli UO, Aue J, Damani J (2008) The biocompatibility and toxicity of magnetic particles. In: Zborowski M, Chalmers JJ (eds) Magnetic cell separation. Elsevier B.V., Amsterdam

Hahn YK, Park JK (2011) Versatile immunoassays based on isomagnetophoresis. Lab Chip 11(12):2045–2048. doi:10.1039/c0lc00569j

Hatch GP, Stelter RE (2001) Magnetic design considerations for devices and particles used for biological high-gradient magnetic separation (HGMS) systems. J Magn Magn Mater 225(1–2):262–276. doi:10.1016/S0304-8853(00)01250-6

Hirota N, Kurashige M, Iwasaka M, Ikehata M, Uetake H, Takayama T, Nakamura H, Ikezoe Y, Ueno S, Kitazawa K (2004) Magneto-Archimedes separation and its application to the separation of biological materials. Phys B 346:267–271. doi:10.1016/j.physb.2004.01.063

Hoyos M, Moore L, Williams PS, Zborowski M (2011) The use of a linear Halbach array combined with a step-SPLITT channel for continuous sorting of magnetic species. J Magn Magn Mater 323(10):1384–1388. doi:10.1016/j.jmmm.2010.11.051

http://www.miltenyibiotec.com

http://www.easysep.com

http://www.sepmag.eu/. Last accessed April 2016

http://www.miltenyibiotec.com. Last accessed April 2016

https://m.bdbiosciences.com/us/reagents/research/magnetic-cell-separation/other-species-cell-separation-reagents/cell-separation-magnet/p/552311. Last accessed April 2016

https://www.thermofisher.com/us/en/home/brands/product-brand/dynal.html. Last accessed April 2016

Hu X, Abedini-Nassab R, Lim B, Yang Y, Howdyshell M, Sooryakumar R, Yellen BB, Kim C (2015) Dynamic trajectory analysis of superparamagnetic beads driven by on-chip micromagnets. J Appl Phys 118(20):203904. doi:10.1063/1.4936219

Hwang JY, Takayasu M, Friedlaender FJ, Kullerud G (1984) Application of magnetic susceptibility gradients to magnetic separation. J Appl Phys 55(6):2592–2594

Ijiri Y, Poudel C, Williams PS, Moore LR, Orita T, Zborowski M (2013) Inverted linear Halbach array for separation of magnetic nanoparticles. IEEE Trans Magn 49(7):3449–3452. doi:10.1109/TMAG.2013.2244577

Jakubovics JP (1994) Magnetism and magnetic materials. Cambridge University Press, Cambridge

Jiles D (2016) Introduction to magnetism and magnetic materials, 3rd edn. CRC Press, Boca Raton

Jin X, Zhao Y, Richardson A, Moore L, Williams PS, Zborowski M, Chalmers JJ (2008) Differences in magnetically induced motion of diamagnetic, paramagnetic, and superparamagnetic microparticles detected by cell tracking velocimetry. Analyst 133(12):1767–1775. doi:10.1039/b802113a

Jin X, Yazer MH, Chalmers JJ, Zborowski M (2011) Quantification of changes in oxygen release from red blood cells as a function of age based on magnetic susceptibility measurements. Analyst 136(14):2996–3003

Jin X, Abbot S, Zhang X, Kang L, Voskinarian-Berse V, Zhao R, Kameneva MV, Moore LR, Chalmers JJ, Zborowski M (2012) Erythrocyte enrichment in hematopoietic progenitor cell cultures based on magnetic susceptibility of the hemoglobin. PLoS One 7(8):e39491

Joshi P, Williams PS, Moore LR, Caralla T, Boehm C, Muschler G, Zborowski M (2015) Circular Halbach array for fast magnetic separation of hyaluronan-expressing tissue progenitors. Anal Chem 87(19):9908–9915. doi:10.1021/acs.analchem.5b02431

Kantor AB, Gibbons I, Miltenyi S, Schmitz J (1998) Magnetic cell sorting with colloidal superparamagnetic particles. In: Recktenwald D, Radbruch A (eds) Cell separation methods and applications. Marcel Dekker, New York, pp 153–173

Karabacak NM, Spuhler PS, Fachin F, Lim EJ, Pai V, Ozkumur E, Martel JM, Kojic N, Smith K, Chen PI, Yang J, Hwang H, Morgan B, Trautwein J, Barber TA, Stott SL, Maheswaran S, Kapur R, Haber DA, Toner M (2014) Microfluidic, marker-free isolation of circulating tumor cells from blood samples. Nat Protoc 9(3):694–710. doi:10.1038/nprot.2014.044

Karl S, David M, Moore L, Grimberg BT, Michon P, Mueller I, Zborowski M, Zimmerman PA (2008) Enhanced detection of gametocytes by magnetic deposition microscopy predicts higher potential for *Plasmodium falciparum* transmission. Malar J 7:66

Karle M, Miwa J, Czilwik G, Auwarter V, Roth G, Zengerle R, von Stetten F (2010) Continuous microfluidic DNA extraction using phase-transfer magnetophoresis. Lab Chip 10(23):3284–3290. doi:10.1039/c0lc00129e

Knowlton SM, Sencan I, Aytar Y, Khoory J, Heeney MM, Ghiran IC, Tasoglu S (2015) Sickle cell detection using a smartphone. Sci Rep 5:15022. doi:10.1038/srep15022

Krishnan KM (2010) Biomedical nanomagnetics: a spin through possibilities in imaging, diagnostics, and therapy. IEEE Trans Magn 46(7):2523–2558. doi:10.1109/TMAG.2010.2046907

Krishnan KM (2016) Fundamentals and applications of magnetic materials. Oxford University Press, Oxford, UK

Lara O, Tong X, Zborowski M, Farag SS, Chalmers JJ (2006) Comparison of two technologies to deplete T cells from human blood samples. Biotechnol Bioeng 94(1):66–80. doi:10.1002/bit.20807

Leigh DR, Steinert S, Moore LR, Chalmers JJ, Zborowski M (2005) Cell tracking velocimetry as a tool for defining saturation binding of magnetically conjugated antibodies. Cytometry Part A J Int Soc Anal Cytol 66(2):103–108. doi:10.1002/cyto.a.20155

Lenshof A, Laurell T (2010) Continuous separation of cells and particles in microfluidic systems. Chem Soc Rev 39(3):1203–1217. doi:10.1039/b915999c

Mahajan KD, Vieira GB, Ruan G, Miller BL, Lustberg MB, Chalmers JJ, Sooryakumar R, Winter JO (2012) A MagDot-nanoconveyor assay detects and isolates molecular biomarkers. Chem Eng Prog 108:41–46

McCloskey KE, Chalmers JJ, Zborowski M (2000) Magnetophoretic mobilities correlate to antibody binding capacities. Cytometry 40(4):307–315

Melnik K, Sun J, Fleischman A, Roy S, Zborowski M, Chalmers JJ (2007) Quantification of magnetic susceptibility in several strains of *Bacillus* spores: implications for separation and detection. Biotechnol Bioeng 98(1):186–192. doi:10.1002/bit.21400

Miltenyi S, Muller W, Weichel W, Radbruch A (1990) High gradient magnetic cell separation with MACS. Cytometry 11(2):231–238. doi:10.1002/cyto.990110203

Mirica KA, Shevkoplyas SS, Phillips ST, Gupta M, Whitesides GM (2009) Measuring densities of solids and liquids using magnetic levitation: fundamentals. J Am Chem Soc 131(29):10049–10058. doi:10.1021/ja900920s

Mirica KA, Phillips ST, Mace CR, Whitesides GM (2010) Magnetic levitation in the analysis of foods and water. J Agric Food Chem 58(11):6565–6569. doi:10.1021/jf100377n

Moore LR, Milliron S, Williams PS, Chalmers JJ, Margel S, Zborowski M (2004) Control of magnetophoretic mobility by susceptibility-modified solutions as evaluated by cell tracking velocimetry and continuous magnetic sorting. Anal Chem 76(14):3899–3907. doi:10.1021/ac049910f

Moore LR, Nehl F, Dorn J, Chalmers JJ, Zborowski M (2013) Open gradient magnetic red blood cell sorter evaluation on model cell mixtures. IEEE Trans Magn 49(1):309–315. doi:10.1109/Tmag.2012.2225098

Nath P, Strelnik J, Vasanji A, Moore LR, Williams PS, Zborowski M, Roy S, Fleischman AJ (2009) Development of multistage magnetic deposition microscopy. Anal Chem 81(1):43–49. doi:10.1021/ac8010186

Nishijima S, Takeda S (2006) Superconducting high gradient magnetic separation for purification of wastewater from paper factory. IEEE Trans Appl Supercond 16(2):1142–1145. doi:10.1109/TASC.2006.871346

Osman O, Zanini LF, Frenea-Robin M, Dumas-Bouchiat F, Dempsey NM, Reyne G, Buret F, Haddour N (2012) Monitoring the endocytosis of magnetic nanoparticles by cells using permanent micro-flux sources. Biomed Microdev 14(5):947–954. doi:10.1007/s10544-012-9673-4

Pamme N (2012) On-chip bioanalysis with magnetic particles. Curr Opin Chem Biol 16(3–4):436–443. doi:10.1016/j.cbpa.2012.05.181

Pamme N, Manz A (2004) On-chip free-flow magnetophoresis: continuous flow separation of magnetic particles and agglomerates. Anal Chem 76(24):7250–7256. doi:10.1021/ac049183o

Pauling L, Coryell CD (1936) The magnetic properties and structure of hemoglobin, oxyhemoglobin and carbonmonoxyhemoglobin. Proc Natl Acad Sci USA 22(4):210–216

Peyman SA, Kwan EY, Margarson O, Iles A, Pamme N (2009) Diamagnetic repulsion—a versatile tool for label-free particle handling in microfluidic devices. J Chromatogr A 1216(52):9055–9062. doi:10.1016/j.chroma.2009.06.039

Posfai M, Lefevre CT, Trubitsyn D, Bazylinski DA, Frankel RB (2013) Phylogenetic significance of composition and crystal morphology of magnetosome minerals. Front Microbiol 4:344. doi:10.3389/fmicb.2013.00344

Ramadan Q, Samper V, Poenar DP, Yu C (2006) An integrated microfluidic platform for magnetic microbeads separation and confinement. Biosens Bioelectron 21(9):1693–1702. doi:10.1016/j.bios.2005.08.006

Ramsey NF (1990) Molecular beams. The international series of monographs on physics. Oxford University Press, Oxford

Rosensweig RE (1997) Ferrohydrodynamics. Dover, Mineola

Russell AP, Evans CH, Westcott VC (1987) Measurement of the susceptibility of paramagnetically labeled cells with paramagnetic solutions. Anal Biochem 164:181–189

Sahore V, Fritsch I (2014) Redox-magnetohydrodynamics, flat flow profile-guided enzyme assay detection: toward multiple, parallel analyses. Anal Chem 86(19):9405–9411. doi:10.1021/ac502014t

Schneider T, Karl S, Moore LR, Chalmers JJ, Williams PS, Zborowski M (2010) Sequential CD34 cell fractionation by magnetophoresis in a magnetic dipole flow sorter. Analyst 135(1):62–70. doi:10.1039/b908210g

Schwinger J, DeRaad LLJ, Milton KA, W-y Tsai (1998) Classical electrodynamics. Perseus Books, Reading

Shen F, Hwang H, Hahn YK, Park JK (2012) Label-free cell separation using a tunable magnetophoretic repulsion force. Anal Chem 84(7):3075–3081. doi:10.1021/ac201505j

Simon MD, Geim AK (2000) Diamagnetic levitation: flying frogs and floating magnets (invited). J Appl Phys 87:6200–6204

Sumari D, Grimberg BT, Blankenship D, Mugasa J, Mugittu K, Moore L, Gwakisa P, Zborowski M (2016) Application of magnetic cytosmear for the estimation of *Plasmodium falciparum* gametocyte density and detection of asexual stages in asymptomatic children. Malar J 15(1):113. doi:10.1186/s12936-016-1170-4

Sun JJ (1980) Methods and apparatus for separating particles using a magnetic barrier. U.S. Patent

Sun J, Zborowski M, Chalmers JJ (2011) Quantification of both the presence, and oxidation state, of Mn in *Bacillus atrophaeus* spores and its imparting of magnetic susceptibility to the spores. Biotechnol Bioeng 108(5):1119–1129

Takayasu M, Kelland DR, Minervini JV (2000) Continuous magnetic separation of blood components from whole blood. IEEE Trans Appl Supercond 10(1):927–930

Tasoglu S, Khoory JA, Tekin HC, Thomas C, Karnoub AE, Ghiran IC, Demirci U (2015) Levitational image cytometry with temporal resolution. Adv Mater 27(26):3901–3908. doi:10.1002/adma.201405660

Thanh NTK (2012) Magnetic nanoparticles: from fabrication to clinical applications. CRC Press, Boca Raton

Ugelstad J, Stenstad P, Kilaas L, Prestvik WS, Herje R, Berge A, Hornes E (1993) Monodisperse magnetic polymer particles. New biochemical and biomedical applications. Blood Purif 11(6):349–369

Vojtisek M, Tarn M, Hirota N, Pamme N (2012) Microfluidic devices in superconducting magnets: on-chip free-flow diamagnetophoresis of polymer particles and bubbles. Microfluid Nanofluid 13:625–635. doi:10.1007/s10404-012-0979-6

Vyas KN, Palfreyman JJ, Love DM, Mitrelias T, Barnes CH (2012) Magnetically labelled gold and epoxy bi-functional microcarriers for suspension based bioassay technologies. Lab Chip 12(24):5272–5278. doi:10.1039/c2lc41022b

Watarai H, Namba M (2001) Magnetophoretic behavior of single polystyrene particles in aqueous manganese(II) chloride. Anal Sci 17(10):1233–1236

Watson JHP (1973) Magnetic filtration. J Appl Phys 44(9):4209–4213. doi:10.1063/1.1662920
Weston MC, Gerner MD, Fritsch I (2010) Magnetic fields for fluid motion. Anal Chem 82(9):3411–3418. doi:10.1021/ac901783n
Williams PS, Zborowski M, Chalmers JJ (1999) Flow rate optimization for the quadrupole magnetic cell sorter. Anal Chem 71(17):3799–3807
Williams PS, Carpino F, Zborowski M (2010) Characterization of magnetic nanoparticles using programmed quadrupole magnetic. Philos Trans Ser A Math Phys Eng Sci 368(1927):4419–4437. doi:10.1098/rsta.2010.0133
Xue W (2016) Measurements of Cellular Intrinsic Magnetism with Cell Tracking Velocimetry and Separation with Magnetic Deposition Microscopy, Ph.D. Thesis, The Ohio State University
Yavuz CT, Prakash A, Mayo JT, Colvin VL (2009) Magnetic separations: from steel plants to biotechnology. Chem Eng Sci 64:2510–2521
Zborowski M, Chalmers JJ (2008) Magnetic cell separation, vol 32. Laboratory techniques in biochemistry and molecular biology, vol 32. Elsevier, B.V., Amsterdam
Zborowski M, Chalmers JJ (2015) Magnetophoresis: fundamentals and applications. Wiley Encycl Electr Electron Eng. doi:10.1002/047134608X.W8236
Zborowski M, Malchesky PS, Jan TF, Hall GS (1992) Quantitative separation of bacteria in saline solution using lanthanide Er(III) and a magnetic field. J Gen Microbiol 138(1):63–68. doi:10.1099/00221287-138-1-63
Zborowski M, Fuh CB, Green R, Sun L, Chalmers JJ (1995) Analytical magnetapheresis of ferritin-labeled lymphocytes. Anal Chem 67(20):3702–3712
Zborowski M, Ostera GR, Moore LR, Milliron S, Chalmers JJ, Schechter AN (2003) Red blood cell magnetophoresis. Biophys J 84(4):2638–2645. doi:10.1016/S0006-3495(03)75069-3
Zhang H, Moore LR, Zborowski M, Williams PS, Margel S, Chalmers JJ (2005) Establishment and implications of a characterization method for magnetic nanoparticle using cell tracking velocimetry and magnetic susceptibility modified solutions. Analyst 130(4):514–527. doi:10.1039/b412723d
Zimmels Y, Yaniv I (1976) Characterization of magnetic forces by means of suspended particles in paramagnetic solutions. IEEE Trans Magn 4:359–368
Zimmerman PA, Thomson JM, Fujioka H, Collins WE, Zborowski M (2006) Diagnosis of malaria by magnetic deposition microscopy. Am J Trop Med Hyg 74(4):568–572

Electrical Manipulation and Sorting of Cells

Jaka Cemazar, Arindam Ghosh and Rafael V. Davalos

Abstract Electric fields have been widely used to manipulate cells in microfluidic devices. The versatility and the ease of implementation and fabrication of electric field-based microfluidic systems have made them very popular for a whole host of different biomedical applications. In this chapter, various techniques that are commonly used for manipulating, characterizing, and separating cells in lab-on-a-chip devices and their applications are discussed. Starting from a description of the polarization of a cell and the forces that can act on it in an electric field, the theory that drives different electrokinetic phenomena and the application of these phenomena for on-chip cellular manipulation are herein reviewed. The models that are used to predict the responses of cells in electric fields, as well as techniques commonly used for the numerical modeling of various electrokinetic and electric field-based cellular manipulation techniques, are also detailed. Finally, the electrical modifications of cells in microfluidic devices, specifically electroporation and electrofusion, have been reviewed.

Keywords Lab-on-a-chip · Microfluidics · Electrokinetics · Dielectrophoresis · Electrorotation · AC electroosmosis · Cell sorting · Cell focusing · Micro flow cytometer · Electroporation · Electrofusion · Polarization · Electric field · Electric field gradient · Electrical double layer · Dipole · Clausius–Mossotti factor · Electrophoresis · Induced charge electroosmosis · Traveing wave dielectrophoresis · Dielectrophoretic force · Cell-to-cell interactions · Transmembrane voltage · Shell model · Maxwell stress tensor · Numerical methods · Fluorescence-activated cell sorting · Electrical impedance · Cytometer · Field flow fractionation · Electrodes · Tumor initiating cells · Circulating tumor cells · Immunocapture · Joule heating · Cell lysis · Cell pairing · Phenotype

J. Cemazar · A. Ghosh · R.V. Davalos (✉)
School of Biomedical Engineering and Sciences, Virginia Tech – Wake Forest University, Blacksburg, VA 24061, USA
e-mail: davalos@vt.edu

A. Ghosh · R.V. Davalos
Department of Mechanical Engineering, Virginia Tech, Blacksburg, VA 24061, USA

W. Lee et al. (eds.), *Microtechnology for Cell Manipulation and Sorting*, Microsystems and Nanosystems, DOI 10.1007/978-3-319-44139-9_3

Abbreviations

DEP	Dielectrophoresis
twDEP	Traveling wave dielectrophoresis
ICEO	Induced charge electroosmosis
DEP-FFF	Dielectrophoretic field-flow fractionation
iDEP	Insulator dielectrophoresis
cDEP	Contactless dielectrophoresis
EO	Electroosmosis
FACS	Fluorescence-activated cell sorting
LOC	Lab-on-a-chip
RBC	Red blood cells

To understand the undergoing changes in the cells and tissues due to different diseases it would be helpful to provide a platform of cell cultures that mimics their natural environment while retaining the ability to regulate cellular surroundings. In vitro microfluidic studies can be used for the early detection of diseases like cancer, malaria, and HIV as well as for investigating possible therapeutic schemes as an intermediate step between cell-based and tissue-based testing. Microfluidic lab-on-a-chip (LOC) devices offer an easy platform for carrying out such in vitro studies in controlled environments. However, without the ability to precisely manipulate the cells, these devices cannot reach their full potential to practical application. A cell is composed of an insulating cell membrane and a conductive cytoplasm and it is polarized when exposed to an electric field. Electric fields are commonly used to manipulate, sort, separate, or characterize cells in microfluidic LOC devices because different fields may be generated by changing the frequency of the electric fields and actuating individually addressable electrodes. Multiple electrokinetic phenomena can be combined to create an even richer array of cell manipulation techniques which can be easily reconfigured by tuning parameters.

In this chapter, we start with the basic theory of how biological cells behave in electric fields and then we describe a number of electric field-based techniques commonly used to manipulate cells in microfluidic devices. We discuss models used to describe the dielectric nature of the cell as well as numerical approaches for modeling the electrokinetic phenomenon. Finally, we present some of the applications of these techniques used to sort, separate, and otherwise manipulate cells.

1 The Cell in an Electric Field

A cell membrane insulates the cell interior from some of the electric fields that can be present in the environment. Composed of lipid bilayer, the cell membrane allows for selective transport into and out of the cell to maintain homeostasis. The cell interior consists of organelles and the cytosol, which is an electrically

conductive fluid. When a polarizable particle such as a biological cell is subjected to an electric field, an electrical dipole is induced in the particle. Charged mobile particles (ions) rearrange in response to the applied exogenous electric field and accumulate at the membrane. The rearrangement of ions takes some time to occur and its timing and magnitude depends on the electrical conductivity of the media. The type of polarization depends on frequency of the electric field. In aqueous solutions, Maxwell–Wagner interfacial polarization dominates at low frequencies: ions can follow the changing direction of the field and accumulate at the interfaces of high and low conductivity materials. At higher frequencies, typically tens of kHz, ion migration cannot follow the electric field oscillations, and manifests as a reduced effective polarization. At frequencies from hundreds of MHz to GHz the orientation of molecules stops following the field. At even higher frequencies atomic and electronic polarization slowly diminishes (Jones 1995; Morgan and Green 2003). The lipid bilayer also expresses orientational polarization, which arises from the alignment of permanent dipoles in polar materials, however, due to its large dimensions; polarization diminishes in the frequency range of tens of MHz (Klösgen et al. 1996; Kotnik and Miklavčič 2000).

The two components that mainly contribute to polarization of a cell are physical movement of free charges and perturbation of bound charges induced by an electric field. Bound and free charges can be modeled as a lossy dielectric—a material having both significant conductivity and permittivity. In the phasor representation of an electric field with angular frequency ω, the current I through the material may be modeled as a sum of current though a resistor (I_R) and a capacitor (I_C), connected in parallel

$$I = I_R + I_C = \frac{V}{R} + C\frac{dV}{dt} = V\frac{A}{d}(\sigma + i\omega\varepsilon), \tag{1}$$

where V is the voltage across the resistor and capacitor, $i^2 = -1$, $C = \varepsilon A/d$, $R = A/(d\,\sigma)$, A and d are area and separation distance of the capacitor plates, respectively, ε is the electrical permittivity and σ electrical conductivity of the material. The total current can then be expressed using the complex permittivity, $\varepsilon^* = \varepsilon - \frac{i\sigma}{\omega}$

$$I = \frac{i\omega A}{d}\left(\varepsilon - \frac{i\sigma}{\omega}\right)V = \frac{i\omega A}{d}\varepsilon^* V. \tag{2}$$

This equation shows that low-frequency polarization is governed by electrical conductivity while high frequency polarization by permittivity, since the charge carriers cannot follow the alternating voltage (Gagnon 2011).

Cells typically have ionizable molecules at the surface of the membrane, such as carboxyl (–COOH) or amine ($–NH_2$) functional groups, and most cells have more acidic than basic groups. Acidic groups are charged negatively and basic groups positively, and therefore the cell surface is typically negatively charged. In order to maintain charge neutrality, ions of opposite charge are attracted to the surface forming a double layer—a thin layer of counter charge. The thickness of this layer is defined as by the Debye length

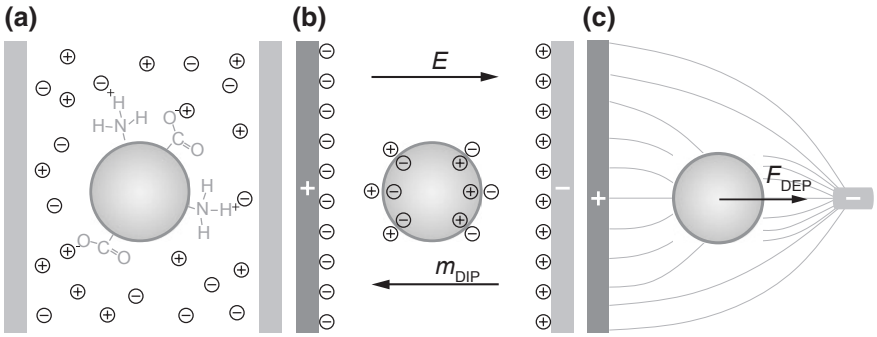

Fig. 1 A cell in an electric field; **a** charged molecules on the surface of a cell, **b** induced dipole, **c** force on a cell in an inhomogeneous electric field. Panels **a**, **b** are adapted from Morgan and Green (2003)

$$\kappa = \sqrt{\frac{\sigma}{D\varepsilon}} \tag{3}$$

where D is a diffusion constant. When a cell is exposed to an external electric field, the double layer moves around the cell towards the electrodes, radially accumulating at the interface between the cell and the electrolyte. This spatial charge redistribution is shown in Fig. 1.

This charge polarization acts as an effective dipole moment that is dependent upon the properties of the cell, the suspending fluid, and the frequency of applied electric field. Thus, the cell can be modeled as a dipole consisting of two opposite charges, q, separated by a distance $\mathbf{d}$. Assuming that we are measuring far from the cell, the dipole charges exposed to electric field $\mathbf{E}(\mathbf{r})$ and $\mathbf{E}(\mathbf{r}+\mathbf{d})$ for $|\mathbf{d}| \ll |\mathbf{r}|$, we can write Taylor expansion for $\mathbf{E}(\mathbf{r}+\mathbf{d})$ as

$$\mathbf{E}(\mathbf{r}+\mathbf{d}) = \mathbf{E}(\mathbf{r}) + \mathbf{d}\nabla\mathbf{E}(\mathbf{r}) + \cdots . \tag{4}$$

Assuming the dipole is small, higher order terms can be neglected and the force on a dipole, $\mathbf{F}_{\mathrm{DIP}}$, is effectively

$$\mathbf{F}_{\mathrm{DIP}} = q\mathbf{E}(\mathbf{r}+\mathbf{d}) - q\mathbf{E}(\mathbf{r}) \cong q\mathbf{E}(\mathbf{r}) + q\mathbf{d}\nabla\mathbf{E}(\mathbf{r}) - q\mathbf{E}(\mathbf{r}) = q\mathbf{d}\nabla\mathbf{E}(\mathbf{r}). \tag{5}$$

The dipole moment, $\mathbf{p}$, is defined as $\mathbf{p} = \mathrm{q}\mathbf{d}$ and the force on a dipole becomes

$$\mathbf{F}_{\mathrm{DIP}} = \mathbf{p}\nabla\mathbf{E}(\mathbf{r}). \tag{6}$$

The force on a dipole is a good approximation of the dielectrophoretic force, $\mathbf{F}_{\mathrm{DEP}}$, on a particle that is much smaller than surrounding features (i.e., $|\mathbf{d}| \ll |\mathbf{r}|$).

If the induced dipole is not in the same direction as the electric field, a torque $\mathbf{T}$ rotates the dipole in the electric field is observed. This torque tends to align the cell's induced dipole with direction of applied electric field and can be expressed as

$$\mathbf{T} = \mathbf{p} \times \mathbf{E}. \tag{7}$$

The effective dipole moment of a cell, approximated as spherical particle is

$$\mathbf{p} = 4\pi\epsilon_{\mathrm{e}} r^3 \left(\frac{\varepsilon_p^* - \varepsilon_e^*}{\varepsilon_p^* + 2\varepsilon_e^*} \right) \mathbf{E}, \tag{8}$$

where indices p and e denote particle and exterior medium, respectively. The term in the parentheses is commonly referred to as the Clausius–Mossotti factor, f_{CM}

$$f_{\mathrm{CM}}(\omega) = \frac{\left(\varepsilon_p^* - \varepsilon_e^*\right)}{\left(\varepsilon_p^* + 2\varepsilon_e^*\right)}. \tag{9}$$

The real and imaginary parts of the Clausius–Mossotti factor can be written as

$$\begin{aligned} \mathrm{Re}\left[f_{\mathrm{CM}}(\omega)\right] &= \frac{\left(\varepsilon_p - \varepsilon_e\right)}{\left(\varepsilon_p + 2\varepsilon_e\right)} + \frac{\frac{(\sigma_p - \sigma_e)}{(\sigma_p + 2\sigma_e)} - \frac{(\varepsilon_p - \varepsilon_e)}{(\varepsilon_p + 2\varepsilon_e)}}{1 + \omega^2 \tau_{rel}^2}, \\ \mathrm{Im}\left[f_{\mathrm{CM}}(\omega)\right] &= \frac{\left[\frac{(\varepsilon_p - \varepsilon_e)}{(\varepsilon_p + 2\varepsilon_e)} - \frac{(\sigma_p - \sigma_e)}{(\sigma_p + 2\sigma_e)}\right] \omega\tau_{rel}}{1 + \omega^2 \tau_{rel}^2}, \end{aligned} \tag{10}$$

where τ_{rel} is the particle relaxation time

$$\tau_{\mathrm{rel}} = \left(\frac{\epsilon_{\mathrm{p}} + 2\epsilon_{\mathrm{e}}}{\sigma_p + 2\sigma_e} \right). \tag{11}$$

The relaxation time is the reciprocal value of angular frequency, often referred to as the Maxwell–Wagner relaxation frequency. It is related to the dispersion of the dipole moment due to interfacial polarization. The Clausius–Mossotti factor is frequency dependent and its real part can span from -0.5 to $+1$ and imaginary part from -0.75 to $+0.75$ (Fig. 2).

When the particle is exposed to electric field with an zero amplitude ($|\mathbf{E}| = 0$) but nonzero higher order derivatives or the particle is about the same size as surrounding features, higher order terms have to be considered. The i-directional component of the force considering quadrupole and octopole terms is

$$\begin{aligned} \mathbf{F}_i = {} & 2\pi\epsilon_{\mathrm{e}} r^3 \mathrm{Re}\left(\frac{\left(\varepsilon_p^* - \varepsilon_e^*\right)}{\left(\varepsilon_p^* + 2\varepsilon_e^*\right)} \mathbf{E}_m \frac{\partial \mathbf{E}_i^*}{\partial x_m} \right) \\ & + \frac{2}{3}\pi\epsilon_{\mathrm{e}} r^5 \mathrm{Re}\left(\frac{\left(\varepsilon_p^* - \varepsilon_e^*\right)}{\left(2\varepsilon_p^* + 3\varepsilon_e^*\right)} \frac{\partial \mathbf{E}_n}{\partial x_m} \frac{\partial^2 \mathbf{E}_i^*}{\partial x_n \partial x_m} \right) \\ & + \frac{1}{15}\pi\epsilon_{\mathrm{e}} r^7 \mathrm{Re}\left(\frac{\left(\varepsilon_p^* - \varepsilon_e^*\right)}{\left(3\varepsilon_p^* + 4\varepsilon_e^*\right)} \frac{\partial^2 \mathbf{E}_n}{\partial x_l \partial x_m} \frac{\partial^3 \mathbf{E}_i^*}{\partial x_n \partial x_m \partial x_l} \right). \end{aligned} \tag{12}$$

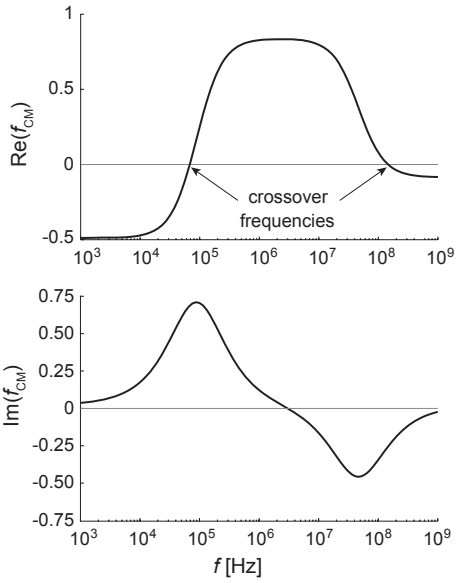

Fig. 2 Real and Imaginary part of the Clausius–Mossotti factor of a typical mammalian cell calculated using single shell model. Dielectrophoresis depends on real part, electrorotation on imaginary part and traveling wave dielectrophoresis on both parts of the Clausius–Mossotti factor

In this notation each index m, n, and l go through all three of spatial coordinates. A more detailed derivation and the differences in DEP force with or without higher order terms can be found in Jones (1995) and Jones and Washizu (1996).

2 Electrokinetics

Electrokinetics describes the motion of particles and fluids due to applied electric fields. Phenomena typically related to cell manipulation in microfluidic devices are electrophoresis, electroosmosis, dielectrophoresis, traveling wave dielectrophoresis, and electrorotation. Electroporation does not involve movement of cells, but it is related to exposure of a cell to an electric field and will be explained in this chapter.

2.1 Electrophoresis

Electrophoresis is the motion of a charged particle due to action of Coulomb force. Cells typically have negative charge on the surface and they can be manipulated in electric field. The Coulomb force F_{EP} on a particle is

$$\mathbf{F}_{\mathrm{EP}} = Q\mathbf{E} = \int_S \sigma_Q dS\, \mathbf{E}, \tag{13}$$

where Q is the total charge of the particle, σ_Q is the surface charge density and S is the surface of the particle over which surface charge density is integrated. Cells suspended in an electrolyte solution are surrounded by a double layer of ions. The inner layer of ions, called the Stern layer, is adsorbed on the interior membrane surface. The outer layer, where ions are freely moving due to thermal motion, is called the diffuse electrical double layer and it spans a distance on the order of the Debye length. Including the double layer in force calculations to more precisely describe cellular motion adds complexity and is explained in detail in Chapter 7 of Morgan and Green (2003).

2.2 Electroosmosis

Electroosmosis (EO) is the motion of a polarizable medium in an electric field due to the net Coulombic forces acting on the charged molecules in the medium. Conventional DC-driven EO flow is observed in microchannels and around particles where the electrical double layer is formed to shield the surface charge. The Coulombic forces experienced by the net excess charges in the double layer drive the EO flow in the microchannel. In microchannels, DC EO flow creates a plug flow where the velocity outside the double layer remains constant. Compared to the parabolic flow profile caused by pressure driven flow, plug flows ensure that mixing in the flow direction is minimized. Thus, this kind of EO flow is of particular importance in LOC microdevices, because it can be used to generate electrokinetically driven on-chip flows without moving parts as opposed to pressure driven flows. An example of such a microdevice is a cell culture platform that uses EO pumping to generate sheer stress on the cells and recreate physiological conditions (Chang et al. 2014). EO also plays an important role in electrophoretic separation by modifying the elution times of the charged analytes.

Induced Charge Electroosmosis (ICEO) describes a type of electrokinetic phenomena in which the applied electric field induces the formation of charges on polarizing (metal and dielectric) surfaces and dielectric media which further interact with the applied or induced electric fields and can produce a wide range of fluid motion. Unlike conventional DC electroosmosis (EO), ICEO is a nonlinear phenomenon and the flow fields are dependent on the geometry and configuration of the electrodes and other surfaces as well as the strength and frequency of the applied electric field (Squires and Bazant 2004).

AC electroosmosis (ACEO) is a case of ICEO where the applied electric field acts on its own induced charges at the electrode surfaces to create fluid flow. ACEO-based devices generally require much smaller operational voltages (in mV) and undesirable Faradaic reactions are reduced or eliminated. ACEO using micropatterned electrode arrays has been applied to particle focusing and concentration. Hoettges et al. (2003) demonstrated the use of an interdigitated electrode array to trap particles on top of the electrodes using a combination of DEP and ACEO. The two sets of electrodes create a pair of counter rotating vortices which focuses and traps cells and particles on top of the electrodes (Fig. 3).

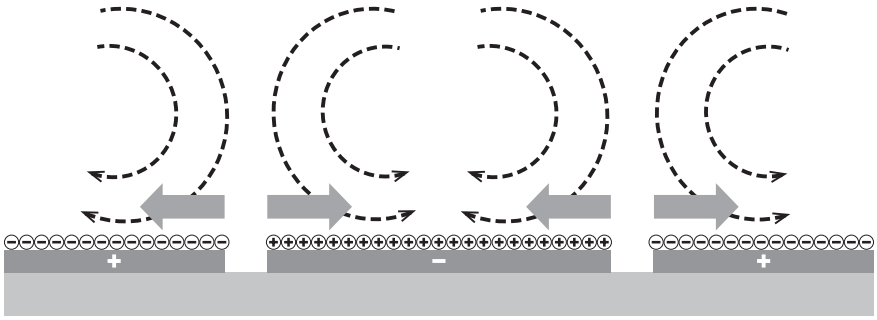

Fig. 3 Schematic diagram of AC electroosmotic flow. The *dotted arrows* represent the fluid motion while the *solid lines* indicate the motion of the particles suspended in the fluid

2.3 Dielectrophoresis

As shown before, when a biological cell is subjected to an electric field, a dipole is induced in the cell. When an electric field is inhomogeneous, the cell experiences a dielectrophoretic force, which drives the cell toward the high region of electric field if the cell is more polarizable than the medium (positive DEP, Fig. 1c) or toward lower field if the cell is less polarizable (negative DEP). The process was first described by Pohl and Crane (1971) and the detailed theory is described in several books and articles (Voldman et al. 2000; Jones 1995, 2003; Morgan and Green 2003).

The electric field can be written in the form $E_i = E_{0i}\sin(\omega t + \varphi_i)$, where E_0 is the amplitude of the sine wave, φ is the phase shift angle and subscript i indicates spatial components x, y, z. E_{RMS} is the root mean value of E_0. The time averaged dielectrophoretic force can be approximated as:

$$\langle \mathbf{F}_{DEP}(t)\rangle = 2\pi\epsilon_{\mathrm{e}} r^3 \Big(\mathrm{Re}(f_{\mathrm{CM}}(\omega))\nabla E_{RMS}^2 + \mathrm{Im}(f_{\mathrm{CM}}(\omega))\Big(E_x^2\nabla\varphi_x + E_y^2\nabla\varphi_y \tag{14}$$

This equation has two parts, one with a real part and one with an imaginary part of the Clausius–Mossotti factor. When an electric field is applied using only one pair of electrodes or in general when it does not have phase shifted components, the imaginary part is zero and the equation above simplifies to

$$\mathbf{F}_{DEP} = 2\pi\epsilon_{\mathrm{e}} r^3 \mathrm{Re}(f_{\mathrm{CM}}(\omega))\nabla E_{RMS}^2. \tag{15}$$

This equation can be roughly divided into two parts; a device contribution $\epsilon_{\mathrm{e}}\nabla E_{RMS}^2$ and particle contribution $2\pi r^3 \mathrm{Re}(f_{\mathrm{CM}}(\omega))$. Two particles can be separated if they have significantly different size and/or electrical properties included in the Clausius–Mossotti factor. If two populations of cells have a wide distribution of cell sizes, the strong dependence on cell size can impede separation of cells with different properties of their membrane.

The Clausius–Mossotti factor is frequency dependent and most cells in a low or moderately conductive medium exhibit positive and negative DEP at different frequencies. The point where the real part of the Clausius–Mossotti factor changes sign and the DEP force is zero is called the crossover frequency. Typically cells can have one or two crossover frequencies.

Dielectrophoresis can be used to manipulate, characterize and separate cells in a label free and noninvasive method. Sufficiently large electric field gradients are limited to short distances from the electrodes or structures distorting the field. Therefore, the full potential of DEP can be achieved in microfluidic devices as a contact-free method of manipulating cells. In most cases, the small distances between electrodes in microchannels result in high electric field strengths being obtained from a function generator, allowing for relatively low-voltage contact-free cellular manipulation. No markers, optics, or bulky on-chip components are needed. However, the drawback of using DEP for practical purposes is the necessity to suspend cells in a buffer with conductivity lower than physiological values to mitigate Joule heating. Examples of DEP uses are described in the Sect. 5. Typically, DEP can be used for single cell or for high-throughput cell manipulation, and can be used to perform characterization and separation based on cell's biophysical properties. Some of the most popular target cells are different blood cells (Minerick et al. 2003; Gagnon et al. 2008), rare cells (Gascoyne et al. 2009; Salmanzadeh et al. 2012; Salamanzadeh and Davalos 2014) and various cancer cells (Gascoyne et al. 2013). DEP is a popular research topic and in the last few years DEP-based devices have become commercially available as well.

2.4 Electrorotation

Electrorotation is typically used as a tool to characterize electrical properties of single cells. The same biophysical properties are responsible for cell rotation as for DEP translation. Electrodes placed around a cell and energized with phased shifted AC voltage generate a rotational field. An induced dipole in the middle of the electrodes will experience torque and rotate (Fig. 4a). When the field has four components, phase shifted for 90° the torque on a cell is

$$\mathbf{T}_{ROT} = -4\pi\epsilon_e r^3 \mathrm{Im}(f_{\mathrm{CM}}(\omega))|\mathbf{E}|^2. \tag{16}$$

The cells can rotate in the same direction or in the opposite direction than the electric field, depending on the frequency of electric field and imaginary part of the Clausius–Mossotti factor. In most of the dielectrophoretic devices, the field gradient is not constant enough to fit measurements of motion of individual cells to the model and other forces influence the motion of cells. Electrorotation chambers have an area of constant field gradient in the middle between the electrodes and it is easier to determine the field at the location of a cell. Still cell-to-cell interactions distort the electric field and influence the motion of cells, fluctuations of the medium move cells in unwanted directions and gravity pulls the cell to the bottom

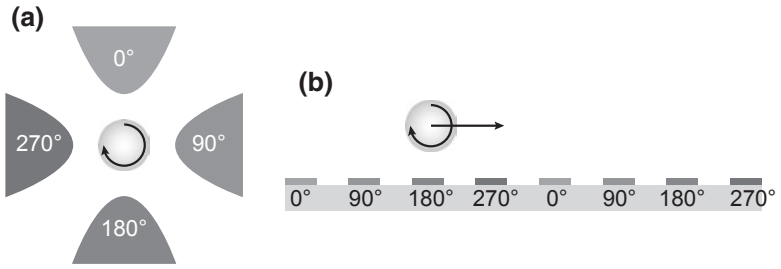

Fig. 4 Energizing electrodes with phase-shifted voltage induces motion of cells that depends on imaginary part of the Clausius–Mossotti factor; **a** electrorotation, **b** traveling wave DEP

of the chamber and therefore friction with the bottom surface influences the rotational speed of a cell. To minimize cell-to-cell interactions, the concentration of the cells in suspension must be low. To keep the cell levitating, a combination of electrorotation with negative dielectrophoresis is often used. The voltage to induce electrorotation can be superpositioned with the voltage to induce dielectrophoresis and levitation or dielectrophoresis and electrorotation voltages can be applied sequentially to keep the cell levitating in the middle of the electrodes. To energize the electrodes, four sine signals can be generated with four synchronized generators or two generators with 90° phase shift and two inverters. Vibrations and evaporation of water cause uncontrolled motion of cells, which can be minimized by using a gasket and covering a device with a cover slip.

The rotational velocity of individual cells can be measured by recording videos and determining differences in orientation of the cells. Cells have a nonuniform surface and are not ideally spherical. This asymmetry allows one to recognize cellular orientation on each frame of the video and determine the rotational velocity. From the velocity measured at different frequencies, the imaginary part of the Clausius–Mossotti factor can be fitted to measurements and the values of electrical conductivities and permittivities of cells can be calculated.

The advantage of electrorotational characterization is minimization of influence of other forces and ability to measure single cells, while the disadvantage is extremely low throughput. Electrorotation spectra have peak velocities close to crossover frequencies of dielectrophoretic spectra (see Fig. 2) and it can be a useful tool to calculate biophysical properties of cells and predict the possibility of dielectrophoretic cell separation.

2.5 Traveling Wave Dielectrophoresis

Similar to rotational field devices, planar interdigitated electrodes can be energized by phase shifted voltages while the dielectrophoretic force propels cells along an

array of electrodes (Fig. 4b). In this case both components of Eq. (14) are nonzero. A cell can effectively move if the DEP force is negative in order to levitate the particle and the traveling wave dielectrophoresis (twDEP) component is large enough to produce translational motion. For a typical mammalian cell in low conductivity medium, these conditions are fulfilled just above the first crossover frequency. While single phase electrodes can be easily fabricated in one layer, four phase-shifted signals require metal deposited in multiple layers or a manifold to individually connect each electrode bar of the electrode array.

3 Electroporation

Exposure of a cell to a strong electric field causes the formation of pores in the cellular membrane. The phenomenon is called electroporation and it allows for the exchange of molecules through otherwise impermeable membrane (Neumann et al. 1982; Davalos et al. 2000; Kotnik et al. 2012). Pores form when the induced transmembrane voltage (ITV) reaches the threshold that is typically between 0.2 and 1 V, depending on the cell type (Chen et al. 2006; Henslee et al. 2011a). The ITV at a point on the surface of a spherical cell in suspension can be described with the following equation (Schwan 1983; Marszalek et al. 1990)

$$ITV = 1.5Er\frac{1}{\sqrt{1+\omega^2\tau^2}}\cos(\theta), \tag{17}$$

where θ is a polar angle, measured from the center of the cell between the given point on the membrane and the applied field direction, and τ is the relaxation time of the cell membrane [Eq. (11)]. A diagram of the cell with θ defined and a graph of the ITV magnitude is shown in Fig. 5.

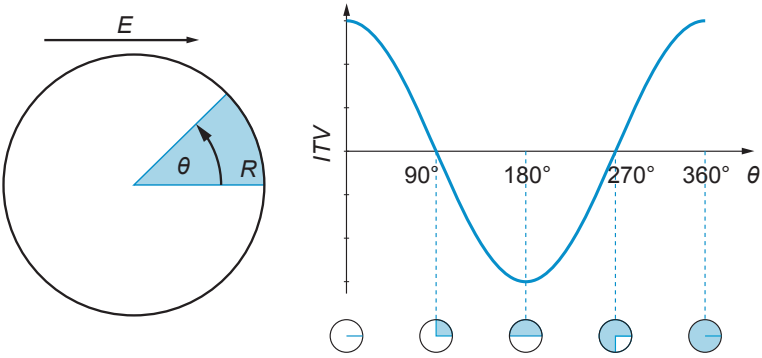

Fig. 5 When a cell is exposed to electric field, the transmembrane voltage depends on a position on the membrane

Pores, which form during exposure of a cell to electric pulses, close in a few microseconds after pulse delivery. However, the cell membrane remains permeable for several minutes (Pucihar et al. 2008).

While electroporation generally does not induce motion of cells, it is useful for the manipulation of transport across the cell membrane. Depending on the duration and amplitude of electrical pulses, electroporation can be reversible or irreversible. If the pores close following electroporation, the cell recovers (reversible electroporation), but if the pores do not close or damage to the cell is too severe, the cell dies (irreversible electroporation) (Lee 2006). Reversible electroporation is typically used to introduce drugs or DNA material into cells and to fuse cells together, while irreversible electroporation is typically used to non-thermally lyse cells or induce apoptosis.

4 Model of a Cell

A cell is a complex particle, but from an electrical point of view it can be approximated as a conductive sphere (cytoplasm), surrounded by a thin dielectric shell (cell membrane). The equivalent complex permittivity of the cell, ε_c^*, using this geometric approximation can be expressed as

$$\varepsilon_c^* = \varepsilon_{mem}^* \frac{\gamma^3 + 2\left(\frac{\varepsilon_{cyt}^* - \varepsilon_{mem}^*}{\varepsilon_{cyt}^* + 2\varepsilon_{mem}^*}\right)}{\gamma^3 - \left(\frac{\varepsilon_{cyt}^* - \varepsilon_{mem}^*}{\varepsilon_{cyt}^* + 2\varepsilon_{mem}^*}\right)}, \tag{18}$$

where, ε_{cyt}^* and ε_{mem}^* are the complex permittivities of the cytoplasm and membrane, respectively. The factor γ is a function of the cell radius, r, and the membrane thickness, d_{mem}, and can be expressed as $\gamma = r/(r - d_{mem})$. The complex permittivity of the cell, ε_c^*, is a function of the frequency of the electric field, geometrical and electrical properties of the cell including the cytoskeleton, membrane morphology and capacitance as well as cytoplasm conductivity.

At high frequencies, in the MHz range, an electric field can easily penetrate the cell membrane and the model can be improved by adding additional concentric shells representing the cell nucleus, nuclear membrane and cell wall for some types of cells. Most eukaryotic cells are modeled by approximating the cell as three concentric shells around a central sphere, with the outer shell representing the cell membrane, followed by cytosol, the nuclear envelope and the nucleoplasm as the innermost volume (Fig. 6). The complex permittivity of the double shell model can be expressed as

$$\gamma_1 = r_{ne}/(r_{ne} - d_{ne}) \tag{19}$$

$$\gamma_2 = (r - d_{mem})/r_{ne} \tag{20}$$

$$\gamma_3 = r/(r - d_{mem}) \tag{21}$$

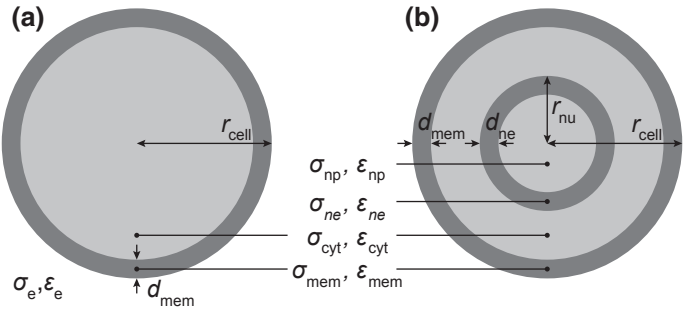

Fig. 6 Schematic for the single shell and double shell models. **a** Schematic diagram for modeling a biological cell of radius r using a single shell of thickness d_{mem} representing the cell membrane. **b** Schematic diagram for modeling a eukaryotic cell of radius r and nuclear radius r_{ne} as two concentric shells of thickness d_{mem} and d_{ne} representing the cell membrane and the nuclear envelope, respectively

$$\varepsilon_1^* = \varepsilon_{ne}^* \frac{\gamma_1^3 + 2\left(\frac{\varepsilon_{np}^* - \varepsilon_{ne}^*}{\varepsilon_{np}^* + 2\varepsilon_{ne}^*}\right)}{\gamma_1^3 - \left(\frac{\varepsilon_{np}^* - \varepsilon_{ne}^*}{\varepsilon_{np}^* + 2\varepsilon_{ne}^*}\right)} \tag{22}$$

$$\varepsilon_2^* = \varepsilon_{cyt}^* \frac{\gamma_2^3 + 2\left(\frac{\varepsilon_1^* - \varepsilon_{cyt}^*}{\varepsilon_1^* + 2\varepsilon_{cyt}^*}\right)}{\gamma_2^3 - \left(\frac{\varepsilon_1^* - \varepsilon_{cyt}^*}{\varepsilon_1^* + 2\varepsilon_{cyt}^*}\right)} \tag{23}$$

$$\varepsilon_c^* = \varepsilon_{mem}^* \frac{\gamma_3^3 + 2\left(\frac{\varepsilon_2^* - \varepsilon_{mem}^*}{\varepsilon_2^* + 2\varepsilon_{mem}^*}\right)}{\gamma_3^3 - \left(\frac{\varepsilon_2^* - \varepsilon_{mem}^*}{\varepsilon_2^* + 2\varepsilon_{mem}^*}\right)} \tag{24}$$

Here, the *mem*, *cyt*, *ne* and *np* subscripts denote the cell membrane, cytoplasm, nuclear envelope and nucleoplasm properties, respectively. The cell and nuclear radii are denoted by r and r_{ne}, respectively. The cell membrane thickness and the nuclear membrane thickness are denoted by d_{mem} and d_{ne}, respectively.

The single shell model is accurate for human red blood cells and prokaryotic cells. The double shell model is generally used to model most eukaryotic animal cells (except non-nucleated cells). Differences between the single shell and double shell models are most pronounced at high frequencies (>200 kHz) but are minimal at low frequencies. Therefore, when modeling the low frequency response of eukaryotic animal cells, the single shell model is a sufficient approximation, as the cell membrane partly insulates the cell interior. Plant and yeast cells, which are surrounded by a thick cell wall and contain large vacuoles/vesicles and multiple chloroplasts (plant cells). These cells can be modeled by a modification of the double shell (Asami and Yamaguchi 1992) and single shell (Asami and Yonezawa 1996) models to include the contribution of vacuoles/vesicles and plastids.

A major limitation of these models is the assumption that the cells are perfectly spherical. Models have also been developed for spheroidal cells (Asami et al. 1980) and for budding cells (Asami et al. 1998).

Analytical solutions of the electric field distribution exist only for a few simple electrode configurations, such as interdigitated electrodes (Morgan et al. 2001). For other configurations, numerical computations are a great tool to optimize the design of the microfluidic devices. The most popular numerical computation tool is finite element method (FEM) software. Some software packages allow the user to compute not only the electric field, but also the fluid flow velocity, evaluate the force balance on particles in the device and calculate particle trajectories. Numerically, computing the electric field and its gradient and then calculating the DEP force on a cell using Eq. (15) is typically the fastest way to predict the DEP force on a cell. However, it has some limitations. When a cell is very close to the channel wall or electrodes, the dipole approximation is not valid, since the scale of the nonuniformity of the electric field and the cell diameter are of comparable size. Such an approach does not consider cell-to-cell interactions and can be used only when cells are far from each other and other objects (Shi et al. 2010). When negative DEP is used cells are repelled from the electrodes and they are less likely to interact with other cells, in which case the dipole approximation is sufficient. However, when cells are trapped using positive DEP, they touch the walls, electrodes and other cells and numerical simulations are typically used to account for these dynamic changes.

The DEP force on a cell can be computed numerically using the Maxwell stress tensor. This formula is general and is not restricted to a specific cell shape or distance to channel walls or other particles. The DEP force on a particle can be computed by integrating the Maxwell stress tensor, $\bar{\mathbf{T}}$, over the surface of the particle

$$\mathbf{F}_{DEP} = \oint \left(\vec{\mathbf{T}} \cdot \mathbf{n} \right) dA, \tag{25}$$

where $\mathbf{n}$ is the unit vector normal to the surface. The time-averaged tensor $\mathbf{T}$ is defined as

$$\mathrm{T} = \frac{1}{4} \varepsilon_e \left(\left(\mathbf{E}\mathbf{E}^* + \mathbf{E}^*\mathbf{E} \right) - |\mathbf{E}|^2 \mathrm{I} \right), \tag{26}$$

where $\mathbf{E}^*$ denotes the complex conjugate of the electric field and $\mathbf{I}$ a unit tensor. This method is the most rigorous approach to calculate the DEP force and can be used to evaluate other methods (Wang et al. 1997; Rosales and Lim 2005). The analytical expression of the DEP force on a spherical particle can be alternatively derived from Eqs. (25) and (26), resulting in a typical expression for DEP force [Eq. (14)] (Wang et al. 1997).

Several numerical models and methods have been proposed to predict the motion of cells in cell manipulation devices (Lee et al. 2011; Jubery et al. 2014). The most common is the effective moment Stokes-drag method. Here, the particle is considered small enough that it does not affect the flow and electric field around

the cell significantly. The DEP force can be computed separately from the drag force. The fluid flow in microfluidic devices is creeping in nature and the Reynolds number is typically low, therefore the Stokes drag force, $\mathbf{F}_{\mathrm{DRAG}}$, on a spherical particle can be expressed as

$$\mathbf{F}_{\mathrm{DRAG}} = 6\eta r\pi(\mathbf{u}_p - \mathbf{u}_f), \tag{27}$$

where $\mathbf{u}_{\mathrm{p}}$ and $\mathbf{u}_{\mathrm{f}}$ are the velocities of the particle and medium, respectively, and η is viscosity of the medium. DEP and drag force are used to iteratively to simulate trajectories of particles. Trajectory of the particle is determined by the balance of DEP and Stokes drag forces and assuming that the inertial terms are negligible.

$$\mathbf{F}_{\mathrm{DRAG}} + \mathbf{F}_{\mathrm{DEP}} = 0 \tag{28}$$

The velocity of a particle, $\mathbf{u}_{\mathrm{p}}$, can be expressed as

$$\begin{aligned} \mathbf{u}_{\mathrm{p}} &= \mathbf{u}_{\mathrm{f}} - \frac{2\pi\epsilon_{\mathrm{e}} r^3 \mathrm{Re}(f_{\mathrm{CM}}(\omega))\nabla E_{RMS}^2}{6\eta r\pi} \\ \mathbf{u}_{\mathrm{p}} &= \mathbf{u}_{\mathrm{f}} - \mu_{DEP}\nabla E_{RMS}^2, \end{aligned} \tag{29}$$

where μ_{DEP} is the DEP mobility of the particle defined as

$$\mu_{DEP} = \frac{\epsilon_{\mathrm{e}} r^2}{3\eta}\mathrm{Re}(f_{\mathrm{CM}}(\omega)) \tag{30}$$

The DEP mobility is independent of the electric field gradient and therefore it is intrinsic to the particles. When particles significantly influence the electric field and fluid flow distribution, then other methods can be used. The arbitrary Lagrangian–Eulerian (ALE) method, a finite element method technique, captures the physics very well. The flow and electric field are solved separately and the interface conditions are matched iteratively to obtain the solution. A moving mesh is used to follow the motion of the particle. This method is computationally demanding and only useful for single particle simulations. Using different meshes for solid and fluid domains significantly reduces the computation time. The immersed finite element method, unified finite volume method and immersed interface method offer faster simulation of cell trajectories and allow one to study the interactions of several cells close together (Jubery et al. 2014).

5 Applications

Electrokinetics has been investigated for decades and has been widely adopted as a method for molecule separation. Electrokinetics for cellular manipulation became popular in the 1990s and since 2000 there has been a strong increase in the number of publications focusing on applications, especially dielectrophoresis (Pethig 2010). Although electrokinetics can be used to manipulate various kinds of

polarizable particles, it is most commonly used for biomedical applications, such as DNA and cell manipulation.

5.1 Non-Specific Manipulation of Cells

AC electroosmosis (ACEO) has emerged as a precise and easily implemented method of local flow control without moving parts. Unlike DC electroosmosis, which requires large voltages and involves Faradaic reactions at the electrodes, ACEO can work with small applied voltages while Faradaic reactions are mostly eliminated. The fluid flow generated can be used to concentrate and trap particles and cells in certain locations. The strength and structure of the fluid flow can be tuned by changing the electrode geometries and applied electric fields. While ACEO is not selective, it is versatile and robust, and can be implemented for a wide range of particles ranging from strands of DNA to live cells. However, ACEO flows have been shown to decay strongly with increasing salt concentrations and the flows are negligibly small for solutions with ionic concentrations greater than 10 mM.

The fluid flow generated by ACEO has been used to focus cells on electrodes where they can be trapped by strong short range DEP and electrophoretic forces (Wong et al. 2004; Bhatt et al. 2005). ACEO trapping has also been used with electrical impedance spectroscopy to concentrate and detect *E. coli* bacteria (Wu et al. 2005). Asymmetric electrode patterns have been shown to produce flows that can be used for pumping in microdevices. Melvin et al. (2011) designed an on-chip particle collection device using ACEO pumping DEP for the rapid concentration and collection of yeast cells and other particles in a stagnant region of the device. The applied electric fields can be tuned for different dilute electrolytes, particle sizes and concentrations making this design robust and versatile. ACEO can be used to build several components of LOC systems. Fu et al. (2015) developed contactless metal electroosmotic micropump to perform fluid pumping, routing and metering on a single chip.

Sheath flows, where the flow of interest is focused by a surrounding bulk flow, are the most commonly used method to focus cells in a microchannel. However, sheath flows increase the complexity of the device and dilute the particle concentration. DEP has been extensively used as a sheathless cell focusing mechanism in microchannels. By creating nonuniform electric field normal to the streamlines, particles and cells can be focused in tight streams (Hughes 2002; Gascoyne and Vykoual 2004). This approach uses negative DEP to push the cells away from the electrodes and counteracts the gravitational sedimentation of cells in the microchannel. Combined with a hydrodynamic "lift" force (F_{HDLF}) it forms the basis of DEP Field-Flow-Fractionation (DEP-FFF), which will be discussed in the following section. Müller et al. (1999) developed microelectrode device that is capable of multiple electrical manipulation of cells. The electrode elements are designed to focus, trap, rotate and separate cells or latex particles using negative DEP.

Khoshmanesh et al. (2011) used DEP to trap live nonadherent cells during environmental scanning electron microscopy, avoiding the need of chemically preparing the cells for scanning.

Insulated posts and other barriers can be used to form electric field gradients, which can be used to dielectrophoretically focus particles in a microchannel. Cummins and Singh used insulated posts (Cummings and Singh 2003) while Xuan et al. (2006) used a constriction to focus latex beads with DC DEP. A major difficulty with such methods is that the obstacles need to be of the same order of magnitude as the particles to generate large enough DEP forces. However, Zhu and Xuan (2009) demonstrated the use of DC biased AC fields to focus particles in a constriction. The tightness of the focused stream could be tuned by changing the ratio of the DC to AC applied electric fields. X-shaped insulated posts have also been used to focus (Huang et al. 2011) and simultaneously filter live and dead HeLa cells (Fig. 7) (Jen and Chen 2011).

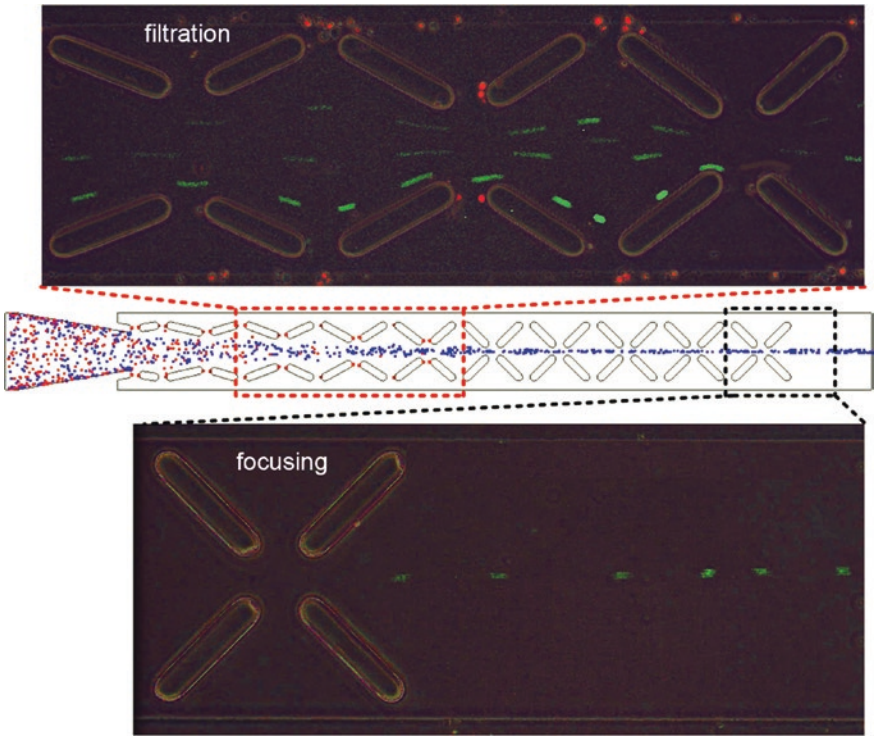

Fig. 7 Insulator-based DEP filtration (*top*) and focusing (*bottom*) of live (*stained green*) and dead (*stained red*) HeLa cells using a series of X-shaped insulated posts. The dead cells are filtered at the edges of the insulating structures upstream while the live cells are focused to the center. Reproduced with permission from Jen and Chen (2011). Copyright 2011, AIP Publishing LLC

5.2 Sorting Based on Cell Characterization

Flow cytometry has emerged as an important method of cell sorting and has been used for characterizing cells suspended in a medium based on their properties and separating them for further analysis. Flow cytometry has also become a vital tool for the purification and analysis of rare cells such as stem cells, circulating tumor cells and rare bacterial species that cannot be cultured in lab environments.

Rapid advances in LOC technology have enabled the miniaturization of flow cytometers. These miniaturized systems are designed for point-of-care clinical diagnostic purposes and are inexpensive, portable and disposable while still retaining most of the functionality of bulky and expensive commercial benchtop systems. Fluorescence activated cell sorting and impedance based cell sorting are two technologies that are commonly used by flow cytometers to count and sort cells. Both these methods identify the cells based on their properties and use electric fields to sort them at a downstream location.

5.2.1 Fluorescence-Based Cell Sorting

Fluorescence-activated cell sorting (FACS) is a popular method of counting and sorting cells based on their fluorescence intensity. The target cells are tagged with a fluorescent dye that binds to specific proteins and the cell suspension is then pumped through a nozzle one at a time. Light scattering is used to size the cell while the presence or absence of the fluorescent tag is used to identify the cell of interest.

Conventional benchtop FACS devices use a vibrating nozzle to encapsulate the cell in a droplet, which is then positively or negatively charged based on its fluorescence signal. The charged droplet is dropped in an electric field where it is sorted into different bins based on the charge on the droplet. Yao et al. (2004) designed an integrated micro flow cytometer with a FACS system that is driven by gravity. However, most LOC fluorescence-based cell sorting systems use a number of different electrokinetic technologies, both for driving the fluid flow through the microchannels and for sorting the cells once a positive identification has been made. Fu et al. (2004) demonstrated an electrokinetically driven LOC fluorescence-based cell cytometer. This system uses electrokinetic flows to focus the cells or particles in the center of the microchannel as well as to switch the flow after the identification has been made. Holmes et al. (2006) used DEP to focus fluorescent particles in the center of a microchannel where they could be sorted. Baret et al. (2009) used a fluorinated oil with surfactants to encapsulate *E. coli* cells in droplets which when detected by the fluorescent intensity were deflected into a side chamber using DEP. This system can sort accurately up to 2000 droplets per second.

LOC systems that identify cells based on their fluorescence signals and sort them using various electrokinetic phenomenon have seen a great deal of improvement in recent years. These systems can now sort cells with throughputs

approaching conventional benchtop FACS systems while still being price efficient and portable. However, one major drawback of these systems is that they are still reliant on fluorescent markers to classify the cells.

Fabbri et al. (2008) developed a microfluidic device that uses negative DEP to manipulate and position the cells in the middle of DEP cage. Individual cells are then analyzed and separated based on their fluorescence labeling or morphological features and sorted using DEP.

5.2.2 Impedance-Based Cell Sorting

In recent years, impedance-based cell sorting has been investigated as an alternative to sorting cells using fluorescence identification of cells. Unlike FACS, impedance-based cell sorting is a label-free non-invasive method of identifying cells and sorting them based on their dielectric properties. Impedance-based micro flow cytometers generally measure the impedance of cells at various discrete frequencies and use this impedance data to identify the cells of interest.

The first impedance-based flow cytometer was devised by Coulter (1953). Microfluidic Coulter Counters use impedance sensing of single cells in a microchannel for a variety of purposes ranging from simple counting and sizing of the cells to non-invasively monitoring single cell functions. When the cell passes between two electrodes in a microchannel, the measured electrical impedance of the system will increase. This change is proportional to the radius and dielectric properties of the cell as well as the frequency of the applied voltage used for the impedance measurement. The characterization and classification of the cell based on this change in the electrical impedance is the operating principle behind all impedance-based cell sorters. In contrast to electrorotation or the measurement of DEP crossover frequencies, impedance cytometry directly measures the impedance and thus, the dielectric properties of the cell.

The first impedance-based cytometers used DC or low frequency AC voltages to size and count the cells. As the cell membrane is a poor conductor at these frequencies, the resistance change is a measure of the change in the amount of electrolyte between the two electrodes. The conductivity of the cell-media system (k_o) can be calculated as $k_o = k_s(1-p)(1+p/2)$ where k_s is the conductivity of the medium and p is the ratio of the cell volume to the total detection volume of the electrodes. At higher frequencies, (>1 MHz) the cell membrane conducts more current and parameters such as the cell membrane capacitance and the cytoplasmic conductivity can be obtained.

Recently, there has been a great deal of research focused on developing on-chip impedance-based flow cytometers as the first step for complete cell sorting devices. Ayliffe et al. (1999, 2002) developed the first on-chip microfluidic impedance-based cell sorter which was used to differentiate human polymorphonuclear leukocytes from teleost nucleated red blood cells. Gawad et al. (2001) modeled and simulated the impedance spectra for cells in a microchannel for different electrode combinations. The resulting microfabricated impedance cytometer used two

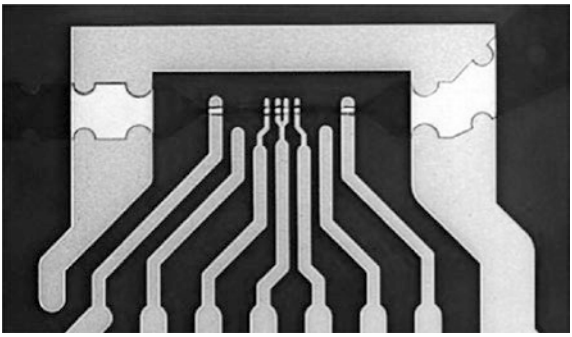

Fig. 8 Microfabricated impedance sensor for impedance cytometry with measurement channel and, coplanar measuring and shielding electrodes. The fork in the middle provides a separate ground to each of the two sets of electrodes. Reproduced from Gawad et al. (2001) with permission from The Royal Society of Chemistry

sets of coplanar electrodes to investigate and differentiate between latex beads of different radii and also erythrocytes and ghost cells using a low frequency and a high frequency voltage (Fig. 8). While both of the high-frequency and low-frequency impedances vary with the height of the cell in the microchannel, the opacity, which is the ratio of these impedances remain almost constant. This coplanar electrode design has been adapted and used for impedance cytometry and counting by many other authors.

The coplanar electrode design is easy to fabricate and effective at differentiating between cells, but the nonuniform electric field in the microchannel is responsible for large variations in the impedance signal. Gawad et al. (2004) proposed a parallel electrode configuration and used a 3D finite element simulation to model the impedance and compared the numerical solution to the Maxwell mixture model solution. Due to the more uniform electric fields in the parallel electrodes, the effect of the position of the cell in the microchannel is less significant. This amplitudes and phase of the impedance as well as the opacity obtained from this design were used to differentiate cell sizes (Fig. 9), membrane capacitances and cytoplasmic conductivities at up to a 1000 cells/s (Cheung et al. 2005; Morgan et al. 2007). This design was also adapted by Valero et al. (2010) and Mernier et al. (2012) to fabricate LOC devices with liquid electrode arrays, capable of both impedance cytometry and dielectrophoretic sorting.

Some of the more recent advances in impedance-based cell sorting have been to utilize a larger frequency range to investigate the cell. Fuller et al. (2000) developed a multi-frequency impedance cytometer which could differentiate the radius and the membrane capacitance of cells at up to 100 cells/s. Sun et al. and Gawad et al. developed a broadband impedance spectroscopy cytometry technique that could measure the impedance at 512 evenly spaced frequency points within a 1 ms time interval. This measurement capacity was made possible by the use of a maximum length sequence analysis that obtains an impulse response of

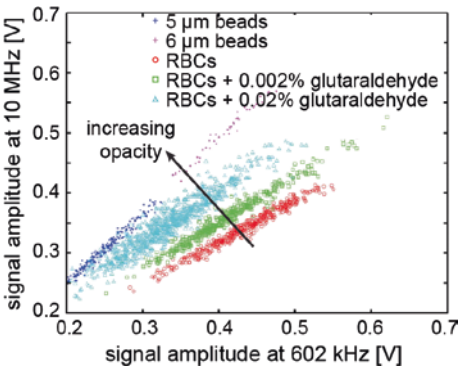

Fig. 9 Correlation plot of the high frequency (10 MHz) versus low frequency (602 kHz) signal amplitudes for living and fixed red blood cells (RBCs) and latex beads of different radii. The living RBCs can be differentiated from the fixed RBCs and the latex beads. Adapted from Cheung et al. (2005) with permission from John Wiley and Sons

the particle. This system has the advantage of having a much higher signal-to-noise ratio than conventional FFT or discrete frequency techniques and this can be further improved using digital signal processing techniques (Sun et al. 2009). Impedance sensing has also been combined with fluorescence cytometry on the same chip making for a more versatile cell sorting system (Morgan et al. 2006; Baret et al. 2009) capable of differentiating leukocytes and obtaining total blood counts (Holmes et al. 2009). Small antibody conjugated beads have also been bound to CD4-T cells to enable identification and sorting analogous to fluorescent labeling (Holmes and Morgan 2010).

5.3 Direct Cell Separation

Dielectrophoresis is a cell separation method that uses cells' intrinsic properties, regardless of their genetic information or expression. Different cells have different DEP response and they can be directly sorted based on the sign or magnitude of DEP force. Cells can be separated by directing them to different outlets in continuous flow or they can be separated in batches. Continuous separation requires a focused stream of a cells suspension and the DEP force changes the trajectory to route cells in different directions depending on their DEP response. Batch separation is typically based on selective trapping of one type of cells. Target cells are typically trapped/immobilized by positive DEP while background cells pass through the device.

Cell trapping is strongly determined by cell size as follows from Eq. (15). For example, a 10 % increase in radius increases the DEP force by 33 % allowing it to dominate over small differences in electrical conductivity or permittivity. To minimize the effect of cell size, a balance of forces can be used. A great example of balancing forces is Dielectrophoretic Field Flow Fractionation (DEP-FFF) (Huang et al. 1997; Markx et al. 1997; Čemažar et al. 2013) where a DEP-FFF device consists of array of interdigitated electrodes at the bottom of the channel, generating

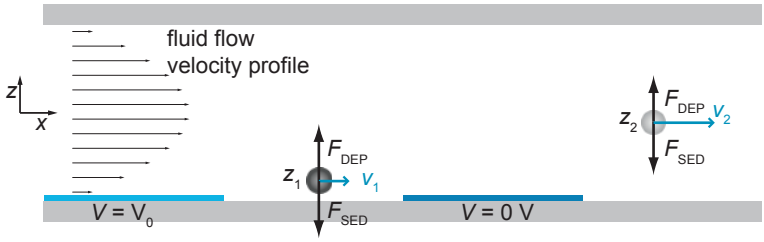

Fig. 10 Dielectrophoretic field-flow fractionation. Laminar flow carries the cells through device at different equilibrium heights

electric field that pushes up the cells via negative DEP (Fig. 10). Since cells have higher density than the surrounding buffer, a sedimentation force acts in the opposite direction. Both forces are dependent on r^3, which is the key in the reduction of cell size influence. The DEP force decreases rapidly with distance from the electrodes and a cell reaches its equilibrium vertical position within the lower half of the channel. The channel is thin and wide therefore the fluid flow is laminar. Cells with equilibrium position in the middle height of the channel flow through device the fastest, while cells close to the bottom flow the slowest.

DEP-FFF sorting can be either batch or continuous. In batch sorting, a small volume of cell suspension is injected into the channel and elution buffer is pumped into the device to move the cells through the channel. Cells reach their equilibrium vertical position depending on their properties and then they flow at different velocities. Cells that arrive at the outlet first are collected in the first bin, and the cells that flow through the channel slower are collected in the second bin. The advantage of batch mode sorting is simple fabrication in comparison to the continuous mode device.

In continuous mode devices, cells and elution buffer are pumped into device. Cells reach their equilibrium position and the channel has a splitter at the end to direct cells into two outlets based on their vertical position. This type of DEP-FFF device generally has higher throughput and it is easier to fine tune the voltage and flow rates to split two populations of cells. The disadvantage is fabrication difficulty, since cells need to be split at the end of the channel and one withdrawal pump in addition to two infusion pumps are needed for stable fluid flow. The downside of DEP-FFF is the length of the channels. Devices that allow high throughput separation can have a 30 cm long channel making it necessary to fabricate the chamber with several sections of interdigitated arrays and using a flexible substrate to prevent breaking of the electrode array (Vykoukal et al. 2008).

Cells can be characterized using DEP to measure some of their biophysical properties and to determine the feasibility of DEP separation. Characterization is typically done by exposing cells to a predefined electric field for a short time and visually tracking their motion. Changes in their position at different frequencies are then fitted to the model described in Sects. 2.3 and 4 to obtain the Clausius–Mossotti curve. Gagnon et al. (2008) used quadrupolar electrodes to measure f_{CM}

of bovine red blood cells of different starvation ages that reflects in surface protein density. In a typical DEP buffer the second crossover frequency is in the order of hundreds of MHz and electromagnetic interference impedes the measurements. Therefore, they modified the composition of the DEP buffer with a zwitterionic solution to lower the second crossover frequency to tens of MHz. Salmanzadeh et al. (2013) measured the first crossover frequency of different stages of cancer cells using a contactless DEP device. They found that sphingosine treatment can change the properties of late stage of mouse ovarian surface epithelial cells to have the same crossover frequency as the benign cancer cells. Fatoyinbo et al. (2008) characterized cells with the DEP dot microsystem (Fig. 11). They did not measure the position of individual cells, but the intensity of transmitted light in each dot chamber. When cells experienced positive DEP they moved towards the electrodes on the perimeter of the chamber, and when they experienced negative DEP they concentrated in the middle of the chamber.

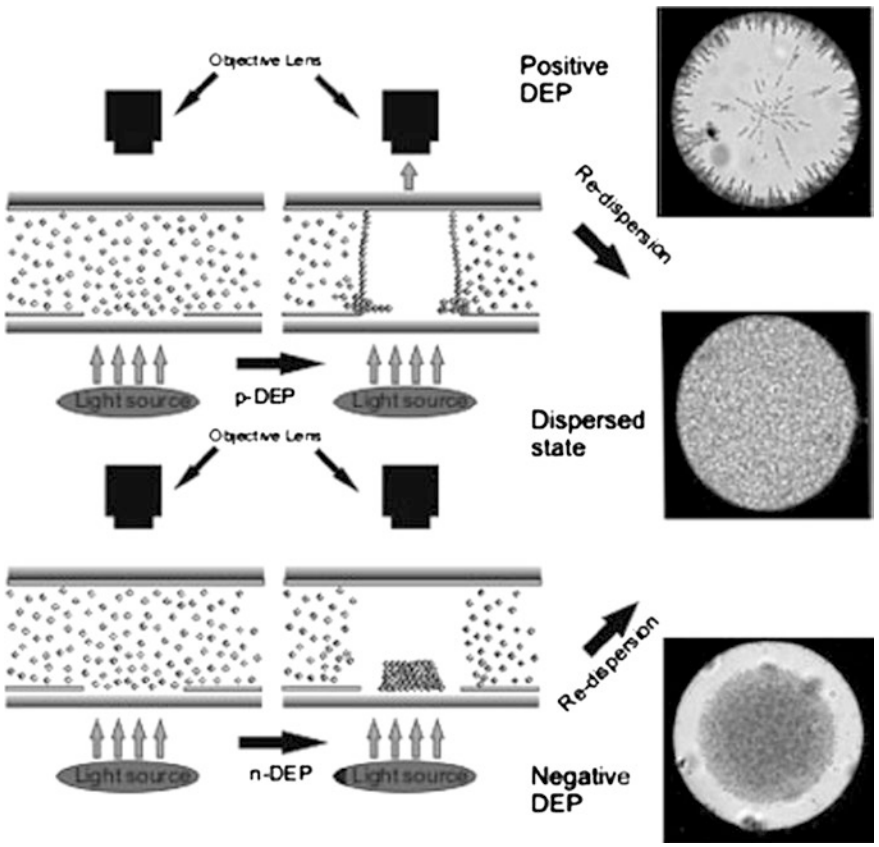

Fig. 11 Characteristic dispersions of the dielectrophoretically manipulated cells in the dot microsystem. Reproduced from Fatoyinbo et al. (2008) with permission from John Wiley and Sons

Metal electrodes have some disadvantages, such as electrolysis, electrode delamination, and bubble formation. Some of these complications can be minimized by using gold electrodes (inert metal) and AC voltage to reduce electrochemical damage to the material. An alternative to forming inhomogeneous electric fields with the physical pattern and geometry of metal electrodes is to use insulating structures to distort the otherwise homogeneous electric field. This technique is called insulator dielectrophoresis (iDEP) (Cummings and Singh 2003; Lapizco-Encinas et al. 2004) and it has some advantages over classical DEP using metal electrodes. iDEP systems offer reduced chemical reactions, elimination of the metal deposition and patterning step required for metal electrode arrays and no electrode delamination. Using insulating structures to distort the electric field also minimizes damage to the cells due to the extremely high electric field that may appear on the edges of metal electrodes. Many iDEP systems are reviewed in (Simmons et al. 2006; Srivastava et al. 2010; Regtmeier et al. 2011). For example, cellular studies have been performed on the concentration and separation of bacteria in water using a glass device with insulating pillars (Lapizco-Encinas et al. 2004) and sorting of cells by size in a continuous sorting device (Kang et al. 2008).

The concept of eliminating contact of cell suspension with metal electrodes was taken even further in contactless dielectrophoresis (cDEP) devices (Shafiee et al. 2009). Insulating structures are used to distort otherwise homogeneous electric fields as in some iDEP devices, however, the electrodes are completely separated from the cell suspension by a thin insulating membrane. This barrier negates possibility of electrochemical damage to the cells and minimizes electroosmosis within the sample. A voltage is applied to the main channel via liquid electrodes. cDEP has been used to selectively separate, concentrate and isolate different types of human breast cancer cells (Henslee et al. 2011b) and it was the first reported dielectrophoretic isolation of tumor initiating cells (Salmanzadeh et al. 2012). Early cDEP devices had electrode channels and cell suspension channels in the same layer, but the latest multilayer cDEP devices have electrodes in a different layer than cell suspension, which has allowed for the design of high throughput cell separation devices that have flow rate of 2.2 ml/h at cell density of 2.5 million cells per ml (Čemažar et al. 2016). These high throughput cDEP devices have unique cell-sized (20 μm) insulating pillars (Fig. 12) that reduce cell-to-cell interaction and increase specificity of trapping in comparison to typical 100 μm pillars (Lapizco-Encinas et al. 2004; Shafiee et al. 2010).

DEP has been used to separate many different types of cells. The purity of separating viable cells from non-viable ones is very high. For example, Doh and Cho (2005) achieved 96 % purity of viable yeast cells in DEP device. Separation of cells with large differences in size and other properties can also yield in high purity; Yang et al. (2011) designed the cascade DEP cell sorter with two DEP sorters to separate LNCaP cells from HCT116, achieving the purity of 96 %. Kang et al. (2008) used a DC-DEP-based insulating hurdle design to separate white blood cells from red blood cells and platelets and also MCF-7 cells from whole blood. This device separates based on cell sizes and this separation can be tuned by changing the applied voltages at the different branches of the device. Demirican et al. (2015) developed a device with metal electrodes covered with 0.5 μm thick

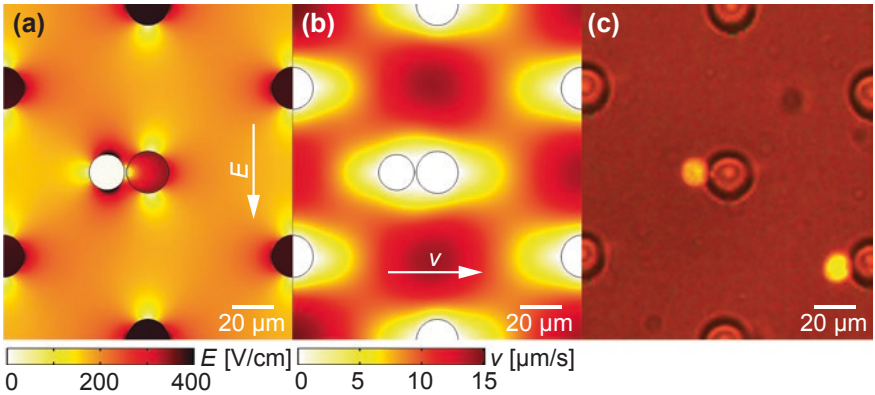

Fig. 12 A section of a high throughput contactless dielectrophoresis device; **a** electric field, **b** fluid velocity and **c** photo of trapped cell. Target cells trap in front of pillars while other cells continue towards the outlet

parylene C coating to eliminate the contact of metal with cell suspension. They used it to separate multidrug resistant K562 cells from drug sensitive ones.

In the past decade, great efforts have been directed towards developing label-free detection and isolation of rare cells, such as circulating tumor cells from blood or tumor initiating cells (TIC) from tumor samples. The initial concentration of these cells is extremely low, ranging between 1 and 10 circulating tumor cells per ml of blood (Alix-Panabières and Pantel 2014) such that about 10 ml of blood needs to be processed for meaningful analysis (Gascoyne and Shim 2014). The most relevant targets are separation of stem cells from somatic cells, cancer stem cells from normal cancer cells, progenitor cells from stromal cells, cancer cells from blood cells, separation of differentiated cells and separation of different stages of cancer cells (Salamanzadeh and Davalos 2014). Stem cells and cancer stem cells have different protein expression, membrane morphology and surface charge, nucleus to cytoplasm ratio, etc. Some of these properties are responsible for different electrical properties and that can be used to separate cells using DEP.

Mulhall et al. (2011) measured the Clausius–Mossotti factor to show that the electrical properties of normal, pre-cancerous and cancerous oral keratinocytes are distinct. Shim et al. (2013) developed a high throughput DEP-FFF device, able to continuously separate one million nucleated cells per min. Unlike in most DEP devices, in this device cells are suspended in physiological media and in the first section of the device the cell suspension is diluted to lower the electrical conductivity of the media. In the second section of the device, tumor cells are pulled down towards the electrodes, while other PNBCs are repelled away. The tumor cells are isolated by skimming the bottom part of the chamber while the other cells are directed towards a waste channel.

Achieving high purity of rare cells in high throughput separation device might be difficult in a device that uses only DEP, however, DEP can be combined with

other techniques of cell isolation. Smith et al. (2015) showed that antibody-based immunocapture can be combined with dielectrophoresis (DEP) to differentially isolate cancer cells from leukocytes in a characterization device. DEP was used to bring target cells in close contact with pillars to increase probability of trapping on an antibody-terminated surface. Moon et al. (2011) developed a device capable of separating MCF-7 human breast cancer cells from spiked whole blood at flow-rates up to 126 μl/min. Multi-orifice-flow fractionation, a hydrodynamic separation technique which takes advantage of the size difference of the cancerous cells and other blood cells, was initially used to separate the MCF-7 cells from blood and DEP was used downstream as a precise post processing separator to achieve combined separation efficiencies of 99.2 and 94.2 % for red and white blood cells, respectively, and, to concentrate the MCF-7 cells 162-fold.

5.3.1 DEP Separation in High Conductivity Media

Historically, most DEP identification and separation are carried out in isotonic, low-conductivity media to avoid Joule heating and electrochemical reactions (Gielen et al. 2010; Gallo-Villanueva et al. 2013). Joule heating is proportional to the conductivity of the buffer and square of electric field; therefore many DEP buffers have conductivity in the order of 0.01 S/m (Hyun and Jung 2013). However, the cells in these low conductivity buffers are stressed and long-term cell viability is severely affected. Sabuncu et al. (2015) has also observed a time dependent DEP response for Jurkat cells in low conductivity buffers, which results from a continuous leakage of ions and increase of the cytoplasmic conductivity, membrane capacitance and conductance. However, there are several challenges associated with using DEP for cell manipulation in physiological high conductivity buffers. In such buffers, most cells generally experience only negative DEP (the cells are always less polarizable than the media). The lack of a transition between positive and negative DEP makes it difficult to identify and separate cells in these conditions. Other difficulties associated with high conductivity buffers are electrode polarization, Joule heating and electrochemical damage. However, some of these difficulties can be reduced by using a platinum black coating to increase the electrode surface area and by using low actuation voltages and high frequencies (Schwan 1968; Pless 2002; Sridharan et al. 2011).

Despite these difficulties, different strategies have been investigated to utilize negative DEP for cell separation in highly conductive buffers. Gao et al. (2011) used a combination of DEP, electrophoresis and AC electrothermal motion to continually isolate bacteria from urine and buffy coats. Gielen et al. (2011) use a DEP-FFF-based system to slow the cells in a microchannel. The slowing factor depends on the dielectric properties of the cells and at 40 MHz, the authors were able to distinguish between live and dead Jurkat cells. Park et al. (2011) also used a DEP-FFF-based system to concentrate bacteria from high conductivity physiological fluids like cerebrospinal fluid and blood.

5.3.2 Traveling Wave DEP Separation

An example of a high throughput twDEP separation device was presented by Cheng et al. (2009) and was used to separate red blood cells from debris and it consisted of a 1.3 mm long and 1 mm wide channel with interdigitated electrodes. Cells were first focused in a single stream in the middle of the channel by negative DEP and then twDEP was used to change the trajectories of cells based on their electrical and geometrical properties. The maximum flow rate was 10 μl/min, giving a theoretical throughput of 0.6 million cells per hour. van den Driesche et al. (2012) designed a device that does not require precise focusing with DEP, however, it has two inlets, one for cell suspension and one for DEP buffer. The device with 200 μm wide channel was used to separate viable Jurkat cells from bacteria, debris and non-viable cells, yielding in 86 % recovery of viable Jurkat cells.

5.4 Modification of Cells Using Electric Fields

5.4.1 Electroporation in Microfluidic Devices

Electroporation of cells in vitro can be miniaturized on microfluidic platforms. Microfluidic electroporation systems overcome many drawbacks of bench-scale electroporators. The distance between the electrodes is typically on the order of 100 μm, ten times smaller than the macro scale. Voltages needed to generate the necessary electric field in a microfluidic device are in the range of tens of volts and can be applied using standard laboratory function generators. In comparison, large-scale electroporation requires application of hundreds of volts. Second, microfluidic channels provide more favorable chemical and fluidic conditions and have a large surface to volume ratio for rapid heat dissipation. The small electroporation volume allows for manipulation and observation of individual cells, giving information about the heterogeneity of the cell population. A small sample size is especially attractive for the study of rare cells, but some flow-through devices allow for high throughput electroporation. Transparent devices allow for in situ observation of electroporation under the microscope.

Two design elements are commonly used in microfluidic electroporation: metal electrodes of various configurations and constriction chambers. The most straightforward electrodes consist of two parallel metal plates, separated by a small distance. The electric field is largely uniform, but observation under a microscope is difficult, as only indium-tin-oxide is a transparent highly conductive material. Coplanar electrodes offer much easier observation of cells, but the electric field is not homogeneous in these devices and cells in the microfluidic channel are exposed to different amplitudes of the electric field. Pulsing unipolar electric fields can cause delamination of thin metal electrodes due to electrolysis. More robust electrodes have vertical sidewalls; they offer a more uniform electric field, but the fabrication is more difficult.

The other approach to microfluidic electroporation is to implement constrictions in the channel to locally amplify the electric field. The electric field is applied along the channel by using planar electrodes or simply metal needles at the inlet and outlet. A simple approximation can be made if the device is constructed of a long wide channel and a much shorter narrow section connected in series. The average electric field in a channel can be approximated as the voltage-to-distance ratio $E_{\mathrm{av}} = V_0/d$. Current density is defined as $\boldsymbol{j} = \boldsymbol{E}\sigma$, where σ is the conductivity of the medium. Since the same total current flows through the wide and the narrow part of the channel, the current density is higher in the narrow section. Typically the height of the channel is constant and the electric field in the constriction can be approximated as

$$E_{\mathrm{constriction}} \approx \frac{w_{\mathrm{wide}}}{w_{\mathrm{narrow}}} \frac{V_0}{d} \tag{31}$$

The actual electric field is inhomogeneous especially just before and just after the constriction and the design must be carefully adjusted to make the field as homogeneous as possible at constriction inlets and outlets. Electric field intensity and duration of the exposure(s) can be adjusted by varying the channel and constriction dimensions, flow rate and applied voltage. Cells are exposed to high electric field for the duration when they are in the narrow section(s) and multiple constrictions are the equivalent of exposing cells to multiple pulses.

Huang and Rubinsky (1999) fabricated the first microfluidic devices to electroporate single cells. They used plate electrodes in the floor and ceiling of the channel with an insulation layer between them. They made a hole in the insulation layer with a diameter of 2 μm to trap a cell and focus the electric field. By measuring the electric current they could detect the presence of a cell in the hole and deliver electric pulses accordingly. Small nanostructure and channel features with subcellular dimension can trap single cells and further enhance the precision of electroporation (Ionescu-Zanetti et al. 2007; Hung and Chang 2012; Kang et al. 2013). Microfluidic devices that can controllably electroporate cells in a high throughput manner were also developed (Fig. 13) (Fox et al. 2006; Wang and Lu 2006; Bao et al. 2010; Selmeczi et al. 2011).

Irreversible electroporation can also be used to lyse cells and analyze intracellular components. The advantage of cell lysis achieved with electric field pulses, in comparison to chemical lysis, is that no chemicals are introduced and only the outer cell membrane is damaged, while the organelle membranes remain intact as the transmembrane voltage typically does not reach the threshold value. Pulsed field lysis is also non-thermal and therefore proteins remain intact.

5.4.2 Electrofusion

The purpose of cell fusion is the formation of hybridoma cells that have genetic materials from both parent cells. Fused cells can have beneficial properties

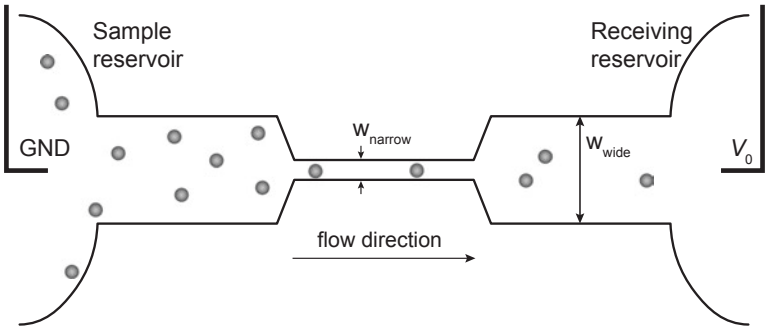

Fig. 13 Microfluidic electroporation channel with geometric variation. Adapted from Wang and Lu (2006) with permission from John Wiley and Sons

derived from both parent cells. Electrofusion can be beneficial over chemical fusion or transfection using inactivated viruses, since it does not introduce any cytotoxic chemicals or viral DNA, is highly efficient and has widespread adaptability (Zimmermann et al. 2000; Hu et al. 2013). Cell fusion is a useful tool in many medical and biological research fields such as mammal cloning and cancer immunotherapy (Chen et al. 2007). For example, fusion of a cell producing antibodies with an immortal cell can give the immortal cell line the ability to produce antibodies.

Cell fusion is a generally a two-step procedure. First, the cells must be brought into close contact, often achieved by dielectrophoretic force or microstructures. Second, electric pulses are delivered to electroporate cells that they can reach a "fusogenic" state. The fusogenic state correlates with the area of the cell membrane where the induced transmembrane voltage exceeds the threshold value (Usaj et al. 2013). Using an inhomogeneous electric field is beneficial for causing close cell contact, but on the other hand the electric field used to electroporate cells also varies with position regarding to the electrodes. Some cells may be exposed to a strong electric field that irreversibly electroporates cells while some other cells may not reach fusogenic state. Therefore, a compromise between dielectrophoretic alignment and electroporation must be achieved.

An important advantage of microfluidic electrofusion is high pairing efficiency. By mixing cells of type A and B together in equal ratios without the use of microfluidics, the chance of an A–B pairing is only 50 %. Microfluidic devices that allow for controlled pairing of cells were developed to overcome this low efficiency. For example, Kimura et al. (2011) used micro orifices to form pairs of cells using dielectrophoresis and fuse only cells that were paired at the orifice (Fig. 14), thus improving the fusion yield to 78–90 %. Skelley et al. (2009) used weir structures to first trap cells of one type and then reverse the direction of the flow to trap and pair the second type of cells to fuse them using electric pulses or chemical methods achieving pairing efficiencies up to 70 %.

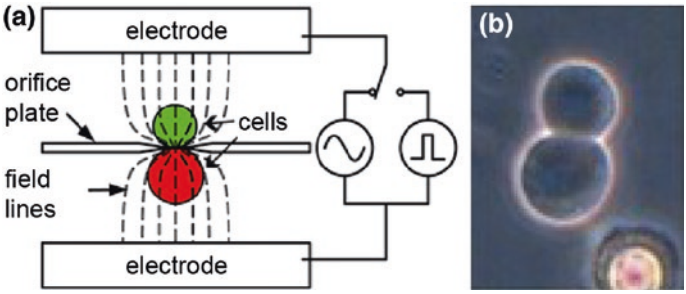

Fig. 14 Cell fusion in a micro-orifice array device; **a** cell are brought into contact using dielectrophoresis and then electroporated to initiate fusion, **b** an example of fused cell. Adapted from Kimura et al. (2011) with permission from John Wiley and Sons

6 Summary

Manipulation, sorting and separation of cells using electric fields has been shown many times to be an effective stand-alone method and useful as a part of another cellular application device. Electrokinetic techniques such as electroosmosis, electrophoresis, electrorotation, and dielectrophoresis have been widely used for manipulating cells in LOC devices. Electroosmosis can be used for fabricating micropumps that generate flows in LOC devices. Microfluidic platforms can also be used for characterizing cells; electrorotation, dielectrophoresis and microfluidic impedance cytometers can characterize cells based on their dielectric properties. Electroporation in microfluidic devices can be used to lyse cells without introduction of any chemicals and is a critical part of the cell fusion process. DEP in particular has been proven to successfully distinguish and separate cells that are genetically identical but phenotypically distinct, such as circulating tumor cells and cancer stem cells. Various cell lines have been isolated, proving the robustness of DEP separation. However, the ability to process uncharacterized patient samples still needs to be demonstrated in clinical studies. Due to its label-free nature and scalability, DEP separation is cost-efficient and convenient. DEP can be also be integrated with other methods of cell separation to achieve even higher purity of samples at high flow rates.

Acknowledgments This work was supported by NIH 5R21 CA173092-01.

References

Alix-Panabières C, Pantel K (2014) Challenges in circulating tumour cell research. Nat Rev Cancer 14:623–631. doi:10.1038/nrc3686

Asami K, Gheorghiu E, Yonezawa T (1998) Dielectric behavior of budding yeast in cell separation. Biochim Biophys Acta 1381:234–240. doi:10.1016/S0304-4165(98)00033-6

Asami K, Hanai T, Koizumi N (1980) Dielectric approach to suspensions of ellipsoidal particles covered with a shell in particular reference to biological cells. Jpn J Appl Phys 19:359–365. doi:10.1143/JJAP.19.359

Asami K, Yamaguchi T (1992) Dielectric spectroscopy of plant protoplasts. Biophys J 63:1493–1499. doi:10.1016/S0006-3495(92)81734-4

Asami K, Yonezawa T (1996) Dielectric behavior of wild-type yeast and vacuole-deficient mutant over a frequency range of 10 kHz to 10 GHz. Biophys J 71:2192–2200. doi:10.1016/S0006-3495(96)79420-1

Ayliffe HE, Brown SD, Rabbitt RD (2002) Micro-electric impedance spectra of isolated cells recorded in micro-channels. In: Engineering in medicine and biology, 2002. 24th annual conference and the annual fall meeting of the biomedical engineering society EMBS/BMES conference, 2002. Proceedings of the Second Joint. vol 2, pp 1692–1693

Ayliffe HE, Bruno Frazier A, Rabbitt RD (1999) Electric impedance spectroscopy using microchannels with integrated metal electrodes. J Microelectromech Syst 8:50–57. doi:10.1109/84.749402

Bao N, Le TT, Cheng J-X, Lu C (2010) Microfluidic electroporation of tumor and blood cells: observation of nucleus expansion and implications on selective analysis and purging of circulating tumor cells. Integr Biol 2:113–120. doi:10.1039/b919820b

Baret J-C, Miller OJ, Taly V et al (2009) Fluorescence-activated droplet sorting (FADS): efficient microfluidic cell sorting based on enzymatic activity. Lab Chip 9:1850–1858. doi:10.1039/b902504a

Bhatt KH, Grego S, Velev OD (2005) An AC electrokinetic technique for collection and concentration of particles and cells on patterned electrodes. Langmuir 21:6603–6612. doi:10.1021/la050658w

Čemažar J, Douglas TA, Schmelz EM, Davalos RV (2016) Enhanced contactless dielectrophoresis enrichment and isolation platform via cell-scale microstructures. Biomicrofluidics 10:014109. doi:10.1063/1.4939947

Čemažar J, Miklavčič D, Kotnik T (2013) Microfluidic devices for manipulation, modification and characterization of biological cells in electric fields—a review. J Microelectron Electron Compon Mater 43:143–161

Chang J-Y, Wang S, Allen JS et al (2014) A novel miniature dynamic microfluidic cell culture platform using electro-osmosis diode pumping. Biomicrofluidics 8:044116. doi:10.1063/1.4892894

Chen C, Smye SW, Robinson MP, Evans JA (2006) Membrane electroporation theories: a review. Med Biol Eng Comput 44:5–14. doi:10.1007/s11517-005-0020-2

Chen EH, Grote E, Mohler W, Vignery A (2007) Cell–cell fusion. FEBS Lett 581:2181–2193. doi:10.1016/j.febslet.2007.03.033

Cheng I-F, Froude VE, Zhu Y et al (2009) A continuous high-throughput bioparticle sorter based on 3D traveling-wave dielectrophoresis. Lab Chip 9:3193–3201. doi:10.1039/B910587E

Cheung K, Gawad S, Renaud P (2005) Impedance spectroscopy flow cytometry: on-chip label-free cell differentiation. Cytom Part J Int Soc Anal Cytol 65:124–132. doi:10.1002/cyto.a.20141

Coulter WH (1953) Means for counting particles suspended in a fluid. US2656508 A

Cummings EB, Singh AK (2003) Dielectrophoresis in microchips containing arrays of insulating posts: theoretical and experimental results. Anal Chem 75:4724–4731. doi:10.1021/ac0340612

Davalos R, Huang Y, Rubinsky B (2000) Electroporation: bio-electrochemical mass transfer at the nano scale. Microscale Thermophys Eng 4:147–159. doi:10.1080/10893950050148115

Demircan Y, Koyuncuoglu A, Erdem M et al (2015) Label-free detection of multidrug resistance in K562 cells through isolated 3D-electrode dielectrophoresis. Electrophoresis 36:1149–1157. doi:10.1002/elps.201400391

Doh I, Cho YH (2005) A continuous cell separation chip using hydrodynamic dielectrophoresis (DEP) process. Sens Actuators Phys 121:59–65

Fabbri E, Borgatti M, Manaresi N et al (2008) Levitation and movement of tripalmitin-based cationic lipospheres on a dielectrophoresis-based lab-on-a-chip device. J Appl Polym Sci 109:3484–3491. doi:10.1002/app.28413

Fatoyinbo HO, Hoeftges KF, Hughes MP (2008) Rapid-on-chip determination of dielectric properties of biological cells using imaging techniques in a dielectrophoresis dot microsystem. Electrophoresis 29:3–10. doi:10.1002/elps.200700586

Fox MB, Esveld DC, Valero A et al (2006) Electroporation of cells in microfluidic devices: a review. Anal Bioanal Chem 385:474–485

Fuller CK, Hamilton J, Ackler H et al (2000) Microfabricated multi-frequency particle impedance characterization system. In: Proceedings of the μTAS 2000 symposium. Springer, The Netherlands

Fu L-M, Yang R-J, Lin C-H et al (2004) Electrokinetically driven micro flow cytometers with integrated fiber optics for on-line cell/particle detection. Anal Chim Acta 507:163–169. doi:10.1016/j.aca.2003.10.028

Fu X, Mavrogiannis N, Doria S, Gagnon Z (2015) Microfluidic pumping, routing and metering by contactless metal-based electro-osmosis. Lab Chip 15:3600–3608. doi:10.1039/C5LC00504C

Gagnon Z, Gordon J, Sengupta S, Chang H-C (2008) Bovine red blood cell starvation age discrimination through a glutaraldehyde-amplified dielectrophoretic approach with buffer selection and membrane cross-linking. Electrophoresis 29:2272–2279. doi:10.1002/elps.200700604

Gagnon ZR (2011) Cellular dielectrophoresis: applications to the characterization, manipulation, separation and patterning of cells. Electrophoresis 32:2466–2487. doi:10.1002/elps.201100060

Gallo-Villanueva RC, Sano MB, Lapizco-Encinas BH, Davalos RV (2013) Joule heating effects on particle immobilization in insulator-based dielectrophoretic devices. Electrophoresis. doi:10.1002/elps.201300171

Gao J, Sin MLY, Liu T et al (2011) Hybrid electrokinetic manipulation in high-conductivity media. Lab Chip 11:1770–1775. doi:10.1039/c1lc20054b

Gascoyne PRC, Noshari J, Anderson TJ, Becker FF (2009) Isolation of rare cells from cell mixtures by dielectrophoresis. Electrophoresis 30:1388–1398. doi:10.1002/elps.200800373

Gascoyne PRC, Shim S, Noshari J et al (2013) Correlations between the dielectric properties and exterior morphology of cells revealed by dielectrophoretic field-flow fractionation. Electrophoresis 34:1042–1050. doi:10.1002/elps.201200496

Gascoyne PRC, Vykoual JV (2004) Dielectrophoresis-based sample handling in general-purpose programmable diagnostic instruments. Proc IEEE 92:22–42. doi:10.1109/JPROC.2003.820535

Gascoyne P, Shim S (2014) Isolation of circulating tumor cells by dielectrophoresis. Cancers 6:545–579. doi:10.3390/cancers6010545

Gawad S, Cheung K et al (2004) Dielectric spectroscopy in a micromachined flow cytometer: theoretical and practical considerations. Lab Chip 4:241–251. doi:10.1039/b313761a

Gawad S, Schild L, Renaud P (2001) Micromachined impedance spectroscopy flow cytometer for cell analysis and particle sizing. Lab Chip 1:76–82. doi:10.1039/B103933B

Gielen F, deMello AJ, Edel JB (2011) Dielectric cell response in highly conductive buffers. Anal Chem 84:1849–1853. doi:10.1021/ac2022103

Gielen F, Pereira F, deMello AJ, Edel JB (2010) High-resolution local imaging of temperature in dielectrophoretic platforms. Anal Chem 82:7509–7514. doi:10.1021/ac101557g

Henslee BE, Morss A, Hu X et al (2011a) Electroporation dependence on cell size: optical tweezers study. Anal Chem 83:3998–4003. doi:10.1021/ac1019649

Henslee EA, Sano MB, Rojas AD et al (2011b) Selective concentration of human cancer cells using contactless dielectrophoresis. Electrophoresis 32:2523–2529. doi:10.1002/elps.201100081

Hoettges KF, McDonnell MB, Hughes MP (2003) Use of combined dielectrophoretic/electrohydrodynamic forces for biosensor enhancement. J Phys Appl Phys 36:L101–L104. doi:10.1088/0022-3727/36/20/L01

Holmes D, Morgan H (2010) Single cell impedance cytometry for identification and counting of CD4 T-cells in human blood using impedance labels. Anal Chem 82:1455–1461. doi:10.1021/ac902568p

Holmes D, Morgan H, Green NG (2006) High throughput particle analysis: combining dielectrophoretic particle focussing with confocal optical detection. Biosens Bioelectron 21:1621–1630. doi:10.1016/j.bios.2005.10.017

Holmes D, Pettigrew D, Reccius CH et al (2009) Leukocyte analysis and differentiation using high speed microfluidic single cell impedance cytometry. Lab Chip 9:2881. doi:10.1039/b910053a

Huang C-T, Weng C-H, Jen C-P (2011) Three-dimensional cellular focusing utilizing a combination of insulator-based and metallic dielectrophoresis. Biomicrofluidics 5:44101–4410111. doi:10.1063/1.3646757

Huang Y, Rubinsky B (1999) Micro-electroporation: improving the efficiency and understanding of electrical permeabilization of cells. Biomed Microdevices 2:145–150. doi:10.1023/A:1009901821588

Huang Y, Wang XB, Becker FF, Gascoyne PR (1997) Introducing dielectrophoresis as a new force field for field-flow fractionation. Biophys J 73:1118–1129. doi:10.1016/S0006-3495(97)78144-X

Hughes MP (2002) Strategies for dielectrophoretic separation in laboratory-on-a-chip systems. Electrophoresis 23:2569–2582. doi:10.1002/1522-2683(200208)23:16<2569:AID-ELPS2569>3.0.CO;2-M

Hung M-S, Chang Y-T (2012) Single cell lysis and DNA extending using electroporation microfluidic device. BioChip J 6:84–90. doi:10.1007/s13206-012-6111-x

Hu N, Yang J, Joo SW et al (2013) Cell electrofusion in microfluidic devices: a review. Sens Actuators B Chem 178:63–85. doi:10.1016/j.snb.2012.12.034

Hyun K-A, Jung H-I (2013) Microfluidic devices for the isolation of circulating rare cells: a focus on affinity-based, dielectrophoresis, and hydrophoresis. Electrophoresis 34:1028–1041. doi:10.1002/elps.201200417

Ionescu-Zanetti C, Blatz A, Khine M (2007) Electrophoresis-assisted single-cell electroporation for efficient intracellular delivery. Biomed Microdevices 10:113–116. doi:10.1007/s10544-007-9115-x

Jen C-P, Chen W-F (2011) An insulator-based dielectrophoretic microdevice for the simultaneous filtration and focusing of biological cells. Biomicrofluidics 5:044105. doi:10.1063/1.3658644

Jones TB (1995) Electromechanics of particles, Digitally printed 1st pbk. version. Cambridge University Press, Cambridge; New York

Jones TB (2003) Basic theory of dielectrophoresis and electrorotation. IEEE Eng Med Biol Mag 22:33–42

Jones TB, Washizu M (1996) Multipolar dielectrophoretic and electrorotation theory. J Electrost 37:121–134. doi:10.1016/0304-3886(96)00006-X

Jubery TZ, Srivastava SK, Dutta P (2014) Dielectrophoretic separation of bioparticles in microdevices: a review: microfluidics and Miniaturization. Electrophoresis 35:691–713. doi:10.1002/elps.201300424

Kang W, Yavari F, Minary-Jolandan M et al (2013) Nanofountain probe electroporation (NFP-E) of single cells. Nano Lett 13:2448–2457. doi:10.1021/nl400423c

Kang Y, Li D, Kalams SA, Eid JE (2008) DC-dielectrophoretic separation of biological cells by size. Biomed Microdevices 10:243–249. doi:10.1007/s10544-007-9130-y

Khoshmanesh K, Akagi J, Nahavandi S et al (2011) Interfacing cell-based assays in environmental scanning electron microscopy using dielectrophoresis. Anal Chem 83:3217–3221. doi:10.1021/ac2002142

Kimura Y, Gel M, Techaumnat B et al (2011) Dielectrophoresis-assisted massively parallel cell pairing and fusion based on field constriction created by a micro-orifice array sheet. Electrophoresis 32:2496–2501. doi:10.1002/elps.201100129

Klösgen B, Reichle C, Kohlsmann S, Kramer KD (1996) Dielectric spectroscopy as a sensor of membrane headgroup mobility and hydration. Biophys J 71:3251–3260
Kotnik T, Kramar P, Pucihar G et al (2012) Cell membrane electroporation—part 1: the phenomenon. IEEE Electr Insul Mag 28:14–23. doi:10.1109/MEI.2012.6268438
Kotnik T, Miklavčič D (2000) Theoretical evaluation of the distributed power dissipation in biological cells exposed to electric field. Bioelectromagnetics 21:385–394
Lapizco-Encinas BH, Simmons BA, Cummings EB, Fintschenko Y (2004) Dielectrophoretic concentration and separation of live and dead bacteria in an array of insulators. Anal Chem 76:1571–1579
Lee D, Yu C, Papazoglou E et al (2011) Dielectrophoretic particle–particle interaction under AC electrohydrodynamic flow conditions. Electrophoresis 32:2298–2306. doi:10.1002/elps.201100070
Lee RC (2006) Cell injury by electric forces. Ann N Y Acad Sci 1066:85–91. doi:10.1196/annals.1363.007
Markx GH, Rousselet J, Pethig R (1997) DEP-FFF: field-flow fractionation using non-uniform electric fields. J Liq Chromatogr Relat Technol 20:2857–2872. doi:10.1080/10826079708005597
Marszalek P, Liu DS, Tsong TY (1990) Schwan equation and transmembrane potential induced by alternating electric field. Biophys J 58:1053–1058. doi:10.1016/S0006-3495(90)82447-4
Melvin EM, Moore BR, Gilchrist KH et al (2011) On-chip collection of particles and cells by AC electroosmotic pumping and dielectrophoresis using asymmetric microelectrodes. Biomicrofluidics 5:034113. doi:10.1063/1.3620419
Mernier G, Majocchi S, Mermod N, Renaud P (2012) In situ evaluation of single-cell lysis by cytosol extraction observation through fluorescence decay and dielectrophoretic trapping time. Sens Actuators B Chem 166–167:907–912. doi:10.1016/j.snb.2012.03.057
Minerick AR, Zhou RH, Takhistov P, Chang HC (2003) Manipulation and characterization of red blood cells with alternating current fields in microdevices. Electrophoresis 24:3703–3717. doi:10.1002/elps.200305644
Moon H-S, Kwon K, Kim S-I et al (2011) Continuous separation of breast cancer cells from blood samples using multi-orifice flow fractionation (MOFF) and dielectrophoresis (DEP). Lab Chip 11:1118. doi:10.1039/c0lc00345j
Morgan H, Green NG (2003) AC electrokinetics: colloids and nanoparticles. Research Studies, Baldock, Hertfordshire
Morgan H, Holmes D, Green NG (2006) High speed simultaneous single particle impedance and fluorescence analysis on a chip. Curr Appl Phys 6:367–370. doi:10.1016/j.cap.2005.11.020
Morgan H, Izquierdo AG, Bakewell D et al (2001) The dielectrophoretic and travelling wave forces generated by interdigitated electrode arrays: analytical solution using Fourier series. J Phys Appl Phys 34:1553. doi:10.1088/0022-3727/34/10/316
Morgan H, Sun T, Holmes D et al (2007) Single cell dielectric spectroscopy. J Phys Appl Phys 40:61–70. doi:10.1088/0022-3727/40/1/S10
Mulhall HJ, Labeed FH, Kazmi B et al (2011) Cancer, pre-cancer and normal oral cells distinguished by dielectrophoresis. Anal Bioanal Chem 401:2455–2463. doi:10.1007/s00216-011-5337-0
Müller T, Gradl G, Howitz S et al (1999) A 3-D microelectrode system for handling and caging single cells and particles. Biosens Bioelectron 14:247–256. doi:10.1016/S0956-5663(99)00006-8
Neumann E, Schaeferridder M, Wang Y, Hofschneider P (1982) Gene-transfer into mouse lyoma cells by electroporation in high electric-fields. EMBO J 1:841–845
Park S, Zhang Y, Wang T-H, Yang S (2011) Continuous dielectrophoretic bacterial separation and concentration from physiological media of high conductivity. Lab Chip 11:2893. doi:10.1039/c1lc20307j
Pethig R (2010) Dielectrophoresis: status of the theory, technology, and applications. Biomicrofluidics 4:022811. doi:10.1063/1.3456626
Pless BD (2002) Ambulatory blood pump. US6342071 B1
Pohl HA, Crane JS (1971) Dielectrophoresis of cells. Biophys J 11:711–727

Pucihar G, Kotnik T, Miklavčič D, Teissié J (2008) Kinetics of transmembrane transport of small molecules into electropermeabilized cells. Biophys J 95:2837–2848. doi:10.1529/biophysj.108.135541

Regtmeier J, Eichhorn R, Viefhues M et al (2011) Electrodeless dielectrophoresis for bioanalysis: theory, devices and applications. Electrophoresis 32:2253–2273. doi:10.1002/elps.201100055

Rosales C, Lim KM (2005) Numerical comparison between Maxwell stress method and equivalent multipole approach for calculation of the dielectrophoretic force in single-cell traps. Electrophoresis 26:2057–2065. doi:10.1002/elps.200410298

Sabuncu AC, Asmar AJ, Stacey MW, Beskok A (2015) Differential dielectric responses of chondrocyte and Jurkat cells in electromanipulation buffers. Electrophoresis 36:1499–1506. doi:10.1002/elps.201500119

Salamanzadeh A, Davalos RV (2014) Electrokinetics and rare-cell detection. In: Microfluidics in detection science, Lab-on-a-chip Technologies

Salmanzadeh A, Romero L, Shafiee H et al (2012) Isolation of prostate tumor initiating cells (TICs) through their dielectrophoretic signature. Lab Chip 12:182–189. doi:10.1039/c1lc20701f

Salmanzadeh A, Sano MB, Gallo-Villanueva RC et al (2013) Investigating dielectric properties of different stages of syngeneic murine ovarian cancer cells. Biomicrofluidics 7:11809. doi:10.1063/1.4788921

Schwan HP (1983) Biophysics of the interaction of electromagnetic energy with cells and membranes. In: Grandolfo M, Michaelson SM, Rindi A (eds) Biological effects and dosimetry of nonionizing radiation. Springer, New York, pp 213–231

Schwan HP (1968) Electrode polarization impedance and measurements in biological materials. Ann N Y Acad Sci 148:191–209. doi:10.1111/j.1749-6632.1968.tb20349.x

Selmeczi D, Hansen TS, Met Ö et al (2011) Efficient large volume electroporation of dendritic cells through micrometer scale manipulation of flow in a disposable polymer chip. Biomed Microdevices 13:383–392. doi:10.1007/s10544-010-9507-1

Shafiee H, Caldwell J, Sano M, Davalos R (2009) Contactless dielectrophoresis: a new technique for cell manipulation. Biomed Microdevices 11:997–1006. doi:10.1007/s10544-009-9317-5

Shafiee H, Sano MB, Henslee EA et al (2010) Selective isolation of live/dead cells using contactless dielectrophoresis (cDEP). Lab Chip 10:438. doi:10.1039/b920590j

Shim S, Stemke-Hale K, Tsimberidou AM et al (2013) Antibody-independent isolation of circulating tumor cells by continuous-flow dielectrophoresis. Biomicrofluidics 7:011807–011812. doi:10.1063/1.4774304

Shi Y, Yu Z, Shao X (2010) Combination of direct-forcing fictitious domain method and sharp interface method for dielectrophoresis of particles. Particuology 8:351–359. doi:10.1016/j.partic.2010.01.008

Simmons BA, McGraw GJ, Davalos RV et al (2006) The development of polymeric devices as dielectrophoretic separators and concentrators. MRS Bull 31:120–124. doi:10.1557/mrs2006.26

Skelley AM, Kirak O, Suh H et al (2009) Microfluidic control of cell pairing and fusion. Nat Methods 6:147–152. doi:10.1038/nmeth.1290

Smith JP, Huang C, Kirby BJ (2015) Enhancing sensitivity and specificity in rare cell capture microdevices with dielectrophoresis. Biomicrofluidics 9:014116. doi:10.1063/1.4908049

Squires TM, Bazant MZ (2004) Induced-charge electro-osmosis. J Fluid Mech 509:217–252. doi:10.1017/S0022112004009309

Sridharan S, Zhu J, Hu G, Xuan X (2011) Joule heating effects on electroosmotic flow in insulator-based dielectrophoresis. Electrophoresis. doi:10.1002/elps.201100011

Srivastava SK, Gencoglu A, Minerick AR (2010) DC insulator dielectrophoretic applications in microdevice technology: a review. Anal Bioanal Chem 399:301–321. doi:10.1007/s00216-010-4222-6

Sun T, van Berkel C, Green NG, Morgan H (2009) Digital signal processing methods for impedance microfluidic cytometry. Microfluid Nanofluidics 6:179–187. doi:10.1007/s10404-008-0315-3

Usaj M, Flisar K, Miklavcic D, Kanduser M (2013) Electrofusion of B16-F1 and CHO cells: the comparison of the pulse first and contact first protocols. Bioelectrochemistry 89:34–41. doi:10.1016/j.bioelechem.2012.09.001

Valero A, Braschler T, Renaud P (2010) A unified approach to dielectric single cell analysis: Impedance and dielectrophoretic force spectroscopy. Lab Chip 10:2216–2225. doi:10.1039/C003982A

van den Driesche S, Rao V, Puchberger-Enengl D et al (2012) Continuous cell from cell separation by traveling wave dielectrophoresis. Sens Actuators B Chem 170:207–214. doi:10.1016/j.snb.2011.01.012

Voldman J, Braff RA, Toner M, et al (2000) Quantitative design and analysis of singleparticle dielectrophoretic traps. In: Micro total analysis systems. Springer, pp 431–434

Vykoukal J, Vykoukal DM, Freyberg S et al (2008) Enrichment of putative stem cells from adipose tissue using dielectrophoretic field-flow fractionation. Lab Chip 8:1386–1393. doi:10.1039/b717043b

Wang HY, Lu C (2006) High-throughput and real-time study of single cell electroporation using microfluidics: effects of medium osmolarity. Biotechnol Bioeng 95:1116–1125. doi:10.1002/bit.21066

Wang X, Wang X-B, Gascoyne PRC (1997) General expressions for dielectrophoretic force and electrorotational torque derived using the Maxwell stress tensor method. J Electrost 39:277–295. doi:10.1016/S0304-3886(97)00126-5

Wong PK, Chen C-Y, Wang T-H, Ho C-M (2004) Electrokinetic bioprocessor for concentrating cells and molecules. Anal Chem 76:6908–6914. doi:10.1021/ac049479u

Wu J, Ben Y, Chang H-C (2005) Particle detection by electrical impedance spectroscopy with asymmetric-polarization AC electroosmotic trapping. Microfluid Nanofluidics 1:161–167. doi:10.1007/s10404-004-0024-5

Xuan X, Raghibizadeh S, Li D (2006) Wall effects on electrophoretic motion of spherical polystyrene particles in a rectangular poly(dimethylsiloxane) microchannel. J Colloid Interface Sci 296:743–748. doi:10.1016/j.jcis.2005.09.039

Yang F, Yang X, Jiang H, Wang G (2011) Cascade and staggered dielectrophoretic cell sorters. Electrophoresis 32:2377–2384. doi:10.1002/elps.201100039

Yao B, Luo G, Feng X et al (2004) A microfluidic device based on gravity and electric force driving for flow cytometry and fluorescence activated cell sorting. Lab Chip 4:603–607. doi:10.1039/b408422e

Zhu J, Xuan X (2009) Dielectrophoretic focusing of particles in a microchannel constriction using DC-biased AC flectric fields. Electrophoresis 30:2668–2675. doi:10.1002/elps.200900017

Zimmermann U, Friedrich U, Mussauer H et al (2000) Electromanipulation of mammalian cells: fundamentals and application. IEEE-Inst Electrical Electronics Engineers Inc, pp 72–82

Optical Manipulation of Cells

Julian Cheng, M. Arifur Rahman and Aaron T. Ohta

Abstract Single-cell analysis can reveal cell behaviors that are unobservable by traditional bulk measurements. The analysis of single cells is made possible by technology that enables the addressing and manipulation of microscale objects. Optical manipulators are capable of micro- and nano-manipulation and are attractive for single-cell procedures, due to their inherent flexibility and adaptability. This chapter reviews major types of optical manipulation techniques. Optical gradient and scattering forces, used in optical tweezers, holographic optical tweezers, and other optical traps, are introduced first. Next, optically controlled electrokinetic forces are discussed, with a focus on optically induced dielectrophoresis. Optically induced thermal effects are also introduced, including thermophoresis and thermocapillary force. Specific examples of applications of these techniques for procedures related to single-cell analysis are also covered, including cell culturing, cell sorting, cell surgery, and measurements of single cells.

Keywords Single-cell analysis · Cell manipulation · Optical manipulation · Optical tweezers · Holographic optical tweezers · Optically induced dielectrophoresis · Opto-thermocapillary flow · Cell culturing · Cell sorting · Cell trapping · Molecular delivery · Cell lysis

1 Introduction

Cellular behavior has traditionally been studied by observing the response of a population of cells. While this has led to breakthroughs in understanding biological processes, there is the risk of losing information on the behavior of rare cells

J. Cheng · M.A. Rahman · A.T. Ohta (✉)
Department of Electrical Engineering, University of Hawaii, Honolulu, HI, USA
e-mail: aohta@hawaii.edu

W. Lee et al. (eds.), *Microtechnology for Cell Manipulation and Sorting*,
Microsystems and Nanosystems, DOI 10.1007/978-3-319-44139-9_4

or cells with responses that deviate substantially from the mean (Di Carlo and Lee 2006). Thus, as the capability to handle individual cells arose, measurements at the cellular level have yielded new insights (Lindström and Andersson-Svahn 2010; Wang and Bodovitz 2010). In order to study single cells, desirable capabilities include

- Cell culturing
- Cell separation and sorting
- Cell trapping, isolation, and transport
- Operations on cells, such as cell lysis and molecular delivery
- Measurements of cellular properties, such as mechanical stiffness and mass

All of these capabilities can be performed or assisted by optical systems. This includes systems that use optical forces, such as optical gradient and scattering forces, as well as systems that use optical control of other types of forces, such as optically induced electrokinetic forces, and optically induced thermal forces. These types of optical systems will be described in this chapter, with an emphasis on their applications for the manipulation of single cells.

An important advantage of optical systems is their adaptability. An optical system is capable of being reconfigured on the fly, in contrast to mechanical micromanipulation systems. The optical patterns used to realize cell manipulation can be dynamically adjusted to switch between various functions, such as trapping and sorting, or to optimize the system for a specific need or application. Furthermore, optical patterns can be programmed or made part of feedback control systems, making it possible to automate complex operations. Optical manipulation is also noncontact, which can be gentler on fragile objects such as mammalian cells.

For cell manipulation applications, optical systems also have the advantage that it is straightforward to integrate optical manipulation with microfluidic structures by using transparent materials or optical waveguides. Furthermore, the use of optical manipulation within a microfluidic device adds functionality, which means that the mechanical microfluidic structures can be relatively simple. This results in reduced fabrication costs for the microfluidic devices, which are often disposable to reduce sample cross-contamination.

When using optical manipulation systems for cell manipulation, there are some limitations that arise. Some types of optical manipulation require highly intense light, which can affect the cells under manipulation. However, this is not true for all of the optical manipulation methods described in this chapter, especially those that do not rely on optical gradient forces.

The working area of optical manipulators is determined by the optical setup. Some types of optical manipulators have working areas of less than a square millimeter, while others can operate over hundreds of square millimeters. It may also be possible to mitigate some of the effects of a small working area by translating a microfluidic device in relation to the working area of the optical manipulator.

Optical systems typically require skilled technicians to set them up, and are relatively expensive. Commercial optical systems address this with preassembled optical components, but have increased cost and space requirements, and still

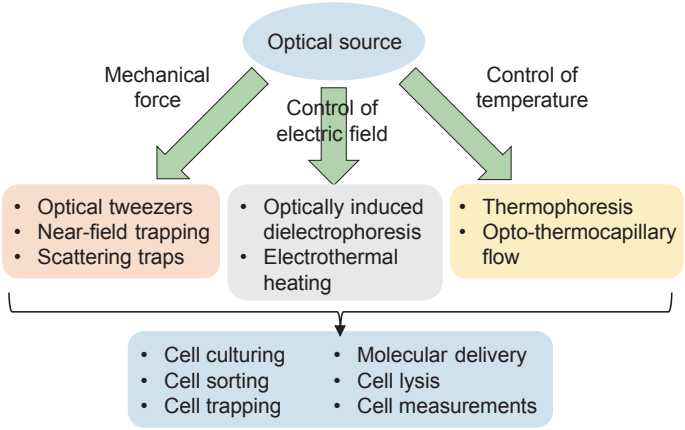

Fig. 1 Various methods of optical manipulation discussed in this chapter, and their applicability to single-cell analysis functions. Direct optical forces, where optical energy is converted to a mechanical force, are discussed, along with optically controlled manipulation mechanisms, including optical control of electric fields and temperatures

usually require a technician for the initial setup. Some optical manipulation systems use lower cost, compact components to address these limitations.

This chapter will describe various types of optical systems that are suitable for the manipulation of cells, include those that use direct optical forces, such as optical tweezers, and those that use optical control of other forces, such as optically controlled electrokinetics and optothermal manipulation (Fig. 1). The optical manipulation of cells using the various optical systems will then be discussed in more detail, organized by the capabilities mentioned at the beginning of this introduction.

2 Direct Optical Forces

Direct optical forces convert photon energy to mechanical force, resulting in optical gradient forces and scattering forces. These forces have been harnessed to create optical tweezers, near-field optical traps, and other types of traps.

2.1 Optical Tweezers

Optical tweezers are optical traps that can generate forces on the order of 0.1–100 piconewtons on micro- to nanoscale particles (Ashkin et al. 1986). Optical tweezers use the optical gradient force produced by a single tightly focused laser beam,

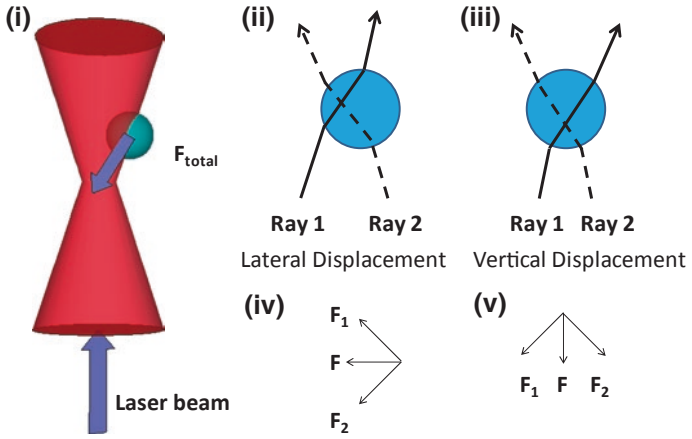

Fig. 2 Diagrams of a particle being trapped by optical tweezers. **i** The particle undergoes lateral and vertical displacement due to the gradient force and is attracted toward the focal point of the laser. **ii** A particle offset laterally from the laser focal point will move left toward the focal point of the beam. **iii** A particle offset vertically from the laser focal point will move down toward to the focal point of the beam. **iv** The free-body force diagram corresponding to the particle in **ii**. **v** The free-body force diagram corresponding to the particle in **iii**

which results from the refraction of light as it passes through a particle. Particles with an index of refraction greater than that of the surrounding media are attracted to the focal point, the region with the highest light intensity. If the laser is not focused, the gradient force only becomes significant in the transverse plane, confining the particle laterally, but propelling the particle along the laser beam by radiation pressure (Ashkin 1970). A tightly focused laser beam generates enough gradient force along the beam direction to counteract the radiation pressure, stably trapping a particle in space (Fig. 2). The difference in index of refraction between the particle and the surrounding medium, along with the optical power of the trap, contribute to how strongly the particle is trapped. The force exerted by an optical tweezers trap can be described by Hooke's Law according to $F = -kx$, where F is the force on an object, and x is the displacement of the object from the middle of the trap. The spring constant, k, depends on the properties of the laser, and describes how "stiff" the trap is.

2.1.1 Optical Tweezers for the Manipulation of Biological Materials

Optical tweezers have been used for the manipulation of many biological materials, including DNA strands (Waleed et al. 2013), proteins in DNA (van Loenhout et al. 2013), nucleic acid motor enzymes (Yin et al. 1995), and tobacco mosaic viruses (Ashkin and Dziedzic 1987). Optical tweezers have also been used to manipulate cells, including *E. coli* bacteria (Ashkin and Dziedzic 1987),

plant cells (Ashkin et al. 1987), algal cells (Tanaka et al. 2008), yeast cells (Landenberger et al. 2012), live sperm cells (Chen et al. 2011), red blood cells (Constable et al. 1993), and embryonic stem cells (Wang et al. 2011). When manipulating biological materials, optical tweezers are usually combined with microfluidic systems, which can be used to provide the appropriate media. The optical tweezers functionality can then be used to supplement or complement the microfluidic system. For example, optical tweezers can be used to move cells into different sets of media (Enger et al. 2004).

When using optical tweezers, the laser energy absorbed by the biological material under manipulation should be considered. The high optical intensities in an optical trap (megawatts per cm^2) can cause photodamage (Dholakia and Reece 2006). The damage threshold varies for different types of cells, and is also dependent on the amount of absorption, which in turn is a function of laser wavelength. *E. coli* exhibited maximum photodamage at wavelengths of 870 and 930 nm, while minimum photodamage was seen at 830 and 970 nm (Neuman et al. 1999). Chinese ovary cells are also affected by laser energy, as quantified by measurements of their cloning efficiency: cloning efficiencies were greater than 75 % for wavelengths between 950 and 990 nm when the cell receives an optical energy dosage of approximately 9×10^9 J/cm^2 (Liang et al. 1996). Therefore, careful consideration must be made regarding the laser chosen for an optical tweezers system, especially when manipulating biological materials.

One way to reduce the possibility of photodamage is through the indirect manipulation of cells using optical tweezers. Microparticles are attached to the cells under manipulation, and optical tweezers are used to trap and position the microparticles, thus moving the attached cells (Arai et al. 2003). This avoids direct illumination of the cells, reducing photodamage. The use of these microparticles, or microtools, slightly reduces the flexibility of optical tweezers, since microtools need to be added to the working area, and cells need to be attached to the microtools. This has been addressed through the in situ creation of microtools using photopolymerizing polymers (Maruyama et al. 2005) or temperature-sensitive polymers (Ichikawa et al. 2005). The use of microtools also can add functionality to optical tweezers systems, including using the microtools as a pH sensor (Maruyama et al. 2007).

2.1.2 Multiple Optical Tweezers Traps

While single-beam force gradients have various applications in both sorting and manipulating both particles and cells, it is also important to consider the use of multiple optical traps in one setup. Having multiple optical traps would further expand the usefulness of optical tweezers as a large number of particles could be trapped and manipulated at once, enabling increased throughput and both parallel and cooperative manipulation.

Multiple-beam force gradients can be generated by splitting a single laser beam. This can be done by time-sharing, where a single beam is directed to

multiple locations within a small period of time. This allows for multiple optical traps to be controlled, as long as the trap can prevent cell under observation from escaping. Time-sharing can be achieved by acousto-optical deflectors (AODs), although the diffraction efficiency is only about 80 % (Visscher et al. 1996), reducing the power available for trapping. An alternative is electro-optic deflectors (EOD), which compared to AODs, have less optical loss (Valentine et al. 2008). However, this method is limited to smaller deflection angles, thus confining particles to a smaller workspace. Another option is the use of scanning mirrors, which can operate at up to 1 kHz (Arai et al. 2004; Tanaka et al. 2008). However, like all time-sharing methods, the number of optical traps that can be created is limited by the minimum amount of time that each trap needs to be active.

2.2 Holographic Optical Tweezers

Holographic optical tweezers (HOT) takes a different approach to the creation of multiple optical traps (Fig. 3). In an HOT system, a diffraction pattern splits a single laser beam into several different beams, allowing for the control of multiple optical traps (Dufresne et al. 2001). Like single-beam optical tweezers, HOT are capable of three-dimensional manipulation (Grier and Roichman 2006; Lee and Grier 2007).

The spatial locations of the HOT traps can be reconfigured in real time by using a spatial light modulator (SLM), which uses computer-generated holograms to dynamically split an incident laser beam. The holograms displayed on the SLM can be easily changed using a computer, adjusting the optical trap positions (Curtis et al. 2002). HOT systems have been used for the manipulation of a variety of particles and cells, and have made it possible to create patterns of groups of cells. For example, HOT systems have manipulated 5-μm-diameter mouse embryonic stem cells into structures such as lines and curves (Leach et al. 2009).

An issue with multiple HOT traps is additional traps can be accidentally generated in undesired locations, creating "ghost traps" (Bianchi and Di Leonardo 2010), especially if a complex or symmetric pattern is used. Optical aberrations can also affect the effectiveness of an optical trap, causing the trap to be less focused. In addition, creating a homogeneous distribution of optical power among all the optical traps in an HOT system is not straightforward. In most cases, iterative algorithms (Di Leonardo et al. 2007) can be used to solve these issues. These algorithms add to the computing time, but most consumer graphic cards and GPU-based systems can generate the appropriate holograms to correct for intrinsic and induced optical aberrations before the Brownian motion of the particle occurs (Bianci and Di Leonardo 2010; Bowman and Padgett 2013; Bowman et al. 2014; Martín-Badosa et al. 2007). Algorithms such as an iterative Fourier transform can eliminate the majority of ghost spots and reduce the intensity of remaining ghost spots to less than 5 % of the mean intensity, making it difficult for particles to be trapped in the wrong locations (Hesseling et al. 2011). Another iterative algorithm uses a Shack–Hartmann array to help correct aberrations before the hologram is projected

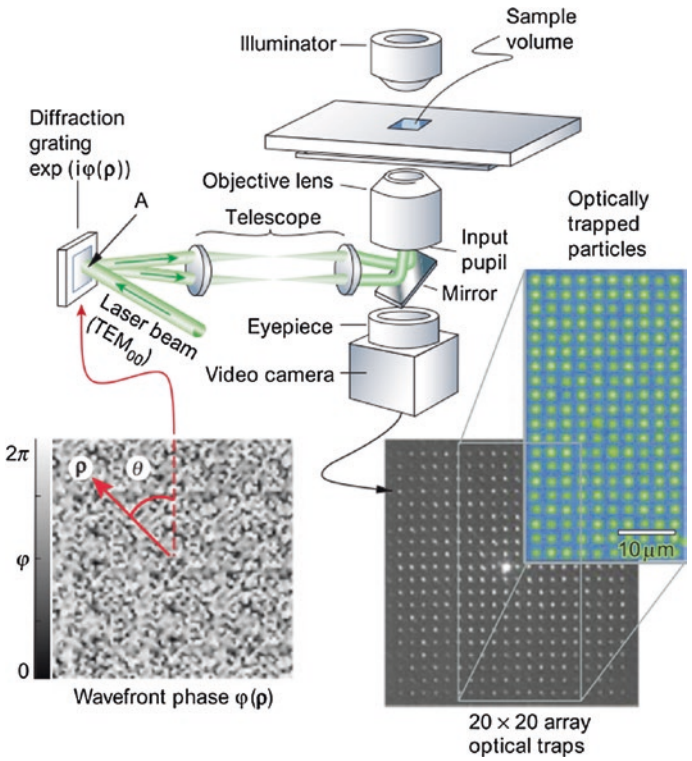

Fig. 3 A holographic optical tweezers system uses a diffraction pattern to split a single laser beam into multiple optical tweezers traps. Reprinted from Grier (2003) with permission from MacMillian Publishers Limited

to the SLM (Bowman et al. 2010), reducing possible errors while trapping a particle. Through the use of iterative algorithms, multiple HOT traps can be made more effective. Red Tweezers, a HOT control program developed by the University of Cambridge, is an example of software that utilizes iterative algorithms (Bowman et al. 2014). The program, which runs in LabVIEW (National Instruments), is able to generate holograms at high speed and deliver the data to an SLM.

2.3 Other Optical Traps

2.3.1 Near-Field Optical Traps

Near-field optical traps use evanescent optical fields to generate optical gradient forces capable of trapping particles. It is particularly effective for trapping nanoscale particles. One way to realize near-field optical trapping is near the surface of optical waveguides (Yang et al. 2009; Soltani et al. 2014) or optical

resonators (Lin et al. 2010; Mandal et al. 2010; Hu et al. 2010). Near-field optical trapping can also be achieved through the use of plasmonic nanostructures, which have been shown to be capable of trapping biological materials, such as yeast cells (Huang et al. 2009). However, one concern when working with biological materials is the high temperature near the plasmonic structures.

2.3.2 Scattering Forces and Other Forces

Optical scattering forces can also be used for cell manipulation instead of optical gradient forces. Unlike an optical tweezers trap, where cells are trapped in three dimensions, optical scattering forces can push cells along the direction of laser beam propagation. Two or more laser beams can use scattering forces to stably trap objects in three dimensions, if the laser beams are directed toward each other (Constable et al. 1993; Yuan et al. 2008; Jess et al. 2006; Lincoln et al. 2007). Particles are attracted toward the dual beams by their gradient forces, and the scattering forces of each beam dictate the position of the particle relative to the laser sources. Assuming the laser powers are equal, the stable trapping position will be in the center of the laser beams, at a point midway between the two lasers. Unlike a single-beam optical trap, a dual-beam optical trap does not require high numerical aperture optics or a tightly focused beam; this means less photodamage on cells or biomolecules (Jonáš and Zemánek 2008). However, scaling up the number of discrete optical traps using dual beams is more complex than with a single-beam optical tweezers trap.

Optical scattering forces can be used to extract specific cells out of microwells for further analysis or disposal (Kovac and Voldman 2007), or for continuous-flow microfluidic cell sorters (Lee et al. 2013). Optical interference patterns and other sculpted optical landscapes can also be used to direct the trajectories of cells for sorting (MacDonald et al. 2003; Jákl et al. 2014). These sorting methods are explained in more detail in Sect. 5.2.

Another interesting method for cell manipulation is the use of a “tractor beam” (Brzobohatý et al. 2013). Unlike optical tweezers, tractor beams use a pulling force to transport particles against the direction of beam propagation, while gradient force is only used to keep the particle in the plane transverse to the propagation direction. This pulling force is achieved with two interfering plane waves intersecting at an angle, and depends on the beam polarization. Notably, this method should be compatible with biological particles, including cells, which have similar properties to the polystyrene beads used in these experiments.

3 Optically Induced Dielectrophoresis (ODEP)

The contactless manipulation of cells can also be accomplished using a low-frequency analogue to optical tweezers, dielectrophoresis (DEP) (Gagnon 2011; Pethig 2013). An applied electric field can induce a dipole across a cell;

if the electric field is nonuniform, each end of the dipole experiences a different Coulombic force, resulting in a net dielectrophoretic force. The nonuniform electric fields necessary for DEP can be created by microfabricated electrodes (Jubery et al. 2014; Cetin and Li 2011), but DEP can also be optically controlled using optoelectronic tweezers, or optically induced dielectrophoresis (ODEP) (Chiou et al. 2005; Wu 2011). Many cell types have been manipulated by ODEP, including bacteria (Chiou et al. 2004), many types of mammalian cells (Ohta et al. 2007a, b; Hwang et al. 2008a; Neale et al. 2009a), and protozoa (Choi et al. 2008). ODEP has also been used for trapping DNA (Lin et al. 2009) and cells encapsulated in hydrogel beads (Lin et al. 2012a).

In ODEP, a photosensitive material is used to create the nonuniform electric field necessary for DEP using optical patterns (Fig. 4i). This is done by using light to change the electrical impedance of the photosensitive material. In turn, this changes the strength of the electric field in a liquid layer abutting the photosensitive material, and the resulting non-uniform electric field generates a DEP force.

As ODEP is optically controlled, this technique retains the flexibility and dynamic control of direct optical manipulation. However, since the optical energy is not directly converted to the trapping force, the optical requirements can be relaxed. Significantly lower optical intensities can be used to control ODEP as compared to optical gradient traps; typically, intensities from 10 to 1000 mW/cm^2 are used for ODEP. The optical sources can be coherent (Neale et al. 2007) or non-coherent, such as mercury lamps (Ohta et al. 2007a) or LEDs (Chiou et al. 2005; Zarowna-Dabrowska et al. 2011). Light patterns can be formed from a single light source using micromirror arrays and other spatial light modulators, or by simply taking the output of a computer projector (Ohta et al. 2007a) or LCD (Choi et al. 2007; Hwang et al. 2008a). Computer projectors and LCDs have the advantage that the light source and the mechanism for patterning the light are integrated, facilitating the setup of the ODEP system, and enabling a relatively compact footprint.

3.1 Operation of a Typical ODEP System

A typical ODEP device has a transparent planar electrode made of indium-tin oxide (ITO) on glass and a photosensitive electrode (Fig. 4i). The two electrodes house a fluidic chamber between them, which contains the cells under manipulation. An electric field is created in the fluidic chamber by applying an AC voltage across the electrodes, typically at a frequency in the range of tens to hundreds of kilohertz.

Optical patterns are focused onto the photosensitive electrode to modulate the electric field. Under dark or ambient lighting, the photosensitive electrode has a low conductivity, and its impedance, Z_{PC}, is larger than the impedance of the liquid layer, Z_L. This means that the majority of the applied AC voltage is across the photosensitive layer. However, when light is focused on the photosensitive electrode, Z_{PC} is lowered enough that a significant voltage is dropped across the liquid

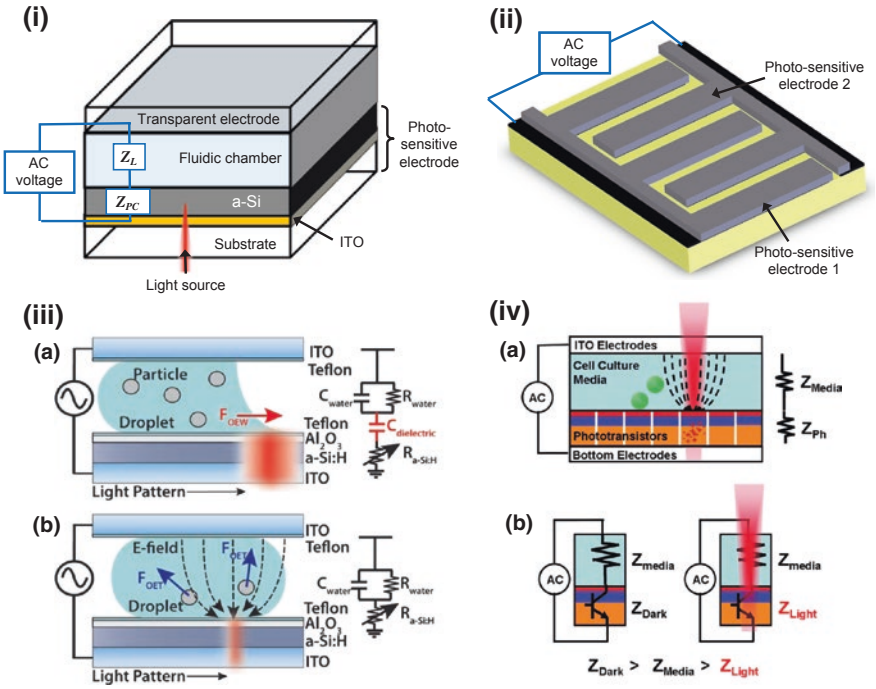

Fig. 4 Various configurations of optically induced dielectrophoresis devices. **i** The standard device for optically induced dielectrophoresis. It consists of a fluidic chamber bounded by a transparent electrode and a photosensitive electrode. The photosensitive electrode is usually amorphous silicon (a-Si) on indium-tin oxide (ITO). **ii** Lateral-field optoelectronic tweezers create electric fields that are primarily parallel to the surface, and consolidates the ODEP electrodes to one surface. **iii** Optoelectrowetting and optically induced dielectrophoresis can be realized on the same device by changing the frequency of the electric field. Reproduced from Valley et al. (2011) with permission from the Royal Society of Chemistry. **iv** Phototransistor-based optoelectronic tweezers have increased conductivity under illumination, enabling operation in cell culture media and other physiological solutions. Reproduced from Hsu et al. (2010) with permission from the Royal Society of Chemistry

layer. This switching between a normally low-conductivity state and high-conductivity illuminated state enables the creation of optically defined electrodes on the photosensitive electrode (Ohta et al. 2007a). Thus, the light patterns shape the electric field landscape, creating electric field gradients in the liquid layer between the illuminated and dark areas of the photosensitive electrode, generating ODEP force, which, for spherical particles such as cells, is given by the following equation (Jones 1995):

$$F_{\mathrm{DEP}} = 2\pi r^3 \varepsilon_m \mathrm{Re}[K(\omega)] \nabla E_{\mathrm{rms}}^2 \tag{1}$$

where r is the particle radius, ε_m is the permittivity of the medium surrounding the particles, $K(\omega)$ is the Clausius–Mossotti factor, and E is the electric field.

The Clausius–Mossotti factor is a complex number that depends upon the frequency of the applied electric field and the properties of the particle and the surrounding medium, as given by (Jones 1995):

$$K(\omega) = \frac{\varepsilon_p^* - \varepsilon_m^*}{\varepsilon_p^* + 2\varepsilon_m^*} \tag{2}$$

where ε_p^* and ε_m^* are the complex permittivities of the particle and medium, respectively. These are given by (Jones 1995):

$$\varepsilon_{p,m}^* = \varepsilon_{p,m} - j\frac{\sigma_{p,m}}{\omega} \tag{3}$$

where the permittivity, ε, and conductivity, σ, are for either the particle, p, or medium, m. The angular frequency of the electric field is represented by ω. Thus, the ODEP force depends not only on the volume of the particles, but also on the difference in the electrical properties of the particles and the surrounding media.

The most popular photosensitive electrode for ODEP consists of a layer of intrinsic amorphous silicon (a-Si) deposited on a layer of ITO, but other materials can also be used. Cadmium sulfide is another photoconductive semiconductor that has been used for ODEP (Higuchi et al. 2008), with the advantage that its chemical deposition is more inexpensive than the plasma-enhanced chemical vapor deposition used for a-Si. Organic photoconductors and polymers can simplify fabrication even more, such as spin-coated layers of titanium oxide phthalocyanine (Yang et al. 2011, 2013) or a blend of regioregular poly (3-hexylthiophene) and phenyl-C61-butyric acid methyl ester (Wang et al. 2010a). These materials are also compatible with flexible substrates (Lin et al. 2012b). Another photosensitive material, lithium niobate, enables the retention of the electric field patterns even after the illumination is removed, although it does take longer to switch the conductivity of this material between the light and dark states (60 s to a few minutes) (Glaesner et al. 2012). Other materials can also be added to the traditional a-Si layer; nanoparticles can be tethered to a lipid bilayer on the a-Si surface of the ODEP device, ensuring that these particles experience the maximum possible ODEP force (Ota et al. 2013).

Variants of the typical ODEP device have been created to add more functionality. To allow the easier integration of ODEP with polydimethylsiloxane (PDMS) microfluidic channels, the transparent planar electrode made of ITO-coated-glass was replaced with a different transparent structure consisting of carbon nanotubes embedded in PDMS (Huang et al. 2013a). It is also possible to facilitate the integration of ODEP with microchannels and other microfabricated structures by placing both ODEP electrodes on a single surface. This was accomplished with an interdigitated array of a-Si-coated electrodes (Fig. 4ii) (Ohta et al. 2007b). Placing the ODEP electrodes on a single surface has another effect: the electric field is primarily parallel to the plane of the electrodes, in contrast to the electric field that is normal to the electrodes in the typical ODEP device. Thus, in this variant of the ODEP device, anisotropic particles (Tien et al. 2009; Ohta et al. 2007c, 2008;

Neale et al. 2009b) align their long axis parallel to the surface of the substrate, which contrasts with the standard ODEP device (Jamshidi et al. 2008). Besides affecting the orientation of anisotropic particles, the single-side ODEP architecture allowed the integration of ODEP force for cell trapping and transport with electrowetting-on-dielectric (EWOD) for droplet manipulation (Shah et al. 2009).

Droplet manipulation can also be achieved by adding a dielectric layer and hydrophobic coating over the photosensitive electrode (Valley et al. 2011) (Fig. 4iii). At AC voltages around 10 kHz, this device acts as an optically controlled EWOD device, and the light patterns control the movement of droplets (Fig. 4iii-a). When the frequency of the applied voltage is increased to around 200 kHz, the device acts as a standard ODEP device, and is capable of moving particles within the droplets using DEP force (Fig. 4iii-b).

3.2 Limitations of ODEP

There are several limitations of the standard ODEP system with respect to cellular manipulation. The first concern is throughput; in optical manipulation, this is typically limited by the area over which the optical patterns can be generated. This is less of an issue with ODEP as compared to optical tweezers, as the optical intensity and focusing requirements are more relaxed. Instead, throughput in a conventional ODEP system is limited by the system used to visualize the cells under manipulation, which is usually a microscope with a field-of-view a few square millimeters. Lens-free holographic imaging can greatly increase the area over which cells and other particles can be imaged (Mudanyali et al. 2010), and coupled with ODEP, can improve the throughput (Huang et al. 2013b). The working area of 240 mm^2 reported by Huang et al. is the largest effective area of any optical manipulator to date.

Although manipulation throughput can be higher using ODEP compared to optical tweezers, especially with larger particles such as cells, ODEP does have issues associated with the electrical conductivity of the media containing the cells under manipulation. Many types of physiological media, including phosphate-buffered saline and commonly used cell culture media, have relatively high concentrations of ions, resulting in high electrical conductivities (typically 1–2 S/m). This presents a problem for the photosensitive electrodes mentioned thus far, as the illuminated (on-state) conductivity is too low to meet the condition that $Z_{PC} < Z_L$, so the optical control of the electric field will not work, and DEP force will not be generated. This does not prevent the use of these ODEP devices with cells, as osmotically balanced low-conductivity buffer solutions can be used. However, the cells can only survive up to several hours in these low-conductivity buffers.

ODEP can be made to work in physiological media if the conductivity of the photosensitive electrode under illumination can be increased. This was accomplished by using an arrayed phototransistor structure as a replacement for the

photosensitive electrode (Fig. 4iv), and operation in physiological media was demonstrated (Hsu et al. 2010). However, as with conventional DEP, Joule heating becomes of a concern when operating in physiological media, as the amount of electrical current conducted by the media increases. In the phototransistor-based ODEP device, Joule heating caused a temperature increase, but only by 1–2 °C, and the addition of heat sinks decreased this rise in temperature to less than 1 °C (Pauzauskie et al. 2010).

Unlike optical tweezers, ODEP is not capable of full three-dimensional manipulation; the DEP force decreases with distance from the photosensitive electrode. Thus, the cells under manipulation are always close to a surface, so the nonspecific adherence of cells can be an issue. If cells adhere when it is not desired, their adhesion forces can be on the order of nanonewtons, much larger than typical ODEP forces of tens to hundreds of piconewtons. This nonspecific cell adhesion can be reduced by a factor of 30 by coating the electrodes with a layer of poly(ethylene glycol) (PEG), a common antifouling polymer (Lau et al. 2009). It is also possible to use two photosensitive electrodes and repulsive DEP forces to achieve pseudo-3D manipulation, and to keep the cells under manipulation from contacting the ODEP surfaces (Hwang et al. 2008b). However, the addition of the second photosensitive electrode makes it harder to image the cells, and cells must be constantly manipulated to keep them contacting the electrode surfaces.

3.3 Other Electrokinetic Phenomena

Other electrokinetic forces can be created in a standard ODEP device (Valley et al. 2008). If the applied electric field has a frequency on the order of 100 Hz or less, electrolysis can occur. Bubbles generated by electrolysis can interfere with normal ODEP operation, harm cell membranes, and damage the photosensitive electrode layer, so this operating regime is usually avoided.

As the frequency of the applied electric field increases to a few kHz, light-induced AC electroosmosis (LACE) can result. The optical patterns control the electric field and the zeta potential at the liquid–photoconductor interface, resulting in electroosmotic flow that can be used to transport particles (Chiou et al. 2008; Hwang 2009).

Electrothermal heating can be observed in a standard OET device or similar structures when using high optical intensities or large electric fields. Electrothermal heating can also be exploited to drive optically controllable fluid flows, which can be used to trap and pattern particles (Kumar et al. 2009; Williams et al. 2010; Mishra et al. 2014). Optically controlled electrothermal heating relies on the absorption of light in a substrate to create thermal gradients in a fluid. The thermal gradients result in gradients in the electrical conductivity and permittivity of the fluid, driving electrothermal flow. This flow has been harnessed for the trapping of bacteria and the sorting of microorganisms based on size (Kwon et al. 2012).

4 Optothermal Manipulation

The use of direct optical forces for cell manipulation is limited by the magnitude of forces that can be exerted, which is typically in the piconewton range. However, light can be used to exert larger forces through indirect mechanisms that use the transfer of energy rather than the transfer of photon momentum. Unlike direct optical actuation, photothermal or optothermal actuation methods use light to generate heat through absorption in a material, creating thermal forces.

One optothermal force is thermophoresis, which is the motion of particles due to a temperature gradient. Optothermal heating can also induce thermocapillary effects, which can move bubbles, droplets, and thin liquid films, and can be harnessed to manipulate cells.

4.1 Thermophoresis

Thermophoresis, also known as thermomigration or thermodiffusion, is the response of particles subjected to a temperature gradient, and can be described by

$$U = -D_T \nabla T \tag{4}$$

where U is the drift velocity, D_T is the particle mobility, and T is temperature (Würger 2010). The temperature gradient necessary for thermophoresis can be created by opto-thermal heating, and used for the trapping and transport of biological particles, such as DNA (Duhr and Braun 2006; Weinert and Braun 2009; Maeda et al. 2011), or even the stretching of DNA (Ichikawa et al. 2007), but its use for larger objects such as cells is limited (Helden et al. 2014). However, thermophoresis has been shown to be useful for the manipulation of DNA and other molecules inside living cells (Reichl and Braun 2014), providing a method for the in vivo measurement of intercellular activity.

4.2 Opto-Thermocapillary Cell Manipulation

The thermocapillary or thermal Marangoni effect refers to mass transfer along a liquid–gas interface due to a surface tension gradient created by a temperature gradient. If optical heating creates the temperature gradient that induces the surface tension gradient, the resulting effect can be termed as opto-thermocapillary force. Opto-thermocapillary force has been utilized for actuating various fluidic elements such as bubbles (Ohta et al. 2007d; Tan and Takeuchi 2007; Hu et al. 2011; Rahman et al. 2015a), droplets (Kotz et al. 2004; Farahi et al. 2005; Baroud et al. 2007; Hu and Ohta 2011), and liquid films (Garnier et al. 2003), and can be harnessed for the manipulation of the cells and biomolecules.

Opto-thermocapillary force can be used to actuate microbubbles that are capable of manipulating cells and biomolecules (Hu et al. 2011). Optical patterns are used to create localized hot spots on an absorbing substrate, which are used actuate the microbubbles (Fig. 5). The microbubbles can function as untethered micrometer-scale actuators, and can manipulate various types of cells, including yeast cells (Hu et al. 2012a) and NIH-3T3 fibroblasts (Hu et al. 2013a).

Unlike optical tweezers, opto-thermocapillary actuation is not dependent on the optical properties of the object under manipulation. Opto-thermocapillary actuation is also insensitive to the electrical properties of the liquid medium and the object under manipulation, in contrast to ODEP. However, opto-thermocapillary actuation does share the flexibility of optical control with the other cell manipulation methods described in this chapter, enabling parallel, independent actuation of multiple micro-objects. Although opto-thermocapillary actuation has only been

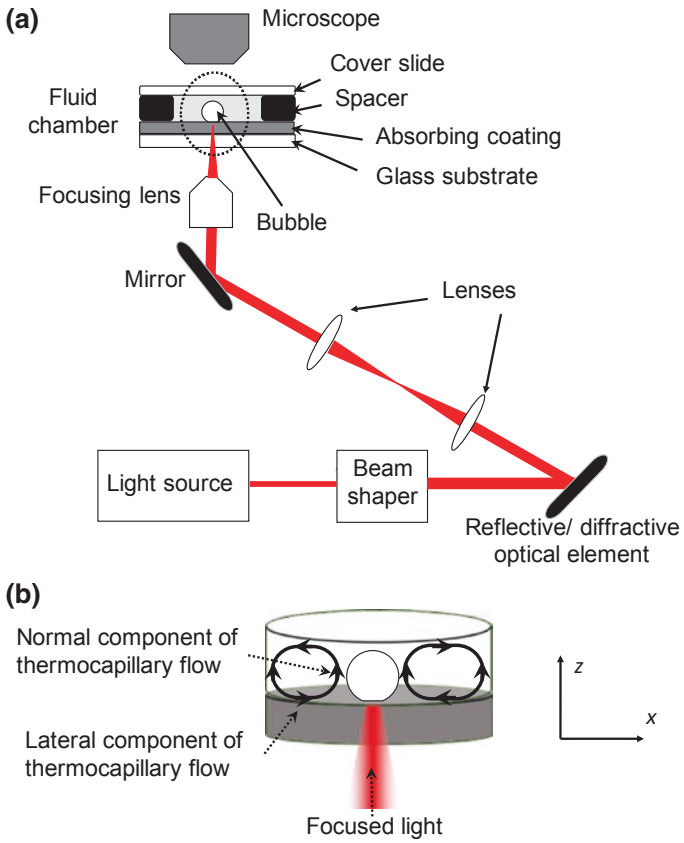

Fig. 5 Opto-thermocapillary bubble manipulation setup. **a** The overall optical setup. The light source is focused on an absorbing coating (typically 1-μm-thick amorphous silicon on 200-nm-thick indium tin oxide) at the floor of a fluidic chamber. **b** Close-up of the portion of the setup circled by the dashed line in **a**, showing the opto-thermocapillary flow surrounding the bubble

demonstrated on up to 12 microbubbles in parallel to date, it has the potential to control at least 50 microbubbles simultaneously (Rahman et al. 2015a).

The microbubbles for opto-thermocapillary actuation are generated in a liquid media by the optothermal heating of the substrate (Fig. 5). A laser beam is focused on the absorptive coating of the substrate, which converts the light energy to thermal energy, causing localized heating in the fluid adjacent to the hot spot (Ohta et al. 2007d). This results in the vaporization of the working fluid at the hot spot, nucleating the bubble.

Once the bubble has been created, the temperature gradient created by the laser-heated region drives a toroidal thermocapillary flow that can be divided into two principal components of interest (Fig. 5b): lateral and normal. The flow that is parallel to the substrate is the lateral part of the thermocapillary flow. Another thermocapillary flow component normal to the substrate is present around the bubble perimeter, due to the temperature gradient in the z-direction. If an object has a density greater than that of the carrier fluid, interaction with the normal flow can be minimized, and the object can be pulled toward the bubble without having the object circulate in the toroidal thermocapillary flow.

The lateral opto-thermocapillary flow was used to pattern yeast cells in an agarose solution. After the yeast cells were patterned, the agarose solution was gelled, and 92 % of the original cells underwent multiple cell divisions over a period of 9 h (Fig. 6) (Hu et al. 2012a). A 980-nm diode laser focused to an intensity of 508 kW/cm^2, pulsed with 60-μs pulses at 60 Hz, was used to generate the bubbles and thermocapillary flow used for manipulation.

Opto-thermocapillary flow has also been used to trap and transport NIH/3T3 fibroblasts (Hu et al. 2013a). The cells were suspended in cell media mixed with a hydrogel or agarose pre-polymer, and patterned using opto-thermocapillary flow in an open reservoir. Fibroblasts in a polyethylene glycol diacrylate (PEGDA) prepolymer solution were manipulated into a 4 × 4 cell array in 6.5 min (Fig. 7a–d), at a velocity of 30 μm/s. After the assembly, the PEGDA solution was photopolymerized (Fig. 7e), and cell viability was tested (Fig. 7f). Fibroblasts were also assembled into a 3 × 3 cell matrix in a 4 % agarose solution at an average velocity

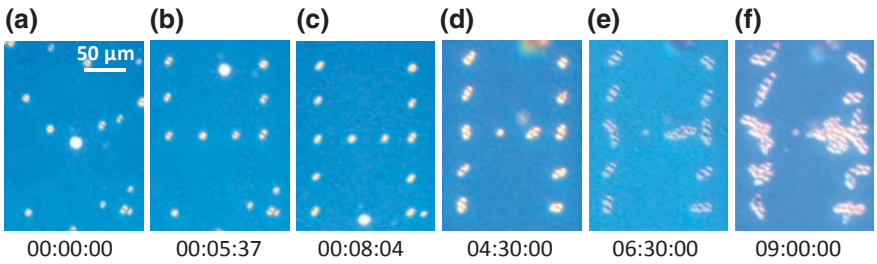

Fig. 6 Yeast cells assembled using opto-thermocapillary flow. **a–c** Assembly of yeast cells assembly into an "H" shape in agarose solution. The agarose was subsequently gelled by lowering the solution temperature to 15 °C. **d–f** Cell culturing for 9 h after agarose gelation. Reproduced with permission from Hu et al. (2012a)

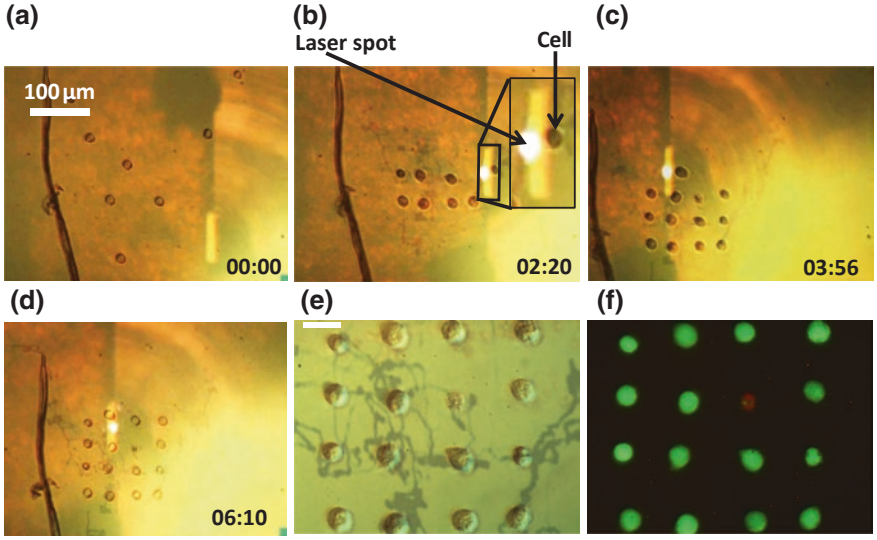

Fig. 7 Opto-thermocapillary assembly of NIH/3T3 fibroblasts. The time stamp format is minutes: seconds. **a**–**d** Cells are assembled by the opto-thermocapillary flow. The *inset* shows a close-up image of the cell being manipulated. **e** Single-cell pattern after PEGDA gelation. The dark tracks may be due to the laser heating of the substrate, but they do not affect the experiment. The *scale bar* is 20 mm, and also applies to **f**. **f** Green fluorescence indicates viable cells. Only one cell displays red fluorescence, indicating a nonviable cell. Reproduced from Hu et al. (2013a) with permission from the Royal Society of Chemistry

of 8 µm/s. The reduced opto-thermocapillary flow in the more viscous agarose solution resulted in a lower cell manipulation speed, but subsequent agarose gelation and culturing also showed high cell viability.

Additional functionality may be added by using opto-thermocapillary actuated bubbles to move secondary hydrogel structures with features to aid in the assembly of cells (Hu et al. 2012b). Hydrogel structures made of photopolymerized poly(ethylene glycol) diacrylate (PEGDA) were created in various geometries, such as disk-shaped structures with 40–70 µm-radii with a 5-µm-radii cavity at the center. A bubble in this central cavity is opto-thermally actuated, actuating the hydrogel structure. This enables the assembly of cells in an uncovered fluid reservoir, providing easy access to the cells under manipulation for downstream culturing or assays. The hydrogel structures can also be made to absorb the incident laser light by adding carbon particles (Hu et al. 2013b). This means that the opto-thermocapillary actuation of the hydrogel structures does not require a light-absorbing substrate.

To achieve the parallel manipulation of the microbubbles using opto-thermocapillary actuation, optical patterns are created from a single laser by a scanning mirror (Hu et al. 2014) or a spatial light modulator (Rahman et al. 2015a). Both systems are similar to methods used to create multiple optical tweezers traps.

Using orthogonal scanning mirrors, a single beam of light can be directed to multiple locations on a two-dimensional plane, controlling up to 10 microbubbles independently at once (Hu et al. 2014). The maximum number of microbubbles was limited by the manual control system, but the time-sharing of one laser beam fundamentally limits the maximum number of microbubbles, just as with time-sharing optical tweezers systems.

Thus, as with holographic optical tweezers, an alternate method is the use of an SLM to create a holographic control system (Rahman et al. 2015a). Instead of redirecting a single beam multiple times, an SLM is able to split the beam using a computer-generated hologram, eliminating the need for time-sharing, and allowing the bubbles to be continuously actuated on a sample.

The control system that was used to realize the control of multiple microbubbles using an SLM was a modified version of the Red Tweezers program (Bowman et al. 2014). Some modifications to the program were necessary, including a bubble-collision-detection system and an error detection system. In addition, an automatic sequence generator was added that allows the microbubbles to move in independent trajectories at the same time. A user defines the path of microbubbles by planning out a sequence of holograms, which is then played on the SLM at specific time intervals for the purpose of particle manipulation (Fig. 8).

Like other cellular manipulation systems, opto-thermocapillary flow has its limitations, some of which are shared with HOT. If a holographic control system is

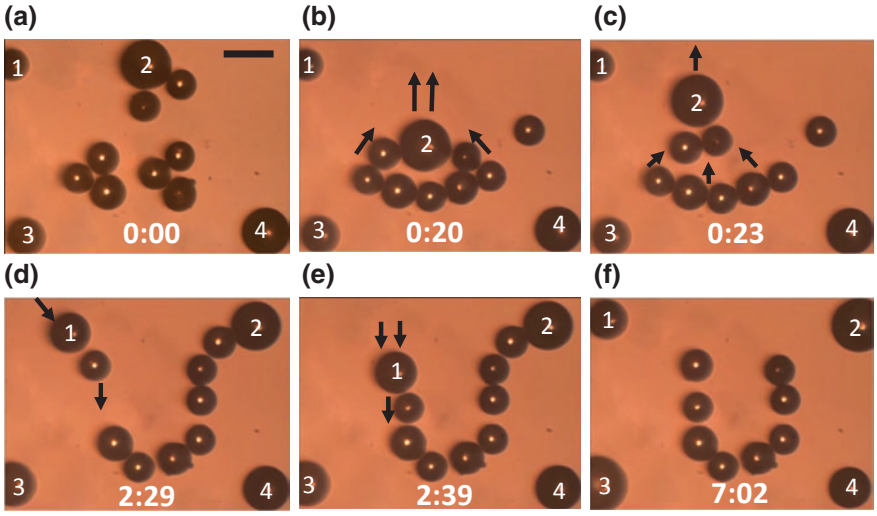

Fig. 8 Assembly of glass beads using multiple opto-thermocapillary flow-actuated microbubbles. Two microbubbles were used to assemble eight glass beads. Each microbubble in the field-of-view is numbered (a total of four); the *scale bar* is 200 μm. **a** Initial position of the microbubbles and the beads. **b**, **c** Bubble 2 pulling the beads into place. **d**, **e** Bubble 1 pushing the beads into place. **f** The final U-shaped pattern, after a total assembly time of 7 min. Reproduced with permission from Rahman et al. (2015b)

used, "ghost traps" may occur, just as in HOT. This can be resolved by using the same iterative algorithms used for HOT systems, resulting in the reduction of aberrations in the system.

In addition, the number of bubbles available for micromanipulation is limited by the available laser power and the working area. Currently, micromanipulation occurs over an area of 1.1 mm by 0.83 mm, and is limited by the magnification of the focusing lens (Rahman et al. 2015b). A smaller magnification provides a larger area of manipulation, but reduces the resolution, as this also increases the minimum size of the optical features that can be created. Therefore, there is a tradeoff between working area and resolution. This could be addressed by using a high-magnification focusing lens for higher resolution, and moving the fluid chamber and microrobots independently to cover a large working area; however, this will increase the complexity of the control system.

Like ODEP, opto-thermocapillary manipulation is currently restricted to two-dimensional motion. However, the potential for three-dimensional opto-thermocapillary manipulation exists, especially if the normal thermocapillary flow can be exploited.

5 Optical Manipulation for Single-Cell Analysis

The optical manipulation methods described in this chapter are useful for enabling or augmenting functions related to single-cell analysis, including cell culturing, cell separation and sorting, cell trapping, isolation, and transport, molecular delivery to cells, cell lysis, and measurements of cellular properties. Specific examples that realize these functions will be described in this section.

5.1 Cell Culturing

The first step in single-cell analysis is the culturing of cells. Optical manipulation can assist with this by enabling the patterning of cells to study cell–cell interactions, or to build cocultures of different types of cells. Traditional cell culture is performed on two-dimensional surfaces, such as tissue culture polystyrene (TCPS). However, cells can be grown on other surfaces, including glass and silicon. Thus, optical manipulation can be used to position cells before subsequent culturing. This has been demonstrated with optical tweezers (Townes-Anderson et al. 1998), phototransistor-based ODEP (Hsu et al. 2010), and optothermal manipulation (Hu et al. 2013a). Although standard ODEP devices do not work in cell culture media, microfluidic structures can be added to automatically exchange low-conductivity ODEP media with cell culture media (Lee et al. 2014), so cell culturing with these types of structures can be possible.

While cell culturing on a two-dimensional planar surface is widespread, more accurate models of cell behavior can be obtained by culturing cells in three dimension, which more closely approximates an in vivo environment. This is typically done by culturing cells in some type of scaffold material made of natural extracellular matrix materials or synthetic materials such as hydrogels. Cells embedded in microscale scaffolds form "microgels" (Yeh et al. 2006) which can be used as building blocks of in vitro tissues and organ-like structures. Optical manipulation can be used to position and organize these microgels, by direct optical manipulation (Kirkham et al. 2015), ODEP (Lin et al. 2012a), or optothermal manipulation (Hu et al. 2012b). Optical manipulation can also assist with the transport and release of chemicals to control cell growth and differentiation during culturing (Kirkham et al. 2015).

5.2 Cell Sorting

Once cells are cultured, cells of interest need to be separated from unwanted cells through some form of cell sorting. This can also be the first step in a single-cell analysis process that uses primary cells, which undergo minimal, if any, culturing. Some examples of sorting that are interesting include sorting by the type of cell, such as red blood cells from white blood cells, or cancerous cells from healthy cells. Sorting of live cells from dead cells can also help with downstream processes, as well as the isolation of rare cells from a larger cell population.

Various mechanisms can be used to obtain these sorting results (Fig. 9), and can broadly be classified as passive sorters, which use static optical patterns, or active sorters, which use dynamic optical patterns. Cell types can be sorted by size, using various mechanisms including direct optical force or ODEP. Direct optical forces can also distinguish cells based upon their optical properties, while ODEP can be used to differentiate cells based on their electrical properties. Importantly, sorting upon these intrinsic properties means that labeling is not required, minimizing sample preparation and adverse effects on the cells to be sorted. All types of optical manipulation systems can also sort cells based upon visual characteristics identified by image-based control systems, such as morphology or fluorescent markers.

5.2.1 Cell Sorting with Direct Optical Forces

The forces resulting from optical landscapes can enable sorting through the variation in the strength of particle interactions. A three-dimensional optical lattice produced by multi-beam interferences creates a landscape in which particles can be separated by size and refractive index (Fig. 9ii) (MacDonald et al. 2003). These variations in force can be used to separate cells that are otherwise indistinguishable. Moving optical interference patterns can also enable size- and shape-based separation of cells (Jákl et al. 2014).

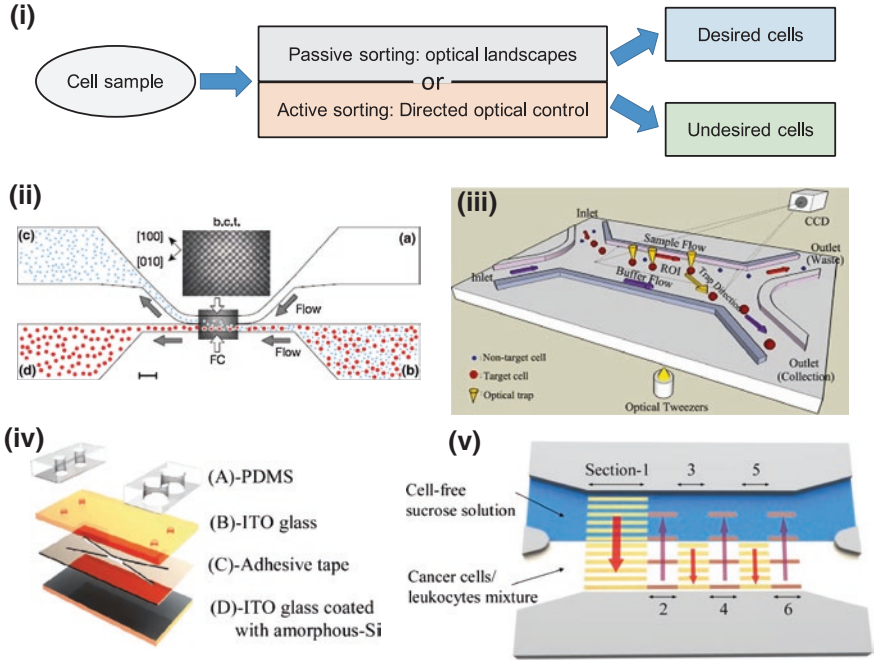

Fig. 9 Optical cell sorting. **i** Block diagram of an optical cell sorter. A cell sample is sorted by either a passive (static) optical landscape, or by an active (dynamic) force applied to the cells. **ii** An example of a passive cell sorter, in which an optical lattice is used to sort objects based on their size or index of refraction. Reproduced with permission from MacDonald et al. (2003). **iii** An active cell sorter that uses multiple optical tweezers traps to move desired cells into an outlet channel. Reproduced from Wang et al. (2011) with permission from the Royal Society of Chemistry. **iv** An exploded view of active cell sorting device that uses ODEP. **v** The operation of the ODEP-based active cell sorter, showing dynamic light patterns that are used to sort the cells by cell type. **iv** and **v** are reproduced from Huang et al. (2013c) with permission from the Royal Society of Chemistry

Optical tweezers can provide the force needed to sort cells in a microfluidic device. Many of these systems have automatic image-based sorting that allows cells to be sorted by parameters including size, shape, and fluorescence. For example, image processing was used to identify the size of cells, triggering optical tweezers to move particular cells into a collection channel, achieving the sorting of 3- to 5-μm-diameter yeast cells from 10-μm-diameter polystyrene beads at a yield of 100 % and a recovery rate of 90 % (Lin et al. 2008). Cells can also be sorted based on more than one parameter. One such microfluidic sorter is able to sort cells by size, shape, and fluorescence (Landenberger et al. 2012). Using this system, 2-μm-diameter yeast cells were sorted with a throughput of 1.4 cells per second and a recovery rate of 95 % using fluorescence, size, and a combination of fluorescence and size.

HOT systems can also be integrated with microfluidic systems for automatic cell sorting (Fig. 9iii). Using HOT to generate multiple optical traps can also result in a higher sorting throughput. An HOT-enabled automatic cell sorter is able to sort particles by both size and fluorescence, as demonstrated by the sorting of 5- to 8-μm-diameter yeast from 2-μm-diameter polystyrene micro-beads, and 10- to 15-μm-diameter fluorescently tagged stem cells from a mixture other similarly sized cells with a 90 % recovery rate and 90 % purity (Wang et al. 2011).

Cell sorters can also utilize the optical scattering force, which can be used to extract cells out of microwells and transported downstream for further analysis or disposal (Kovac and Voldman 2007). This image-based sorter has a large workspace for increased sorting throughput, although cells do need to be fluorescently tagged. However, the intrinsic response of cells to an optical scattering force can also be used for label-free sorting. This was demonstrated in a continuous-flow microfluidic sorter of red blood cells, lymphocytes, granulocytes, and monocytes (Lee et al. 2013). Each of these blood cells has different scattering forces, allowing each type of cell to be successfully distinguished from each other.

5.2.2 Cell Sorting with ODEP

Different cell types may also have different electrical properties, such as permittivity and conductivity, which can be distinguished using ODEP. Sorting based upon electrical properties can enable sorting that is not possible solely based on physical size, such as the separation of live cells from dead cells (Chiou et al. 2005). A live cell can maintain an ion differential across its interior and the surrounding medium. If the cell is in a low-conductivity medium, as in the case for standard ODEP manipulation, the interior of the cell will have an electrical conductivity greater than the medium. If the cell dies, the ion differential is no longer maintained, and the conductivity of the cell interior becomes similar to that of the low-conductivity medium. This makes the ODEP force exerted on live and dead cells different, according to Eqs. 1–3, and can even result in a change in the direction of the ODEP force. For instance, live white blood cells were observed to have a positive ODEP force, while dead cells had a negative ODEP force. This difference in force was used to selectively concentrate the live cells (Chiou et al. 2005). A similar observation with sperm cells enabled the discrimination between live and dead spermatozoa, even among completely nonmotile cells (Ohta et al. 2010). Variations in the electrical properties of different types of cells can also be exploited by ODEP. Physiological differences between B lymphocytes and red blood cells resulted in a difference in DEP force (Zhao et al. 2013), as well as for HeLa and Jurkat cells (Ohta et al. 2007b), prostate cancer cells and leukocytes (Huang et al. 2012, 2013c), and oral cancer cells and leukocytes (Huang et al. 2013c). These separations can be used to realize constant-flow cell sorting; up to 80 % cell purity and 80 % cell recovery with 95 % cell viability was achieved using such a device (Fig. 9iv, v) (Huang et al. 2013c).

Visual characteristics can also be an important sorting trigger for ODEP-based sorting. This can include checking for different cell morphologies and features, or by checking for visual tags, such as fluorescent markers. For example, T-cells and dendritic cells were distinguished via fluorescent tags, and ODEP was used to separate the different cell types (Jeorrett et al. 2014). The tags provided visual differentiation between the cells, enabling sorting; this separation was not possible based solely on electrical properties, as the two types of cells experienced similar ODEP forces.

5.3 Cell Trapping and Isolation

Once cells of interest are sorted, single cells need to be isolated for analysis. All of the optical trapping techniques discussed here are capable of this task, as described earlier in this chapter. The trapping of cells is usually done in vitro, which is suitable for single-cell analysis procedures. However, for some applications, it may be desirable to trap cells in vivo. Optical manipulation in vivo is more challenging, due to optical absorption by tissues, and inhomogeneous indices of refraction, but optical tweezers have been used to manipulate red blood cells in vivo, in the bloodstream of living mice (Zhong et al. 2013). The trapped red blood cells were manipulated in three dimensions, and the optical trap was shown to be capable of causing and clearing artificial clots in capillaries by transporting the blood cells to the appropriate locations. The stiffness of these optical traps was approximately 10 pN/μm with a power of 168 mW at the trap focus. Importantly, no thermal damage was observed on the cells that were trapped or the tissues in the path of the laser, showing the promise of optical tweezers for in vivo cell manipulation.

5.4 Cell Surgery and Lysis

Further analysis of single cells is necessary to enable a deeper understanding of cellular behavior. This type of analysis may require access to the cell interior, which can be achieved by using lasers to cut into cell membranes (Berns 1998). Organelles can then be extracted from the cell (Shelby et al. 2005), or cargo can be delivered to the cell. Lasers can also be used to realize cell fusion (Steubing et al. 1991) and the attachment of cells to one another without fusion (Katchinskiy et al. 2014). Cell lysis can also be induced through a more indirect process in which pulsed lasers are used to create cavitation bubbles that disrupt the cell membrane (Rau et al. 2004; Lai et al. 2008). Single-cell resolution is possible if cells are confined in microchannels (Lai et al. 2008), or in picoliter or femtoliter droplets (He et al. 2005). Alternatively, cell lysis can also be done using ODEP

(Lin and Lee 2009; Witte et al. 2014), including selective lysis depending upon the cell's shape (Kremer et al. 2014).

A related method of optically controlled cell surgery is the photothermal nanoblade, which utilizes titanium-coated microcapillaries (Wu et al. 2011) or vias (Wu et al. 2015) to convert nanosecond laser pulses to localized cavitation bubbles. These bubbles create pores in cell membranes, allowing cargo to be delivered into the cells. The cargo can cover a very large size range: 1 nm (RNA) up to 2 μm (bacteria) (Wu et al. 2011), and a throughput of up to 100,000 cells per minute can be achieved (Wu et al. 2015). This method can be nondestructive and used to deliver payloads to cells, like the methods that are covered next, in Sect. 5.5.

5.5 Molecular Delivery to Cells

A gentler operation than cell lysis is the creation of pores in the cell membrane, which can be reversible, where the pores self-heal, or irreversible, where the pores remain. Cell lysis, previously covered in Sect. 5.4, is irreversible membrane poration taken to the extreme. However, if the membrane pores are small enough, cells can recover from this operation, enabling molecular delivery. This enables techniques such as gene therapy or cell transformation. ODEP can use electric field pulses to open pores in the membrane of cells, enabling molecular delivery. In addition, the light patterns used by ODEP can be used to select specific cells for the membrane poration operation, while leaving other cells unaffected (Valley et al. 2009; Wang et al. 2014).

Opto-thermal heating of the cell membrane by a continuous-wave laser, facilitated by light-absorbing dyes, can temporarily increase membrane permeability, enabling molecular delivery (Palumbo et al. 1996; Schneckenburger et al. 2002; Nikolskaya et al. 2006). Single-cell resolution is possible with this method, although the transfection efficiency is relatively low (less than 30 %) (Stevenson et al. 2010).

Another method of selective cell poration is opto-thermocapillary size-oscillating microbubbles (Fan et al. 2014, 2015). Microsecond laser pulses focused on a light-absorbing surface nucleate a vapor microbubble. The size of the bubble is controlled by the laser pulses, causing the bubble to expand and collapse. This oscillation in the size of the bubble produces a fluid flow that can induce transient pores in a nearby cell membrane (Fig. 10i). This method has single-cell resolution, and can reach up to 95 % of molecular delivery efficiency while maintaining 95 % cell viability. Multiple molecules have been delivered to the same cell sample using this method (Fig. 10ii).

Nanosecond-pulsed lasers create shockwaves by laser-induced cavitation bubble expansion, which can open pores in cell membranes (Tsukakoshi et al. 1984; Soughayer et al. 2000; Venugopalan et al. 2002; Hellman et al. 2008; Wang et al. 2010b). This mechanism has a relatively low resolution; the shockwaves can affect cells up to 60 μm away from the laser focal point (Soughayer et al. 2000).

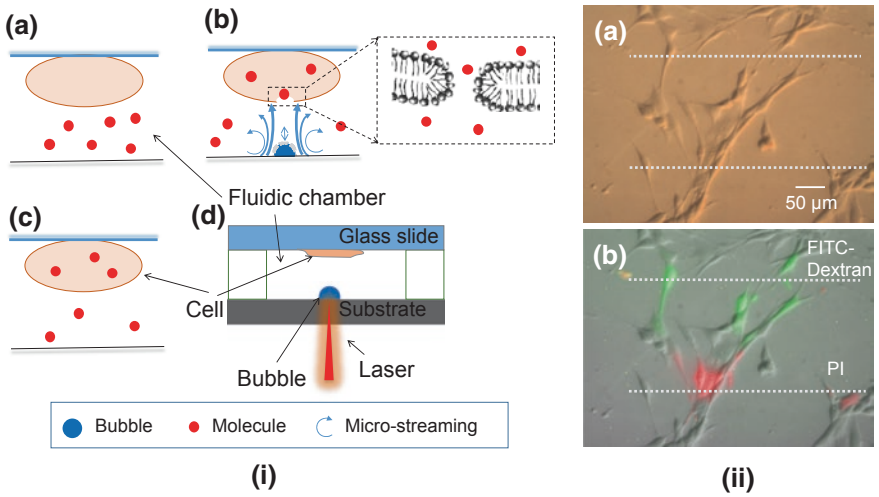

Fig. 10 Molecular delivery by laser-induced microbubbles. **i** The molecular delivery process. *(i-a)* The cell membrane is initially impermeable to the molecules. *(i-b)* A size-oscillating bubble is nucleated below the target cell by laser heating, creating shear stress that opens transient pores in the cell membrane, allowing the molecules to enter the cell interior. *(i-c)* The laser excitation ceases, and the cell membrane heals. *(i-d)* Cross section of the fluidic chamber. The laser is absorbed by the substrate, nucleating the bubble. **ii** Targeted delivery of multiple molecules. *(ii-a)* Bright-field image of fibroblasts. Molecular delivery of 3-kDa FITC-Dextran dye is performed on the cells in the vicinity of the *upper dashed line*. Propidium iodide (PI) is delivered to the cells marked by the *lower dashed line*. *(ii-b)* Composite image showing successful molecular delivery of FITC-Dextran (green fluorescence) and PI (red fluorescence). Reproduced from Fan et al. (2015) with permission from the Royal Society of Chemistry

However, single-cell resolution can still be achieved by nanosecond-pulsed lasers with the assistance of microfluidic structures to localize and confine cells (Le Gac et al. 2007; Li et al. 2013).

Femtosecond-pulsed lasers can also open transient pores in cell membranes via multiphoton ionization and plasma formation (Vogel et al. 2005). Transfection efficiencies using femtosecond-pulsed lasers are greater than 90 % for various cell lines (Tirlapur and Konig 2002; Baumgart et al. 2008; Uchugonova et al. 2008), and slightly lower (around 70 %) for stem cells and primary cells (Baumgart et al. 2008; Uchugonova et al. 2008). However, submicron focusing accuracy on the cell membrane is necessary for two-photon absorption to occur; a focusing error of 3 μm can decrease transfection efficiency by more than 50 % (Tsampoula et al. 2007). This focusing issue can be mitigated by using microparticles trapped by optical tweezers to focus the femtosecond laser precisely on the cell membrane (Waleed et al. 2013), or by using a Bessel beam (Tsampoula et al. 2007; Cižmár et al. 2008). In vivo transfection with femtosecond lasers has also been demonstrated (Zeira et al. 2007). The main barrier to the wide deployment of femtosecond-pulsed laser systems is the high cost of the laser and other equipment, which is on the order of $100,000.

5.6 Measuring Cellular Properties

The final step in a single-cell analysis procedure is to do measurements on the single cells of interest. This is primarily done with some form of microscopy, which is well suited to integration with optical systems, as most optical manipulations are built around or integrated into microscopes. Optical microscopy and sensing will not be reviewed here, but some measurement techniques unique to optical manipulation should be mentioned. For example, the mechanical properties of cells can be measured using optical manipulation (Fig. 11). Optical tweezers can be used to stretch cells, which provides information about the various cell moduli (Lim et al. 2004). Similarly, HOT can be used to measure the dynamic mechanical response of stem cells, from which information such as Young's modulus and viscosity can be extracted (Tan et al. 2012). This can be used to distinguish between differentiated and undifferentiated stem cells.

Optical tweezers can also help with the measurement of the Raman spectrum of cells, which is useful for determining their chemical composition and structure. Optical tweezers are a natural fit for Raman spectroscopy, as the optical trap stabilizes the particle under observation, even if it is in suspension, allowing cells to be accurately measured (Ajito and Torimitsu 2002). The focused laser beam used to create the optical trap can also be used to excite the particle for Raman measurements, or a separate laser can be used. Optical tweezers integrated with Raman spectroscopy has successfully measured various characteristics of cells, including distinguishing between live and dead cells (Xie et al. 2002), changes

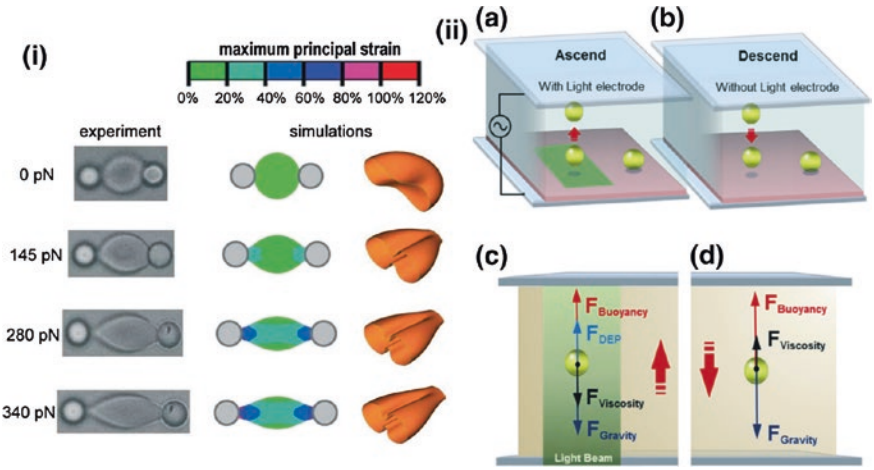

Fig. 11 Measuring cell properties using optical manipulation. **i** Optical tweezers can be used to stretch cells in order to gain information on the cell's mechanical properties. Reproduced from Lim et al. (2004) with permission. **ii** Measuring the mass and density of single cells by levitating the cells using ODEP, then observing the descent of the cells. Reproduced from Zhao et al. (2014) with permission from the Royal Society of Chemistry

in heat-treated cells (Xie et al. 2003), and the oxygenation capability of healthy and diseased red blood cells (De Luca et al. 2008). By adding optical tweezers, Raman spectroscopy and cell sorting can be achieved in the same platform (Lau et al. 2008).

Optical tweezers can be useful for the positioning of cells undergoing measurements. Synchrotron-radiation-based X-ray fluorescence (XRF) microscopy can provide spatial information on the material composition of cells, but this measurement requires that the sample remain still for up to hours at a time. Thus, cells measured using XRF need to be fixed in place, but traditional methods of immobilizing the cells can affect the measurement. To address this, an XRF system was integrated with a HOT system, allowing the cells to be immobilized with minimal effects on the XRF measurement (Vergucht et al. 2015). This system allows the cell under observation to be kept in its natural aqueous environment, reducing sample preparation, and increasing the biological relevance of the results.

HOT systems can collect more complex data such as the three-dimensional refractive index of a cell, which provides information about the composition and the structure of the cell (Habaza et al. 2015). Using HOT, cells could be captured and rotated 180° while in suspension. This is an easier and more efficient way to collect the three-dimensional refractive index data since a wide angular range can be achieved by HOT manipulation without an external rotation stage for the sample.

Cell stiffness is another important mechanical property, as this is an indicator of cellular behavior and cellular health. The relative stiffness of red blood cells can be measured using ODEP, by observing the change in the diameter of the cells when the electric field is applied (Neale et al. 2012). ODEP can also be used to measure the mass of single cells (Zhao et al. 2014, 2015). This method uses ODEP force to levitate cells; subsequently, the ODEP force is removed, and the rate of the descent of the cells is measured. This allows calculation of the density and mass of the cells (Fig. 11ii). ODEP force can also be used to detect the health of a cell, such as oocytes cultured under normal conditions compared to oocytes kept in a nutrient-free solution for 3 days (Hwang et al. 2009). A similar principle was used to differentiate between healthy and unhealthy embryos (Valley et al. 2010).

6 Summary

Optical manipulation encompasses a variety of technologies that are useful for single-cell analysis. Compared to other micromanipulation techniques, optical manipulation is usually the most flexible and adaptable, as reconfiguration of the manipulators can be done by altering the optical pattern. It is even possible to create reconfigurable microfluidic channels using optical control (Haulot et al. 2012), making it possible to realize a complete, optically controlled single-cell analysis platform.

Optical manipulation is especially suitable as an adaptable tool that can be reconfigured for different applications. It also excels at the manipulation of *specific* single cells, as appropriate optical patterns can be generated on the fly to target cells of interest.

However, optical manipulation usually requires expensive or complicated equipment, or both. Thus, it begins to lose some attractiveness for highly repetitive tasks that do not take advantage of the dynamic, flexible nature of optical control. In addition, if the manipulation of specific cells is not required, optical manipulation is less favorable, as it tends to have lower throughput than batch processes.

Optical manipulation has already proven useful in the analysis of single cells, and there is much potential for its continued use and expansion to other applications, especially if the inherent advantages of optical manipulation are exploited.

References

Ajito K, Torimitsu K (2002) Laser trapping and Raman spectroscopy of single cellular organelles in the nanometer range. Lab Chip 2:11–14

Arai F, Maruyama H, Sakami T, Ichikawa A, Fukuda T (2003) Pinpoint injection of microtools for minimally invasive micromanipulation of microbe by laser trap. IEEE/ASME Trans Mechatron 8:3–9

Arai F, Yoshikawa K, Sakami T, Fukuda T (2004) Synchronized laser micromanipulation of multiple targets along each trajectory by single laser. Appl Phys Lett 85:4301

Ashkin A (1970) Acceleration and trapping of particles by radiation pressure. Phys Rev Lett 24:156–159

Ashkin A, Dziedzic JM, Bjorkholm JE, Chu S (1986) Observation of a single-beam gradient force optical trap for dielectric particles. Opt Lett 11:288–290

Ashkin A, Dziedzic JM (1987) Optical trapping and manipulation of viruses and bacteria. Science 235:1517–1520

Ashkin A, Dziedzic JM, Yamane TM (1987) Optical trapping and manipulation of single cells using infrared laser beams. Nature 330:769–771

Baroud CN, de Saint Vincent MR, Delville JP (2007) An optical toolbox for total control of droplet microfluidics. Lab Chip 7:1029–1033

Baumgart J, Bintig W, Ngezahayo A, Willenbrock S, Murua Escobar H, Ertmer W, Lubatschowski H, Heisterkamp A (2008) Quantified femtosecond laser based opto-perforation of living GFSHR-17 and MTH53a cells. Opt Express 16:3021–3031

Berns MW (1998) Laser scissors and tweezers. Sci Am 278:52–57

Bianchi S, Di Leonardo R (2010) Real-time optical micro-manipulation using optimized holograms generated on the GPU. Comp Phys Commun 181:1444–1448

Bowman RW, Wright AJ, Padgett MJ (2010) An SLM-based Shack–Hartmann wavefront sensor for aberration correction in optical tweezers. J Opt 12:124004

Bowman RW, Padgett MJ (2013) Optical trapping and binding. Rep Prog Phys 76:026401

Bowman RW, Gibson GM, Linnenberger A, Phillips DB, Grieve JA, Carberry DM, Serati S, Miles MJ, Padgett MJ (2014) 'Red tweezers': fast, customisable hologram generation for optical tweezers. Comp Phys Commun 185:268–273

Brzobohatý O, Karásek V, Šiler M, Chvátal L, Čižmár T, Zemánek P (2013) Experimental demonstration of optical transport sorting and self-arrangement using a 'tractor beam'. Nat Photonics 7:123–127

Cetin B, Li DQ (2011) Dielectrophoresis in microfluidics technology. Electrophoresis 32:2410–2427

Chen T, Shi LZ, Zhu Q, Chandsawangbhuwana C, Berns MW (2011) Optical tweezers and non-ratiometric fluorescent-dye-based studies of respiration in sperm mitochondria. J Opt 13:044010

Chiou PY, Wong W, Liao JC, Wu MC (2004) Cell addressing and trapping using novel optoelectronic tweezers. In: Proceedings of the 17th IEEE international conference on micro electro mechanical systems (MEMS), Maastricht, Netherlands, 2004

Chiou PY, Ohta AT, Wu MC (2005) Massively parallel manipulation of single cells and microparticles using optical images. Nature 436:370–372

Chiou PY, Ohta AT, Jamshidi A, Hsu HY, Wu MC (2008) Light-actuated ac electroosmosis for nanoparticle manipulation. J Microelectromech Sys 17:525–531

Choi W, Kim SH, Jang J, Park JK (2007) Lab-on-a-display: a new microparticle manipulation platform using a liquid crystal display (LCD). Microfluid Nanofluid 3:217–225

Choi W, Nam SW, Hwang H, Park S, Park JK (2008) Programmable manipulation of motile cells in optoelectronic tweezers using a grayscale image. Appl Phys Lett 93:143901

Cižmár T, Kollárová V, Tsampoula X, Gunn-Moore F, Sibbett W, Bouchal Z, Dholakia K (2008) Generation of multiple Bessel beams for a biophotonics workstation. Opt Express 16:14024–14035

Constable A, Kim J, Mervis J, Zarinetchi F, Prentiss M (1993) Demonstration of a fiber-optical light-force trap. Science 18:1867–1869

Curtis JE, Koss BA, Grier DG (2002) Dynamic holographic optical tweezers. Opt Commun 207:169–175

De Luca AC, Rusciano G, Ciancia R, Martinelli V, Pesce G, Rotoli B, Selvaggi L, Sasso A (2008) Spectroscopical and mechanical characterization of normal and thalassemic red blood cells by Raman Tweezers. Opt Express 16:7943–7957

Dholakia K, Reece P (2006) Optical micromanipulation takes hold. Nano Today 1:18–27

Di Carlo D, Lee LP (2006) Dynamic single-cell analysis for quantitative biology. Anal Chem 78:7918–7925

Di Leonardo R, Ianni F, Ruocco G (2007) Computer generation of optimal holograms for optical trap arrays. Opt Express 15:1913–1922

Duhr S, Braun D (2006) Optothermal molecule trapping by opposing fluid flow with thermophoretic drift. Phys Rev Lett 97:038103

Dufresne ER, Spalding GC, Dearing MT, Sheets SA, Grier DG (2001) Computer-generated holographic optical tweezer arrays. Rev Sci Instrum 72:1810

Enger J, Goksör M, Ramser K, Hagberg P, Hanstorp D (2004) Optical tweezers applied to a microfluidic system. Lab Chip 4:196–200

Fan Q, Hu W, Ohta AT (2014) Laser-induced microbubble poration of localized single cells. Lab Chip 14:1572–1578

Fan Q, Hu W, Ohta AT (2015) Efficient single-cell poration by microsecond laser pulses. Lab Chip 15:581–588

Farahi RH, Passian A, Ferrell TL, Thundat T (2005) Marangoni forces created by surface plasmon decay. Opt Lett 30:616–618

Gagnon ZR (2011) Cellular dielectrophoresis: applications to the characterization, manipulation, separation and patterning of cells. Electrophoresis 32:2466–2487

Garnier N, Grigoriev RO, Schatz MF (2003) Optical manipulation of microscale fluid flow. Phys Rev Lett 91:054501

Glaesener S, Esseling M, Denz C (2012) Multiplexing and switching of virtual electrodes in optoelectronic tweezers based on lithium niobate. Opt Lett 37:3744–3746

Grier DG (2003) A revolution in optical manipulation. Nature 424:810–816

Grier DG, Roichman Y (2006) Holographic optical trapping. Appl Opt 45:880–887

Habaza M, Gilboa B, Roichman Y, Shaked NT (2015) Tomographic phase microscopy with 180° rotation of live cells in suspension by holographic optical tweezers. Opt Lett 40:1881–1884

Haulot G, Benahmed AJ, Ho CM (2012) Optoelectronic reconfigurable microchannels. Lab Chip 12:5086–5092

He M, Edgar JS, Jeffries GD, Lorenz RM, Shelby JP, Chiu DT (2005) Selective encapsulation of single cells and subcellular organelles into picoliter-and femtoliter-volume droplets. Anal Chem 77:1539–1544

Helden L, Eichhorn R, Bechinger C (2014) Direct measurement of thermophoretic forces. Soft Matter 11:2379–2386

Hellman AN, Rau KR, Yoon HH, Venugopalan V (2008) Biophysical response to pulsed laser microbeam-induced cell lysis and molecular delivery. J Biophotonics 1:24–35

Hesseling C, Woerdemann M, Hermerschmidt A, Denz C (2011) Controlling ghost traps in holographic optical tweezers. Opt Lett 36:3657–3659

Higuchi Y, Kusakab T, Tanemura T, Sugano K, Tsuchiya T, Tabata O (2008) Manipulation system for nano/micro components integration via transportation and self-assembly. In: Proceedings of the IEEE 21st international conference on micro electro mechanical systems (MEMS), Tucson, AZ, USA, 2008

Hsu HY, Ohta AT, Chiou PY, Jamshidi A, Neale SL, Wu MC (2010) Phototransistor-based optoelectronic tweezers for dynamic cell manipulation in cell culture media. Lab Chip 10:165–172

Hu J, Lin S, Kimerling LC, Crozier K (2010) Optical trapping of dielectric nanoparticles in resonant cavities. Phys Rev A 82:053819

Hu W, Ohta AT (2011) Aqueous droplet manipulation by optically induced Marangoni circulation. Microfluid Nanofluid 11:307–316

Hu W, Ishii KS, Ohta AT (2011) Micro-assembly using optically controlled bubble microrobots. Appl Phys Lett 99:094103

Hu W, Fan Q, Ohta AT (2012a) An opto-thermocapillary cell micromanipulator. Paper presented at the 16th international conference on miniaturized systems for chemistry and life sciences, Okinawa, Japan, 28 Oct–1 Nov 2012

Hu W, Ishii KS, Fan Q, Ohta AT (2012b) Hydrogel microrobots actuated by optically generated vapour bubbles. Lab Chip 12:3821–3826

Hu W, Fan Q, Ohta AT (2013a) An opto-thermocapillary cell micromanipulator. Lab Chip 13:2285–2291

Hu W, Fan Q, Tonaki W, Ohta AT (2013b) Bubble-driven light-absorbing hydrogel microrobot for the assembly of bio-objects. Paper presented at the annual international conference of the ieee engineering in medicine and biology society, Osaka, Japan, 3–7 July 2013

Hu W, Fan Q, Ohta AT (2014) Interactive actuation of multiple opto-thermocapillary flow-addressed bubble microrobots. Robot Biomim 1:14

Huang KW, Wu YC, Lee JA, Chiou PY (2013a) Microfluidic integrated optoelectronic tweezers for single-cell preparation and analysis. Lab Chip 13:3721–3727

Huang KW, Su TW, Ozcan A, Chiou PY (2013b) Optoelectronic tweezers integrated with lens-free holographic microscopy for wide-field interactive cell and particle manipulation on a chip. Lab Chip 13:2278–2284

Huang L, Maerkl SJ, Martin OJ (2009) Integration of plasmonic trapping in a microfluidic environment. Opt Express 17:6018–6024

Huang SB, Chen J, Wang J, Yang CL, Wu MH (2012) A new optically-induced dielectrophoretic (ODEP) force-based scheme for effective cell sorting. Int J Electrochem Sci 7:12656–12667

Huang SB, Wu MH, Lin YH, Hsieh CH, Yang CL, Lin HC, Tseng CP, Lee GB (2013c) High-purity and label-free isolation of circulating tumor cells (CTCs) in a microfluidic platform by using optically-induced-dielectrophoretic (ODEP) force. Lab Chip 13:1371–1383

Hwang H, Choi YJ, Choi W, Kim SH, Jang J, Park JK (2008a) Interactive manipulation of blood cells using a lens-integrated liquid crystal display based optoelectronic tweezers system. Electrophoresis 29:1203–1212

Hwang H, Oh Y, Kim JJ, Choi W, Park JK, Kim SH, Jang J (2008b) Reduction of nonspecific surface-particle interactions in optoelectronic tweezers. Appl Phys Lett 92:024108

Hwang H, Park JK (2009) Rapid and selective concentration of microparticles in an optoelectrofluidic platform. Lab Chip 9:199–206

Hwang H, Lee DH, Choi W, Park JK (2009) Enhanced discrimination of normal oocytes using optically induced pulling-up dielectrophoretic force. Biomicrofluidics 3:014103
Ichikawa A, Arai F, Yoshikawa K, Uchida T, Fukuda T (2005) In situ formation of a gel microbead for indirect laser micromanipulation of microorganisms. Appl Phys Lett 87:191108
Ichikawa M, Ichikawa H, Yoshikawa K, Kimura Y (2007) Extension of a DNA molecule by local heating with a laser. Phys Rev Lett 99:148104
Jákl P, Arzola AV, Šiler M, Chvátal L, Volke-Sepúlveda K, Zemánek P (2014) Optical sorting of nonspherical and living microobjects in moving interference structures. Opt Express 22:29746–29760
Jamshidi A, Pauzauskie PJ, Schuck PJ, Ohta AT, Chiou PY, Chou J, Yang P, Wu MC (2008) Dynamic manipulation and separation of individual semiconducting and metallic nanowires. Nat Photonics 2:85–89
Jeorrett AH, Neale SL, Massoubre D, Gu E, Henderson RK, Millington O, Mathieson K, Dawson MD (2014) Optoelectronic tweezers system for single cell manipulation and fluorescence imaging of live immune cells. Opt Express 22:1372–1380
Jess PRT, Garcés-Chávez V, Smith D, Mazilu M, Paterson L, Riches A, Herring C, Sibbett W, Dholakia K (2006) Dual beam fibre trap for Raman microspectroscopy of single cells. Opt Express 14:5779–5791
Jonáš A, Zemánek P (2008) Light at work: the use of optical forces for particle manipulation, sorting, and analysis. Electrophoresis 29:4813–4851
Jones TB (1995) Electromechanics of particles. Cambridge University Press, Cambridge
Jubery TZ, Srivastava SK, Dutta P (2014) Dielectrophoretic separation of bioparticles in microdevices: a review. Electrophoresis 35:691–713
Katchinskiy N, Godbout R, Goez HR, Elezzabi AY (2014) Femtosecond laser-induced cell-cell surgical attachment. Lasers Surg Med 46:335–341
Kirkham GR, Britchford E, Upton T, Ware J, Gibson GM, Devaud Y, Ehrbar M, Padgett M, Allen S, Buttery LD, Shakesheff K (2015) Precision assembly of complex cellular microenvironments using holographic optical tweezers. Sci Rep 5:8577
Kovac JR, Voldman J (2007) Intuitive, image-based cell sorting using optofluidic cell sorting. Anal Chem 79:9321–9330
Kotz KT, Noble KA, Faris GW (2004) Optical microfluidics. Appl Phys Lett 85:2658
Kremer C, Witte C, Neale SL, Reboud J, Barrett MP, Cooper JM (2014) Shape-dependent optoelectronic cell lysis. Angew Chem Int Ed 126:861–865
Kumar A, Williams SJ, Wereley ST (2009) Experiments on opto-electrically generated microfluidic vortices. Microfluid Nanofluid 6:637–646
Kwon JS, Ravindranath SP, Kumar A, Irudayaraj J, Wereley ST (2012) Opto-electrokinetic manipulation for high-performance on-chip bioassays. Lab Chip 12:4955–4959
Lai HH, Quinto-Su PA, Sims CE, Bachman M, Li GP, Venugopalan V, Allbritton NL (2008) Characterization and use of laser-based lysis for cell analysis on-chip. J R Soc Interface 5:S113–S121
Landenberger B, Höfemann H, Wadle S, Rohrbach A (2012) Microfluidic sorting of arbitrary cells with dynamic optical tweezers. Lab Chip 12:3177–3183
Lau ANK, Ohta AT, Phan HL, Hsu HY, Jamshidi A, Chiou PY, Wu MC (2009) Antifouling coatings for optoelectronic tweezers. Lab Chip 9:2952–2957
Lau AY, Lee LP, Chan JW (2008) An integrated optofluidic platform for Raman-activated cell sorting. Lab Chip 8:1116–1120
Le Gac S, Zwaan E, van den Berg A, Ohl CD (2007) Sonoporation of suspension cells with a single cavitation bubble in a microfluidic confinement. Lab Chip 7:1666–1672
Leach J, Howard D, Roberts S, Gibson G, Gothard D, Cooper J, Shakesheff K, Padgett M, Buttery L (2009) Manipulation of live mouse embryonic stem cells using holographic optical tweezers. J Mod Opt 56:448–452
Lee GB, Wu HC, Yang PF, Mai JD (2014) Optically induced dielectrophoresis sorting with automated medium exchange in an integrated optofluidic device resulting in higher cell viability. Lab Chip 14:2837–2843

Lee KH, Lee KS, Jung JH, Chang CB, Sung HJ (2013) Optical mobility of blood cells for label-free cell separation applications. Appl Phys Lett 102:141911

Lee SH, Grier DG (2007) Holographic microscopy of holographically trapped three-dimensional structures. Opt Express 15:1505–1512

Li ZG, Liu AQ, Klaseboer E, Zhang JB, Ohl CD (2013) Single cell membrane poration by bubble-induced microjets in a microfluidic chip. Lab Chip 13:1144–1150

Liang H, Vu KT, Krishnan P, Trang TC, Shin D, Kimel S, Berns MW (1996) Wavelength dependence of cell cloning efficiency after optical trapping. Biophys J 70:1529–1533

Lim CT, Dao M, Suresh S, Sow CH, Chew KT (2004) Large deformation of living cells using laser traps. Acta Mater 52:1837–1845

Lin CC, Chen A, Lin CH (2008) Microfluidic cell counter/sorter utilizing multiple particle tracing technique and optically switching approach. Biomed Microdevices 10:55–63

Lin S, Schonbrun E, Crozier K (2010) Optical manipulation with planar silicon microring resonators. Nano Lett 10:2408–2411

Lin SJ, Hung SH, Jeng JY, Guo TF, Lee GB (2012a) Manipulation of micro-particles by flexible polymer-based optically-induced dielectrophoretic devices. Opt Express 20:583–592

Lin YH, Lee GB (2009) An optically induced cell lysis device using dielectrophoresis. Appl Phys Lett 94:033901

Lin YH, Chang CM, Lee GB (2009) Manipulation of single DNA molecules by using optically projected images. Opt Express 17:15318–15329

Lin YH, Yang YW, Chen YD, Wang SS, Chang YH, Wu MH (2012b) The application of an optically switched dielectrophoretic (ODEP) force for the manipulation and assembly of cell-encapsulating alginate microbeads in a microfluidic perfusion cell culture system for bottom-up tissue engineering. Lab Chip 12:1164–1173

Lincoln B, Schinkinger S, Travis K, Wottawah F, Ebert S, Sauer F, Guck J (2007) Reconfigurable microfluidic integration of a dual-beam laser trap with biomedical applications. Biomed Microdevices 9:703–710

Lindström S, Andersson-Svahn H (2010) Overview of single-cell analyses: microdevices and applications. Lab Chip 10:3363–3372

MacDonald MP, Spalding GC, Dholakia K (2003) Microfluidic sorting in an optical lattice. Nature 426:421–424

Maeda YT, Buguin A, Libchaber A (2011) Thermal separation: interplay between the Soret effect and entropic force gradient. Phys Rev Lett 107:038301

Mandal S, Serey X, Erickson D (2010) Nanomanipulation using silicon photonic crystal resonators. Nano Lett 10:99–104

Martín-Badosa E, Montes-Usategui M, Carnicer A, Andilla J, Pleguezuelos E, Juvells I (2007) Design strategies for optimizing holographic optical tweezers set-ups. J Opt A Pure Appl Opt 9:S267–S277

Maruyama H, Arai F, Fukuda T (2005) Microfabrication and laser manipulation of functional microtool using in-situ photofabrication. J Robot Mechatron 17:335–341

Maruyama H, Arai F, Fukuda T (2007) Gel-tool sensor positioned by optical tweezers for local pH measurement in a microchip. In: IEEE international conference on robotics and automation, Rome, Italy, 2007

Mishra A, Kwon JS, Thakur R, Wereley S (2014) Optoelectrical microfluidics as a promising tool in biology. Trends Biotechnol 32:415–422

Mudanyali O, Tseng D, Oh C, Isikman SO, Sencan I, Bishara W, Oztoprak C, Seo S, Khademhosseini B, Ozcan A (2010) Compact, light-weight and cost-effective microscope based on lensless incoherent holography for telemedicine applications. Lab Chip 10:1417–1428

Neale SL, Mazilu M, Wilson JIB, Dholakia K, Krauss TF (2007) The resolution of optical traps created by light induced dielectrophoresis (LIDEP). Opt Express 15:12619–12626

Neale SL, Ohta AT, Hsu HY, Valley JK, Jamshidi A, Wu MC (2009a) Trap profiles of projector based optoelectronic tweezers (OET) with HeLa cells. Opt Express 17:5232–5239

Neale SL, Fan Z, Ohta AT, Jamshidi A, Valley JK, Hsu HY, Javey A, Wu MC (2009b) Optofluidic assembly of red/blue/green semiconductor nanowires. In: Proceedings of the conference on lasers and electro-optics (CLEO), Baltimore, MD, USA, 2009

Neale SL, Mody N, Selman C, Cooper JM (2012) Optoelectronic tweezers for the measurement of the relative stiffness of erythrocytes. Proc SPIE 8458:845827

Neuman KC, Chadd EH, Liou GF, Bergman K, Block SM (1999) Characterization of photodamage to Escherichia coli in optical traps. Biophys J 77:2856–2863

Nikolskaya AV, Nikolski VP, Efimov IR (2006) Gene printer: laser-scanning targeted transfection of cultured cardiac neonatal rat cells. Cell Commun Adhes 13:217–222

Ohta AT, Chiou PY, Han TH, Liao JC, Bhardwaj U, McCabe ERB, Yu F, Sun R, Wu MC (2007a) Dynamic cell and microparticle control via optoelectronic tweezers. J Microelectromech Syst 16:491–499

Ohta AT, Chiou PY, Phan HL, Sherwood SW, Yang JM, Lau ANK, Hsu HY, Jamshidi A, Wu MC (2007b) Optically controlled cell discrimination and trapping using optoelectronic tweezers. IEEE J Sel Top Quantum Electron 13:235–243

Ohta AT, Jamshidi A, Pauzauskie PJ, Hsu HY, Yang P, Wu MC (2007c) Trapping and transport of silicon nanowires using lateral-field optoelectronic tweezers. In: Proceedings of the conference on lasers and electro-optics (CLEO), Baltimore, MD, USA, 2007

Ohta AT, Jamshidi A, Valley JK, Hsu HY, Wu MC (2007d) Optically actuated thermocapillary movement of gas bubbles on an absorbing substrate. Appl Phys Lett 91:074103

Ohta AT, Neale SL, Hsu HY, Valley JK, Wu MC (2008) Parallel assembly of nanowires using lateral-field optoelectronic tweezers. In: Proceedings of the IEEE/LEOS international conference on optical MEMs and nanophotonics, Freiburg, Germany, 2008

Ohta AT, Garcia M, Valley JK, Banie L, Hsu HY, Jamshidi A, Neale SL, Lue T, Wu MC (2010) Motile and non-motile sperm diagnostic manipulation using optoelectronic tweezers. Lab Chip 10:3213–3217

Ota S, Wang S, Wang Y, Yin X, Zhang X (2013) Lipid bilayer-integrated optoelectronic tweezers for nanoparticle manipulations. Nano Lett 13:2766–2770

Palumbo G, Caruso M, Crescenzi E, Tecce MF, Roberti G, Colasanti A (1996) Targeted gene transfer in eucaryotic cells by dye-assisted laser optoporation. J Photochem Photobiol B Biol 36:41–46

Pauzauskie PJ, Hsu HY, Jamshidi A, Valley JK, Pei SN, Wu MC (2010) Quantifying heat transfer in DMD-based optoelectronic tweezers with infrared thermography. Proc SPIE 7596:759609

Pethig R (2013) Dielectrophoresis: an assessment of its potential to aid the research and practice of drug discovery and delivery. Adv Drug Deliv Rev 65:1589–1599

Rahman MA, Cheng J, Fan Q, Ohta AT (2015a) Automated actuation of multiple bubble microrobots using computer-generated holograms. Proc SPIE 9494:94940G

Rahman MA, Cheng J, Ohta AT (2015b) Automated cooperative micro-assembly using multiple bubble microrobots. Paper presented at the 9th IEEE international conference on nano/molecular medicine and engineering, Honolulu, Hawaii, 15–18 November 2015

Rau KR, Guerra A III, Vogel A, Venugopalan V (2004) Investigation of laser-induced cell lysis using time-resolved imaging. Appl Phys Lett 84:2940–2942

Reichl MR, Braun D (2014) Thermophoretic manipulation of molecules inside living cells. J Am Chem Soc 136:15955–15960

Schneckenburger H, Hendinger A, Sailer R, Strauss WS, Schmitt M (2002) Laser-assisted optoporation of single cells. J Biomed Opt 7:410–416

Shah GJ, Ohta AT, Chiou EPY, Wu MC, Kim CJ (2009) EWOD-driven droplet microfluidic device integrated with optoelectronic tweezers as an automated platform for cellular isolation and analysis. Lab Chip 9:1732–1739

Shelby JP, Edgar JS, Chiu DT (2005) Monitoring cell survival after extraction of a single subcellular organelle using optical trapping and pulsed-nitrogen laser ablation. Photochem Photobiol 81:994–1001

Soltani M, Lin J, Forties RA, Inman J, Saraf SN, Fulbright R, Lipson M, Wang MD (2014) Nanophotonic trapping for precise manipulation of biomolecular arrays. Nat Nanotechnol 9:448–452

Soughayer JS, Krasieva T, Jacobson SC, Ramsey JM, Tromberg BJ, Allbritton NL (2000) Characterization of cellular optoporation with distance. Anal Chem 72:1342–1347

Steubing RW, Cheng S, Wright WH, Numajiri Y, Berns MW (1991) Laser induced cell fusion in combination with optical tweezers: the laser cell fusion trap. Cytometry 12:505–510

Stevenson DJ, Gunn-Moore FJ, Campbell P, Dholakia K (2010) Single cell optical transfection. J R Soc Interface 7:863–871

Tan WH, Takeuchi S (2007) A trap-and-release integrated microfluidic system for dynamic microarray applications. Proc Natl Acad Sci 104:1146–1151

Tan Y, Kong CW, Chen S, Cheng SH, Li RA, Sun D (2012) Probing the mechanobiological properties of human embryonic stem cells in cardiac differentiation by optical tweezers. J Biomech 45:123–128

Tanaka Y, Kawada H, Hirano K, Ishikawa M, Kitajima H (2008) Automated manipulation of non-spherical micro-objects using optical tweezers combined with image process. Opt Express 16:15115–15122

Tien MC, Ohta AT, Yu K, Neale SL, Wu MC (2009) Heterogeneous integration of InGaAsP microdisk laser on a silicon platform using optofluidic assembly. Appl Phys A Mater Sci Process 95:967–972

Tirlapur UK, Konig K (2002) Targeted transfection by femtosecond laser. Nature 418:290–291

Townes-Anderson E, St. Jules RS, Sherry DM, Lichtenberger J, Hassanain M (1998) Micromanipulation of retinal neurons by optical tweezers. Mol Vis 4:1–12

Tsampoula X, Garcés-Chávez V, Comrie M, Stevenson DJ, Agate B, Brown CTA, Gunn-Moore F, Dholakia K (2007) Femtosecond cellular transfection using a nondiffracting light beam. Appl Phys Lett 91:053902

Tsukakoshi M, Kurata S, Nomiya Y, Ikawa Y, Kasuya T (1984) A novel method of DNA transfection by laser microbeam cell surgery. Appl Phys B 35:135–140

Uchugonova A, König K, Bueckle R, Isemann A, Tempea G (2008) Targeted transfection of stem cells with sub-20 femtosecond laser pulses. Opt Express 16:9357–9364

Valentine MT, Guydosh NR, Gutierrez-Medina B, Fehr A, Andreasson JO, Block SM (2008) Precision steering of an optical trap by electro-optic deflection. Opt Lett 33:599–601

Valley JK, Jamshidi A, Ohta AT, Hsu HY, Wu MC (2008) Operational regimes and physics present in optoelectronic tweezers. J Microelectromech Sys 17:342–350

Valley JK, Neale S, Hsu HY, Ohta AT, Jamshidi A, Wu MC (2009) Parallel single-cell light-induced electroporation and dielectrophoretic manipulation. Lab Chip 9:1714–1720

Valley JK, Swinton P, Boscardin JW, Lue TF, Rinaudo PF, Wu MC, Garcia MM (2010) Preimplantation mouse embryo selection guided by light-induced dielectrophoresis. PLoS ONE 5:e10160

Valley JK, Pei SN, Jamshidi A, Hsu HY, Wu MC (2011) A unified platform for optoelectrowetting and optoelectronic tweezers. Lab Chip 11:1292–1297

van Loenhout MTJ, De Vlaminck I, Flebus B, Blanken JFD, Zweifel LP, Hooning KM, Kerssemakers JWJ, Dekker C (2013) Scanning a DNA molecule for bound proteins using hybrid magnetic and optical tweezers. PLoS ONE 8:e65329

Venugopalan V, Guerra A III, Nahen K, Vogel A (2002) Role of laser-induced plasma formation in pulsed cellular microsurgery and micromanipulation. Phys Rev Lett 88:078103

Vergucht E, Brans T, Beunis F, Garrevoet J, De Rijcke M, Bauters S, Deruytter D, Vandegehuchte M, Van Nieuwenhove I, Janssen C, Burghamme M, Vincze L (2015) In vivo X-ray elemental imaging of single cell model organisms manipulated by laser-based optical tweezers. Sci Rep 5:9049

Visscher K, Gross SP, Block SM (1996) Construction of multiple-beam optical traps with nanometer-resolution position sensing. IEEE J Sel Top Quantum Electron 2:1066–1076

Vogel A, Noack J, Hüttman G, Paltauf G (2005) Mechanisms of femtosecond laser nanosurgery of cells and tissues. Appl Phys B 81:1015–1047

Waleed M, Hwang S, Kim J, Shabbir I, Shin S, Lee Y (2013) Single-cell optoporation and transfection using femtosecond laser and optical tweezers. Biomed Opt Express 4:1533–1547

Wang CH, Lee YH, Kuo HT, Liang WF, Li WJ, Lee GB (2014) Dielectrophoretically-assisted electroporation using light-activated virtual microelectrodes for multiple DNA transfection. Lab Chip 14:592–601

Wang D, Bodovitz S (2010) Single cell analysis: the new frontier in 'omics'. Trends Biotechnol 28:281–290

Wang M, Orwar O, Olofsson J, Weber SG (2010a) Single-cell electroporation. Anal Bioanal Chem 397:3235–3248

Wang W, Lin YH, Wen TC, Guo TF, Lee GB (2010b) Selective manipulation of microparticles using polymer-based optically induced dielectrophoretic devices. Appl Phys Lett 96:113302

Wang X, Chen S, Kong M, Wang Z, Costa KD, Li RA, Sun D (2011) Enhanced cell sorting and manipulation with combined optical tweezer and microfluidic chip technologies. Lab Chip 11:3656–3662

Weinert FM, Braun D (2009) An optical conveyor for molecules. Nano Lett 9:4264–4267

Williams SJ, Kumar A, Green NG, Wereley ST (2010) Optically induced electrokinetic concentration and sorting of colloids. J Micromech Microeng 20:015022

Witte C, Kremer C, Chanasakulniyom M, Reboud J, Wilson R, Cooper JM, Neale SL (2014) Spatially selecting a single cell for lysis using light-induced electric fields. Small 10:3026–3031

Wu MC (2011) Optoelectronic tweezers. Nat Photonics 5:322–324

Wu TH, Teslaa T, Kalim S, French CT, Moghadam S, Wall R, Miller JF, Witte ON, Teitell MA, Chiou PY (2011) Photothermal nanoblade for large cargo delivery into mammalian cells. Anal Chem 83:1321–1327

Wu YC, Wu TH, Clemens DL, Lee BY, Wen X, Horwitz MA, Teitell MA, Chiou PY (2015) Massively parallel delivery of large cargo into mammalian cells with light pulses. Nat Methods 12:439–444

Würger A (2010) Thermal non-equilibrium transport in colloids. Rep Prog Phys 73:126601

Xie C, Dinno MA, Li Y (2002) Near-infrared Raman spectroscopy of single optically trapped biological cells. Opt Lett 27:249–251

Xie C, Li Y, Tang W, Newton RJ (2003) Study of dynamical process of heat denaturation in optically trapped single microorganisms by near-infrared Raman spectroscopy. J Appl Phys 94:6138–6142

Yang AHJ, Moore SD, Schmidt BS, Klug M, Lipson M, Erickson D (2009) Optical manipulation of nanoparticles and biomolecules in sub-wavelength slot waveguides. Nature 457:71–75

Yang SM, Yu TM, Huang HP, Ku MY, Tseng SY, Tsai CL, Chen HP, Hsu L, Liu CH (2011) Light-driven manipulation of picobubbles on a titanium oxide phthalocyanine-based optoelectronic chip. Appl Phys Lett 98:153512

Yang SM, Tseng SY, Chen HP, Hsu L, Liu CH (2013) Cell patterning via diffraction-induced optoelectronic dielectrophoresis force on an organic photoconductive chip. Lab Chip 13:3893–3902

Yeh J, Ling Y, Karp JM, Gantz J, Chandawarkar A, Eng G, Iii JB, Langer R, Khademhosseini A (2006) Micromolding of shape-controlled, harvestable cell-laden hydrogels. Biomaterials 27:5391–5398

Yin H, Wang MD, Svoboda K, Landick R, Bloc SM, Gelles J (1995) Transcription against an applied force. Science 270:1653–1657

Yuan L, Liu Z, Yang J, Guan C (2008) Twin-core fiber optical tweezers. Opt Express 16:4559–4566

Zarowna-Dabrowska A, Neale SL, Massoubre D, McKendry J, Rae BR, Henderson RK, Rose MJ, Yin H, Cooper JM, Gu E, Dawson MD (2011) Miniaturized optoelectronic tweezers controlled by GaN micro-pixel light emitting diode arrays. Opt Express 19:2720–2728

Zeira E, Manevitch A, Manevitch Z, Kedar E, Gropp M, Daudi N, Barsuk R, Harati M, Yotvat H, Troilo PJ, Griffiths TG, Pacchione SJ, Roden DF, Niu Z, Nussbaum O, Zamir G, Papo O, Hemo I, Lewis A, Galun E (2007) Femtosecond laser: a new intradermal DNA delivery method for efficient, long-term gene expression and genetic immunization. FASEB J 21:3522–3533

Zhao Y, Liang W, Zhang G, Mai JD, Liu L, Lee GB, Li WJ (2013) Distinguishing cells by their first-order transient motion response under an optically induced dielectrophoretic force field. Appl Phys Lett 103:183702

Zhao Y, Lai HSS, Zhang G, Lee GB, Li WJ (2014) Rapid determination of cell mass and density using digitally controlled electric field in a microfluidic chip. Lab Chip 14:4426–4434

Zhao Y, Lai HSS, Zhang G, Lee GB, Li WJ (2015) Measurement of single leukemia cell's density and mass using optically induced electric field in a microfluidics chip. Biomicrofluidics 9:022406

Zhong MC, Wei XB, Zhou JH, Wang ZQ, Li YM (2013) Trapping red blood cells in living animals using optical tweezers. Nature 4:1768

Acoustic Cell Manipulation

Andreas Lenshof, Carl Johannesson, Mikael Evander, Johan Nilsson and Thomas Laurell

Abstract This chapter reviews recent developments in the field of acoustic manipulation and processing of cells in microfluidic systems and gives an overview of different acoustofluidic operating modalities. Continuous flow-based acoustophoresis and acoustic trapping are key areas of interest. In view of the topic of this publication we have limited this chapter to mainly cover acoustofluidic work that concerns cell handling and cell-based studies. A focus is therefore maintained on developments that demonstrate how microscale acoustofluidic systems can be designed to solve unmet needs in the everyday work of life science laboratories related to cell biology or clinically relevant research.

Keywords Acoustophoresis · Acoustic trapping · Acoustic cell manipulation · BAW · SAW

1 Acoustophoresis

1.1 The Primary Acoustic Radiation Force

The acoustic radiation force, F^{rad}, on a compressible particle, much smaller than the acoustic wavelength, λ, was originally derived by Gorkov (1962), Eq. 1

$$\begin{aligned} F^{\text{rad}} &= -\nabla U^{\text{rad}} = -\nabla \frac{4\pi}{3} a^3 \left[f_1 \frac{1}{2} \kappa_0 \left\langle p_{\text{in}}^2 \right\rangle - f_2 \frac{3}{4} \rho_0 \left\langle v_{\text{in}}^2 \right\rangle \right] \\ f_1(\tilde{\kappa}) &= 1 - \tilde{\kappa} \quad \text{and} \quad \tilde{\kappa} = \frac{\kappa_{\text{p}}}{\kappa_0} \\ f_2(\tilde{\rho}) &= \frac{2(\tilde{\rho} - 1)}{2\tilde{\rho} + 1} \quad \text{and} \quad \tilde{\rho} = \frac{\rho_{\text{p}}}{\rho_0} \end{aligned} \tag{1}$$

A. Lenshof · C. Johannesson · M. Evander · J. Nilsson · T. Laurell (✉)
Dept. Biomedical Engineering, Lund University, P.O. Box 118, 221 00 Lund, Sweden
e-mail: Thomas.laurell@bme.lth.se

W. Lee et al. (eds.), *Microtechnology for Cell Manipulation and Sorting*,
Microsystems and Nanosystems, DOI 10.1007/978-3-319-44139-9_5

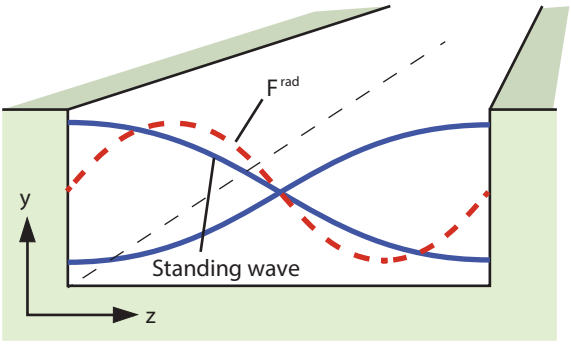

Fig. 1 Schematic of a 1D acoustic standing wave (*solid line*) across a microchannel (z-axis) and the resulting acoustic radiation force (*red dashed*) across the channel width

where U^{rad} denotes the acoustic radiation potential, a is the particle radius, f_1 and f_2 are the monopole and dipole scattering coefficients respectively, κ_0, ρ_0, κ_p and ρ_p are the compressibility and density of the fluid and particle, respectively, $\langle p_{\text{in}} \rangle$ and $\langle v_{\text{in}} \rangle$ are the time averages of the incoming pressure and velocity fields.

In the case of a 1D $\lambda/2$ standing wave (solid line) in a microchannel, Fig. 1, the acoustic radiation force (red-dashed line) in the direction of the wave propagation can be simplified, Eq. 2 (Bruus 2012).

$$\begin{aligned} F_z^{\text{rad}} &= -\partial_z U^{\text{rad}} = 4\pi\phi(\tilde{\kappa},\tilde{\rho})ka^3 E_{\text{ac}} \sin(2kz) \\ E_{\text{ac}} &= \frac{p_{\text{a}}^2}{4\rho_0 c_0^2} \\ \phi(\tilde{\kappa},\tilde{\rho}) &= \frac{1}{3}\left[\frac{5\tilde{\rho}-2}{2\tilde{\rho}+1} - \tilde{\kappa}\right] \end{aligned} \tag{2}$$

where $\phi(\tilde{\kappa},\tilde{\rho})$ is the acoustic contrast factor, k is the wave number ($2\pi/\lambda$), E_{ac} is the acoustic energy density, z is the position of the particle along the wave propagation axis, p_{a} is the pressure amplitude, ρ_0 is the density of the medium, c_0 is the speed of sound in the medium.

The acoustic radiation force, Eq. 2, acting on a particle in a standing wave field is balanced by the Stokes drag force, F_z^{drag}, Eq. 3,

$$F_z^{\text{drag}} = 6\pi a v_z \eta \tag{3}$$

where η is the dynamic viscosity of the suspending fluid and v_z is the particle velocity along the z-axis. Combining Eqs. 2 and 3 yields that the acoustophoretic particle velocity in an acoustic standing wave scales to the radius to the second power:

$$v_z = \frac{2}{3\eta}\phi(\tilde{\kappa},\tilde{\rho})ka^2 E_{\text{ac}} \sin(2kz) \tag{4}$$

Acoustophoresis is operated in two different modes in microfluidic systems: Bulk Acoustic Wave (BAW) or Surface Acoustic Wave (SAW). BAW systems are based

on material properties of the microfluidic system such that the microfluidic compartment (a cavity or a channel) defines a high Q-value acoustic resonator. The material properties are consequently selected from hard materials (e.g. silicon, glass, metal) that display a high difference in acoustic impedance between the fluid and channel walls, minimising energy loss from the resonant compartment. The resonance of the BAW resonators is defined by the dimensions of the resonant cavity and resonance is accomplished by actuating the bulk material at a frequency that matches the dimensions of the channel width at $N \times \lambda/2$. Resonance can thus be accomplished in any direction where a resonance criterion can be fullfiled independent of where the transducer is mounted on the chip. A more detailed survey of how BAW systems can be designed is found in Lenshof et al. (2012).

SAW systems are based on interdigital metal electrode transducers, microfabricated on a piezoelectric substrate, where the interdigital distance defines the frequency of operation. In microfluidic system often two opposing SAW transducers are fabricated on the substrate and a microchannel is positioned between the two transducers. The microchannel is commonly made in a polymer and PDMS is the most frequently reported material. When driving the transducers two counter propagating waves are generated that interfere and compose a standing wave. As the surface acoustic waves reach the PDMS interface and the fluid in the channel the acoustic wave is refracted into the microchannel where acoustic standing wave forces, analogous to BAW systems, can be utilised for cell manipulation. The location of the nodes in the standing wave is dependent of the phase shift of the two transducers and the microchannel have to be aligned with high precision to maintain the nodal positions along the channel length. Likewise, by altering the phase between the two transducers the node location can be arbitrarily localized within the channel. BAW-based resonators accomplish higher acoustic amplitudes than SAW devices since the resonator dissipates less energy to the surrounding material and hence commonly higher flow rates in cell separation applications are reported.

A comprehensive review on surface-based acoustofluidics can be found in Yeo and Friend (2014). Acoustophoresis performed by BAW or SAW have been shown not to influence cell viability, function and proliferation capacity. The readers are referred to Burguillos et al. (2013) and Wiklund (2012) for further reading regarding viability aspects in acoustophoresis-based processing of cells.

1.2 Separation

Acoustophoresis in microfluidic systems is commonly performed in well-defined acoustic standing wave resonators to enable controlled migration/transport of cells or particles in suspension by means of the acoustic radiation force. Extensive work has been done in this field to further the understanding of how acoustic forces can be utilised for microparticle manipulation and processing of biological matter, more specifically cell suspensions. Earlier work done in this area was predominantly

performed on macroscale multinode-layered acoustic resonators utilising the possibility to focus cells in nodal planes in a travelling standing wave configuration (Peterson et al. 1986), demonstrating plasma separation from whole blood at flow rates of 2 mL/min. Multinode macroscale acoustic resonators were also developed for the retention and noncontact filtering of cells in fermentation suspensions (Gröschl et al. 1998) and were later commercialized. An extensive review of multimode resonators for cell and particle manipulation is given (Hawkes and Radel 2013) and recent reports describe technology developments for increasing throughput in sedimentation-based multinode ultrasonic filters (Prest et al. 2015).

One of the first reports on microfabricated devices utilising acoustic standing wave forces for cell manipulation was reported by Hawkes et al. (2004) in a silicon microfabricated Field-Flow-Fractionation (FFF) device designed as an H-filter. The work was preceded by several developments steps of manifolds manufactured by conventional machining as well as microfabrication (Hawkes and Coakley 2001; Harris et al. 2003). In a sample stream of yeast cells suspended in a fluorescent medium, the yeast cells were efficiently transferred into a co-flowing stream of a clean buffer by means of an acoustic standing wave field, Fig. 1. The system reported a significant throughput of 10 mL/min while reducing the fluorescein background to 20 %. The high throughput was accomplished by the plate like design of the H-filter, having a width of the co-flowing streams of 10 mm, which is possible when a layered resonator design is selected. Most interestingly in this work Hawkes also demonstrated that efficient mixing could be accomplished in this layered resonator design when actuating the device at elevated acoustic amplitudes, stating that acoustic streaming was the major source for mixing. The phenomena of acoustic streaming has since gained increased attention (Bengtsson and Laurell 2004; Muller et al. 2012, 2013; Lei et al. 2013, 2016).

Simultaneous developments of microchip-based acoustic cell handling devices were done by the group of Laurell where the design of $\lambda/2$ resonators were done in-plane with the silicon chip (Nilsson et al. 2004), which simplified the further routing of the different sample fractions on-chip to individual outlets or downstream chip integrated unit operations. By exciting the microchannel at its resonance frequency the standing wave was accomplished in a direction orthogonal to the incoming vibration of the piezo electric element, establishing the transversal mode of operation (Lenshof et al. 2012). The first acoustic microchip-based separation involving human cells was the separation of red blood cells from lipid particles (Petersson et al. 2004). Here the need for elimination of lipid microemboli from shed blood during open heart surgery prior to reinfusion to the patient was the goal. The separation of the lipid emboli from the blood cells was successful due to the fact that RBCs and lipid particles displayed different sign of the acoustic contrast factor, forcing the positive contrast factor RBCs to go to the pressure node and the centre outlet while the negative contrast factor lipid particles migrated to the pressure antinode and exited the system through the side outlets, Fig. 2. In order to increase system throughput the group also demonstrated system upscaling by realising an eight parallel channel acoustic lipid/blood cell separator (Jönsson et al. 2004), first presented at the MicroTAS conference 2002 (Nilsson et al. 2002), Fig. 2e–f.

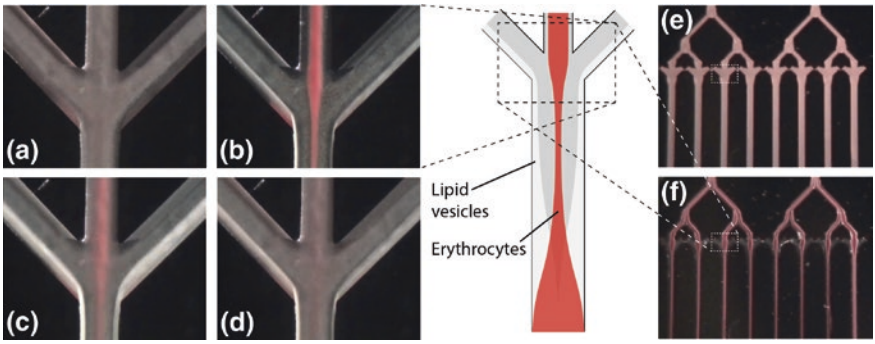

Fig. 2 **a** A mixture of blood and cream without ultrasound, **b** ultra sound active and RBCs (positive acoustic contrast factor) are focused in the centre and lipid vesicles (negative acoustic contrast factor) are seen as a white stream along the side walls, **c** ultrasound just deactivated, **d** ultrasound deactivated but remaining lipid are still exiting the system. **e** eight parallel channel separator for increased throughput—ultrasound inactive, **f** eight parallel channel ultrasound active

The separation of particles with negative acoustic contrast factor and cells (with positive contrast factor) was later exploited by Grenvall et al. developing a system for separating lipid particles from raw milk product (Grenvall et al. 2009). The aim was to clarify the solution and enable somatic cell enumeration without additional chemical steps of dissolving the lipid vesicles, labelling and centrifugation, which is otherwise necessary of the somatic cell counting in raw milk (Grenvall et al. 2012).

By manipulating the acoustic properties of the carrier medium, it is possible to create conditions where cells/particles that normally have acoustic contrast factor of the same sign, to have either opposite signs or that display differently altered acoustic contrast factors for the target species to be separated. This was done by adding caesium chloride to the carrier buffer (Petersson et al. 2007), creating a condition where two polymer particle types (3 μm polystyrene and 3 μm polymethylmethacrylate) that were inseparable in water could be separated in the modified carrier medium. In the same experimental set-up, Fig. 3, it was also shown that the acoustophoretic separation of a mixture of red blood cells and platelets in saline solution (0.9 g/mL) was vastly improved by adding caesium chloride to the central buffer flow, thereby changing the relative acoustophoretic mobility of the platelets relative the red blood cells.

The option to modify the acoustic properties of the suspending medium to enhance acoustophoretic separations has recently been explored by Augustsson et al. (2016a), establishing iso-acoustic focusing as a new acoustophoretic mode of operation. A cell or a particle will only migrate in an acoustic standing wave field if the acoustic contrast factor is non-zero. By establishing a gradient acoustic contrast factor profile (by generating a density gradient of Iodixanol across the channel width) in a perfused microchannel operated as a $\lambda/2$ acoustic resonator, cells will migrate lateral versus flow until the cells reach their iso-acoustic

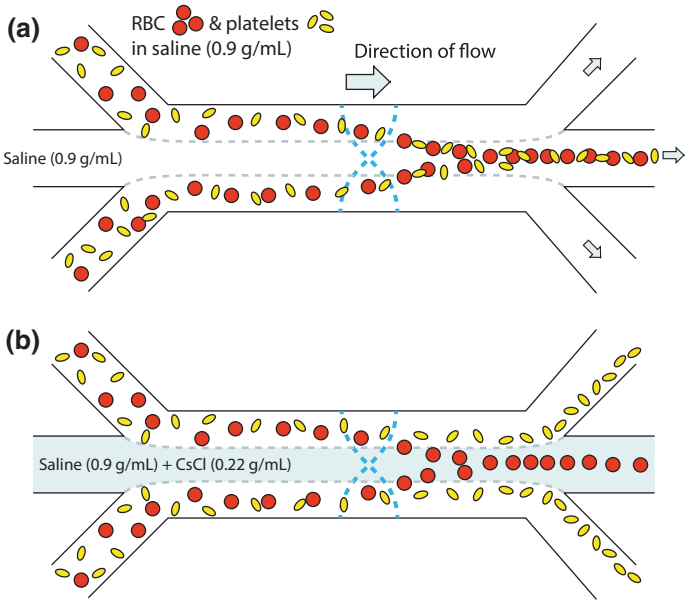

Fig. 3 Schematic of acoustophoretic separation of red blood cells from platelets. Without modifying the central inlet carrier buffer separation was not successful (**a**). By modifying the acoustic contrast factor for the two cell types in the central buffer with an addition of caesium chloride (0.22 g/mL) the two species were separated (**b**) (Petersson et al. 2007)

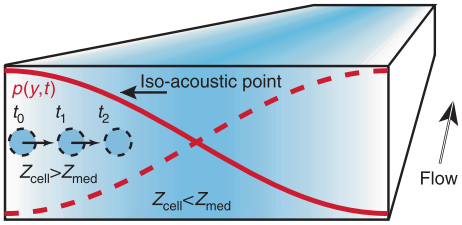

Fig. 4 Principle of iso-acoustic focusing as described by Augstsson et al. (2016a, b), where cells will migrate to the position in the density media gradient with a zero acoustic contrast factor. Reproduced with permission from Nature Communication

point, i.e. they will localise to a position in the density gradient buffer where the cells experience a zero acoustic radiation force (Fig. 4). The lateral position in the channel will thus be an index of the acoustic contrast factor and most importantly the discrimination between different cell types are independent of cell size, which otherwise is a major factor in conventional acoustophoresis systems. Augustsson showed in his work that iso-acoustic focusing can, e.g. discriminate between different subpopulations of white blood cells (neutrophils, monocytes and lymphocytes).

While the binary separation of target cells with different acoustic contrast factor signs would be an ideal way of separation, most separation relies on the fact that the primary acoustic radiation forces scales with the volume of the cell, i.e. larger cells move faster towards the pressure node than smaller cells, Eq. 4. By tuning the flow rate and flow splitter ratios, it is possible to achieve separation by dividing the outlet flow into different fractions before all cells have reached the pressure node, this mode of operation is called Free Flow Acoustophoresis (FFA), Fig. 5.

Petersson et al. (2007) showed microchip FFA in a set-up with four outlets demonstrating discrimination between 2, 5, 8 and 10 μm polystyrene beads and subsequently also showed that white blood cells (WBC), red blood cells (RBC) displayed significantly different distribution across the four outlets when suspended in medium with caesium chloride added (0.22 g/mL).

Size separation by FFA was later also reported by Thevoz et al. (2010) who used acoustophoresis for cell phase synchronisation of mammalian cells, demonstrating an enrichment of cells in the G1 phase of the cell cycle from 54 to 84 %. In a similar set-up Dykes et al. (2011) investigated acoustophoretic separation of platelets from peripheral blood progenitor cells (PBPC) generated by leukapheresis from healthy donor blood. Since too high platelet counts in the PBPC product may compromise the subsequent MACS (magnetic bead-based extraction) separation of CD34+ cells and thereby also the entire therapeutic procedure, a reduction of the platelets is a generic need in the clinical procedure. The goal of the project was therefore to develop a system that could deplete the PBPC product from platelets without any bias of the PBPC cell population, and thereby open a route to facilitate the subsequent step of MACS separation of hematopoietic stem cells.

The separation performance of FFA as outlined by Petersson et al. inherently suffers from the fact that cells are spatially distributed in a sample stream of varying flow velocity when they enter the acoustophoretic separation zone. In doing so they will display a varying retention time in the acoustophoretic force field, resulting in a lateral migration that reflects the Poiseuille flow profile as well as the intrinsic acoustophoretic mobility of a specific cell type, Fig. 6a. Based on the

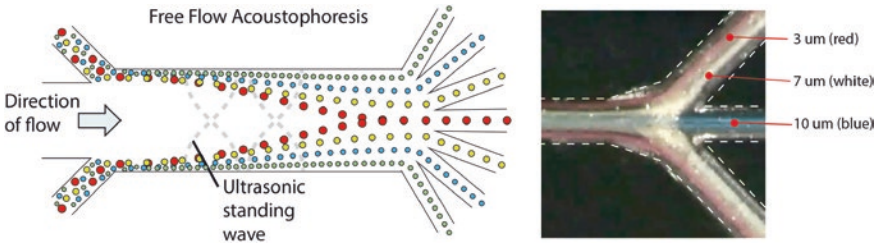

Fig. 5 Schematic of microchip-based Free Flow Acoustophoresis (FFA) where particles entering the separation channel are laminated against the side wall by the central buffer and subsequently migrates towards the channel centre at a rate that is dependent of the particle size, compressibility and density (Petersson et al. 2007). *Inset image* (*right*) shows the original separation of 3, 7 and 10 μm poly styrene particles in water

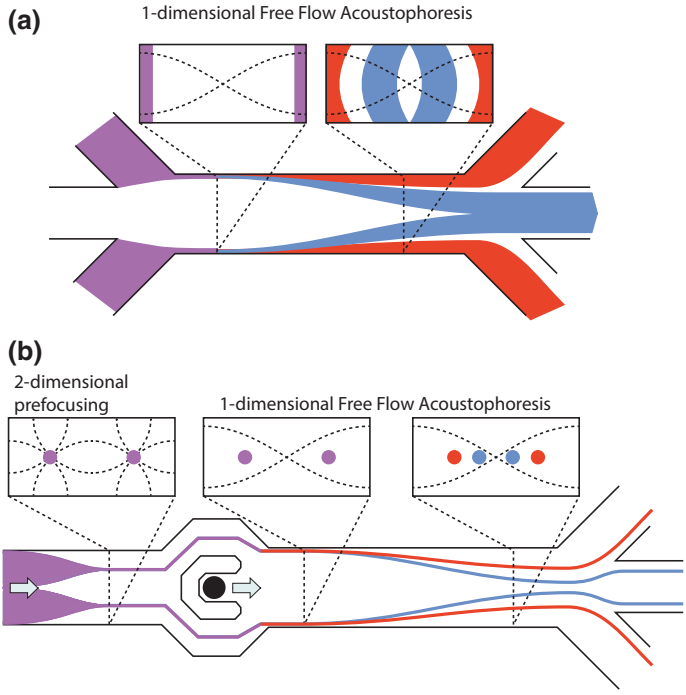

Fig. 6 Free Flow Acoustophoresis (FFA) as originally presented by Petersson et al. (2007) (**a**) and in the improved version encompassing a 2D prefocusing step to reduce lateral dispersion during the acoustophoretic migration (**b**). The difference in band broadening between the two particle fractions (*red* and *blue*) are schematically given

known fact that CTC on an average display a larger average cell size Augustsson et al. presented a study where the basic FFA set-up, Fig. 6a, was used to separate tumor cells from WBC. Initial FFA separations of prostate cancer tumor cell lines (DU145, PC3 and LnCAP) spiked into blood also gave clear evidence that FFA can provide significant enrichment factors of tumor cells in a white blood cell background, recovering >90 % of the tumor cells while discarding >90 % of the WBC (Augustsson et al. 2016b). However, a reduction of the WBC content should preferably be in the range of three orders of magnitude while having a tumor cell recovery of ≥90 % in order to bring the tumor cell/WBC ratio to a level where downstream analytical technologies can assess the tumor cell burden in a clinical sample.

In order to alleviate the dispersion in the FFA separations of the WBC and tumor cells due to the parabolic flow profile Augustsson et al. (2012a, b) introduced an acoustophoretic prefocusing step, where cells were focused in two dimensions in the channel cross-section prior to entering the main acoustophoretic separation channel, Fig. 6b.

A significantly improved separation was thereby accomplished reporting a tumor cell recovery of 93.6–97.9 % and a purity of 97.4–98.4 % when working with a model system of approximately of WBC levels ranging between 1.5×10^5 and 3×10^6 cells/mL) and tumors cells (2.5×10^5 cells/mL) and a sample flow rate of 70 μL/min.

Antfolk et al. (2015a) later simplified the 2D prefocusing system by removing the wash buffer inlet, solely relying on the acoustic prealignment for the preprocessing of the cells before the main separation. The prefocusing channel was 310 μm wide supporting a 4.35 MHz full wavelength resonance while the separation channel, 375 μm wide, was operated at a λ/2 resonance of 2 MHz, Fig. 7.

At a sample flow rate of 100 μL/min a tumor cell recovery of 86.5 ± 6.7 % was obtained while removing 98.9 % of the white blood cells. The 1:10 diluted RBC lysed WBC sample (≈5×10^5 WBC/mL) was spiked with 5×10^4 prostate cancer cells/mL (DU145). In this report Antfolk also demonstrated that the separation between two species can be optimized by ensuring that the total flow rate, outlet flow split ratio and the acoustic energy is matched such that the two fractions to be separated reach the outlet flow splitter when the distance between the two cell streamlines is at maximum, Fig. 8. When two cell types with differing acoustophoretic mobility undergo acoustophoresis a maximum in the distance between the two species can be found since the acoustic force varies sinusoidally across the channel width with a maximum of a ¼ channel width and zero force at the side wall and in the channel centre, Fig. 1. Figure 8a shows the trajectories for two cell types where the acoustic energy is too high and all cells end up in the central fraction. The trajectories, however, display a maximum separation at the location indicated in Fig. 8a. By lowering the acoustic energy and setting the outlet flow rates Φ_1 and Φ_2 such that the midpoint in the maximum separation of the trajectories arrives at the flow split point at the outlet, we translate the optimum separation of the cell trajectories to the outlet flow splitter, Fig. 8b. Antfolk showed with modelling data that for particles of similar acoustic properties where size is the

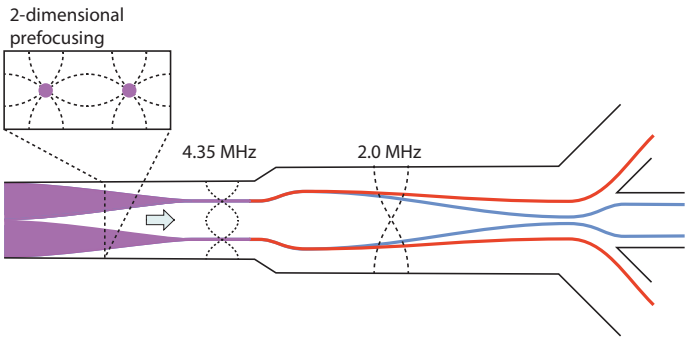

Fig. 7 Schematic of the single inlet acoustophoretic tumor cell separation chip with a 2D prefocusing step followed directly by a half-wavelength acoustophoretic separation of the tumor cells from the WBC

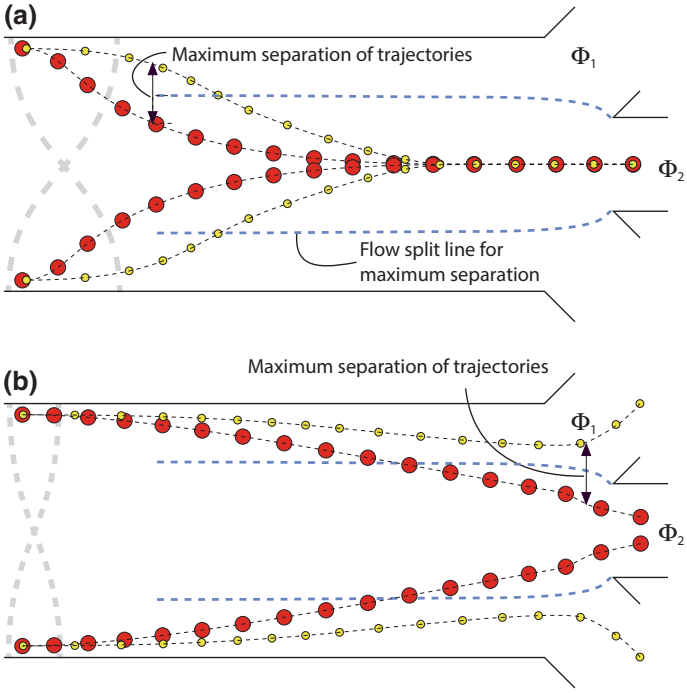

Fig. 8 Schematic of the optimisation of FFA separations where the flow rates are adapted such that the flow splitter divides the sample stream at the point of maximum separation of the species to be separated

main discriminating factor an outlet flow split ratio of side (left + right) to centre of about 75:25 provides optimum separation conditions for 375 μm wide resonators. This was also shown to agree well with experimental data on separation of tumor cells spiked into WBC.

To further integrate unit operations into the tumor cell acoustophoresis system developed by Antfolk, a downstream concentration step was also integrated on the chip version with sheath flow. The rare cell separation product is commonly very dilute after the initial separation, and by increasing the concentration of the final processed product, analysis is facilitated and can be performed faster (Antfolk et al. 2015b). At a sample input flow rate of 100 μL/min, breast cancer cells (MCF7) spiked into red blood cell-lysed human blood were recovered at 92 % with a contamination of 0.6 % of the white blood cell component while simultaneously accomplishing a 24-fold concentration of the final separation product (Fig. 9).

Acoustophoretic tumor cell separations have also been performed on SAW devices. Instead of using standard transducer configurations where two opposing SAW-transducer, orthogonal to flow, define the resonance conditions, Li et al. (2015a) reported a tilted-angle standing surface acoustic wave (taSSAW)

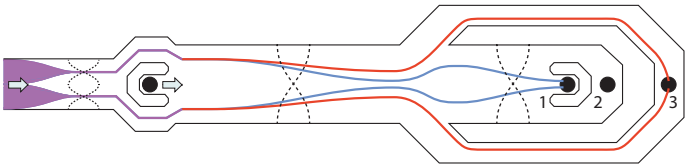

Fig. 9 Schematic of the 2D-prefocusing tumor cell separation system with an integrated enrichment step. The tumor cell fraction is obtained in outlet 1 and the WBC fraction exits through outlet 3. The refocusing of the tumor cells after the WBC/tumor cell flow splitter enables removal of a cell-free fraction to outlet 2, providing a concentration of the tumor cell fraction in outlet 1

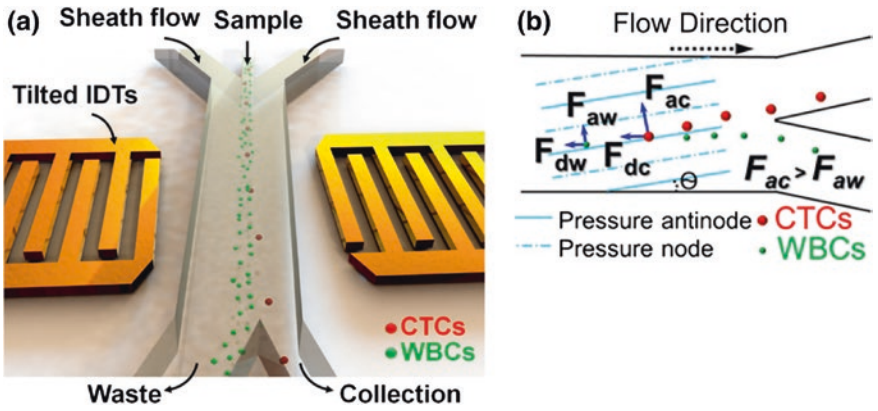

Fig. 10 Schematic of the tilted-angle SAW system for tumor cell separations as presented by Li et al. (2015a). Reproduced with permission from PNAS

transducer that enhanced the migration distance of cells in the sound field compared to the standard SAW configuration (Fig. 10). In order to reduce dispersion, the sample was hydrodynamically focused by a sheath flow from the sides but not in the vertical direction. The increased migration distance improved the separation performance as compared to the standard SAW configuration, reporting a spiked cancer cell recovery rate >83 % (83–96 %) while removing ~90 % of the WBC at a sample input flow rate of 20 μL/min. The sample concentration was in the range of 3–6 × 10^6 cell/mL and the tumor cell spiking ratio was in the range of 1:10^4, tumor cells:WBC.

Multiple outlet FFA with 2D-acoustic prefocusing has also been reported. Grenvall et al. (2015) presented a unilateral acoustophoresis system where cells after prefocusing were laminated to the side wall by a sheath buffer. Figure 11 shows the schematic set-up of the system and colour insert confocal images show the 2D prefocusing and the fluorescent images at outlet 2, 3 and 4 display the separation of 3, 7 and 10 μm polystyrene particles at the corresponding outlets. The system was employed to separation of white blood cell subpopulations: lymphocytes, monocytes and granulocytes. The input sample was prepared from RBC

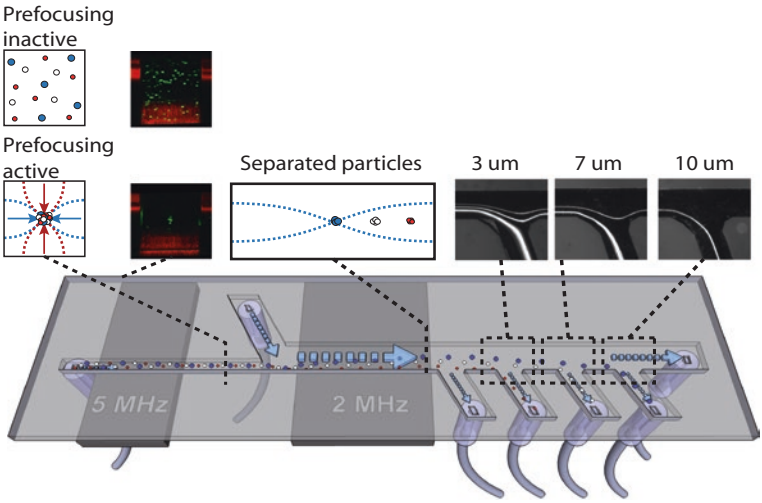

Fig. 11 Schematic set-up of a unilateral 2D-FFA system for separation of white blood cell subpopulations as presented by Grenvall et al. (2015)

lysed whole blood and the WBCs were paraformaldehyde fixed and labelled prior to acoustophoretic separation at a cell concentration of 10^6 cells/mL. Input flow rate was 8 μL/min and primarily limited by the short prefocusing channel, not providing a sufficiently focused cell stream at elevated flow rates before entering the separation zone. Collected sample aliquotes were subsequently analysed by flow cytometry. Lymphocytes with the lowest acoustophoretic mobility were collected at outlet 2 with a purity of 95.1 % and a recovery of 86.5 %. Granulocytes were collected from outlet 4 with a purity of 98.5 % and at recovery of 68.4 %. The monocyte fraction was recovered from outlet 3 at a recovery of 83.1 % and a purity of 25 %.

If cells have similar acoustophoretic mobilities as reported by Grenvall et al. (2015) in the case of the overlapping distributions in the monocyte fraction or if the target species displays a low acoustophoretic mobility, either due to a low acoustic contrast factor or simply a small size, there is still a possibility to achieve separation. Using affinity beads, an antibody specific bead will bind to the target cells and the bead-cell complex will then acoustically differ significantly from the non-bead bound cells and separation will be possible to perform.

This was first demonstrated by Persson et al. (2008) in a study where a subpopulation of bacteriophages was isolated from a phage display library. Bacteriophages are too small to be efficiently focused in a standard 2 MHz acoustophoresis channel. The study targeted a bacteriophage population that expressed a specific antibody on its surface. By incubating the phage library with an antigen-activated bead, specific for the antibody expressed on the target phage population, the obtained bacteriophage-bead complex could be isolated by acoustophoresis using the standard set-up described in Fig. 3a. By integrating two serially

connected acoustophoresis units a high purity of the affinity-bead bound bacteriophage was achieved, Fig. 12. Enrichment factors of the target bacteriophage varied between log 3 and log 4.

In a similar set-up, Lenshof et al. (2014), demonstrated the separation of white blood cell subpopulations by incubating a mono nuclear cell (MNC) fraction, from peripheral blood progenitor cell (PBPC) apheresis products, with 4.2 μm CD4+ Dynabeads™ to specifically target the CD4+ population in the MNC product, Fig. 13. The acoustophoretic separation utilized the 2D-prefocusing acoustophoresis system developed by Augustsson et al. (2012a, b) and separation data was benchmarked versus the corresponding standard magnetic bead-based separation. A cell concentration of 10^7 MNC/mL was used. The sample input flow rate was 30 μL/min and the central buffer flow was set to 60 μL/min. Targeted CD4+ lymphocytes were acoustically isolated with a mean purity of 87 ± 12 %, compared with 96 ± 3 % for the magnetic reference separation. The acoustophoretic separation displayed a recovery of cells in the target outlet, as measured across all outlets, of 65 ± 22 % while the corresponding magnetic separation displayed a slightly lower recovery of 56 ± 15 %. The acoustic and the magnetic separation

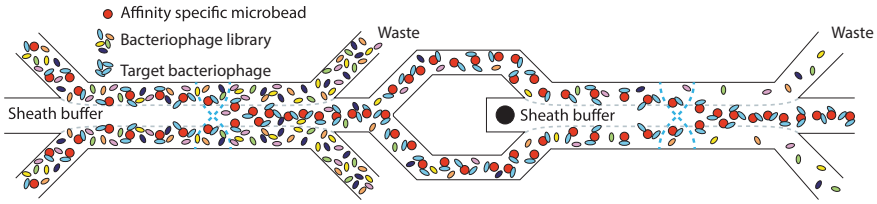

Fig. 12 Schematic of the two step affinity-bead acoustophoresis system that Persson et al. (2008) used for target specific bacteriophage purification from phage display laboratories, see also photograph in Fig. 19a

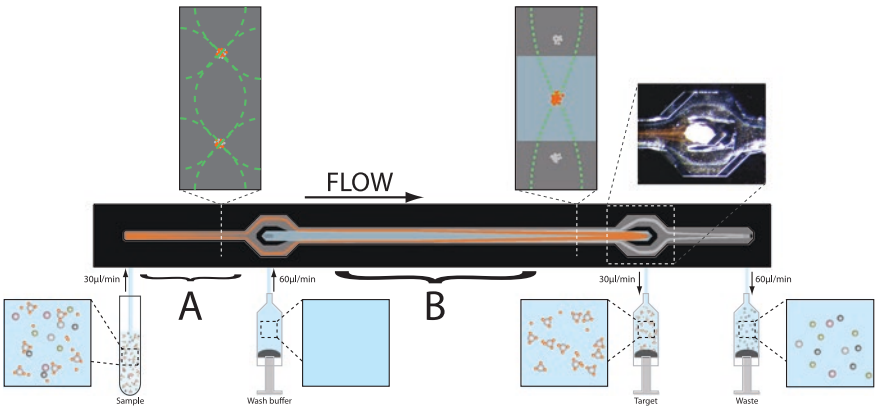

Fig. 13 Schematic set-up for affinity-bead-mediated cell separation as presented in Lenshof et al. (2014) Reproduced with permission from John Wiley and Sons

displayed post separation viabilities of 95 ± 4 and 97 ± 3 % respectively. In a follow up study by Urbansky et al. (2016), a more rare cell population was targeted using the same acoustophoretic set-up, extracting CD8+ cells from an MNC population with a mean purity of 91 ± 8 % and a median recovery in the target outlet of 63 % (measured across the outlets) as compared to 91 ± 14 % purity and a median recovery of 29 % for the magnetic separation.

Park et al. used the same prefocusing set-up in a system where target specific aptamers were selected from a large oligonucleotide library of a 10^{14} random single strand DNA. The target protein PSA (Prostate Specific Antigen) was immobilized on 2.8 μm Dynabeads M-280 and incubated with the oligonucleotide library. The beads with bound aptamers were transferred into the clean buffer stream, discarding the major fraction of unbound aptamers. The recovered bead bound aptamer fraction then followed the standard SELEX protocol of amplification and three repeated incubation rounds with acoustophoretic purifications, whereafter the obtained aptamer sub-library was incubated with microbeads activated with counter targets, i.e. the most abundant proteins in blood, to eliminate enrichment of PSA specific aptamers that display a cross affinity to HSA, IgG and fibrinogen. The resulting acoustic SELEX procedure yielded seven PSA binding aptamers of which the best displayed a PSA specific dissociation constant of 0.7 nM.

The 2D prefocusing acoustophoresis platform has also proven beneficial in several recent cell separation applications. Zalis et al. (2016) reported an investigation where viable cell populations were separated from apoptotic or dead cells in an analogous manner as presented by Yang and Soh (2012) but now also using the prefocusing step for improved separation. Separations of mixed suspensions of viable and non-viable populations of human embryonic stemcells, neuroblastoma cells and cancer cells (MCF7) were investigated and different means of inducing cell death were studied encompassing exposure to dimethyl sulfoxide, staurosporine, osmotic shock or starvation. The separation conditions could be tuned depending on the requirements on purity and recovery of viable cells and typically purities of ≈90 % with recoveries varying between 50 and 75 % depending on the cell death induction mechanism was obtained.

In a different study Park et al. (2016a, b) used the same 2D-prefocusing acoustophoresis platform to separate and enrich algae, *Euglena gracilis*, from pond water containing a variety of other algae and microparticles. A recovery of ≈93 % and a 13 fold enrichment of the *E. gracilis* versus background at an impressive sample input flow rate of 500 μL/min.

1.3 Sorting

Cell sorting is defined as actively identifying and decision-making to collect of individual target cells in a mixed population. Acoustic sorting of cells and particles into a designated target fraction was initially investigated by Johansson et al. (2009). The system comprised a glass microfabricated channel sealed on top of a

PCB substrate with integrated acoustic transducers, Fig. 14a. The sample and the sheath flow used in the system were given different densities such that upon activation of the ultrasonic transducer, the acoustic radiation force acting on the fluid interface produced a lateral movement of the fluid fraction with the particle to be sorted. The deflected sample volume thereafter followed a different flow stream than the non-actuated stream of particles. The device showed a sorting performance of 27 cells/s.

An improved acoustophoretically driven sorter was presented by Jakobsson et al. (2014a). By introducing a 2D acoustic prefocusing step, it was assured that all particles were positioned in the same flow vector and thus having the same velocities and retention times, Fig. 14c. As in all high-performance cell sorters prefocusing in the same flow vector is a prerequisite and in terms of acoustophoretic sorters, positioning the particle to be sorted where the acoustic radiation force is at its maximum is optimal. This was accomplished by prefocusing the cells at ¼ channel width from the channel wall when the cells entered the switching λ/2 resonator. Having an initial sample purity of 19 % and an event rate of 150 particles/s the resulting sort purity was ≈71 % with a recovery of 93 %.

Nawaz et al. (2015) used an inertial flow-based prealignment of the particles followed by a standing surface acoustic wave (SSAW) based system for deflecting the target cells into the sort output stream, Fig. 14b. At a 150 μs SAW-bursts and an event rate of 1200 particles/s yielded a purity of 93 % sorting labelled HeLa cells from unlabelled cells with a starting purity of 51 %.

Although not relying on acoustic forces acting on the cells it is worth mentioning that Franke et al. (2010) proposed a SAW-based cells sorting device where a travelling surface wave actuated a hydrodynamically focused sample stream such that acoustic streaming was induced orthogonal to the sample flow and translated the target cell volume to the target outlet.

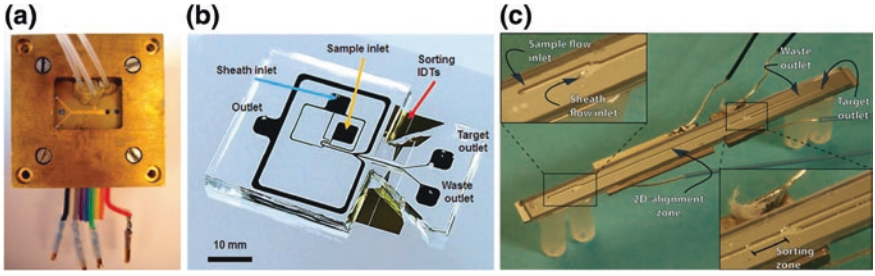

Fig. 14 **a** Sorting device used by Johansson et al. comprised a glass device with microchannels assembled on a PCB substrate with integrated acoustic transducers. Reprinted with permission from Johansson et al. (2009). Copyright (2009) American Chemical Society. **b** Sorter from Nawaz et al. where a PDMS chip containing the fluidics was placed on a SAW actuated LiNb piezoelectric substrate. Reprinted with permission from Nawaz et al. (2015). **c** Acoustic prefocusing and BAW driven fluorescence activated sorter in silicon glass with the piezotransducers glued to the backside used by Jakobsson et al. Reprinted from Jakobsson et al. (2014a) with permission from the Royal Society of Chemistry

1.4 Focusing, Orientation and Cytometry

Following the early work on BAW focusing in planar microfluidic devices (Hawkes et al. 2004; Nilsson et al. 2004; Petersson et al. 2004; Jönsson et al. 2004), Goddard and Kaduchak (2005) reported particle focusing in the centre of a cylindrical soda lime glass tube with an I.D. of 2.2 mm, operated at a resonance of 420 kHz, Fig. 15. This work was later developed to the first application of acoustic particle and cell focusing in flow cytometry (Goddard et al. 2007), reporting side scatter a CV of 7.8 % and fluorescence VC of 2.5 % from 10-μm Flow-Check fluorescent microspheres. A key advancement this work was the elimination of the sheath fluid commonly needed in flow cytometry to locate the cell precisely in the optical interrogation path of the cytometer. Although this first study did not perform cytometric evaluation of cells in the system CHO-K1 cells were run through the system to evaluate impact of the microfluidic and acoustic cell exposure. Unimpaired cell viability was shown after acoustic focusing. The cylindrical cell focusing approach was later commercialised: Attune™, Thermo Scientific.

Further development on the theme of acoustophoretic flow cytometry has been pursued by the group of Stephen Graves. Investigations encompassed microfabricated devices in silicon with rectangular cross-sections. It was shown that cytometric throughput could be vastly increased by operating 13 parallel focusing channels (Austin Suthanthiraraj et al. 2012), analogous to the blood lipid separator by Jönsson et al. (2004), Fig. 2, however each channel here supported a 3λ/2 resonance totally generating 39 parallel cytometry streams. Further work from the group demonstrated acoustophoretic parallel stream focusing and high throughput cytometric analysis, providing analysis rates >50,000/s (Piyasena et al. 2012). In this work, a 1.6 cm wide channel was operated at 1.54 MHz generating 33 parallel streams and focusing performance was estimated to have a CV of 15 %, Fig. 16.

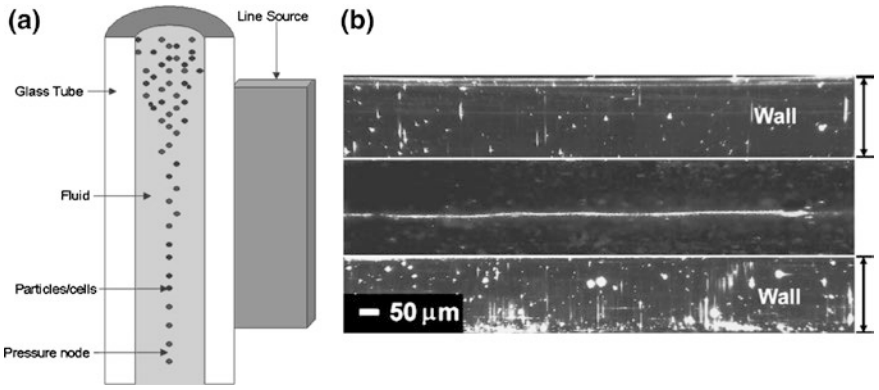

Fig. 15 **a** Schematic of the cylindrical acoustophoretic focusing presented by Goddard and Kaduchak (2005), **b** photograph of focused particle stream in a cylindrical glass tube. Reproduced with permission from the Acoustic Society of America

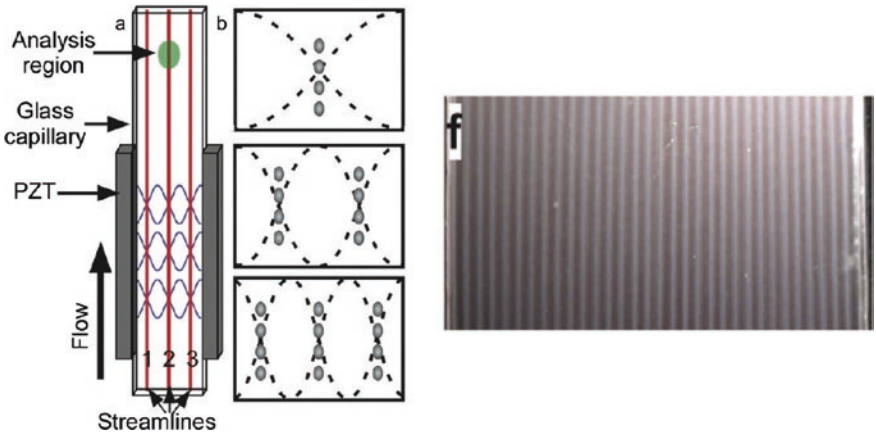

Fig. 16 Schematic (*left*) of the multinode focusing system proposed by Piyasena et al. (2012) and 33 parallel streams of focused RBC (*right*). Reproduced with permission from American Chemical Society

A CD4+ labelled WBC population was also analysed providing scatter plots that clearly isolated granulocytes, monocytes and lymphocytes.

An alternative approach to high throughput cytometry was recently proposed by Zmijan et al. (2015) were rather than focusing the cells in parallel streams, all cells were levitated into the half depth of a wide channel such that all cells are ensured to be in focus. Although not collecting side and forward scatter data, high throughput imaging was performed of ATDC5 (pre-chondrocytic) cell line and primary leukaemia cells at a rate of 52,350 and 60,400 cells per second respectively.

A SAW-based device that provides well-defined focusing in two dimensions in the cross-section of a rectangular PDMS channel was described by Chen et al. (2014) and integrated in an optical set-up for fluorescence detection. The focusing accuracy was recorded by fluorescence intensity measurements with a CV of 19.4 % for 7 μm particles and 10.9 % for 10 μm particles at an event rate of $\approx$1000 s^{-1}.

Grenvall et al. implemented 2D-focusing in a chip integrated Coulter counter, alleviating the common need for sheath fluid based focusing of the cells. The Coulter counter reported a simplified design having only impedance measurement electrodes on the channel bottom, which required absolute positioning of the cells in the channel cross-section to accomplish reproducible measurements, Fig. 17 (top). Figure 17a–d shows a confocal cross-section imaging sequence of the pre-focusing channel with (a) no ultra sound, (b) vertical λ/2 resonance, (c) horizontal λ/2 resonance and (d) both horizontal and vertical λ/2 resonances actuated. The obtained peak amplitude histograms for a mixture of 7 μm calibration beads and RBCs are seen in Fig. 17e–g, where the chip Coulter counter demonstrates a performance equal or better than a commercial Multisizer 3 Coulter counter.

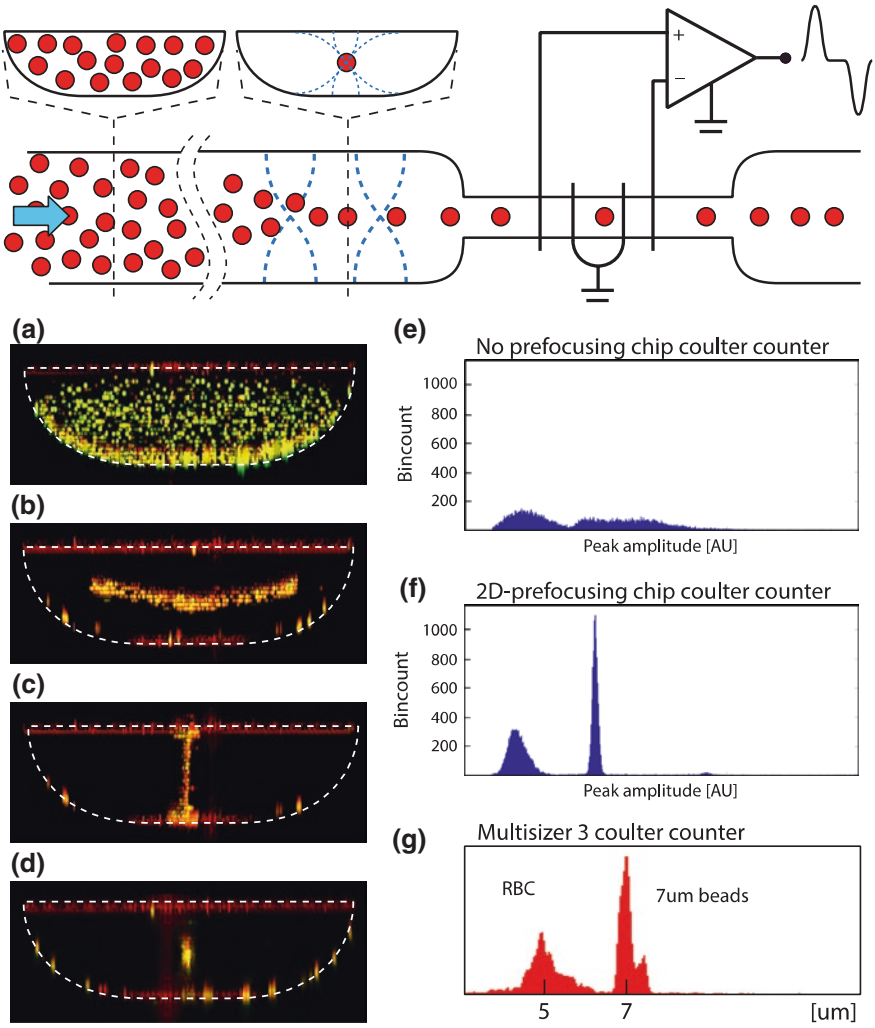

Fig. 17 Schematic of the chip integrated acoustic prefocusing Coulter counter reported by Grenvall et al. (2014) (*top*). Confocal cross-section images of the 2D acoustic prefocusing chip integrated Coulter counter. **a** No-ultrasound, **b** vertical resonance active, **c** horizontal resonance mode active, **d** both horizontal and vertical resonance active. In **e** and **f** the chip Coulter counter peak amplitude event histogram for a mixture of RBC and 7 μm calibration particles is seen without (**e**) and with (**f**) the prefocusing active to be compared with a standard commercial Multisizer 3 recording (**g**)

The orientation of a non-spherical cell is of importance for flow cytometry analysis, as it allows the laser interrogation to be conducted during uniform conditions and thus reduce noise in forward and side scatter data. Jakobsson et al. (2014b) used 2D acoustic focusing to control the orientation of red blood cells and

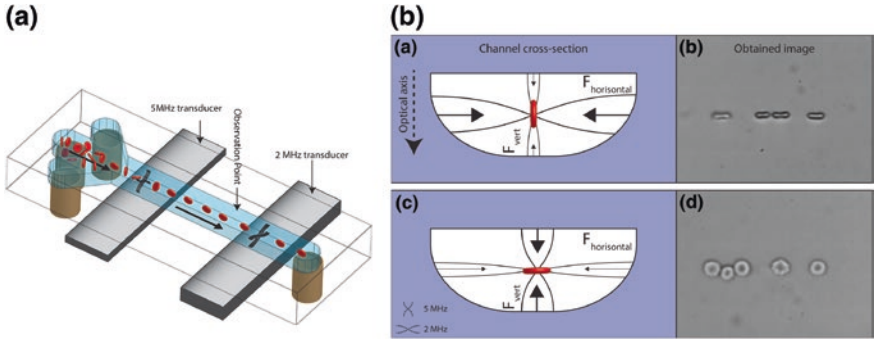

Fig. 18 **a** Schematic set-up of the acoustophoretic system for simultaneous 2D-focusing and orientation of non-spherical cells and particles, **b** channel cross-section showing either dominance of the horizontal or the vertical resonance mode. *Inset microscope images* show RBCs either vertically (*upper*) or horizontally oriented (*lower*). Reproduced with permission from American Chemical Society

demonstrate that by tuning the resonance frequency either allow the horizontal or the vertical resonance mode to dominate and thus orient the RBCs either flat or standing (from the observers view point). It was shown that 87.8 ± 3.8 % of the red blood cells could be horizontally oriented while 98.7 ± 0.3 % could be vertically oriented, Fig. 18.

1.5 Washing

Acoustophoretic transfer of cells across buffer streams was one of the very early microfluidic applications of acoustophoresis where yeast cells in a fluorescent background where transferred into a clean buffer using a layered acoustic resonator design (Hawkes et al. 2004). Hawkes most importantly also noted that washing efficiency was strongly dependent of the cell concentration reporting deteriorating washing performance at yeast cell concentrations above $\approx 10^7$ cells/mL. Augustsson et al. (2012a) investigated this further concluding that at blood cell concentrations $\approx 3 \times 10^6$ cells/mL unperturbed cell separation could be performed. Limiting factor is the average inter-particle distance in the suspension and is thus dependent of the cell size, e.g. volume fraction, in each application. Ley and Bruus (2016) reported a theoretical study on the hydrodynamic particle interaction in high-concentration particle suspensions, concluding that at particle volume fractions exceeding 1 % the hydrodynamic interaction starts to become influential. The first microchip integrated acoustophoretic blood cell washing described by Petersson et al. (2005) utilised the transversal mode of operation in a silicon glass configuration and compassed washing of RBC where 98 % of the molecular background contaminant was removed while recovering 95 % of the

RBC at a sample input flow rate of 100 μL/min and a wash buffer flow of 170 μL/min. The washed RBC central fraction was collected at a flow rate of 100 μL/min. The study also noted that a measurable drop in washing efficiency could be seen at particle volume concentrations of ≈3 %. Subsequent studies on improved cell and particle washing efficiency by Augustsson et al. (2009a) utilised the two-step focusing device reported in Persson et al. (2008), Fig. 19a. The study targeted the need for integrated microscale strategies to remove the molecular background from solid phase extraction microbeads in proteomic studies. Metal Oxide Affinity Capture beads (MOAC) of 3–7 μm size were used to selectively bind to phosphopetides in a complex peptide mixture from digested bovine serum albumin sample. The peptide was not detectable in the crude extract by MALDI mass spectrometry whereas the targeted phosphopetide was identified in the mass spectra obtained from the eluted fraction from the MOAC beads. In agreement with the theoretical limit when hydrodynamic interaction starts to play a role in washing experiments (Lei et al. 2016), Augustsson et al. (2009a) noted a reduction in washing efficiency going from 0.01 to 1 vol% particles that wash efficiency dropped from 99.99 to 98 %.

A slightly different approach to cell and particles washing was also proposed by Augustsson et al. (2009b). A chip design with multiple inlets and outlets along the two sides of the acoustophoresis channel gradually switched the inlet buffer in orthogonal to the flow direction while still retaining the particles in the central flow stream, Fig. 19b. This set-up was subsequently used to sequentially elute surface bound peptides with different pI (isoelectric point) from human spermatozoa

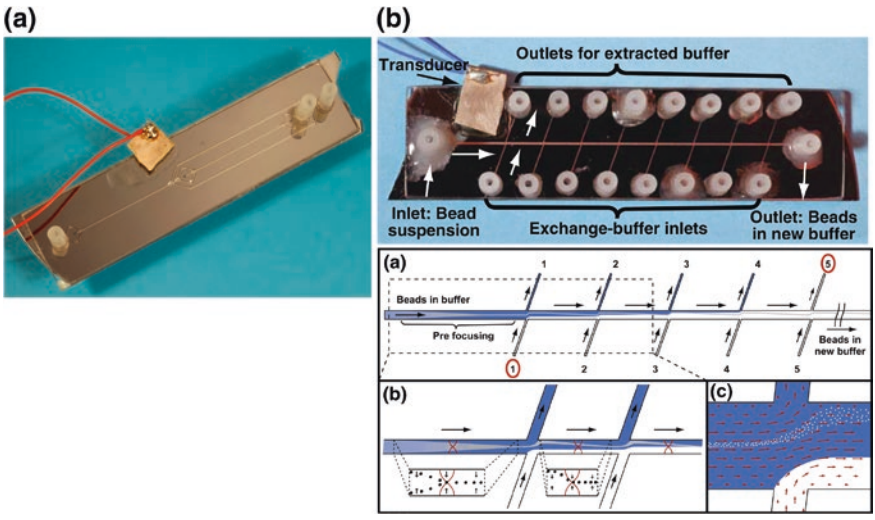

Fig. 19 **a** Photograph of the dual acoustophoresis cell washing chip developed by Augustsson et al. (2009a), Persson et al. (2008). **b** Acoustophoretic cell and particle washing chip where particles are retained in the centre flow by the primary radiation force while input carrier buffer sequentially is shifted to the side outlets (Augustsson et al. 2009b). Reproduced with permission from Springer Science and Business Media

(Augustsson et al. 2012b). By providing the side inlet with sequentially increasing pH the sperm cells were serially exposed to increasing pH and eluted peptides for each pH could be isolated at the corresponding side outlet and subsequently analysed by MALDI mass spectrometry.

When performing acoustophoresis across laminated flow stream as in the case of acoustophoretic washing experiments care must be taken with respect to the acoustic impedance of the different fluids. As already shown by Hertz and Mende (1939) a net force will act on a fluid interface when exposed to a travelling sound wave independent of the wave propagation direction. More recently Deshmukh et al. (2014) suggested that the force acting on the interface is proportional to the difference in the acoustic impedance between the two fluids. It was demonstrated that if the acoustic impedance of the fluid laminated closest to the sidewalls in a standard FFA channel, Fig. 6a, is higher than in the central buffer flow, the two fluids will relocate with the fluid stream having the highest acoustic impedance in the centre. It was experimentally found that minute differences in acoustic impedance of only 0.1 % may induce fluid relocation during acoustophoresis experiments. Augustsson et al. (2016a, b) later utilised these findings in his work on iso-acoustic focusing, and could thereby control that the acoustic impedance gradient in the microchannel was retained. Recently Tenje et al. (2015a, b) used the 2D-prefocusing set-up, Fig. 6b, for washing RBCs from IgA protein as an effort to potentially address the need for improved means of washing donor blood from IgA for transfusion to IgA deficient recipients. The current clinical practice for IgA depleted blood encompasses extensive manual centrifugation-based washing protocols. In order to accomplish successful in the acoustophoretic set-up the central buffer was ensured to have a higher density and thus higher acoustic impedance than the incoming blood sample along the side walls. The washing procedure removed IgA to a level below the limit of detection 0.25 μg/mL while recovering 97 % of the RBCs. Although successful in the IgA washing, the process needs further improvement in throughput as the incoming sample was diluted 1:20 to ensure that a critical cell concentration was not exceed and thus minimising the risk that hydrodynamic coupling between the cells and the incoming carrier fluid contaminated the target outlet fraction.

Cell washing for flow cytometry applications have been addressed both by means of BAW and SAW technologies. Lenshof et al. (2010) first demonstrated a BAW acoustophoresis chip fabricated in glass, configured according to the original FFA chip, Fig. 6a, with a sample inlet along the sides of the acoustophoresis channel and a clean buffer flow in the channel centre. An RBC lysed blood sample was injected in the chip and WBC were translated by means of the primary radiation force into the clean central buffer while a major part of the lysis cell debris was discarded in the side outlets. This system was later linked in-line with a flow cytometer, Fig. 20, demonstrating a 98 ± 6 % WBC recovery, and a 99.6 % removal of cell debris (Warner et al. 2012). A similar approach to remove RBC lysis debris prior to flow cytometry analysis was later also presented by Li et al. (2015b). Li used the *taSSAW* device earlier discussed, Fig. 10, utilising the higher

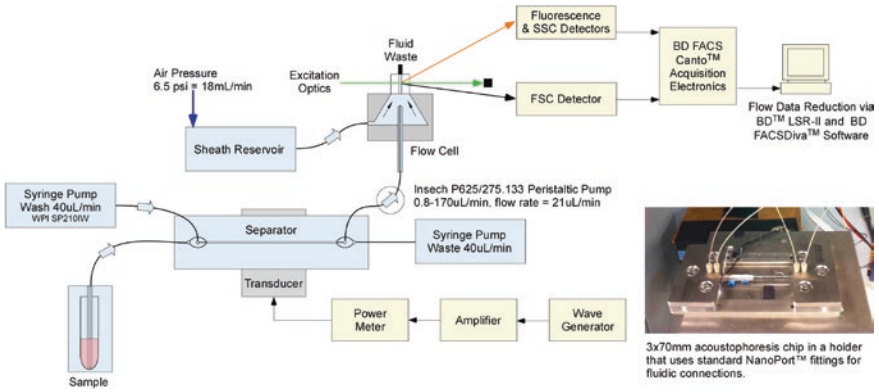

Fig. 20 Schematic set-up of the flow cytometry in-line acoustophoretic WBC washing system

acoustophoretic mobility of WBC as compared to lysis debris. The debris content was reduced from 22.6 to 2.2 % of the total counts.

1.6 Concentration and Depletion

Acoustophoretic concentration is very closely related to focusing, but with an additional step of removing excess fluid, and thereby increasing the cell concentration in the sample. Nordin and Laurell (2012) made a device that could increase the cell concentration 200-fold by introducing sequential exit ports for the cell-free medium stream. The major reason for doing the fluid removal sequentially is that outlet split flow balancing become challenging as, e.g. a 100-fold enrichment step will have to have a 99:1 split ratio in a single step, and simple calculations for a 375 μm wide acoustophoresis channel gives that the width of the sample stream that is collected in the central outlet is about 2.8 μm which is significantly smaller than the width of a cell of 10–15 μm to be concentrated, hence the cell recovery is at significant risk in a single-step concentrator whereas if a concentration factor of 10 times is targeted and done in two steps the cells to be concentrated will locate well within the central outlet stream boundaries. By combining two sequential concentrators enrichment factors of 196 times for prostate cancer cells, DU145, could be obtained at a cell recovery of 98 % and a sample input flow rate of 200 μL/min and an input cell concentration of 2.5×10^4 cells/mL. The corresponding data for red blood cells was an enrichment factor of 146 times at a cell recovery of 97 % having an input sample of 5000 times diluted whole blood, $\approx 10^6$ RBCs/mL. This principle was also utilised by the same group (Antfolk et al. 2015b) where a concentration step was integrated to an upstream separation unit where WBCs were first separated from CTCs and then the CTCs were concentrated 24-fold, Fig. 9.

At concentration factors >200 the use of sequential flow splitters will be strongly dependent of the absolute accuracy in the flow control system since a 1 % flow variation of the input flow, which typically is several hundred microliters per minute, will significantly impact the concentration performance of the final flow splitter which typically operates with an output flow rate in the range of single microliters/minute. An alternative solution that circumvents this shortcoming is to use a looped system and re-circulate the sample while removing some cell-free medium for each passage. This was utilised by Jakobsson et al. (2015) to achieve a 1000-fold enrichment of cells, Fig. 21.

Cell depletion can be seen as the reverse process to concentration, instead of using the concentrated cell fraction it is the cell depleted media that is the target. Lenshof et al. (2009) designed an acoustic plasmapheresis device that could remove cellular content from whole blood and receive a cell-free blood plasma fraction of clinical grade. Working with samples of high cellular content such as whole blood is indeed challenging since an input sample of 40 % haematocrit (HCT) consequently has a solid biomass of 40 vol%, i.e. a maximum theoretical recovery of 60 %vol can be obtained but as the process is performed in a continuous flow format the recovery of cell-free plasma is significantly lower. Analogous to the sequential concentration device by Nordin and Laurell (2012), Lenshof proposed a $\lambda/2$ focusing device where several serially located outlet ports in the centre of the channel floor removed cells from the central region with the high cell concentration in the acoustic pressure node (Fig. 22). The total cell content of the sample was thereby sequentially lowered until the remaining cell product could be discarded in the centre of the trifurcation outlet. The side fraction contained clean plasma and a volume recovery of 21 % with cell numbers sufficiently low to qualify for clinical grade, $<6 \times 10^3$ cell/μL was reported. A follow up study by the same group (Tajudin et al. 2013) integrated the plasmapheresis set-up, having a plasma volume recovery of 33 %, in-line with a protein microarray for Prostate

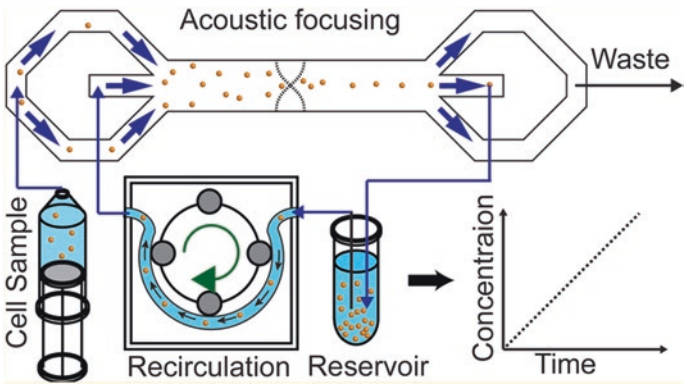

Fig. 21 Schematic of the thousand fold recirculating cell concentration system presented by Jakobsson et al. (2015). Reproduced with permission from American Chemical Society

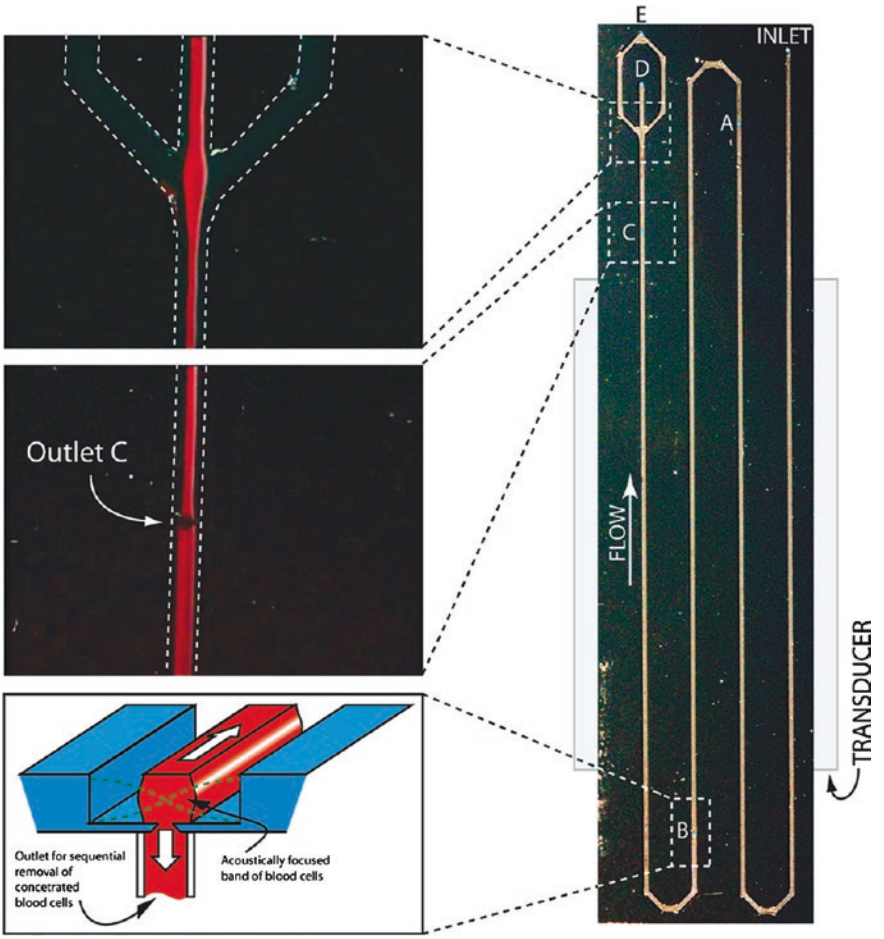

Fig. 22 Acoustophoretic cell depletion system for removal of blood cells from plasma, plasmapheresis (Lenshof et al. 2009), where the cell rich fraction in the acoustic pressure node is removed via outlet ports in the centre of the channel floor. Reproduced with permission from American Chemical Society

Specific Antigen (PSA) diagnostics, reporting a linear readout of female donor blood spiked with PSA 1.7–100 ng/mL.

In a recent study by Olsson et al. (2016) an acoustophoresis system for bacteria isolation from whole blood was described. The system encompassed an initial step of plasmapheresis based on the device reported in Lenshof et al. (2009). The bacteria was marginally influenced by the acoustic radiation force due to the minute size, ≈1 μm, and was thus recovered at 91 % in the clean plasma fraction. The plasmapheresis step delivered the blood cell depleted plasma for an in-line linked acoustic seed trapping unit that enriched the bacteria from 100 μL plasma

volumes and washed the sample, see Sect. 2, before dispensing into a disposable PCR microchip followed by thermocycling and diagnostic readout in less than 2 h. Patient blood samples with bacteria content in the upper range of clinically relevant bacteria concentrations were detected. In a study of 57 clinical samples four samples were found positive for *E. coli* infection in the routine analysis. The acoustophoretic system was able to detect two of the patient samples with the highest bacteria load. The LOD of the system was estimated to be in the range of 10^3–10^4 bacteria/mL blood.

Ngamsom et al. (2016) reported an acoustophoretic system with a trifurcation inlet and outlet design as in Fig. 23, where bacteria contaminated foods samples were clarified from suspended biological debris, leaving a clarified fraction in the side outlets for further processing by conventional culturing and CFU enumeration. The system was also tested in its ability to deplete red blood cells analogous to Olsson et al. (2016), reporting an RBC depletion of 99.8 % and a 10 % recovery of the spiked bacteria in the clarified plasma side outlets, using a 50 % diluted horse blood spiked with *S. typhimurium* at a level of 10^7 CFU/mL.

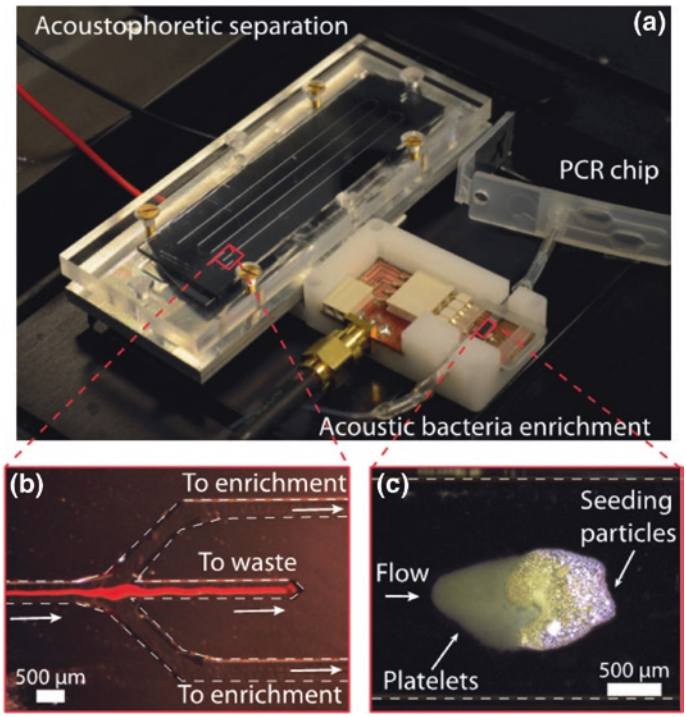

Fig. 23 Acoustic system for bacteria isolation from whole blood and linkage to PCR diagnostics. **a** the assembled hybrid system with the plasmapheresis unit, the acoustic seed trapping unit and the disposable PCR microchip. *Inset image* **b** shows the outlet region of the plasmapheresis unit, and **c** shows a closed up image of the seed trapping process. Reproduced with permission from American Chemical Society

2 Acoustic Trapping

In the previous section on continuous flow-based acoustophoresis, a standing wave is generated along the entire, or at least the major part of a channel and the primary acoustic radiation force is utilised to move the cells/particles orthogonal to the direction of flow. If a standing wave instead is generated in a limited portion of the channel or in a small chamber the gradient in the acoustic radiation potential along the channel or in the chamber will create lateral retention forces that can trap cells/particles against a flow (Bruus 2012). When the particles get in close vicinity, secondary forces (Bjerknes forces) resulting from the scattered waves from neighbouring particles will create attractional forces further packing the particles (Silva and Bruus 2014). The secondary forces will, for example, promote agglomeration of particles lined up in the pressure node by the primary radiation force in a plane perpendicular to the incident sound wave.

The history of acoustic trapping in microfluidic systems began in the later half of the twentieth century after it was discovered that ultrasound can affect microparticles, e.g. red blood cells in a blood vessel (Dyson et al. 1971). One of the pioneers in the field that brought acoustic standing wave technology and particle handling into the life science applications was William Terence Coakley. In early work among several others he demonstrates manipulation of microparticles ultrasonic standing wave fields (Coakley et al. 1989; Withworth et al. 1991) and early work on blood plasma generation by means of cell aggregation in pressure nodes followed by sedimentation was proposed (Cousins et al. 2000). His later developments also pioneered the design of layered acoustic resonators for particle trapping in localised regions in a flow cell, enabling retention, enrichment and stationary studies of cells in perfused systems. In Coakley et al. (2004) a 14 mm wide layered acoustic resonator flow cell operated a λ/2, 2.2 MHz was presented the single layer of chondrocytes, erythrocytes and neural cells were trapped and studied in the presence of cell cross-linking agents.

2.1 Acoustic Trapping Forces

Following Eq. (1) above, an ultrasonic standing wave will push all particles with positive contrast factor, i.e. most of the commonly used cells and particles, to the plane perpendicular to the wave axis with the pressure node in. If several nodes are present, the force will act towards the closest pressure node.

For trapping applications, the lateral component of the radiation force (Fig. 24b) is of importance since this is the retaining force, and it was given by Woodside et al. (1997) as

$$F_{\mathrm{lat}}^{\mathrm{rad}} = \frac{4\pi}{3} a^3 \nabla E_{\mathrm{ac}} \left(\frac{3\left(\rho_{\mathrm{p}} - \rho_0\right)}{\rho_{\mathrm{p}} + 2\rho_0} \cos^2(kx) - \frac{\kappa_0 - \kappa_{\mathrm{p}}}{\kappa_0} \sin^2(kx) \right) \tag{2}$$

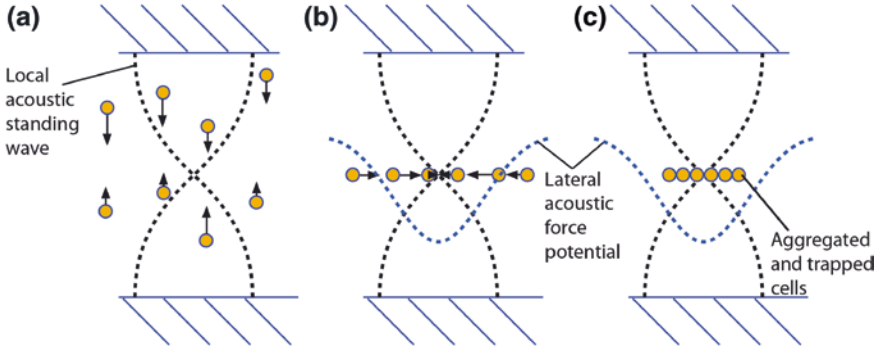

Fig. 24 Principle for trapping particles using acoustic forces. **a** The primary radiation force moves the particles to the node in the centre of the channel. **b** The lateral gradient in the radiation potential subsequently compacts the particles in the nodal plane of the standing wave. **c** The trapped particle cluster is retained against the flow in the channel by the lateral gradient potential

Equation (1) above treats fluids with low particle concentration where the acoustic interaction forces are negligible. With higher particle concentrations, or when the particles get closer to each other, resulting in smaller intraparticle distances, secondary forces become increasingly important. They were early described by Bjerknes (1906), therefore sometimes called Bjerknes forces, and have been more extensively reviewed by Weiser et al. (1984) and Gröschl (1998). They depend on both the velocity field and the pressure field, and the velocity term is also dependent on the angle between the particles and the incident sound wave, Fig. 25.

$$F_{\text{sec}}^{\text{rad}} = 4\pi a^6 \left(\frac{\left(\rho_{\text{p}} - \rho_0\right)^2 (3\cos^2\theta - 1)}{6\rho_0 d^4} v^2(x) - \frac{\omega^2 \rho_0 (\kappa_0 - \kappa_{\text{p}})^2}{\kappa_0} p^2(x) \right) \quad (3)$$

2.2 Acoustic Streaming

Streaming occurs in most acoustically driven systems and will influence the trapping of smaller particles (Wiklund et al. 2012). In Fig. 26, the streaming vortices in a glass capillary in contact with a piezoelectric transducer are visualised together with an example of modelling of the same type of vortices (Lei et al. 2013). The streaming affects the particles through the Stoke's drag which is proportional to the radius of the particles. Since the acoustic radiation force is proportional to r^3 there is a transition region where the streaming forces will start to dominate over the radiation forces and hence prevent trapping of the particles. Barnkob et al. (2012) investigated this and found the transition region to be around a critical particle diameter of 1.4 μm. However, it can also be assumed that the streaming may help to actively move particles closer to the trapping nodes where the lateral forces are stronger, which will improve the trapping performance.

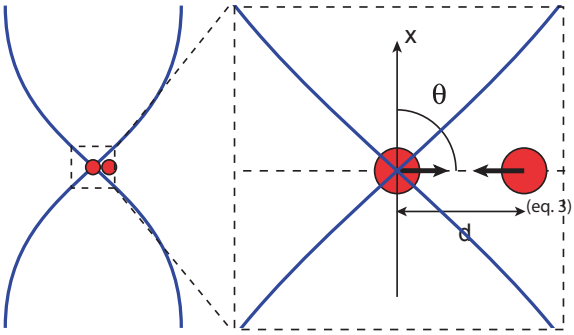

Fig. 25 Secondary forces acting between particles at close distances. As seen in Eq. 3, the secondary forces are dependant on the velocity and the pressure field in the trap, as well as the distance and angle between the particles

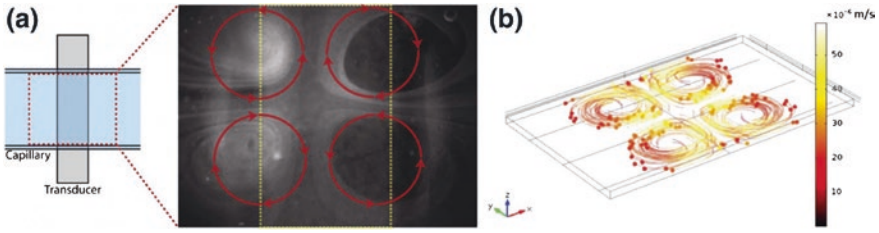

Fig. 26 **a** Streaming vortices in a capillary visualised by 490 nm particles over a small transducer (Hammarström et al. 2012). **b** Streaming vortices modelled (Lei et al. 2013). Reproduced with permission from the Royal Society of Chemistry

2.3 Seed Trapping

One way of overcoming the problem of trapping small particles due to the small acoustic forces or influence from streaming is to preload the trap with larger particles that experience larger forces, according to Eq. 2, and then rely on the secondary forces in Eq. 3 to trap the smaller particles when they get in close vicinity of the larger ones. This method was introduced by Hammarström et al. (2012) where he preloaded a trap with 10 μm polystyrene particles and demonstrated trapping of *E. coli* and 110 nm polymer particles. Figure 27 shows the principle and the resulting fluorescent images of the trapped nanoparticles. Here acoustic streaming is helpful to ensure that the small particles actually will get close to the seed particles.

2.4 Standing Wave Generation for Trapping

The most commonly used approaches of acoustic trapping can be categorized into either BAW or SAW. Both BAW and SAW are widely used for microparticle

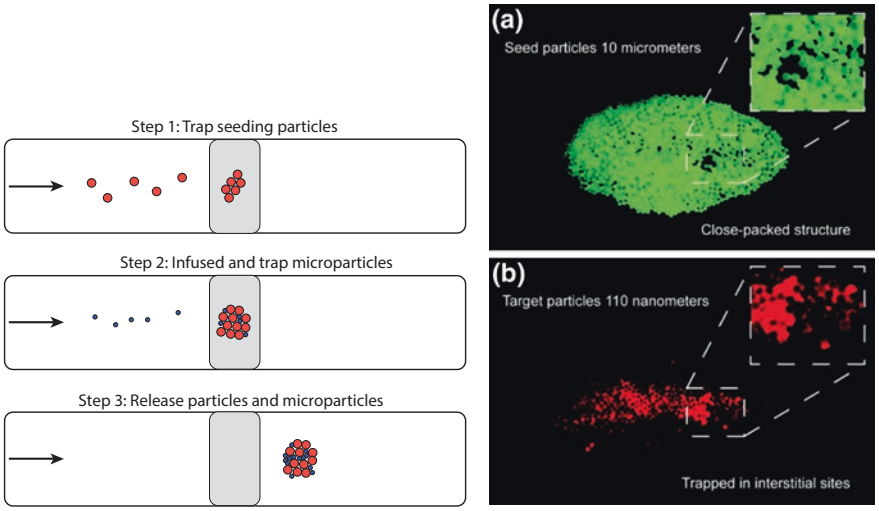

Fig. 27 *Left* the principle of seed trapping; preload with larger particles, then supply the sample with smaller particles that are trapped by secondary forces. *Right* fluorescent images of the trapped 10 μm seed particles and 110 nm fluorescent polymer particles (Hammarström et al. 2012). Reproduced with permission from the Royal Society of Chemistry

manipulation and the number of reported applications is rapidly increasing. As the names reveal, BAW are transferred through the bulk materials and SAW propagates along the surface of a substrate.

2.4.1 BAW: Bulk Acoustic Waves

Bulk acoustic waves are created by applying an alternating voltage over a piezoelectric transducer. BAW techniques use one or several ultrasonic transducers, most often lead zirconate titanate (PZT), which is placed in or in contact with a chip containing a fluidic channel (Lenshof et al. 2012). The transducer can either be attached directly to the chip, with e.g. glue, glycerol (Hammarström et al. 2010) or oil (Ohlin et al. 2013) as a coupling layer, or to a wedge (Manneberg et al. 2008a) that is then glued to the chip. The acoustic waves either generate a resonance locally in the channel or propagate in the chip and set up a standing wave, e.g. in a cavity where the resonance criteria are fulfilled (Lenshof et al. 2012), see Figs. 28 and 29. BAW devices are commonly designed as layered resonators with wavelength-matched layers or transversal resonators, where the lateral dimensions determine the resonance frequency, c.f the resonant cavity in Fig. 29.

An example of a layered resonator for levitation and aggregation of neural cells was presented by Bazou et al. (2005), Fig. 30. The device consisted of a 1.5 MHz piezoelectric transducer mounted on a steel membrane as coupling layer. The flow-through chamber height was 500 μm, closed by a glass lid.

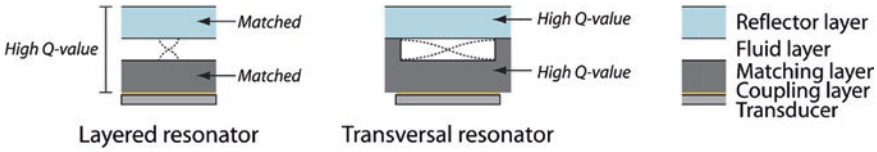

Fig. 28 Principle of layered and transversal acoustic resonators (Lenshof et al. 2012). Reproduced with permission from the Royal Society of Chemistry

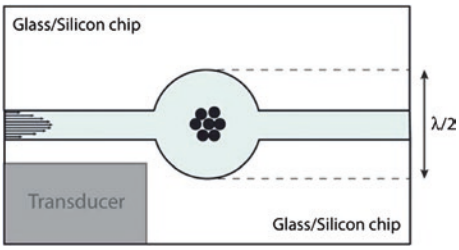

Fig. 29 Schematic of a resonant cavity trapping device using transversal standing waves (Lenshof et al. 2012). Reproduced with permission from the Royal Society of Chemistry

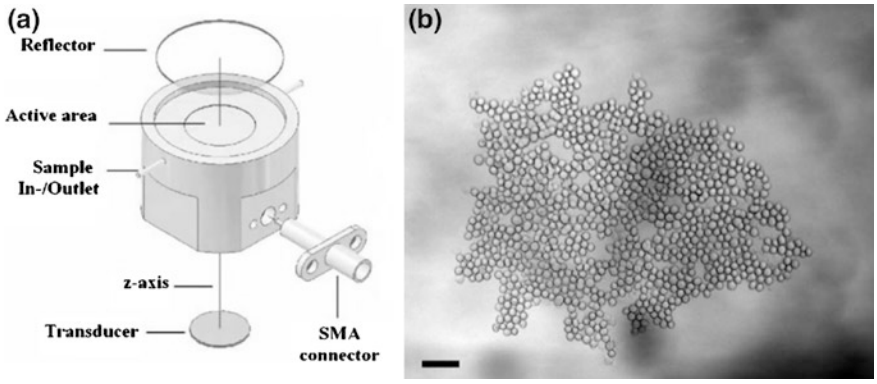

Fig. 30 Layered resonator for aggregation of neural cells (Bazou et al. 2005). Reproduced with permission from Elsevier

2.4.2 SAW: Surface Acoustic Waves

Surface acoustic waves are generated at the surface of a piezoelectric substrate, commonly lithium niobate, using interdigitated transducer (IDT) electrodes, Fig. 31. The interelectrode distances together with the wave propagation speed of the substrate determines the frequency of the waves. Using two opposing IDTs, SSAW are generated that can be coupled into the cell or particle containing liquid

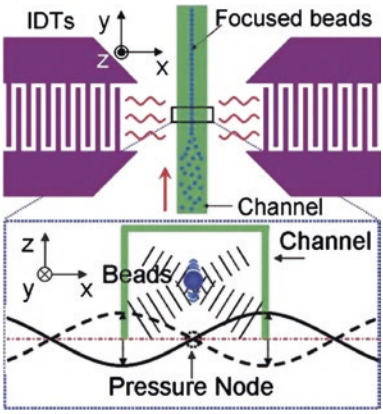

Fig. 31 SAW transducer principle for standing surface acoustic waves, SSAW. Two counter travelling surface waves interfere and generate a standing surface wave that couples into a channel or chamber (Shi et al. 2008). Reproduced with permission from the Royal Society of Chemistry

in a channel or chamber (Shi et al. 2008). The channels or chambers are normally fabricated in PDMS using soft lithography.

2.4.3 Focused Acoustic Beam

A method that is not as common as BAW and SAW is the Bessel beam technique. Generally, an acoustic beam is propagated through a fluid and enables manipulation of cells, particles and droplets (Mitri 2014). A standing wave is not required but rather a controlled node placed at a certain position. For a theoretical description of the radiation force on spheres, see Sapozhnikov and Bailey (2013) for an arbitrary acoustic beam, and Zhang and Zhang (2012), Mitri (2014), Leão-Neto and Silva (2016) for a Bessel beam. The Shung group has used an ultrasound beam to arrange 50 μm particles in an annular pattern on an acoustically transparent mylar film (Lee et al. 2014). A similar set-up has also been used to study deformability of different breast cancer cells, Fig. 32 (Hwang et al. 2016). A different approach to form a Bessel beam have been shown by Courtney et al. (2014) who used a circular arrangement of 64 transducers to arrange and manipulate 45 μm polystyrene particles.

2.5 Enrichment and Washing

2.5.1 BAW in Resonant Cavities

A straight forward method using BAW is to use a wet etched silicon or glass chip where some part has dimensions that fulfil the resonance criteria. This have been used extensively to demonstrate 2D and 3D trapping and enrichment of cells in half-wavelength and multi-wavelength resonant cavities or cages (Manneberg

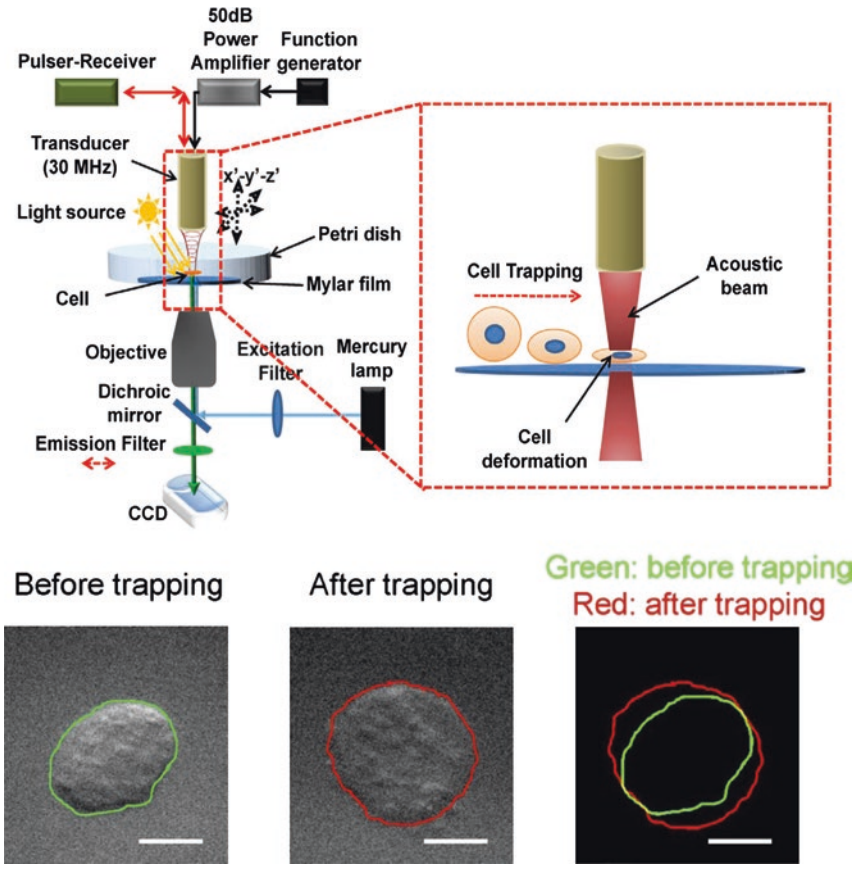

Fig. 32 Acoustic beam trapping to study deformability of breast cancer cells. The cells are pushed against a mylar film by the acoustic forces generated by the beam (Hwang et al. 2016). Reproduced with permission from the Nature publishing group

et al. 2008b; Svennebring et al. 2009). Building on these results, Iranmanesh et al. (2015) have combined three different acoustic regimes and performed both alignment, separation and trapping of lung cancer cells in one chip using a multi-wavelength trapping cavity, Fig. 33,

An alternative way of setting up a layered resonator is to have the piezoelectric transducer in direct contact with the channel omitting the coupling layer. Voorhees Norris et al. (2009) used this in a set-up for enrichment and washing of sperm cells for forensic DNA analysis. A transducer operating at 11.6 MHz was used to generate three trapping nodes in the channel for increased trapping capacity. The sperm cells were trapped from a sample consisting of a mixture of lysed female epithelia cells. After enrichment and washing the sperm cells were released and collected for DNA analysis, Fig. 34.

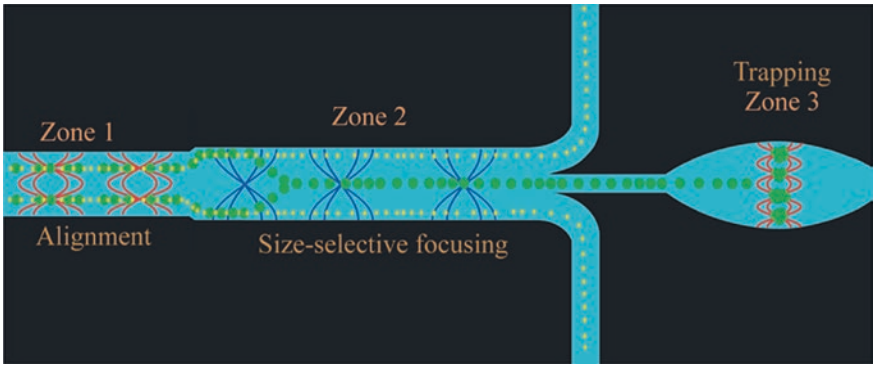

Fig. 33 Multi-wavelength trapping cavity for enrichment of lung cancer cells after separation (Iranmanesh et al. 2015). Reproduced with permission from the Royal Society of Chemistry

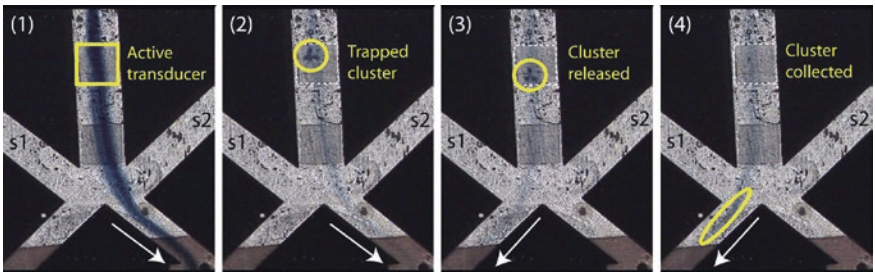

Fig. 34 Enrichment and washing of sperm cells for forensic DNA analysis. The cells are trapped, washed and released for subsequent DNA analysis. A hydrodynamic flow switch was used for selecting the collection outlet (Voorhees Norris et al. 2008). Reproduced with permission from the Chemical and Biological Microsystems Society

2.5.2 BAW in a Glass Capillary

To avoid the need for microfabricated structures in silicon or glass, which is expensive and time consuming, commercially available glass capillaries were proposed by Hammarström et al. (2010) and by the group of Glynne-Jones (Carugo et al. 2011; Glynne-Jones et al. 2012; Mishra et al. 2014) as low-cost acoustic resonators. Hammarström et al. (2010) presented a proof-of-concept with a set-up for trapping red blood cells in a capillary and also evaluated the trapping force to 1.27 $\pm$ 0.11 nN (Fig. 35).

Hammarström et al. (2012) introduced the previously mentioned seed trapping method and demonstrated trapping and enrichment of *E. coli* bacteria in a glass capillary. By pre-filling the trap with 10 μm polymer particles, *E. coli* were enriched during 30 min of constant perfusion, Fig. 36.

By adding resonance frequency tracking to the seed trapping, Hammarström et al. (2014a) opened up for several new applications. The frequency tracking

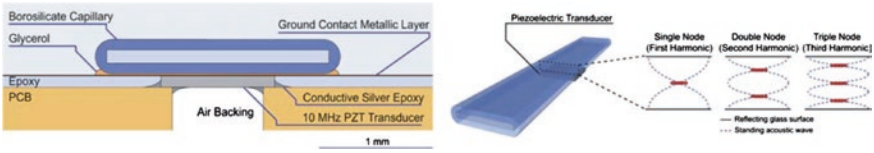

Fig. 35 Schematic of a standard rectangular disposable glass capillary mounted onto a printed circuit board with an integrated piezoelectric actuator for acoustic trapping experiments (*left*). Schematic of RBC trapping in a glass capillary at the fundamental resonance mode and at higher harmonics (*right*) as reported by Hammarström et al. (2010) Reproduced with permission from the Royal Society of Chemistry

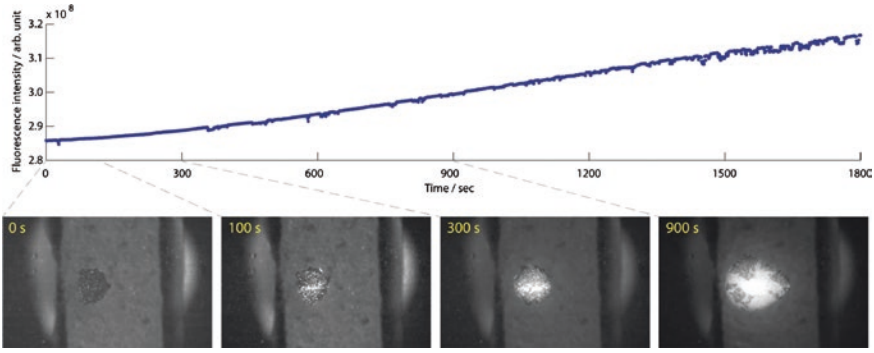

Fig. 36 Trapping and enrichment of *E. coli* using seed particles. The images below show how the *E. coli* fills the trap that was pre-filled with 10 μm polystyrene particles (Hammarström et al. 2012). Reproduced with permission from the Royal Society of Chemistry

continuously adapts the drive frequency to the system resonance, which may shift due to varying media composition or the amount of material collected in the trap. Bacteria identification in sepsis was addressed using the seed trap for bacteria purification in cultured blood followed by mass spectrometry analysis, Fig. 37 (Hammarström et al. 2014b) as well as in a system where PCR identification was used (Olsson et al. 2016). The same platform has been used for trapping of platelet-derived sub-micrometre particles in the size range of 0.1–1 μm (Evander et al. 2015) and as an incubation site for multiplex bead-based assays with increased bead recovery and reduced assay time (Tenje et al. 2015a, b). Systems based on disposable glass capillaries have also been used as perfusion bioreactors for tissue culturing where Li et al. (2014) cultured human articular chondrocytes and promoted cartilage formation after 21 days of culturing.

2.5.3 SAW in a Channel

Cell enrichment applications based on SSAW has started to appear lately. Chen et al. (2014) enriched diluted blood cells in polyethylene tubing attached with

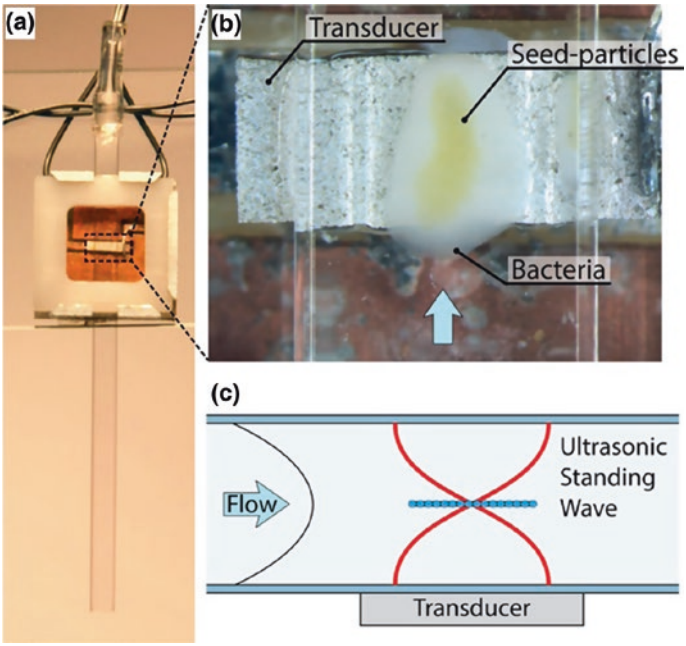

Fig. 37 Capillary-based device for seed trapping of bacteria from cultured blood for subsequent sepsis analysis by mass spectrometry (Hammarström et al. 2014b). Reproduced with permission from the American Chemical Society

coupling gel to a piezoelectric substrate. They created several trapping sites along the tube and enriched against a fluid flow of 10 µL/min, Fig. 38. The method resembles the earlier work of Wiklund et al. (2001, 2003) where 4.7 µm latex spheres were trapped in a glass capillary passing through the centre of a parabolic piezoelectric transducer and a reflector.

Collins et al. (2014) enriched 5 µm fluorescent particles with SAW in a different way where they pushed the particles against a PDMS membrane in the ceiling of a channel. By turning off the ultrasound the particles could be released.

2.6 BAW for Positioning and Arraying

2.6.1 BWF for Positioning and Arraying

Evander et al. (2007) used the layered resonator without coupling layer described above to position and grow yeast cells under constant perfusion of cell medium. The device was designed to operate at 12.4 MHz, half-wavelength resonance, and the yeast cells proliferated during 6 h under constant ultrasound exposure, Fig. 39. Neural stem cells were also shown to be viable after 15 min of trapping. This demonstrated that the high frequency ultrasound did not adversely affect the proliferation.

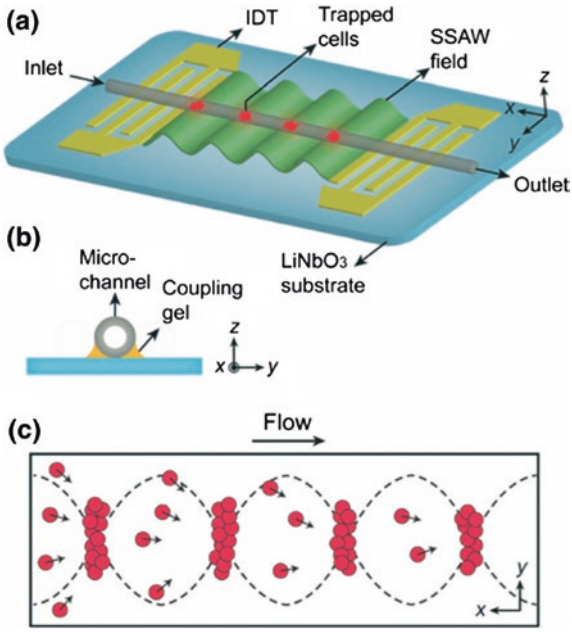

Fig. 38 Enrichment of diluted blood cells using SSAW coupled to a polyethylene tube (Chen et al. 2014). Reproduced with permission from the Royal Society of Chemistry

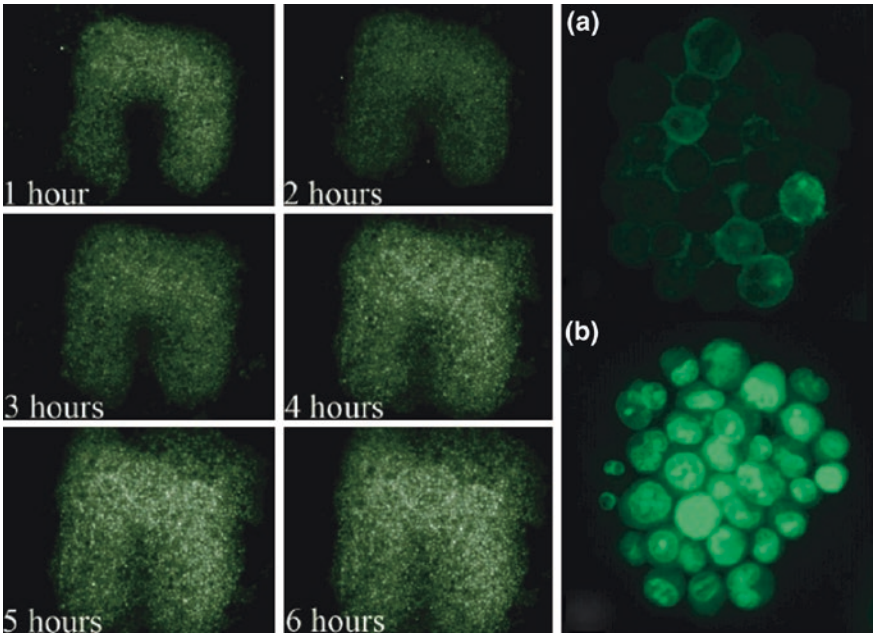

Fig. 39 *Left* trapping and proliferation of yeast cells during 6 h. *Right* uptake of acridine orange by neural stem cells after 15 min of trapping to indicate viability (**b**) (Evander et al. 2007). Reproduced with permission from the American Chemical Society

2.6.2 BAW in 2D Arraying

The BAW resonant cavities presented in Manneberg et al. (2008b) have been developed into an array plate of 10 × 10 nanowells in silicon, each forming a resonator with a size of 0.3 mm × 0.3 mm. The silicon well plate is bonded to a glass plate for parallel cell–cell interaction studies using fluorescence microscopy. By generating a 2D standing wave in each well the cells are focused to the centre (Vanherberghen et al. 2010). The array plate was first actuated by a piezoelectric transducer mounted on a wedge (Christakou et al. 2013). Later a ring-shaped transducer surrounding the well plate was used for improved actuation (Ohlin et al. 2013). To solve the problem of operating all wells at the same frequency the drive frequency was swept around the expected resonance frequency, ±0.05 MHz around 2.6 MHz in this case, which resulted in that the majority of the wells displayed cells focused in the centre, Fig. 40.

The system has been used to grow 3D-tumor cell models and to study the interaction of natural killer cells (NK cells) and tumors at single-cell level using high resolution fluorescence microscopy, Fig. 41 (Wiklund et al. 2014; Christakou et al. 2015).

Courtney et al. (2012) placed ultrasonic transducers both in the floor and the walls in a cm-sized fluidic chamber and actuated them with a phase delay in order to form different interference patterns and achieve a 2D pattern of 10 μm polystyrene beads. The trapping force was estimated at 30 pN. A similar set-up was also used to trap and separate 6 and 10 μm polystyrene particles and dorsal root ganglion cells from cell debris, respectively (Skotis et al. 2015).

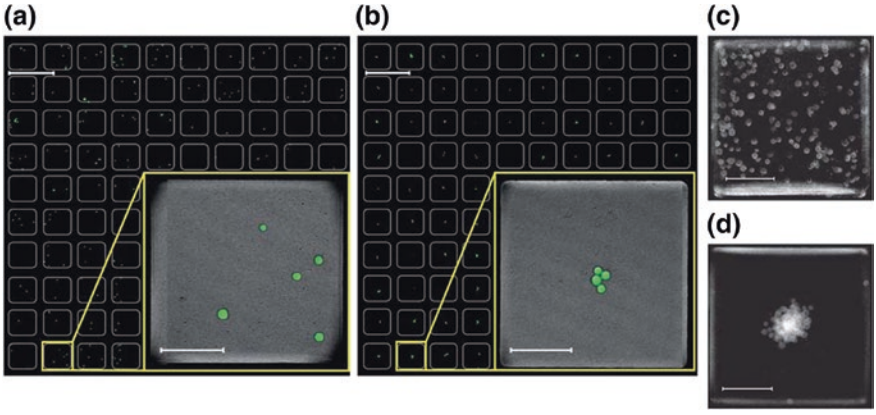

Fig. 40 Focusing of cells in a 100 well plate. The well size is 0.3 × 0.3 × 0.3 mm^3 with a 100 μm thick wall separating them. **a** Without ultrasound. **b** With swept frequency ultrasound. Superimposed images of the wells with cell without (**c**) and with (**d**) ultrasound. The drive frequency was swept around the well resonance frequency to ensure that the cells were focused in the centre in a majority of the wells due to slight variations in the resonance conditions of the wells (Vanherberghen et al. 2010). Reproduced with permission from the Royal Society of Chemistry

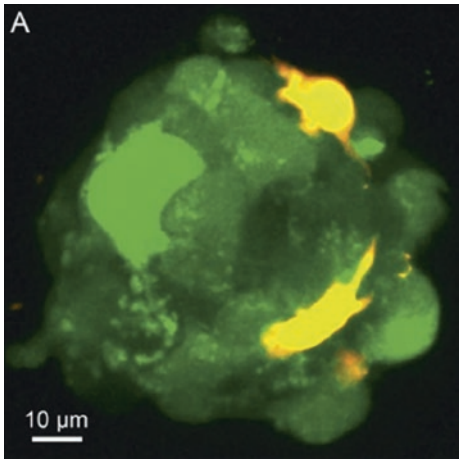

Fig. 41 Two NK cells (*yellow*) docking to a solid HepG2 tumor (*green*) under ultrasonic control in a microwell. The cells are stained and imaged by fluorescence microscopy (Christakou et al. 2015). Reproduced with permission from the Royal Society of Chemistry

2.6.3 SAW for Positioning and Arraying

Early examples of cell positioning and arraying with SAW were shown by Shi et al. (2009). The SSAW pattern was generated by superimposing surface waves from two orthogonal IDT:s, Fig. 42, generating a 2D-pattern of trapping positions. Arraying of bovine RBC and *E. coli* bacteria were demonstrated using a SAW wavelength of 100 µm. Since trapping with SAW is a younger method than with BAW, the governing mechanisms is not as well investigated and understood. Recently the Huang group published two works concerning the forces and mechanisms involved (Mao et al. 2016; Guo et al. 2016).

In a groundbreaking work by Collins et al. (2015) they managed to trap single cells in a 2D array of cell-sized acoustic potential wells with a fluid flow rate

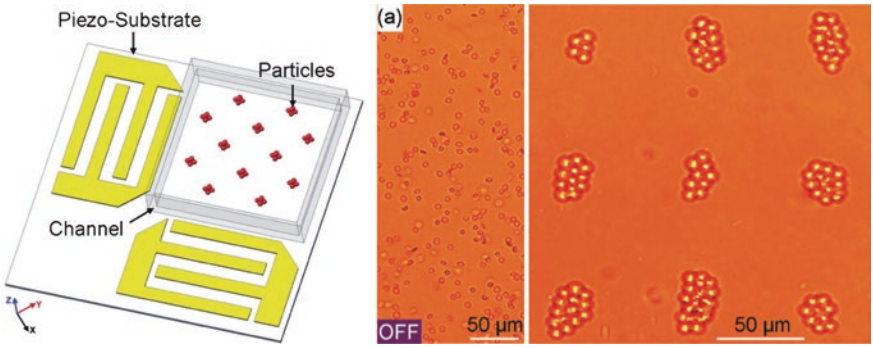

Fig. 42 *Left* 2D SSAW field generated by two orthogonal IDTs. *Right* 2D arraying of bovine RBCs in the SSAW field (Shi et al. 2009). Reproduced with permission from the Royal Society of Chemistry

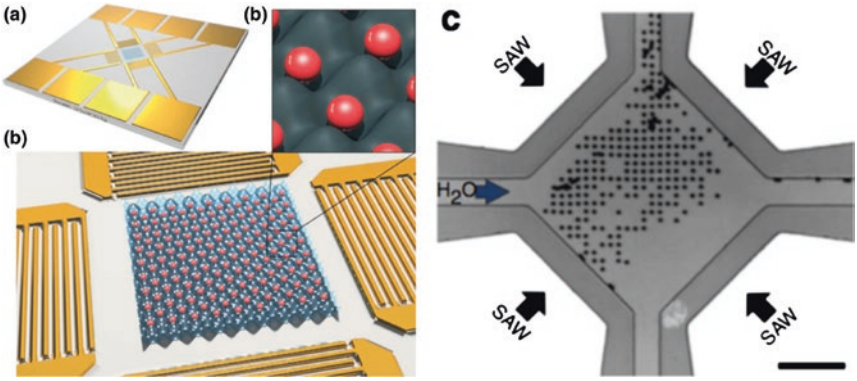

Fig. 43 2-D single-cell patterning with one cell per well driven by surface acoustic waves (Collins et al. 2015). Reproduced with permission from the Nature publishing group

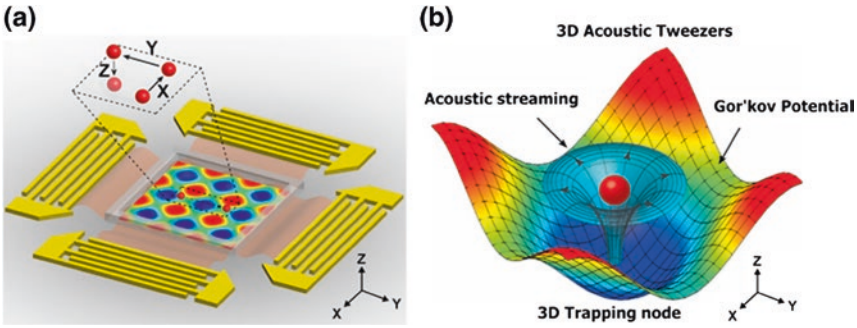

Fig. 44 Schematic of the 2D SAW device, analogous to Collins et al. (2015), that Guo et al. (2016) used to position cells in spatially defined 2D pattern and by phase shifting the transducers enabling transport in the plane. The system utilised the acoustic streaming field localised to each Gorkov potential well to also controllable levitate cells in the third dimension

of 0.5 μL/min. Actuation frequencies in the GHz range gave rise to small enough potential wells to only capture one cell per well, Fig. 43. The system was tested with human lymphocytes and malaria infected red blood cells.

Ding et al. (2012) have positioned and moved both single and clusters of particles, cells and nematodes with high accuracy in flow-free systems by varying the phase shift between the IDT pairs. Recently, Gou et al. investigated and demonstrated 3D positioning of single cells by combining a 2D SSAW field with intensity controlled acoustic streaming to determine the position in the vertical direction. The drag force from the streaming balances the gravitational force on the cells, Fig. 44 (Guo et al. 2016).

References

Antfolk M, Antfolk C, Lilja H et al (2015a) A single inlet two-stage acoustophoresis chip enabling tumor cell enrichment from white blood cells. Lab Chip 15:2102–2109

Antfolk M, Magnusson C, Augustsson P et al (2015b) Acoustofluidic, label-free separation and simultaneous concentration of rare tumor cells from white blood cells. Anal Chem 87:9322–9328

Augustsson P, Persson J, Ekström S et al (2009a) Decomplexing biofluids using microchip based acoustophoresis. Lab Chip 9:810–818

Augustsson P, Åberg LB, Swärd-Nilsson A-M et al (2009b) Buffer medium exchange in continuous cell and particle streams using ultrasonic standing wave focusing. Michrochim Acta 164:269–277

Augustsson P, Magnusson C, Nordin M et al (2012a) Microfluidic, label-free enrichment of prostate cancer cells in blood based on acoustophoresis. Anal Chem 84:7954–7962

Augustsson P, Malm J, Ekström S (2012b) Acoustophoretic microfluidic chip for sequential elution of surface bound molecules from beads or cells. Biomicrofluidics 6:034115

Augustsson P, Karlsen JT, Su HW et al (2016a) Iso-acoustic focusing of cells for size-insensitive acousto-mechanical phenotyping. Nat Commun 7:11556

Augustsson P, Magnusson C, Lilja H, Laurell T (2016b) Acoustophoresis in tumor cell enrichment. In: Fan HZH (ed) Circulating tumor cells: isolation and analysis. Wiley, London, pp 227–238. ISBN 9781118915530

Austin Suthanthiraraj PP, Piyasena ME, Woods TA et al (2012) One-dimensional acoustic waves in rectangular channels flow cytometry. Methods 57:259–271

Barnkob R, Augustsson P, Laurell T, Bruus H (2012) Acoustic radiation- and streaming-induced microparticle velocities determined by micro-PIV in an ultrasound symmetry plane. Phys Rev E 86:056307 2012

Bazou D, Kuznetsova LA, Coakley WT (2005) Physical environment of 2-D animal cell aggregates formed in a short pathlength ultrasound standing wave trap. Ultrasound Med Biol 31(3):423–430 2005

Bengtsson M, Laurell T (2004) Ultrasonic agitation in microchannels. Anal Bioanal Chem 378:1716–1721

Bjerknes VFK (1906) Fields of force. Columbia University, New York

Bruus H (2012) Acoustofluidics 7: the acoustic radiation force on small particles. Lab Chip 12:1014–1021

Burguillos MA, Magnusson C, Nordin M et al (2013) Microchannel acoustophoresis does not impact survival or function of microglia, leukocytes or tumor cells. PLoS ONE 8:e64233

Carugo D, Ankrett DN, Glynne-Jones P et al (2011) Contrast agent-free sonoporation: the use of an ultrasonic standing wave microfluidic system for the delivery of pharmaceutical agents. Biomicrofluidics 5:044108

Chen Y, Li S, Gu Y et al (2014) Continuous enrichment of low-abundance cell samples using standing surface acoustic waves (SSAW). Lab Chip 14:924–930

Christakou AE, Ohlin M, Vanherberghen B et al (2013) Live cell imaging in a micro-array of acoustic traps facilitates quantification of natural killer cell heterogeneity. Integr Biol 5:712–719

Christakou AE, Ohlin M, Önfelt B et al (2015) Ultrasonic three-dimensional on-chip cell culture for dynamic studies of tumor immune surveillance by natural killer cells. Lab Chip 15:3222–3231

Coakley WT, Bardsley DW, Grundy MA et al (1989) Cell manipulation in ultrasonic standing wave fields. J Chem Technol Biotechnol 44:43–62

Coakley WT, Bazou D, Morgan J et al (2004) Cell-cell contact and membrane spreading in an ultrasound trap. Colloids Surf B 34:221–230

Collins DJ, Alan T, Neild A (2014) The particle valve: on-demand particle trapping, filtering, and release from a microfabricated polydimethylsiloxane membrane using surface acoustic waves. Appl Phys Lett 105:033509

Collins DJ, Morahan B, Garcia-Bustos J et al (2015) Two-dimensional single-cell patterning with one cell per well driven by surface acoustic waves. Nat Commun 6:8686
Courtney CRP, Ong C-K, Drinkwater BW et al (2012) Manipulation of particles in two dimensions using phase controllable ultrasonic standing waves. Proc R Soc A Math Phys Eng Sci 468(2138):337–360
Courtney CRP, Demore CEM, Wu H et al (2014) Independent trapping and manipulation of microparticles using dexterous acoustic tweezers. Appl Phys Lett 104:154103
Cousins CM, Holownia P, Hawkes JJ et al (2000) Plasma preparation from whole blood using ultrasound. Ultrasound Med Biol 26(5):881–888
Deshmukh S, Brzozka Z, Augustsson P et al (2014) Acoustic radiation forces at liquid interfaces impact the performance of acoustophoresis. Lab Chip 14:3394–3400
Ding X, Lin S-CS, Kiralya B et al (2012) On-chip manipulation of single microparticles, cells, and organisms using surface acoustic waves. PNAS 109(28):11105–11109
Dykes J, Lenshof A, Åstrand-Grundström I-B et al (2011) Efficient removal of platelets from peripheral blood progenitor cell products using a novel micro-chip based acoustophoretic platform. PLoS ONE 6:e23074
Dyson M, Woodward B, Pond JB (1971) Flow of red blood cells stopped by ultrasound. Nature 232:572–573
Evander M, Johansson L, Lilliehorn T et al (2007) Noninvasive acoustic cell trapping in a microfluidic perfusion system for online bioassays. Anal Chem 79(7):2984–2991
Evander M, Gidlöf O, Olde B et al (2015) Non-contact acoustic capture of microparticles from small plasma volumes. Lab Chip 15:2588–2596
Franke T, Braunmüller S, Schmid L et al (2010) Surface acoustic wave actuated cellsorting (SAWACS). Lab Chip 10:789–794
Glynne-Jones P, Démoré CEM, Ye C et al (2012) Array-controlled ultrasonic manipulation of particles in planar acoustic resonator. IEEE Trans Ultrason Ferroelectr Freq Control 59(6):1258–1266
Goddard G, Kaduchak G (2005) Ultrsonic particle concentration in a line-driven cylindrical tube. JASA 117(6):3440–3447
Goddard GR, Sanders CK, Martin JC et al (2007) Analytical performance of an ultrasonic flow cytometer. Anal Chem 79:8740–8746
Gorkov LP (1962) On the forces acting on a small particle in an acoustical field in a ideal fluid. Sov Phys Dokl 6(9):773–775
Grenvall C, Augustsson P, Folkenberg JR, Laurell T (2009) Harmonic microchip acoustophoresis: A route to online raw milk sample precondition in protein and lipid content quality control. Anal Chem 81:6195–6200
Grenvall C, Folkenberg JR, Augustsson P et al (2012) Label-free somatic cell cytometry in raw milk using acoustophoresis. Cytometry A 81A:1076–1083
Grenvall C, Antfolk C, Bisgaard CZ, Laurell T (2014) Two-dimensional acoustic particle focusing enables sheathless chip Coulter counter with planar electrode configuration. Lab Chip 14(24):4629–4637
Grenvall C, Magnusson C, Lilja H et al (2015) Concurrent isolation of lymphocytes and granulocytes using prefocused free flow acoustophoresis. Anal Chem 87:5596–5604
Gröschl M (1998) Ultrasonic separation of suspended particles—Part I: Fundamentals. Acustica 84:432–447
Gröschl M, Burger W, Handl B et al (1998) Ultrasonic separation of suspended particles—Part III: Application in biotechnology. Acustica 84:815–822
Guo F, Mao Z, Chen Y et al (2016) Three-dimensional manipulation of single cells using surface acoustic waves. PNAS 113(6):1522–1527
Hammarström B, Evander M, Barbeau H et al (2010) Non-contact acoustic cell trapping in disposable glass capillaries. Lab Chip 2010(10):2251–2257
Hammarström B, Laurell T, Nilsson J (2012) Seed particle-enabled acoustic trapping of bacteria and nanoparticles in continuous flow systems. Lab Chip 12:4296–4304

Hammarström B, Evander M, Wahlström J et al (2014a) Frequency tracking in acoustic trapping for improved performance stability and system surveillance. Lab Chip 14:1005–1013
Hammarström B, Nilson B, Laurell T et al (2014b) Acoustic trapping for bacteria identification in positive blood cultures with MALDI-TOF MS. Anal Chem 86:10560–10567
Harris NR, Hill M, Beeby S et al (2003) A silicon microfluidic ultrasonic separator. Sens Act B 95:425–434
Hawkes JJ, Coakley WT (2001) Force field particle filter, combining ultrasound standing waves and laminar flow. Sens Act B 75:213–222
Hawkes JJ, Radel S (2013) Acoustofluidics 22: multi-wavelength resonators, applications and considerations. Lab Chip 13:610–627
Hawkes JJ, Barber RW, Emerson DR et al (2004) Continuous cell washing and mixing driven by an ultrasound standing wave within a microfluidic channel. Lab Chip 4:446–452
Hertz G, Mende H (1939) The acoustic radiation pressure in liquids. Z Phys 114:354–367
Hwang JY, Kim J, Park JM et al (2016) Cell deformation by single-beam acoustic trapping: a promising tool for measurements of cell mechanics. Nat Sci Rep 6:27238. doi:10.1038/srep27238
Iranmanesh I, Ramachandraiah H, Russom A et al (2015) On-chip ultrasonic sample preparation for cell based assays. RSC Adv 5:74304–74311
Jakobsson O, Grenvall C, Nordin M et al (2014a) Acoustic actuated fluorescence activated sorting of microparticles. Lab Chip 14:1943–1950
Jakobsson O, Antfolk M, Laurell T (2014b) Continuous flow two-dimensional acoustic orientation of nonspherical cells. Anal Chem 86:6111–6114
Jakobsson O, Oh SS, Antfolk M et al (2015) Thousand-fold volumetric concentration of live cells with a recirculating acoustofluidic device. Anal Chem 87:8497–8502
Johansson L, Nikolajeff F, Johansson S et al (2009) On-chip fluorescence-activated cell sorting by an integrated miniaturized ultrasonic transducer. Anal Chem 81:5188–5196
Jönsson H, Holm C, Nilsson A et al (2004) Particle separation using ultrasound can radically reduce embolic load to brain after cardiac surgery. Ann Thorac Surg 78:1572–1578
Leão-Neto JP, Silva GT (2016) Acoustic radiation force and torque exerted on a small viscoelastic particle in an ideal fluid. Ultrasonics 71(2016):1–11
Lee C, Jeong JS, Hwang JY et al (2014) Non-contact multi-particle annular patterning and manipulation with ultrasound microbeam. Appl Phys Let 104:244107
Lei J, Glynne-Jones P, Hill M (2013) Acoustic streaming in the transducer plane in ultrasonic particle manipulation devices. Lab Chip 13:2133–2143
Lei J, Glynne-Jones P, Hill (2016) Modal Rayleigh-like streaming in layered acoustofluidic devices. Phys Fluids 28:012004
Lenshof A, Tajudin AA, Järås K et al (2009) Acoustic whole blood plasmapheresis chip for prostate specific antigen microarray diagnostics. Anal Chem 81:6030–6037
Lenshof A, Warner B, Laurell T (2010) Acoustophoretic pretreatment of cell lysate prior to FACS analysis. In: Micro total analysis systems 2010, 3–7 Oct, Groningen, Netherlands, pp 1577–1579
Lenshof A, Evander M, Laurell T et al (2012) Acoustofluidics 5: building microfluidic acoustic resonators. Lab Chip 12:684–695
Lenshof A, Jamal A, Dykes J et al (2014) Efficient purification of CD4+ lymphocytes from peripheral blood progenitor cell products using affinity bead acoustophoresis. Cytometry A 85A:933–941
Ley M, Bruus H (2016) Continuum modeling of hydrodynamic particle–particle interactions in microfluidic high concentration suspensions. Lab Chip 16:1178–1188
Li S, Glynne-Jones P, Andriotis OG et al (2014) Application of an acoustofluidic perfusion bioreactor for cartilage tissue engineering. Lab Chip 14:4475–4485
Li P, Mao Z, Peng Z et al (2015a) Acoustic separation of circulating tumor cells. PNAS 112:4970–4975
Li S, Ding X, Mao Z et al (2015b) Standing surface acoustic wave (SSAW)-based cell washing. Lab Chip 15:331–338

Manneberg O, Svennebring J, Hertz HM, Wiklund M (2008a) Wedge transducer design for two-dimensional ultrasonic manipulation in a microfluidic chip. J Micromech Microeng 18:095025

Manneberg O, Vanherberghen B, Svennebring J et al (2008b) A three-dimensional ultrasonic cage for characterization of individual cells. Appl Phys Lett 93:063901

Mao Z, Xie Y, Guo F et al (2016) Experimental and numerical studies on standing surface acoustic wave microfluidics. Lab Chip 16:515–524

Mishra P, Hill M, Glynne-Jones P (2014) Deformation of red blood cells using acoustic radiation forces. Biomicrofluidics 8:034109

Mitri FG (2014) Single Bessel tractor-beam tweezers. Wave Motion 51(2014):986–993

Muller PB, Barnkob R, Herring Jensen MJ, Bruus H (2012) A numerical study of microparticle acoustophoresis driven by acoustic radiation forces and streaming-induced drag forces. Lab Chip 12:4617–4627

Muller PB, Rossi M, Marín ÁG et al (2013) Ultrasound-induced acoustophoretic motion of microparticles in three dimensions. Phys Rev E 88(2):023006

Nawaz AA, Chen Y, Nama N et al (2015) Acoustofluidic fluorescence activated cell sorter. Anal Chem 87:12051–12058

Ngamsom B, Lopez-Martinez MJ, Raymond J-C et al (2016) On-chip acoustophoretic isolation of microflora including *S. typhimurium* from raw chicken, beef and blood samples. J Microbiol Methods 123:79–86

Nilsson A, Petersson F, Persson H et al (2002) Autologous blood recovery and wash in microfluidic channel arrays utilizing ultrasonic standing waves. In: Micro total analysis systems 2002, pp 625–626, 3–7 Nov, Nara, Japan

Nilsson A, Petersson F, Jönsson H et al (2004) Acoustic control of suspended particles in microfluidic chips. Lab Chip 4:131–135

Nordin M, Laurell T (2012) Two-hundredfold volume concentration of dilute cell and particle suspensions using chip integrated multistage acoustophoresis. Lab Chip 12:4610–4616

Ohlin M, Christakou AE, Frisk T et al (2013) Influence of acoustic streaming on ultrasonic particle manipulation in a 100-well ring-transducer microplate. Micromech Microeng 23:035008

Olsson P, Evander M, Petersson K et al (2016) Integrated acoustic separation, enrichment and microchip PCR detection of bacteria from blood for rapid sepsis diagnostics. Anal Chem. doi:10.1021/acs.analchem.6b00323

Park J-W, Kim S, Ito T, Fujii T et al (2016a) Acoustofluidic harvesting of microalgae on a single chip. Biomicrofluidics 10:034119. doi:10.1063/1.4954744

Park J-W, Lee S, Shuo R, Kim S, Laurell T (2016b) Acousto-microfluidics for screening of ssDNA aptamer. Sci Rep 6:27121. doi:10.1038/srep27121

Persson J, Augustsson P, Laurell T, Ohlin M (2008) Acoustic microfluidic chip technology to facilitate automation of phage display selection of specific binders from protein library es. FEBS J 275:5657–5666

Peterson S, Perkins G, Baker C (1986) Development of an ultrasonic blood cell separator. In: Proceedings of 8th annual conference of the Engineering in Medicine and Biology Society, pp 154–156

Petersson F, Nilsson A, Holm C et al (2004) Separation of lipids from blood utilizing ultrasonic standing waves in microfluidic channels. Analyst 129:938–943

Petersson F, Nilsson A, Jönsson H et al (2005) Carrier medium exchange through ultrasonic particle switching in microfluidic channels. Anal Chem 77:1216–1221

Petersson F, Åberg L, Swärd-Nilsson A-M et al (2007) Free flow acoustophoresis: microfluidic-based mode of particle and cell separation. Anal Chem 79:5117–5123

Piyasena ME, Austin Suthanthiraraj PP, Appelgate Jr RW et al (2012) Multinode acoustic focusing for parallel flow cytometry. Anal Chem 84:1831–1839

Prest JE, Treves Brown BJ, Fielden PR, Wilkinson SJ, Hawkes JJ (2015) Scaling-up ultrasound standing wave enhanced sedimentation filters. Ultrasonics 56:260–270

Sapozhnikov OA, Bailey MR (2013) Radiation force of an arbitrary acoustic beam on an elastic sphere in a fluid. J. Acoust Soc Am 133(2):661–676

Shi J, Mao X, Ahmed D, Colletti A, Huang TJ (2008) Focusing microparticles in a microfluidic channel with standing surface acoustic waves (SSAW). Lab Chip 8:221–223
Shi J, Ahmed D, Xiaole MX et al (2009) Acoustic tweezers: patterning cells and microparticles using standing surface acoustic waves. Lab Chip 2009(9):2890–2895
Silva GT, Bruus H (2014) Acoustic interaction forces between small particles in an ideal fluid. Phys Rev E 90(063007):2014
Skotis GD, Cumming DRS, Roberts JN et al (2015) Dynamic acoustic field activated cell separation (DAFACS). Lab Chip 15:802–810
Svennebring J, Manneberg O, Skafte-Pedersen P et al (2009) Selective bioparticle retention and characterization in a chip-integrated confocal ultrasonic cavity. Biotechnol Bioeng 103(2):323–328
Tajudin AA, Petersson K, Lenshof A et al (2013) Integrated acoustic immunoaffinity-capture (IAI) platform for detection of PSA from whole blood samples. Lab Chip 13:1790–1796
Tenje M, Lundgren MN, Swärd-Nilsson A-M et al (2015a) Acoustophoretic removal of proteins from blood components. Biomed Microdevices 17(2015):95
Tenje M, Xia H, Evander M et al (2015b) Acoustic trapping as a generic non-contact incubation site for multiplex bead-based assays. Anal Chim Acta 853(2015):682–688
Thevoz P, Adams JD, Shea H et al (2010) Acoustophoretic synchronization of mammalian cells in microchannels. Anal Chem 82:3094–3098
Urbansky A, Lenshof A, Dykes J et al (2016) Affinity-bead-mediated enrichment of CD8+ lymphocytes from peripheral blood progenitor cell products using acoustophoresis. Micromachines 7:101
Vanherberghen B, Manneberg O, Christakou A et al (2010) Ultrasound-controlled cell aggregation in a multi-well chip. Lab Chip 10:2727–2732
Voorhees Norris J, Evander M, Horsman-Hall KM et al (2008) Acoustic differential extraction on a microdevice: improvements in fluidic control for separation of sperm cells and epithelial cell lysate. In: Locascio LE, Gaitan M, Paegel BM, Ross DJ, Vreeland WN (eds) Micro total analysis systems. Society for Chemistry and Micro-Nano Systems, San Diego, p 1156
Voorhees Norris J, Evander M, Katie M, Horsman-Hall KM et al (2009) Acoustic differential extraction for forensic analysis of sexual assault evidence. Anal Chem 81:6089–6095
Warner B, Yu L, Blom M, Buesink W et al (2012) Improving flow cytometric assay performance using modular in-line acoustophoretic washing of lysed blood samples. In: CYTO 2012 ISAC XXVII International Congress, B78, p 184, 23–26 June, Leipzig, Germany
Weiser MAH, Apfel RE, Neppiras EA (1984) Interparticle forces on red cells in a standing wave field. Acustica 56:114–119
Wiklund M (2012) Acoustofluidics 12: biocompatibility and cell viability in microfluidic acoustic resonators. Lab Chip 12:2018–2028
Wiklund M, Nilsson S, Hertz H (2001) Ultrasonic trapping in capillaries for trace-amount biomedical analysis. J Appl Phys 90(1):1
Wiklund M, Spegel P, Nilsson S et al (2003) Ultrasonic-trap-enhanced selectivity in capillary electrophoresis. Ultrasonics 41(2003):329–333
Wiklund M, Green R, Ohlin M (2012) Acoustofluidics 14: applications of acoustic streaming in microfluidic devices. Lab Chip 12:2438–2451
Wiklund M, Christakou A, Ida II et al (2014) Ultrasound-induced cell-cell interaction studies in a multi-well microplate. Micromachines 2014(5):27–49
Withworth G, Grundy MA, Coakley WT (1991) Transport and harvesting of suspended microparticles using modulated ultrasound. Ultrasonics 29:439–444
Woodside SM, Bowen BD, Piret JM (1997) Measurement of ultrasonic forces for particle-liquid separations. AIChE J 43(7):1727–1736
Yang AHJ, Soh HT (2012) Acoustophoretic sorting of viable mammalian cell in a microfluidic device. Anal Chem 84:10756–10762
Yeo LY, Friend JR (2014) Surface acoustic wave microfluidics. Annu Rev Fluid Mech 46:379–406

Zalis MC, Reyes JF, Augustsson P et al (2016) Label-free concentration of viable neurons, hESCs, and cancer cells by means of acoutophoresis, Integr Biol 8:332–340
Zhang X, Zhang G (2012) Acoustic radiation force of a gaussian beam incident on spherical particles in water. Ultrasound Med Biol 38(11):2007–2017
Zmijan R, Jonnalagadda US, Carugo D et al (2015) High throughput imaging cytometer with acoustic focusing. RCS Advances 101:83206–83216

Gravity-Driven Fluid Pumping and Cell Manipulation

Sung-Jin Kim, Xiaoyue Zhu and Shuichi Takayama

Abstract Microfluidic systems require fluid pumping. Here, we describe microfluidic devices that utilize gravity—which is free, steady, and ubiquitous on earth—as a driving force for generation of constant fluid flow as well as periodically switching flows. We also describe applications of such devices. Gravity-driven steady flow devices are described that enable microfluidic sperm sorting based on mobility and for cell culture where cells within different regions of a channel are treated with different concentrations of chemicals to analyze gradient responses. Gravity-driven fluidic oscillator devices are also described where a single device enabled the screening of the effect of three different shear stresses at four different frequencies (12 shearing conditions total) to reveal that there is an optimal frequency that endothelial cells respond to in terms of cell shape change.

Keywords Gravity · Pumping · Sperm sorting · Cell motility · Cell culture · Chemical gradient · Oscillator · Actuator · Shear stress · Frequency · Biorhythms · Fluidic switching

S.-J. Kim
Department of Mechanical Engineering, Konkuk University,
Seoul, Republic of Korea

X. Zhu
College of Chemistry, Chemical Engineering, and Biotechnology,
Donghua University, Shanghai 201620, People's Republic of China

S. Takayama (✉)
Department of Biomedical Engineering, University of Michigan,
2800 Plymouth Rd, Ann Arbor, MI 48109-2800, USA
e-mail: takayama@umich.edu

W. Lee et al. (eds.), *Microtechnology for Cell Manipulation and Sorting*,
Microsystems and Nanosystems, DOI 10.1007/978-3-319-44139-9_6

1 Introduction

A key feature of many microfluidic devices is fluid flow. While gravity is a relatively commonly used driving force for flow, there are some challenges for its use. Typically, gravity-driven flow is dependent on the difference in height of the liquid meniscus of the source reservoir relative to the outlet reservoir. In such experiments, the source reservoir is most full and the outlet reservoir most empty at the beginning of the experiment. As the experiment proceeds the source reservoir fluid level decreases and the outlet reservoir fluid level increases. The net result is that most gravity-driven flows, while quite steady measured over short periods of time, will decrease over time. We hypothesized that the usefulness of gravity-driven flows could be greatly increased if these limitations could be overcome. More specifically, we asked the question, would it be possible to design gravity-driven microfluidic systems where the flow rate would not change even as the volume of liquid in the source reservoir decreased and that of the outlet reservoir increased. Additionally, we wondered whether it would be possible to design gravity-driven microfluidic systems that could generate self-switching pulsatile flows that would mimic physiological blood flow pulsing. The following sections describe microfluidic devices that were developed as a result of such motivations.

2 Cell Sorting and Culture Using Gravity-Driven Steady Flow Microfluidic Devices

2.1 Motivation for a Gravity-Driven Steady Flow Rate Microfluidic Pump

Among the many methods to move liquid, the use of potential energy (gravity) for delivery has run through the history of human development. In ancient world, farmers took advantage of contours in the terrain to supply natural flows of water for field and crop irrigation. In modern cities and towns, water towers and tanks located on high grounds provide pressure and send water to community residence through feeder pipes. In places where economical, continuous, robust, and easy to use pumps are needed, gravity-fed water flow system is often preferred.

In the past 20 years, many miniaturized systems have been developed for operation in aqueous environments. These systems, often called lab-on-a-chip or microfluidic devices, are designed to accomplish tasks that are difficult to be performed in large scale (Harrison et al. 1993; Reyes et al. 2002; Thorsen et al. 2002; Whitesides 2006). Multiple sample handling components were integrated into small channels and structures for complete operations or creating reproducible cell culture microenvironments. Benefit by the remarkable features such as fast performance, low reagent consumption, portability, and automation, these devices thrive in bioanalytical (Di Carlo et al. 2005; El-Ali et al. 2006; Yu et al. 2007),

biomedical (Nagrath et al. 2007), chemical (You et al. 2012), and pharmaceutical (Dittrich and Manz 2006; Chen et al. 2011) fields.

However, the adoption of macroscale pumps to small microfluidic channels has been a challenge. Typical mechanical and nonmechanical pumps (such as syringe pumps (Tanaka et al. 2007), pneumatic pumps (Wang and Lee 2006), pumps that utilizes magnetic force (Kimura et al. 2008), surface acoustic waves (Girardo et al. 2008), light (Baigl 2012), or electric force (Xu and Attinger 2008) to control fluid motion) are usually bulky in size and complex to set up. The increased complexity may lead to unstable flow, bubble generation, leakage, and reducing robustness.

In contrast, gravity-driven pumps have many advantages over other formats in microfluidic systems: (1) compatibility with many kinds of materials that make up the device, (2) having little impact on the chemical and biological properties of the fluid and sample (such as cells, DNA, RNA, proteins, etc.), (3) small size and simple components that require no external pump or tubing, (4) requiring no power source as long as the device is on earth.

Due to these advantages, gravitational force has been widely used for introducing samples into microchips (Song et al. 2004; Shao et al. 2009), control fluid flow and droplet movement (You et al. 2012; Lee et al. 2014), separate particles and cells (Devendra and Drazer 2012), perfuse medium for microfluidic cell culture (Chen et al. 2011; Kondo et al. 2014), generate cell and protein patterning (Takayama et al. 1999), and conduct cellular and molecular analysis (Takayama et al. 2001; Dimov et al. 2011; Nagai et al. 2013; Taylor et al. 2015).

As the movement of liquid is caused by a hydraulic head in gravity-driven pumps, flow rates usually decrease with decreasing head pressure. This limit the use of gravity-driven pump for many assays where steady flow is needed. The development of a gravity-driven pump that delivers flow at a constant rate for extended period of time would open a broad range of emerging applications.

2.2 *Mechanism of the Gravity-Driven Steady Flow Rate Microfluidic Pump*

In a typical gravity-driven pump, fluid flow is driven by hydrostatic pressure. When both the inlet and outlet reservoirs are open to the atmosphere, the hydrostatic pressure is related to the height difference between the reservoirs by the following equation.

$$\Delta P = \rho g \Delta h,$$

where ΔP is residual pressure, ρ is the density of the liquid, g is the acceleration due to gravity, and Δh is the height difference between inlet and outlet reservoirs. As more and more fluid leaves the inlet reservoir and enters the outlet reservoir, the height difference between the reservoirs decreases, which drops the hydrostatic pressure and slows down the flow. As a result, it is difficult to maintain a steady flow rate when gravitational force is used.

As the device size shrinks, however, the surface-to-volume ratio increases, making surface-mediated effects similar to or even larger than volume-mediated effects. If dimension becomes sufficiently small, liquid can flow without the assistance of, or even overcome gravitational forces. Common microfluidic devices usually have microchannels with tenth to hundreds of micrometers in width and height, the Reynolds number (which is the ratio of momentum of a fluid to the viscosity effect) usually becomes much less than 2000, which is when turbulence appears. At such small scales, factors such as surface tension, energy dissipation, and fluid resistance start to dominate the system. The force exerted on the liquid by gravity can be readily matched by other types of forces such as capillary force (Fuerstman et al. 2007; Maki et al. 2015) such that if one creates fluid reservoirs that are sufficiently narrow (e.g., 2–3 mm diameter tubes), one can tip the reservoirs horizontally without spilling the fluid because of capillary forces.

Taking advantage of this convergence of forces at the microscale, a constant flow rate gravity-driven pump has been developed (Zhu et al. 2004). This device overcomes the limit of decreasing flow rate due to change of head pressure by utilizing fluid reservoirs that are placed in a horizontal configuration. The diameter of the reservoirs are chosen to be small enough (4 mm) so that surface tension would keep the liquid contained without spilling out even in a horizontal orientation, and large enough so that pipette tips can be used to easily introduce and retrieve liquid or samples. As fluid moves from the reservoir that is placed at a higher level to the one at a lower level, the menisci of the fluid in the reservoirs move laterally, but not up or down, maintaining the height difference and the head pressure. Therefore, flow rate remains constant. The capillary force in each reservoir cancels out, or stay consistent, because the curvature of the menisci stays consistent in shape (within certain flow rate range limit) (Fig. 1).

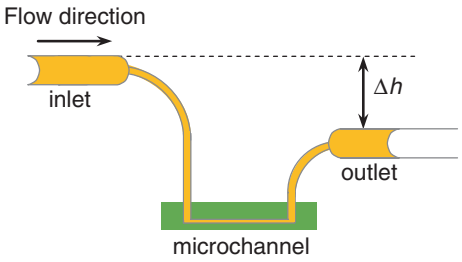

Fig. 1 Schematic diagram of the gravity-driven pump with horizontally oriented fluid reservoirs. The inlet and outlet reservoirs are connected with a microfluidic channel. The menisci in both the reservoirs move as liquid flows, but the height difference (Δh) remains constant (Zhu et al. 2004). Reproduced by permission of The Royal Society of Chemistry

2.3 Application of the Gravity-Driven Steady Flow Rate Microfluidic Pump

2.3.1 Sorting

The separation and manipulation of particles and cells according to their morphological or physical properties is indispensable for biomedical research. Cho et al. embedded horizontally oriented reservoirs in microfluidic chips with K-shape channels and demonstrated separation of motile sperm from nonmotile ones for purposes of infertility treatment using flow generated by the gravity-driven steady flow rate pumps (Cho et al. 2003) (Fig. 2).

For flow in a pipe, the Reynolds number (Re) is defined as:

$$Re = \frac{\rho v D_H}{\mu} = \frac{v D_H}{\nu} = \frac{Q D_H}{\nu A},$$

where ν is the kinematic viscosity of the fluid, ρ is the density of the fluid, D_H is the hydraulic diameter of the pipe, μ is the dynamic viscosity of the fluid, v is the mean velocity of the fluid, Q is the volumetric flow rate, A is the pipe's cross-sectional area.

Microfluidic channels are usually rectangular in shape, the hydraulic diameter is defined as:

$$D_H = \frac{4A}{P},$$

where A is the cross-sectional area, P is the wetted perimeter.

Since the Re is significantly less than 2000, the flow is laminar and two streams can flow in parallel to each other without turbulent mixing. The mixture of motile and nonmotile sperms are introduced to the microfluidic chip from the sample reservoir. As liquid flows, nonmotile sperms stayed within the original stream

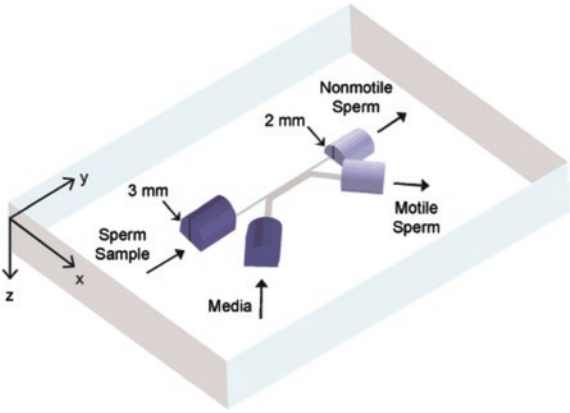

Fig. 2 The drawing illustrates the design of the sperm sorter with embedded horizontally oriented reservoirs. Reprinted with permission from Cho et al. (2003). Copyright (2016) American Chemical Society

because diffusion is slow in short residence time. Motile sperms swim at greater speed and can go across the streamlines. By the end of the separation process, motile and nonmotile sperms can be collected from separate streams. In this process, the relative flow rates between the inlet streams and outlet streams dictate position of the laminar flow interface and critically alter sorting efficiency. Thus, maintaining a steady flow is critical. The horizontally oriented reservoirs are convenient not only for easy sperm sample loading and collection but also allow maintenance of a steady gravity-driven flow.

To maintain steady flow rate for the two streamlines, the two horizontally oriented inlet reservoirs (3 mm in diameter) were 1 mm higher than the two horizontally oriented outlet reservoirs (2 mm in diameter) and integrated within the chip structure for convenience and robust operation. In this design, the capillary forces between the inlet and outlet reservoirs do not completely cancel out, but is 13 N/m^2 toward the outlet reservoir when the contact angle is assumed to be 0 (water on BSA-coated channel). The hydrostatic force of 1.0 mm height difference is 9.8 N/m^2. The flow resistance of the channel is 10^6 times greater than the reservoir, therefore the resistance of the microchannels is approximately equal to the total resistance of the system. Water is assumed to be incompressible and Newtonian, and uniform in viscosity. According to the Hagen–Poiseuille law, the pressure difference between the inlet and outlet of the channel is related to the volumetric flow rate and channel resistance.

$$\Delta P = R_h Q,$$

where R_h is the hydrodynamic resistance, Q is the volumetric flow rate. Therefore, the net pressure drop is capable of driving a bulk flow speed of 0.008 μL/s and to achieve the desired residence time for separation.

Huh et al. reported a gravity-driven particle sorting microfluidic device with hydrodynamic separation amplification. The device is made of a three-inlet two-outlet microchannel with a 90° bend. The region before the turn is placed parallel to gravity for hydrodynamic focusing. The region after the turn is perpendicular to gravity, gradually but asymmetrically widening out, generating laminar flows with widening streamlines for particle separation. In the separating region, particles of different sizes sank at different speeds resulting difference in vertical positions. As fluid flow is perpendicular to gravity and streamlines are widening out, the effect of particle sedimentation due to gravity were amplified as they flow downstream. This device provides a nice example of using gravity-driven flow together with gravity-driven separation (Huh et al. 2007) (Fig. 3).

2.3.2 Sample Loading

Gravity-driven sample loading has been automated by mounting sample vials on a moving platform or ring gear that was driven by stepping-motor controlled with a computer program. The sample vials have slotted opening at the end, but media would not spill out through the slot because of surface tension. As the ring gear rotated, a fixed sampling probe capillary passed through the open slot into the

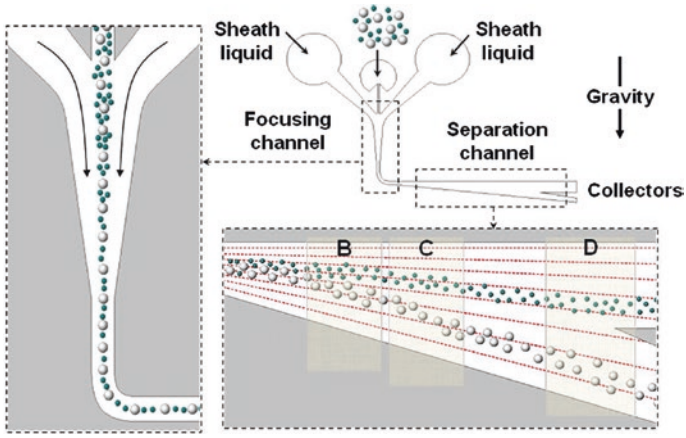

Fig. 3 Particle separation based on hydrodynamic amplification of particle sedimentation. Reprinted with permission from Huh et al. 2007. Copyright (2016) American Chemical Society

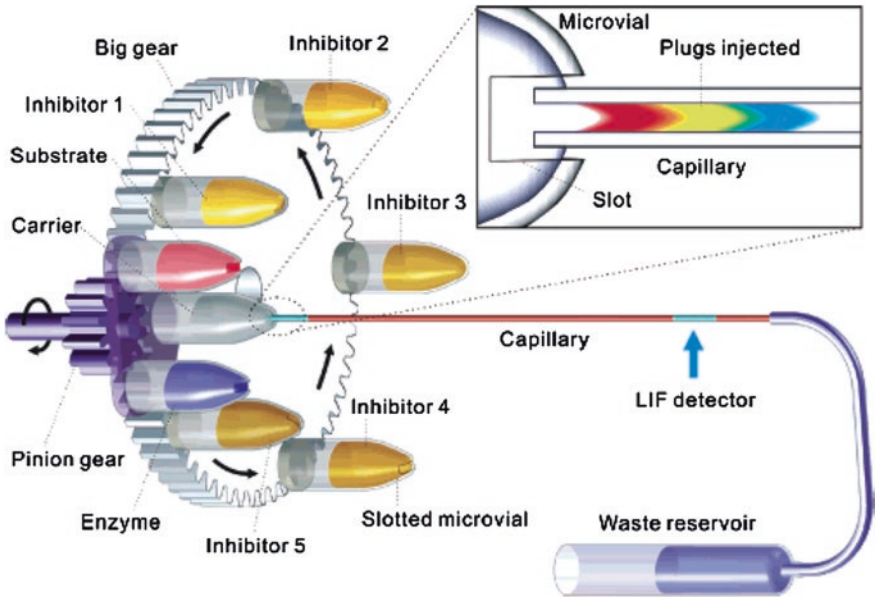

Fig. 4 Schematic diagram of automated gravity-driven sample injection system with sample slots mounted on a ring gear. Reprinted with permission from Du et al. 2006. Copyright (2016) American Chemical Society

center of the vial, then media was driven by gravity to enter the capillary probe and finally the microfluidic channels. This setup allows multiple sample reagents to dispensed sequentially and automatically (Du et al. 2005, 2006; Wang et al. 2008, 2010) (Fig. 4).

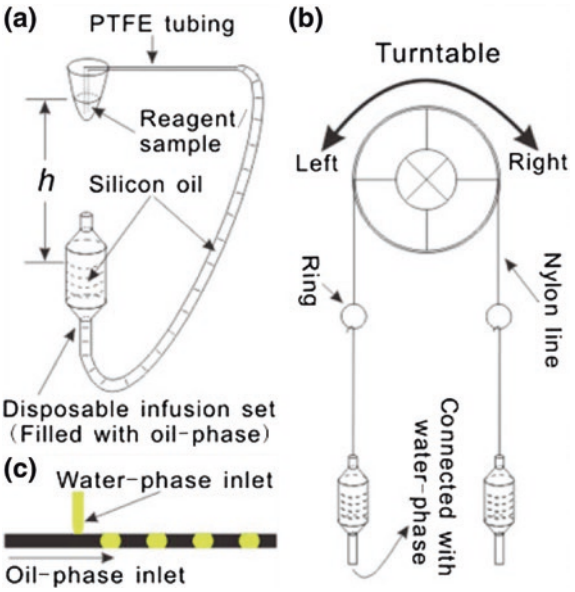

Fig. 5 Schematic drawing of the gravity-actuated pump with infusion set for droplet manipulation (Zhang et al. 2010). With permission of Springer

Zhang et al. developed a pressure-driven droplet manipulation device by using disposable infusion sets filled with dimethylsilicone oil. The tip of the infusion set was connected to a PTFE tubing. For sample loading, the PTFE tubing was submerged in water-based sample/reagent and suck in the reagent when the meniscus of the oil in the infusion set is positioned lower than that of the sample. For droplet generation, two infusion sets were hanged on both sides of a turntable with equal length Nylon lines. Rotating the turntable created height difference in the oil phase and water phase, which determined droplet generation at the water–oil intersection in T-shaped microchannel. The concept has been extended to control droplet generation of various sizes, numbers, and the mixing of two droplets. This method provides a simple, economical, flexible, and robust method for precision microdroplet manipulation (Zhang et al. 2010) (Fig. 5).

2.3.3 Perfusion Cell Culture

Gravity can drive continuous fluid flow through cell culture to simulate physiological microenvironment where nutrients are constantly supplied to the cells and waste are removed. Compared with other fluid-driven mechanism, the devices relying on gravity pumping are usually small, high biocompatibility, and more easily adapted to the high humidity, space confined cell culture incubator environments. Various strategies have been employed to use gravity-driven flow for perfusion cell culture.

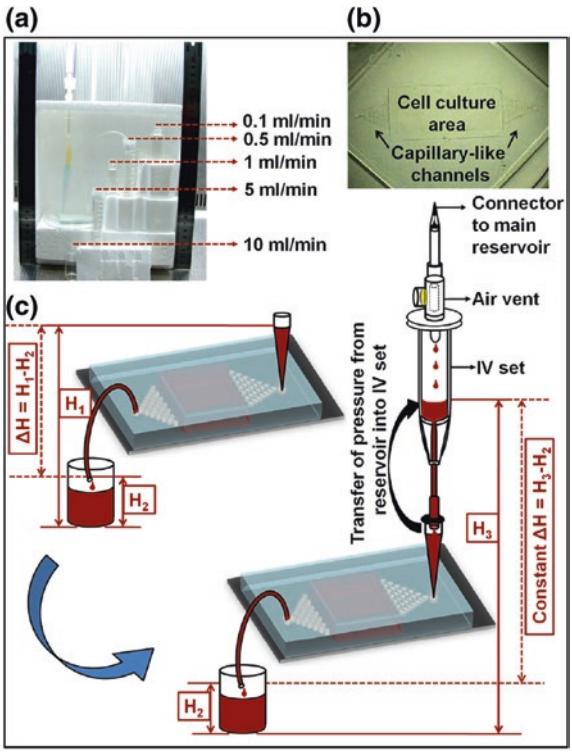

Fig. 6 A microfluidic perfusion chip with IV infusion set for providing constant flow. Reprinted from Marimuthu and Kim 2013. Copyright (2016) with permission from Elsevier

Zhu et al. (2004) designed horizontally oriented fluid reservoir to hold constant hydraulic head pressure between the inlets and outlets. They demonstrated continuous perfusion cell culture at constant and slow flow rate for days and tested the effect of drug toxicity on cells.

Marimuthu and Kim incorporated an intravenous (IV) infusion set between the medium reservoir and the microchannel, keeping a constant hydraulic head pressure between the meniscus in the IV set and the outlet tubing. This setup is capable of generating flow rates ranging from 0.1 to 10 ml/min for studying the effect of shear stress on fibroblast cell cultures (Marimuthu and Kim 2013) (Fig. 6).

2.3.4 Gradient Generation

Gradient generation is a microfluidic technique to expose cells to diffusible signals. As one of the extracellular cues, chemical gradients induce concentration dependent cellular responses, such as neuron axon guidance (Zheng et al. 1994), movement of leukocytes toward inflammatory site (Letterio and Roberts 1998), and cancer metastasis (Raman et al. 2007), etc. To study such responses, it is critical to control the concentration of chemical and biochemical molecules with good spatial resolution and temporal stability.

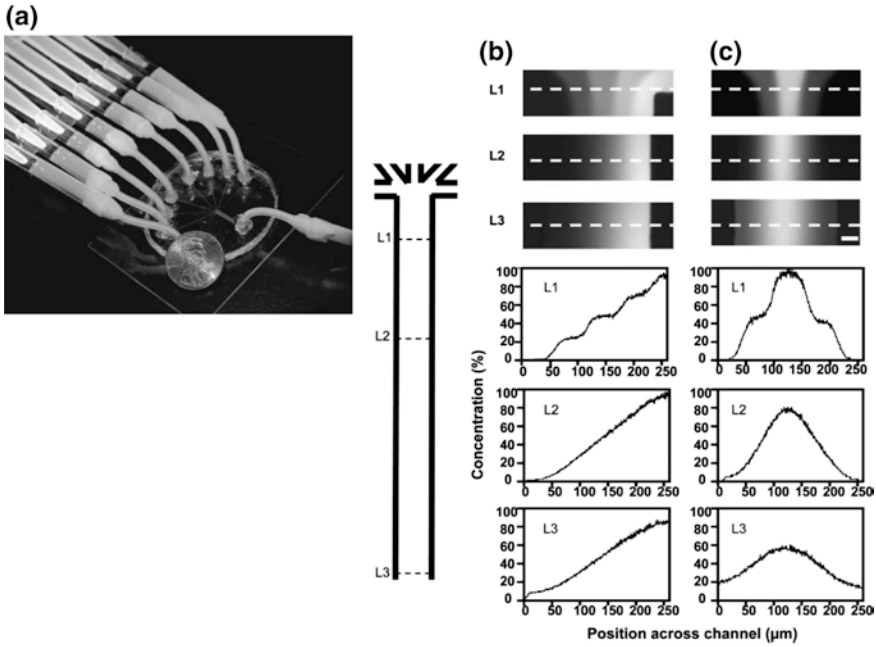

Fig. 7 Gravity-driven perfusion chip with eight horizontally placed reservoirs to provide steady flow of cell culture media with different drug concentrations (Zhu et al. 2004). Reproduced by permission of The Royal Society of Chemistry

Taking advantage of the property of laminar flow in microfluidic channels, chemical gradient can be generated and maintained in microfluidic channels by using steady flow gravity-pump(s). Although there is diffusion of the soluble molecules, the fluid concentration at any fixed location within the channel is fixed at a given flow velocity. Therefore, different fluid layers may maintain different chemical concentration and generate a gradient profile (Zhu et al. 2004). Gradient generation in microfluidic channels reflects a balance between convective and diffusive forces. Depending on the relation between the flow velocity, width of the fluid layer, and the diffusion coefficient, the gradient can be created in various profiles, such as "step," "linear," or "nonlinear," etc. (Fig. 7).

3 Parallel and Periodic Cell Shearing with Gravity-Driven Microfluidic Oscillator

3.1 Motivation of the Gravity-Driven Oscillator

Many cells in the body are subject to periodic biomechanical cues such as vascular flow and periodic biochemical cues such as hormone release. Microfluidic

devices have been instrumental in enabling exploration of the implications of such biorhythms (Jovic et al. 2010; Sumit et al. 2015; Goldbeter 2008). These microfluidic chips typically rely on off-chip controllers and actuators (Thorsen et al. 2002; Ricicova et al. 2013) such as syringe pumps and external mechanical actuators to create the required flow switching. The controllers and actuators, however, present two challenges for experimental scale up: (1) The number of external controllers and actuators required increases linearly with the number of temporally independent switching events required. (2) The number of tubing and interconnects required also increases rapidly. Inspired by electronic circuits that circumvent such power-surge problems by using constant voltage-driven circuits, we describe the development of microfluidic oscillator arrays that are driven by gravity-induced constant pressure.

3.2 Mechanism of the Gravity-Driven Oscillator

Oscillator function The gravity-driven oscillator array generates completely independent parallel flow pulses from two input wells without any off-chip controllers or actuators (Fig. 8). A height difference between the oscillator circuits and the two input wells delivers a constant pressure flow to the oscillators. The pressure drives the alternating opening and closing of two interconnected valves within each oscillator. While each oscillator is connected to each other in parallel to a common pressure source, each oscillator operates with independent timing. This function can be applied to a systematic experiment to analyze endothelial cell elongation and alignment in response to different periodic shear flows.

Oscillator structure Gravity-driven oscillator array with a close up of one of its oscillators is illustrated in Fig. 9. The inset of Fig. 9 shows that the oscillator

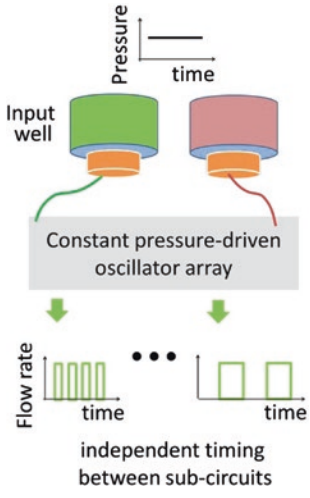

Fig. 8 Gravity-driven microfluidic oscillator. Height difference between input wells and the oscillator applies constant pressure on the oscillator. The oscillator produces multiple parallel periodic flows driven by pressure from a constant gravitational potential source (Kim et al. 2015)

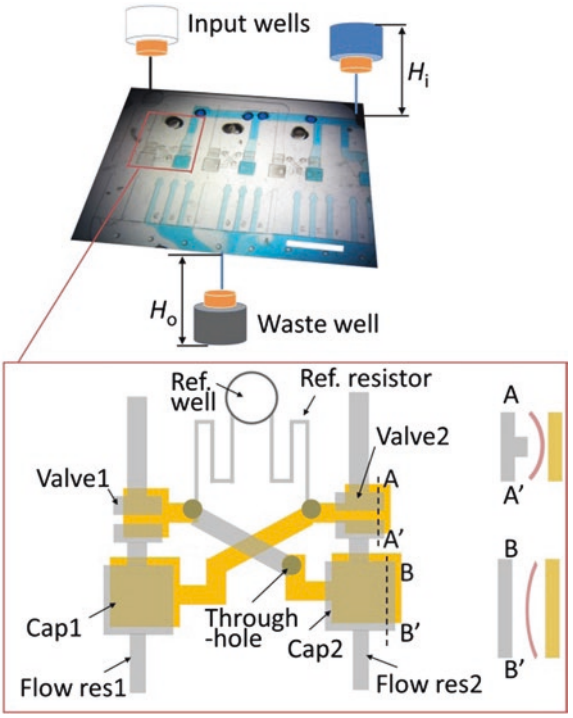

Fig. 9 Schematic of the oscillator system. Each oscillator consists of microfluidic component, such as microfluidic valves, resistors, and capacitors. The microfluidic resistors are channels and the capacitors are chambers having elastomeric membranes (Kim et al. 2015)

consists of three layers including a thin membrane middle layer, and top (gray color), and bottom (dark yellow colors) layers. The top and bottom layers have microfluidic resistor, capacitor and valve features. The microfluidic resistor is a channel that manipulates pressure or flow rate with its fluidic resistance. The microfluidic capacitor is an elastomeric membrane having two chambers on both sides of the membrane, and stores pressure energy with the membrane's elastic deformation. In the oscillator, valve 1 and capacitor 1 are serially linked. Thus, when valve 1 opens, a solution moves from valve 1's top layer to flow resistor 1 through capacitor 1's top layer and then goes to the outlet. In the valve and the capacitor regions, the middle membrane layer prevents direct solution motion across the top to bottom layer. Flow across the top to bottom layer is enabled only at through holes.

Operation of the oscillator The operation process of the oscillator is explained through pressure change of the oscillator components. The relative vertical position of the oscillator is set as 0 and this makes reference well pressure (P_{ref}) to 0 because the reference well is open to the environment (Fig. 10a). Inlet (P_i) and outlet (P_o) pressures of the oscillator have constant positive and negative values, respectively. Under this condition, the open and close states of valve 1 alter capacitor 1's top pressure (P_{C1t}) as follows:

$$P_{C1t} \approx P_i \text{ when valve 1 opens}$$

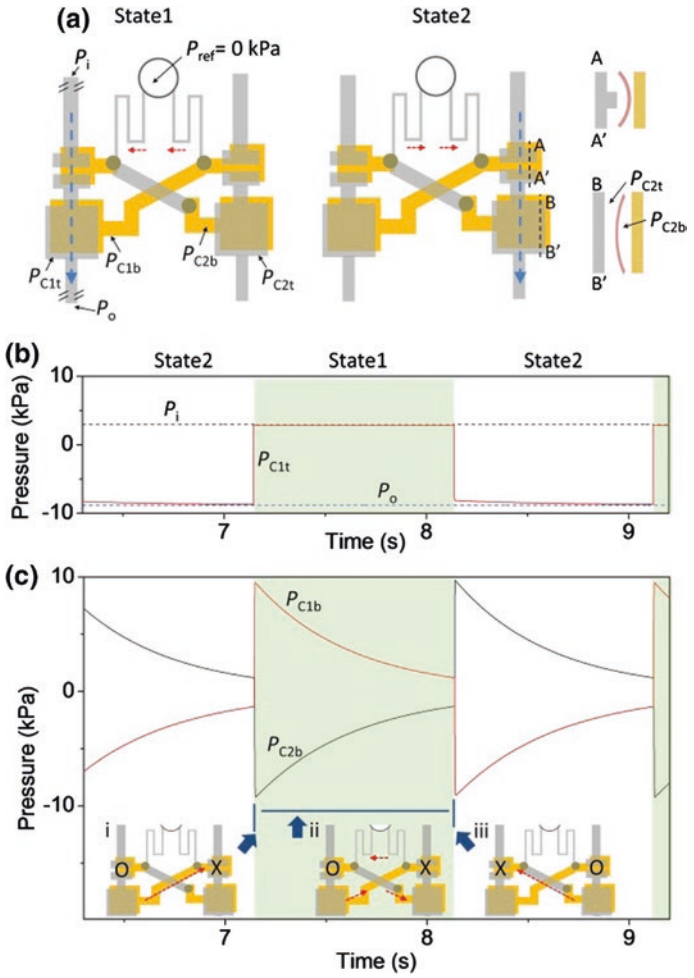

Fig. 10 Self-switching process of the oscillator. **a** Periodic opening and closing of the two valves. When one valve opens, the other valve closes. **b** Theoretical pressure profile of P_{C1t}. P_i and P_o are inlet and outlet pressures of the oscillator, respectively. **c** Theoretical pressure profiles of P_{C1b} and P_{C2b} (Kim et al. 2015)

$$P_{C1t} \approx P_o \text{ when valve 1 closes}$$

Owing to fluidic resistances of the channels connected to valve 1, valve 1's top inlet pressure (P_{V1t}) is constant as P_i regardless of the open and close of valve 1. Additionally, capacitor 1's bottom pressure (P_{C1b}) is nearly the same with valve 2's bottom pressure (P_{V2b}) owing to relatively small fluidic resistance of the channel connecting the bottoms of capacitor 1 and valve 2. These pressure conditions apply to the capacitor 2 and valve 2 because the oscillator is symmetric.

The pressure variations of P_{C1t} are illustrated in Fig. 10b; in state 1 valve 1 is open, whereas in state 2 valve 1 is closed. At the moment of valve 1 open (outset of state 1), the sharp rise of P_{C1t} (Fig. 10b) makes P_{C1b} and P_{V2b} instantly high (Fig. 10c). The high P_{V2b} closes valve 2. This makes capacitor 2's top pressure to ~ P_o and its bottom pressure (P_{C2b}) low (the beginning of green region of 9c). The pressure difference between P_{C1b} and P_{C2b} results in local fluidic motion from the bottom of valve 2 to that of valve 1 through the reference well and resistors; see the red arrows of state 1 of Fig. 10a and 3c-inset. As a result, P_{C1b} decreases and P_{C2b} increases (green region of Fig. 10c). Afterwards, P_{C1b} (i.e. P_{V2b}) becomes sufficiently low in valve 2 (the end of green region of Fig. 10c). Then, valve 2 opens and this raises P_{C2b} and P_{V1b} abruptly. Consequently, valve 1 closes. In this way, alternative open and close of the two valves continue.

Parallel control of oscillation period and flow rate The oscillation period is regulated by the change rate of P_{C1b} and P_{C2b}. Once valve 1 opens, P_{C1b} ($\approx P_{V2b}$) decreases. Then valve 2 opens owing to the low P_{V2b} and valve 1 closes. Because of the connection between capacitor 1 and reference resistor, the change rate of P_{C1b} is proportional to R_rC, where R_r is the fluidic resistance of reference resistor and C is the capacitance of capacitor 1 and 2 (Fig. 9). Thus, oscillation period is approximately proportional to R_rC. On the other hand, output flow rate is determined by the fluidic resistance of flow resistors (Fig. 9).

The power of the oscillator is that once the oscillators are connected in parallel, the oscillator array generates independent, parallel flows. Figure 11a shows an oscillator array and each oscillator Ai ($i = 1, 2, 3$) has flow resistor 1 (Fig. 8a) connected to three downstream flow resistors (a_{i1}, a_{i2}, a_{i3}) that have three different fluidic resistances, respectively. Thus, each oscillator Ai generates three different fluidic pulses through a_{i1}, a_{i2}, and a_{i3} (Fig. 11b). The flow rates of a_{i1}, a_{i2}, and a_{i3}

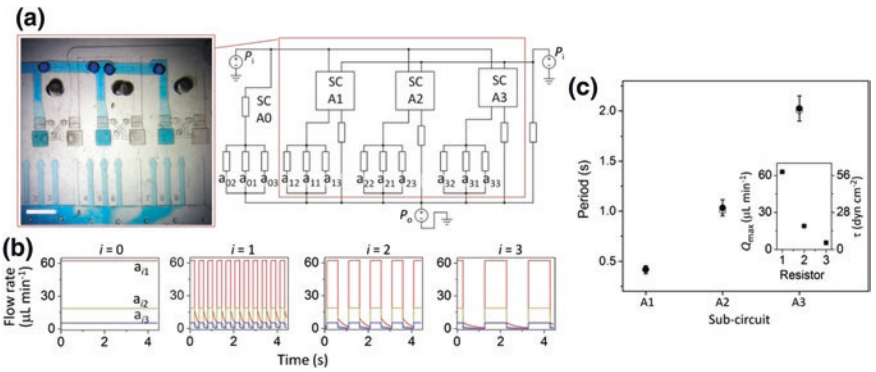

Fig. 11 Microfluidic oscillator array. **a** Oscillator array with fast period and high flow rate. **b** Theoretical flow profiles. Panels from left to right relate to the flows by oscillator unit Ai ($i = 0$–3). Flow profiles from top to bottom lines at each panel are at resistors a_{i1}, a_{i2}, a_{i3} connected to oscillator Ai, respectively. **c** Performance of the oscillator array. Filled and unfilled points are the experimental and theoretical results, respectively. The *insets* show the maximum flow rate (Q_{max}) and shear stress (τ) of resistors a_{i1}, a_{i2}, a_{i3} (Kim et al. 2015)

are 5, 19, and 63 μL/min, respectively, and oscillators A1 to A3 open their valves with periods of 2.0, 1.0, and 0.4 s, respectively (Fig. 11c).

3.3 Application of the Gravity-Driven Oscillator

Parallel shearing for cell morphology change The responsiveness of endothelial cells to different levels of shear stress and periodic pulse is evaluated with the oscillator array. The cells (Human umbilical vein endothelial cells, HUVECs) were seeded in the resistors a_{i1} to a_{i3} of oscillator Ai (Fig. 11a). Periodic flow pulses of 0, 0.5, 1, and 2.5 Hz were generated by the oscillators A0 to A3 respectively. These pulses applied shear stresses of 5, 18, and 58 dyn/cm^2 to the cells in the resistors a_{i1}, a_{i2}, and a_{i3}, respectively. The changes in the cell morphology due to 5 versus 58 dyn/cm^2 at 1 Hz pulse for 12 h are shown in Fig. 12a and the cells at 58 dyn/cm^2 are more elongated than those at 5 dyn/cm^2. The shape of the cells becomes more linear as time goes by. This shape change is quantified by circularity that is defined as $4\pi A/L_p$, which is 1 for a circle and 0 for a line. A is the area of the cell, and L_p is the perimeter of the cell. The variation of the cell elongation for 12 h under different shear stress and frequency is shown in Fig. 12b.

Relative circularity, which is the circularity at 12 h divided by the initial mean circularity at 0 h, is used to quantify the influence of various shear stress levels and pulse frequency on cell morphology. At higher relative circularity, cells are less elongated after 12 h. Figure 12c summarizes the result. Notably, frequency

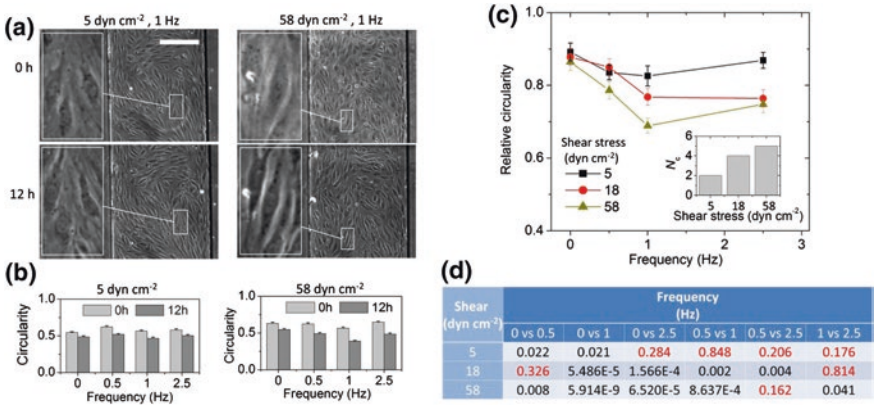

Shear (dyn cm^{-2})	Frequency (Hz)					
	0 vs 0.5	0 vs 1	0 vs 2.5	0.5 vs 1	0.5 vs 2.5	1 vs 2.5
5	0.022	0.021	0.284	0.848	0.206	0.176
18	0.326	5.486E-5	1.566E-4	0.002	0.004	0.814
58	0.008	5.914E-9	6.520E-5	8.637E-4	0.162	0.041

Fig. 12 Cell elongation response to shearing conditions by simultaneous on-chip testing. **a** Photos showing endothelial cell elongation. *Scale bar* 200 μm. **b** Circularity change of cells. **c** Relative circularity at 12 h. *Error bars* of **b** and **c** show the standard error ($n = 80$). The *inset* shows the number (N_c) of frequency pairing-combinations with statistically significant differences ($p < 0.05$) in relative circularity between them. **d** p values by independent two-sample t test at the 5 % significance level. *Red colored p* values indicate that corresponding two-sample groups are not significantly different at the 5 % significance level (Kim et al. 2015)

influences on circularity more prominently as shear stress increases. Statistically different cellular elongation is identified with an independent two-sample *t* test for two frequency conditions. Six combinations of 2 frequency-comparisons at each shear stress condition are produced by the 4 frequency conditions (Fig. 12d). Only 2 out of 6 combinations were significantly different at 5 dyn/cm^2 shearing. The combinations of significantly different pairs increased from 4 to 5, as the shear stress level increased from 18 to 58 dyn/cm^2. The result is summarized in the inset of Fig. 12c and suggests that with increasing shear rate the influence of frequency on circularity increases.

References

Baigl D (2012) Photo-actuation of liquids for light-driven microfluidics: state of the art and perspectives. Lab Chip 12:3637–3653

Chen SY, Hung PJ, Lee PJ (2011) Microfluidic array for three-dimensional perfusion culture of human mammary epithelial cells. Biomed Microdevices 13:753–758

Cho BS, Schuster TG, Zhu XY et al (2003) Passively driven integrated microfluidic system for separation of motile sperm. Anal Chem 75:1671–1675

Devendra R, Drazer G (2012) Gravity driven deterministic lateral displacement for particle separation in microfluidic devices. Anal Chem 84:10621–10627

Di Carlo D, Ionescu-Zanetti C, Zhang Y et al (2005) On-chip cell lysis by local hydroxide generation. Lab Chip 5:171–178

Dimov IK, Kijanka G, Park Y et al (2011) Integrated microfluidic array plate (iMAP) for cellular and molecular analysis. Lab Chip 11:2701–2710

Dittrich PS, Manz A (2006) Lab-on-a-chip: microfluidics in drug discovery. Nat Rev Drug Discov 5(3):210–218

Du WB, Fang Q, He QH et al (2005) High-throughput nanoliter sample introduction microfluidic chip-based flow injection analysis system with gravity-driven flows. Anal Chem 77:1330–1337

Du WB, Fang Q, Fang ZL (2006) Microfluidic sequential injection analysis in a short capillary. Anal Chem 78:6404–6410

El-Ali J, Sorger PK, Jensen KF (2006) Cells on chips. Nature 442:403–411

Fuerstman MJ, Lai A, Thurlow ME et al (2007) The pressure drop along rectangular microchannels containing bubbles. Lab Chip 7:1479–1489

Girardo S, Cecchini M, Beltram F et al (2008) Polydimethylsiloxane–$LiNbO_3$ surface acoustic wave micropump devices for fluid control into microchannels. Lab Chip 8:1557–1563

Goldbeter A (2008) Biological rhythms: clocks for all times. Curr Biol 18:R751–R753

Harrison DJ, Fluri K, Seiler K et al (1993) Micromachining a miniaturized capillary electrophoresis-based system on a chip. Science 261:895–897

Huh D, Bahng JH, Ling Y et al (2007) Gravity-driven microfluidic particle sorting device with hydrodynamic separation amplification. Anal Chem 79:1369–1376

Jovic A, Howell B, Cote M, Wade SM, Mehta K, Miyawaki A, Neubig RR, Linderman JJ, Takayama S (2010) Microfluidic-induced phase-locked calcium signals elucidate circuit architecture of oscillatory calcium pathway. PLoS Comp Biol 6:e1001040

Kim S-J, Yokokawa R, Cai Lesher-Perez S, Takayama S (2015) Multiple independent autonomous hydraulic oscillators driven by a common gravity head. Nat Commun 6:7301

Kimura H, Yamamoto T, Sakai H et al (2008) An integrated microfluidic system for long-term perfusion culture and on-line monitoring of intestinal tissue models. Lab Chip 8:741–746

Kondo E, Wada KI, Hosokawa K et al (2014) Microfluidic perfusion cell culture system confined in 35 mm culture dish for standard biological laboratories. J Biosci Bioeng 118:356–358
Lee M, Collins JW, Aubrecht DM et al (2014) Synchronized reinjection and coalescence of droplets in microfluidics. Lab Chip 14:509–513
Letterio JJ, Roberts AB (1998) Regulation of immune responses by TGF-beta. Annu Rev Immunol 16:137–161
Maki AJ, Hemmila S, Hirvonen J et al (2015) Modeling and Experimental Characterization of Pressure Drop in Gravity-Driven Microfluidic Systems. J Fluid Eng Trans ASME. doi:10.1115/1.4028501
Marimuthu M, Kim S (2013) Pump less steady-flow microfluidic chip for cell culture. Anal Biochem 437:161–163
Nagai M, Matsmoto N, Kawashima T (2013) Reversible motion control of Vorticella stalk in microchannel. Microelectron Eng 108:28–32
Nagrath S, Sequist LV, Maheswaran S et al (2007) Isolation of rare circulating tumour cells in cancer patients by microchip technology. Nature 450:U1210–U1235
Raman D, Baugher PJ, Thu YM et al (2007) Role of chemokines in tumor growth. Cancer Lett 256:137–165
Reyes DR, Iossifidis D, Auroux PA et al (2002) Micro total analysis systems. 1. Introduction, theory, and technology. Anal Chem 74:2623–2636
Ricicova M, Hamidi M, Quiring A, Niemistö A, Emberly E, Hansen CL (2013) Dissecting genealogy and cell cycle as sources of cell-to-cell variability in MAPK signaling using high-throughput lineage tracking. Proc Natl Acad Sci USA 110:11403–11408
Shao J, Wu L, Wu J et al (2009) Integrated microfluidic chip for endothelial cells culture and analysis exposed to a pulsatile and oscillatory shear stress. Lab Chip 9:3118–3125
Song QJ, Greenway GM, McGreedy T (2004) Interfacing a microfluidic electrophoresis chip with inductively coupled plasma mass spectrometry for rapid elemental speciation. J Anal At Spectrom 19:883–887
Sumit M, Neubig RR, Takayama S, Linderman JJ (2015) Band-pass processing in GPCR signaling pathway selects for NFAT transcription factor activation. Integr Biol 7:1378–1386
Takayama S, McDonald JC, Ostuni E et al (1999) Patterning cells and their environments using multiple laminar fluid flows in capillary networks. Proc Natl Acad Sci USA 96:5545–5548
Takayama S, Ostuni E, LeDuc P et al (2001) Laminar flows—Subcellular positioning of small molecules. Nature 411:1016
Tanaka Y, Kikukawa Y, Sato K et al (2007) Culture and leukocyte adhesion assay of human arterial endothelial cells in a glass microchip. Anal Sci 23:261–266
Taylor Am, Menon S, Gupton SL (2015) Passive microfluidic chamber for long-term imaging of axon guidance in response to soluble gradients. Lab Chip 15:2781–2789
Thorsen T, Maerkl SJ, Quake SR (2002) Microfluidic large-scale integration. Science 298:580–584
Wang CH, Lee GB (2006) Pneumatically driven peristaltic micropumps utilizing serpentine-shape channels. J Micromech Microeng 16:341–348
Wang Y, Luo J, Chen H et al (2008) A microchip-based flow injection-amperometry system with mercaptopropionic acid modified electroless gold microelectrode for the selective determination of dopamine. Anal Chim Acta 625:180–187
Wang Y, He Q, Dong Y et al (2010) In-channel modification of biosensor electrodes integrated on a polycarbonate microfluidic chip for micro flow-injection amperometric determination of glucose. Sens Actuator B Chem 145:553–560
Whitesides GM (2006) The origins and the future of microfluidics. Nature 442(7101):368–373
Xu J, Attinger D (2008) Drop on demand in a microfluidic chip. J Micromech Microeng 18:065020
You I, Kang SM, Lee S et al (2012) Polydopamine microfluidic system toward a two-dimensional, gravity-driven mixing device. Angew Chem Int Edit 51:6126–6130

Yu H, Alexander CM, Beebe DJ (2007) Understanding microchannel culture: parameters involved in soluble factor signaling. Lab Chip 7:726–730

Zhang K, Liang Q, Ma S et al (2010) A gravity-actuated technique for flexible and portable microfluidic droplet manipulation. Microfluid Nanofluid 9:995–1001

Zheng JQ, Felder M, Connor JA et al (1994) Turing of nerve growth cones induced by neurotransmitters. Nature 368:140–144

Zhu XY, Chu LY, Chueh BH et al (2004) Arrays of horizontally-oriented mini-reservoirs generate steady microfluidic flows for continuous perfusion cell culture and gradient generation. Analyst 129:1026–1031

Inertial Microfluidic Cell Separation

Joseph M. Martel-Foley

Abstract The ability to rapidly manipulate cells within microfluidic devices has been a fascinating goal for engineers across disciplines over the past two decades. With highly controllable flows and the ability to create microstructures on the same scale as cells, a large variety of technologies to sort and separate cells have been rapidly developed. One of these technologies, inertial focusing, stands out for its ease of use and high throughput. Inertial focusing utilizes passively generated forces within microchannels to align and separate cells based upon numerous factors including size, shape, and deformability of the suspended particles or cells. With so many different technologies, even within the realm of inertial focusing cell separation, it can be difficult to distinguish and choose one for a given application. Here I will attempt to quantify functional differences in separation techniques from both the fundamental perspective and from a perspective of implementation giving perhaps a means of choosing a technology that is right for the application.

Keywords Inertial focusing · Microfluidics · Cell separation · Cell isolation · Equilibrium separation · Dynamic separation

1 Introduction

The ability to rapidly separate and sort cells has paved the way for single cell biology, the understanding of the heterogeneity of gene expression, creating a new paradigm in which biology is studied. With improved understanding of the

J.M. Martel-Foley (✉)
Wentworth Institute of Technology, 550 Huntington Avenue, Boston, MA 02115, USA
e-mail: martelj@wit.edu

W. Lee et al. (eds.), *Microtechnology for Cell Manipulation and Sorting*,
Microsystems and Nanosystems, DOI 10.1007/978-3-319-44139-9_7

importance of different subpopulations of cells in immunology, disease, and homeostasis, the quest for technologies with the ability to isolate these subpopulations was hastened. Perhaps the most ubiquitous technology in this realm is fluorescence activated cell sorting (FACS). The impressive performance of FACS systems using a combination of up to 14 fluorescent signals and 50,000 cells sorted per second along with the standardization of measurements makes it truly a gold standard for new technologies to reach (Hosic et al. 2015). This remarkable engineering achievement comes with a large price tag that limits it to centralized research facilities and makes it difficult to utilize as a means for personalized and point-of-care medicine.

Another popular research tool is magnetic activated cell sorting (MACS) (Miltenyi et al. 1990). Essentially, MACS replaces the fluorophores used in FACS with magnetic beads allowing for separation of cells when exposed to a magnetic field. Most bench-top versions of this technique are extremely high throughput but have lower purity outputs and reduced numbers of different populations that can be separated. Magnetic beads can also hinder imaging and other downstream separation if positive selection is utilized (Ozkumur et al. 2013). Both of these technologies (FACS and MACS) require the a priori knowledge of target surface molecules in order to attach either fluorophores or magnetic particles.

One area that shows promise in developing accessible technologies with the ability to replicate the performance of FACS with improved throughput of MACS is microfluidics. Microfluidics, or the study and application of flows within channels with micrometer scale dimensions, enables highly predictable fluid motion and massively parallelized processing capabilities using fabrication technology adapted from integrated circuit development. Microfluidics also offers new abilities beyond improved performance notably the ability to take advantage of non-antibody-based biomarkers and the ability to obtain and utilize greater information content about the cells being sorted.

One fundamentally rapid microfluidic technology for cell separation that has been studied over the past decade is inertial focusing (Di Carlo et al. 2007, 2008). Inertial focusing is a unique means of separating cells based upon particle size, shape, and other mechanical properties. This separation is achieved at high speeds as the inertia of the fluid becomes significant in microflows thereby imparting forces on cells purely by flowing the cell laden fluid through a device allowing for highly precise separation.

The rest of this chapter will describe how inertial focusing has been studied and used for cell separation categorized by whether the implementation of inertial focusing is based upon an equilibrium or dynamic behavior. This will be followed by recent research in these areas and a comparison of different types of inertial focusing devices. Finally, concluding remarks will be made about the future of inertial focusing and its potential for cell separation and sorting.

2 Background

2.1 Brief History

Inertial focusing was discovered in the 1960s by a pair of scientists, Segré and Silberberg, who were fascinated by the motion of neutrally buoyant particles across streamlines to an annulus in a cylindrical pipe (Segre and Silberberg 1961, 1962; Segré and Silberberg 1961). They were able to determine that the behavior they witnessed of particles migrating to an annulus in a pipe at elevated Reynolds numbers was due to some type of second-order (i.e., inertial) effect. This prompted mathematic and scientific study of the phenomenon over the next few decades with major improvements in understanding of the mechanism of such surprising results. Most notably researchers were able to elucidate the key missing balance of forces that could explain the "tubular pinch effect" as described by Segré and Silberberg (Ho and Leal 1974; Saffman 1965; Vasseur and Cox 1976). The application of numerical methods to these complex problems was able to predict certain forces (Matas et al. 2004, 2009; Feng et al. 1994a, b; Asmolov 1999).

Despite theses improvements in understanding the mechanisms behind the phenomenon, the utility of inertial focusing was not truly discovered until its application within microfluidics. The transition from 1-dimensional (circular) to 2-dimensional (rectangular) cross sections caused new behaviors to emerge and sparked a now flourishing field of study. Figure 1 shows characteristic images of the initially discovered behaviors of alignment and ordering caused by inertial focusing in microchannels (Di Carlo et al. 2007). Alignment refers to the formation of particle-rich and particle-free streams across a channel cross section: Particles enter the channel randomly dispersed (Fig. 1a left) and they migrate across streamlines to equilibrium positions as they flow through the channel (Fig. 1a right). A fluorescent streak image of fluorescent particles being focused along an alternating curvature channel is shown in Fig. 1b. These equilibrium positions depend greatly on the channel shape, flow properties, and particle

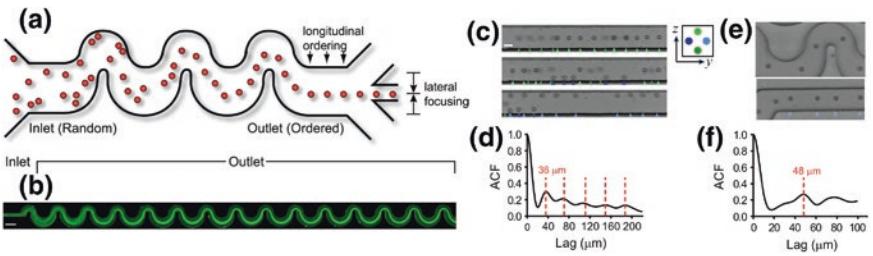

Fig. 1 Schematic representation and images of inertial focusing behaviors of (**a**–**b**) alignment and (**c**–**f**) ordering. ACF is an auto correlation function depicting the likelihood of witnessing a certain downstream spacing, in the flow direction, between consecutive focused particles. Copyright (2007) National Academy of Sciences, USA (Di Carlo et al. 2007)

dimensions. The second observation was that particles not only aligned but also formed trains of particles evenly spaced in the flow direction as shown in Fig. 1c and e with measurements of the probability for particles to be found at different inter-particle spacing distances presented for both straight (Fig. 1d) and alternating curve channels (Fig. 1e) (Di Carlo et al. 2007; Humphry et al. 2010). From these initial discoveries several different microchannel designs have been developed for utilizing the fundamental forces responsible for alignment and ordering to produce separation between particles.

2.2 Basics

The alignment and ordering behaviors occur due to inertial effects of fluid flow imparting shear and pressure forces on suspended particles causing them to migrate across streamlines unlike in low Reynolds number flow where suspended particles predictably follow streamlines except when impacting walls or other particles. Therefore, one of the most important factors for achieving inertial focusing is a high enough Reynolds number when inertial effects become of similar scale to viscous effects. The channel Reynolds number defines this ratio and is given in Eq. 1, where ρ is the fluid density, μ is the fluid viscosity, U_{Max} is the maximum velocity of the fluid, and D_{h} is the hydraulic diameter of the channel, defined as $D_{\mathrm{h}} = 2hw/(h + w)$, where h and w are the height and width, respectively, of the channel cross section.

$$Re_C = \rho U_{\mathrm{Max}} D_{\mathrm{h}}/\mu \tag{1}$$

This ratio along with a particle large enough to take up a significant portion of the channel cross section, also known as the particle confinement ratio, a/D_{h}, where a is the particle diameter, are the essential criteria for achieving inertial focusing. Combining these form the particle Reynolds number as shown in Eq. 2. It is generally accepted that particle focusing can be achieved when $Re_{\mathrm{P}} > 1$ and $a/D_{\mathrm{h}} > 0.07$.

$$Re_{\mathrm{P}} = Re_{\mathrm{C}}(a/D_{\mathrm{h}}) = \rho U_{\mathrm{Max}} a^2/(\mu D_{\mathrm{h}}) \tag{2}$$

Within curved channels another nondimensional number is also important to characterize a secondary flow that forms in such channels called Dean flow. Dean flow is the consequence of the momentum of faster moving fluid in the center of the channel being carried to the outer wall of the channel and setting up a dual recirculation flow. The strength of this secondary flow is characterized by the nondimensional Dean number, defined in Eq. 3, which is dependent on the shape of the cross section, the Reynolds number of the channel flow, and the radius of the channel curvature, R:

$$De = Re_{\mathrm{C}}(D_{\mathrm{h}}/(2R))^{1/2} \tag{3}$$

These nondimensional variables characterize most inertial focusing flows and while they can range between different styles of separation devices their average values and standard deviations are 112 ± 76.5, 3.59 ± 7.86, and 24.1 ± 26.8 for Re_C, Re_P, and De, respectively, across 59 individual inertial focusing studies.

2.2.1 Forces

There are three essential forces that are prominent in inertial focusing systems leading to the alignment of particles within a channel; 1, a wall interaction force, 2, a shear gradient lift force, and 3, when applicable, a secondary flow drag force, all depicted schematically in Fig. 2. Briefly, the wall interaction force is due to the pressure buildup between the wall and a particle moving nearby and is directed away from the wall. This near-field force drops off quickly with distance from the wall. This force can be estimated for a channel using Eq. 4, assuming a lift coefficient, $C_{WI} = 0.5$. This coefficient is dependent upon Reynolds number and position within a channel (Martel and Toner 2014).

$$F_{WI} = C_{WI}\rho U_{Max}^2 a^6 / D_h^4 \tag{4}$$

The shear gradient lift force is due to the nonlinear velocity profile associated with flow through pipes that imparts a pressure and shear-based lift force toward the walls of a channel, where on the scale of a particle, the velocity gradient across the particle is more linear. The magnitude of this force can be estimated using Eq. 5, assuming a lift coefficient, $C_{SG} = 0.5$. This coefficient is again dependent upon Reynolds number and position within a channel.

$$F_{SG} = C_{SG}\rho U_{Max}^2 a^3 / D_h \tag{5}$$

Finally, in many inertial focusing separation systems, secondary flows perpendicular to the main flow direction, such as Dean flow, impart a drag force whose magnitude is proportional to the secondary flow velocity that can be estimated assuming a Stokes' drag relationship as defined in Eq. 6. The secondary flow

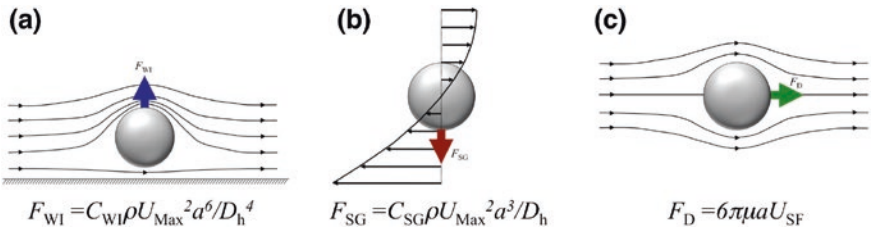

Fig. 2 Schematics presenting the three major forces that are used in inertial focusing systems; **a** Wall interaction force, **b** shear gradient lift force, and **c** secondary flow drag force (Martel and Toner 2014)

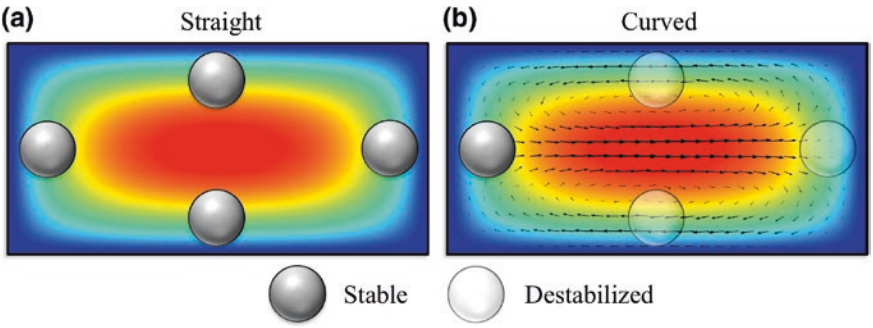

Fig. 3 Typical inertial focusing equilibrium position locations within a rectangular cross-sectioned channel in both **a** straight and, **b** curved variations. The center of curvature for the curved channel, in (**b**), would be to the *left* (Martel and Toner 2014)

velocities vary significantly in both magnitude and direction within the channel cross section. More in-depth reviews of the physics of inertial focusing are available elsewhere (Martel and Toner 2014; Amini et al. 2014; Di Carlo 2009).

$$F_{\mathrm{D}} = 6\pi\mu a U_{\mathrm{SF}} \tag{6}$$

In straight channels with a rectangular cross section, the equilibrium positions are centered on each face as depicted in Fig. 3a with the number of particles ended up at each position related to the aspect ratio. Once curvature is added to the channel's path secondary flows, of sufficient magnitude, will destabilize three of the equilibria leaving a single focused stream of particles at the wall closest to the radius of curvature as depicted in Fig. 3b.

The take home point is that these forces are the key to utilizing separation and the greater understanding we can generate about each improves our ability to precisely design microfluidic separators.

2.2.2 Channel Configurations

As previously mentioned, the magnitudes of these three primary forces can be adjusted using both flow parameters as well as channel design. Several different channel designs have been utilized for separation and have been categorized into the following groups: Straight, curved, spiral, alternating curves, contraction/expansion and posts. As a particle passes through each channel configuration, it will experience different instantaneous and cumulative effects of the three primary forces. Schematic representations of these forces experienced by a particle are presented for each configuration in Fig. 4. Straight channels achieve focusing based upon solely the balance between wall interaction and shear gradient lift. Curved channels have an additional constant secondary Dean flow whose force is dependent upon cross-sectional position but mostly competes with the shear

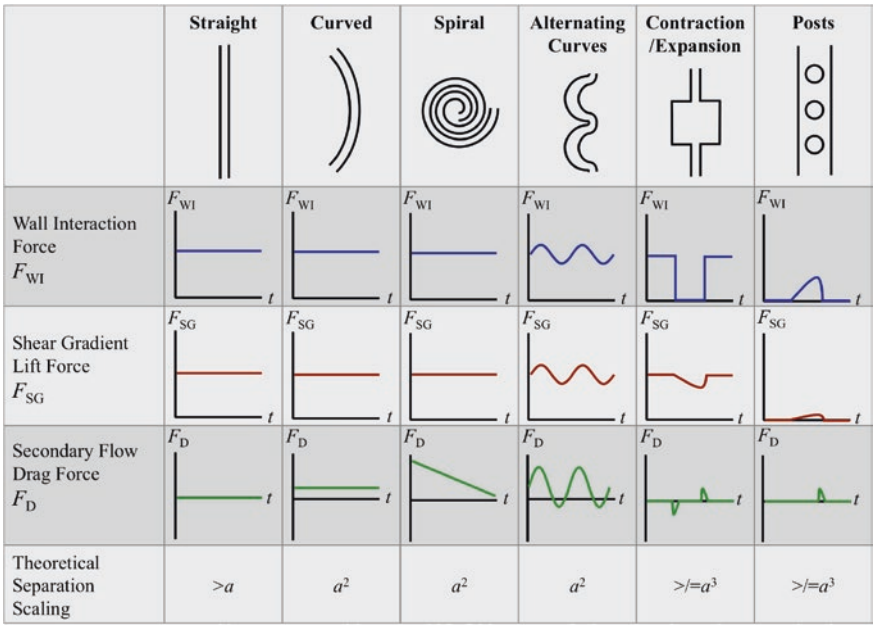

Fig. 4 Types of channel designs and structures used for inertial focusing separation. Each can be used in either an equilibrium or dynamic fashion to achieve separation. Adapted from Martel and Toner (2014)

gradient lift. Spirals, if the inlet is in the center, will have a diminishing Dean flow as the particle travels along the increasing radius of curvature. Alternating curves are broadly defined as channels with more than one center of curvature and have corresponding morphing secondary flows. Contraction/expansion devices create sudden changes in the wall interaction force in addition to small amounts of secondary flows. Finally, post designs use the interaction of previously aligned particles with a post and the secondary flow caused by such a structure to achieve separation.

Based upon the magnitudes of these forces, an estimate of the channel length required in order to achieve inertial focusing across the shorter channel cross-sectional dimension can be created:

$$L_f \cong \pi \mu D_h^2 / \left(C_{SG} \rho U_{Max} a^2 \right) \tag{7}$$

For a curved channel this can be estimated as slightly shorter than the straight channels with limits based upon the ratio of dean to inertial effects. In reality, this enhancement is minimal for cross-sections with an aspect ratio close to unity. Wide channels, which if straight, that would not be able to achieve meaningful focusing across the long dimension are able to achieve focusing across widths as large as 200 particle diameters. For contraction/expansion devices this is value is

also theoretically shorter due to enhancement in transverse fluid motion from secondary flows but most channels effectively require a similar total length.

While all devices fall into one of these geometrical channel categories separation can still be achieved in two distinct manners. Firstly, one can expose cells to the forces long enough for the cells to reach an equilibrium position, or secondly, one can use the abrupt addition or removal of a force to take advantage of the dynamic changes of the forces.

3 Separation

The ability to separate cells and particles based upon their diameter without filters and at a high throughput is an important tool for biology. While typically accomplished using centrifugation, microfluidic methods more precisely separate cells based upon size alone rather than size, density, and initial position within a centrifugation tube. Not surprisingly, size-based separation is one of the most utilized applications of inertial focusing in microfluidics and has been accomplished using all of the possible channel configurations. I will attempt to simply describe each type of separation in terms of the main forces and then compare them in terms of published specifications and operation.

3.1 Equilibrium Separation

In equilibrium separation particles or cells experience a fairly constant or oscillating force field for a sufficient period of time until they reach final equilibrium positions within a channel cross section where they remain until they translate out of the channel. In some alternating curvature and contraction/expansion channels, this position will oscillate slightly but will still be considered an equilibrium type of separation.

3.1.1 Straight Channels

In straight channels, the equilibrium position of a particle varies only slightly based upon size making separation possible. Due to the quick drop-off in wall interaction forces it is difficult to obtain high purity without a large discrepancy in particle size. As such, applications of pure equilibrium straight channel inertial focusing separation are limited but clever applications of the principles at work have produced other more effective designs.

As previously stated, particles above a certain size ($a/D_h > 0.07$) will focus in a given channel cross section if the flow is at a high enough Reynolds number, while particles smaller will not. Straight channels can be used to separate cells and

particles above and below this threshold by having the equilibrium position for the larger particles designed to be outside the initial sample stream. For instance, in a high aspect ratio channel ($h/w > 1$), if a central sample stream is flanked by buffer streams, larger particles will migrate out of the sample stream into the buffer causing separation (Nieuwstadt et al. 2010). This can also be done in a low aspect ratio ($h/w < 1$) channel using a central buffer stream and flanking sample streams. This second variation has been used for isolating exosomes captured on polystyrene beads from a plasma sample with a 100 % yield of the capture beads and 99 % purity from the plasma (Dudani et al. 2015). A single-sided version of this concept was also implemented for separating intact white blood cells (WBCs) from lysed blood samples at a rate of 5800 cells/s (4.2 mL/h) with a 90 % yield and a 70 % reduction in the background stain included in the lysed blood sample (Gossett et al. 2012).

Another manner in which straight channels can be used for equilibrium separation is by adjusting the aspect ratio of the channel along the length channel. In this style of separation, two different size particles are focused in a high aspect ratio channel that then expands to a slightly low aspect ratio channel. This allows the larger particles to focus to the center of the expanded channel but the now weaker inertial forces do not adjust the smaller particles locations (Zhou et al. 2013). Using this technique, HPET cancer cells were separated from dilute blood (0.8 % hematocrit) at a throughput of 1.5×10^5 cells/s including red blood cells (RBCs) achieving a yield of 100 % (purity not provided).

The final method of separation using equilibrium inertial focusing in a straight channel takes advantage of the cell free layer formation near the walls of the channel to enable the separation of cancer cells from blood. Through a series of bifurcations, as shown in Fig. 5, this unique method can separate larger cells from blood by slowly moving the equilibrium position out of the stream of blood cells and into the cell free layer. This device achieves 85 % yield of MB-231 cells from

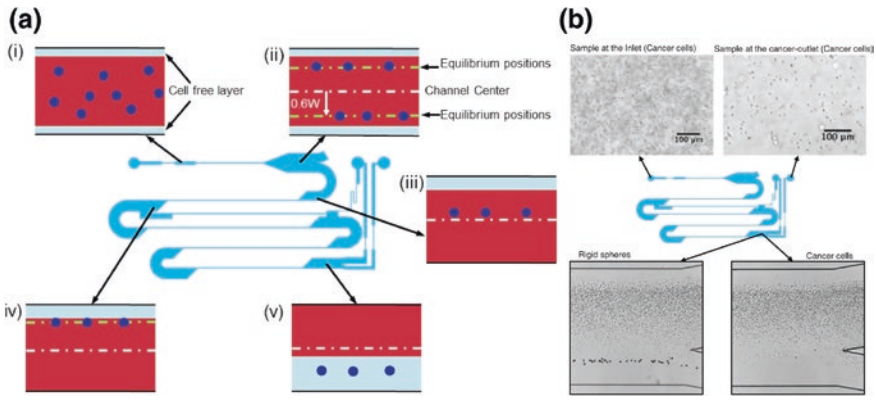

Fig. 5 **a** Schematic representation of bifurcating straight channels used to gradually shift cancer cells from blood into cell free region near the walls of the channel and **b** images of input and output solutions (*top*) and final bifurcation on the microfluidic device (*bottom*). Reproduced from Tanaka et al. (2012) with permission of The Royal Society of Chemistry

1 % hematocrit blood at a throughput of 1×10^6 cells/s (33.9 mL/h) (Tanaka et al. 2012). The caveat with this technique is the lower purity achieved (0.00024 %). While applications utilizing equilibrium focusing in straight channels are few and far between the essential understandings learned from straight channels are continuing to elucidate essential principles about inertial focusing.

3.1.2 Curved and Spiral Channels

Curved channels have proven to be advantageous over straight channels for improved throughput and the ability to enhance the separation distance between streams of cells. However, these channels can be more difficult to parallelize in order to further improve throughput as compared to straight channels. The improved throughput is an effect of the use of larger channel cross sections, but still being able to focus cells into a single stream. The improved separation distance between particles of different sizes is due to a competitive balance of the shear gradient lift force and the secondary flow drag for (Dean drag). Almost half (48 %) of all application-based publications on inertial focusing use curved or spiral channels for the simplicity and efficiency of equilibrium separation. The typical channel Reynolds numbers for these channels range from about 80–200 and the Dean number ranges from 10 to 70. This type of separation has been shown to have a size resolution close to 1 μm, where researchers designed a channel which separated 3.2 and 2.1 μm microspheres with a 96 % yield and 99.1 % purity at a throughput of 5000 particles/s (0.6 mL/h) (Johnston et al. 2014). While not the highest throughput, this resolution is one of the highest seen in any inertial focusing device. It should also be stated that larger particles (up to 60 μm in diameter have been tested) are still able to be separated with larger spiral channels (Hasni et al. 2011). More detailed studies of the dynamics of this type of inertial focusing and separation can be found elsewhere (Martel and Toner 2012, 2013; Xiang et al. 2012, 2013, 2014, 2015). While much of the research on equilibrium separation in spiral or curved channels has utilized polystyrene microparticles, these mimic cells focus fairly well when they are of similar size to the cells.

Several spiral devices using equilibrium separation have been created and applied to rare cell isolation (Burke et al. 2014; Kim et al. 2014; Sun et al. 2012). Each study achieved >87 % yield of cancer cells from different dilutions of whole blood or isolated WBCs. Complete separation was achieved in one of the studies between isolated WBCs and MCF7 cells (100 % purity) at 16,000 cells/s (45 mL/h) (Burke et al. 2014). As expected with an increased number of RBCs the purity of isolated rare cells decreased to <1 % albeit with higher throughput 550,000 cells/s (20 mL/h) (Sun et al. 2012). Separation can also be achieved between different cell types (SH-S5Y5 neuroblastoma cells and C6 glioma cells) with dissimilar sizes, 15 and 8 μm, respectively, at a high throughput 50,000 cells/s (120 mL/h) (Kuntaegowdanahalli et al. 2009). White blood cells have been separated from diluted whole blood (0.09 % hematocrit) using equilibrium inertial focusing in a curved channels achieving 95 % yield of WBCs with a purity of

1.6 % at a rate of 300,000 cells/second (108 mL/h) (Nivedita and Papautsky 2013). An intriguing application of this type of cell separation is the ability to separate cells based upon what stage of the cell cycle they are currently experiencing, if such cells have significant enough changes in size during the cell cycle. Some examples of cells that were able to be separated based upon the cell cycle include bone-marrow derived human mesenchymal stem cells (hMSCs), CHO-CD36, HeLa, and KKU-100 (Lee et al. 2011). These separations achieved high yields (>85 %) of cells in G0/G1 phases at 4000 cells/s (150 mL/h).

One unique means of improving the separation between different sizes of particles is to use a non-rectangular cross-sectional shape to cause a gradient in Dean flow velocities across the width of the channel. By doing so, a spiral that is taller on the outer part of the channel cross section and shorter toward the center of curvature will have enhanced separation due to smaller particles being entrained in the center of the Dean vortices which are located toward the higher outer wall (Guan et al. 2013). The trapezoidal cross-sectional shape increased the separation distance between the equilibrium streams of 10 and 6 μm polystyrene microspheres by several times as shown in Fig. 6. Consequent testing of separation of WBCs from diluted blood (1–2 % hematocrit) achieved a 90 % yield with 0.60 % purity at a throughput of 3×10^6 cells/s (48 mL/h) (Wu et al. 2012). This same device design was applied to rare cell isolation from RBC lysed blood achieving approximately 80 % yield and 15.6 % purity average across three cell lines (MCF7, T24, and MB231) at a throughput of 71,000 cells/s (102 mL/h) (Warkiani et al. 2014b).

3.1.3 Other Channels

The last two types of equilibrium separation channel variations, alternating curves and contraction/expansion, have inherent oscillations in both channel design and equilibrium positions and yet can still be used to cause a difference in average

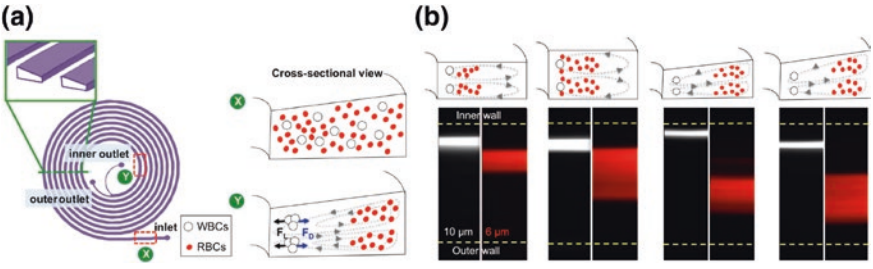

Fig. 6 **a** Schematic representation of inertial focusing spiral microchannel for separating WBCs and RBCs. **b** Comparison of similarly sized rectangular and trapezoidal cross-sectioned spirals highlighting the improved separation in the trapezoidal versions (*white* = 10 μm particles, *red* = 6 μm particles). Reprinted with permission from Wu et al. (2012). Copyright (2012) American Chemical Society

equilibrium behavior of cells or particles based upon size. Alternating curves cause Dean flow which transitions from one vortex direction to the other rather than a consistent direction like curved or spiral channels. This alternation causes the secondary flow drag force to oscillate as well, but in general, causes the motion of particles to equilibrium positions to be faster than in a similar cross-sectioned straight channel (Gossett and Di Carlo 2009). One of the initial channels used for inertial focusing in microfluidics was of this type of design with the addition of a changing cross-section as well. These asymmetric curves were able to focus wide ranges of particle sizes and even fractionate platelets from other blood cells with 99 % purity at a rate of 1.5×10^6 cells/s (54 mL/h). Symmetric curves have also been studied leading to different equilibrium behaviors (Zhang et al. 2013). Particle separation can be achieved in these symmetrically curved channels by balancing secondary flow drag and shear gradient forces in such a way that larger particles focus to the center of the channel and smaller particles focus to the sides of the channels in the direction of curvature changes. This style of separation has shown the ability to isolate rare cells from dilute blood (0.45 % hematocrit) achieving a purity of 45.4 % at a rate of 5000 cells/s (36 mL/h) (Zhang et al. 2014b).

Sequences of contractions and expansions also cause transient secondary flows that assist in the focusing of cells. These devices can achieve one or two equilibrium positions depending on if the expansions are symmetric or asymmetric but still achieve separation based upon the balance of shear gradient lift and the transient secondary flow effects. Sometimes called multi-orifice flow fractionation (MOFF), contraction/expansion devices like these have been shown to cause different patterns of equilibrium positions based upon particle Reynolds number and changing secondary flow effects. If $Re_P < 0.5$ typically minimal focusing occurs. Particle Reynolds numbers between 0.5 and 2 achieves two equilibrium positions on the sides of the channel where expansions are occurring, $Re_P > 2$ leading to a centralized equilibrium position within the channel. As Re_P scales with the particle diameter squared, significant separation can be achieved. In an initial study of these channels, polystyrene microspheres 15 μm in diameter were separated from 7 to 2 μm spheres with a yield of 65 % and a purity of 36 % at a throughput of a 2000 particles/s (15 and 7 μm only—8.4 mL/h) (Park and Jung 2009; Park et al. 2009). This type of separation was also applied to rare cell isolation where MCF7 cells were separated from 20× diluted blood (2.25 % hematocrit) achieving a yield of 80 % with a purity of 0.001 % at a throughput of ~1×10^6 cells/s (24 mL/h) (Bhagat et al. 2011).

3.2 Dynamic Separation

Dynamic separation is herein defined as separation caused by a transient force field with respect to either population of the particles or cells being separated. For example, dynamic separation can be cause the sudden addition or removal of a force or an effect that if continued would not result in an equilibrium type separation.

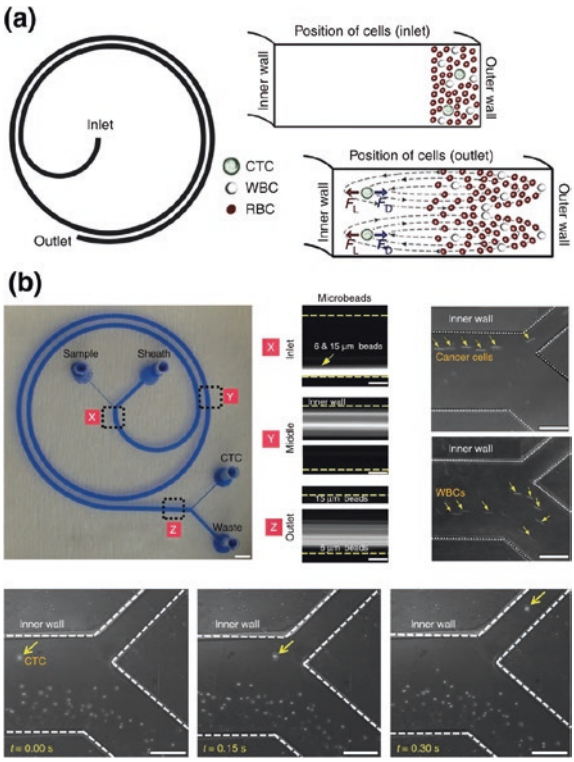

Fig. 7 **a** Schematic representation of Dean flow fractionation (DFF). In a correctly designed spiral (*left*), dilute blood cells are injected on the outer wall of the channel curvature with buffer used as a sheath flow on the inner side. After one full Dean circulation as the fluid moves through the channel, the larger cancer cells focus to the inner wall and the smaller RBCs, entrained in the Dean flow, recirculate back to the outer portion of the channel cross section. **b** Example images of a DFF device and its operation. Reprinted by permission from Macmillan Publishers Ltd: Nature Protocols (Khoo et al. 2015) copyright (2015)

3.2.1 Dean Flow Fractionation

Dean flow fractionation (DFF) is a very adaptable style of dynamic separation utilizing inertial focusing that takes advantage of the focusing of one particle size and the Dean flow cycling of smaller non-focusing particles to create separation as depicted in Fig. 7. Essentially, DFF avoids the necessary requirement of a having all particles large enough to focus by utilizing multiple inlet streams, one with the cell mixture and the other with buffer. By designing the curvature and length of the spiral to achieve a single Dean cycle, a single recirculation of fluid in the cross section as depicted in Fig. 6, particles larger than $0.07a/D_h$ will focus normally while smaller particles will be entrained in the Dean flow and end up on the same side of the channel where the sample stream initially entered (Bhagat et al. 2008). While this technique uses equilibrium focusing of larger particles, separation is achieved through the dynamic motion of the Dean flow and is characterized as such. DFF is one of the highest throughput technologies using inertial focusing despite using a co-flow of buffer achieving ~5×10^6 cells/s with a sample as concentrated as 15 % hematocrit (~9 mL/h) (Hou et al. 2015). The minimum tested resolution for the technique is ~5 μm difference in diameter between cancer cells and white blood

cells (Khoo et al. 2014, 2015; Warkiani et al. 2014a). In terms of rare cell isolation from blood components, DFF has achieved a yield of 88 % and a purity of 1.9 % (Hou et al. 2013). DFF technology for rare cell isolation is one of a select few inertial focusing-based devices on the commercialization path (Clearbridge BioMedics, Singapore, Singapore). Beyond rare cell isolation, DFF has been applied to the sampling of bacteria from blood (67 % yield, 99.9 % purity) (Hou et al. 2015), removal of nanoparticles from cell suspensions after treatments (90 % yield, 95 % purity from free nanoparticles) (Yeo et al. 2015), and the removal of unbound aptamers (washing) for rapid profiling of RBC surface proteins (85 % yield of RBCs and 100 % purity from unbound aptamers) (Birch et al. 2015).

3.2.2 Post Channels

Inertial microfluidic programming or micropillar sequencing also uses a combination of secondary flows and inertial focusing to accomplish separation, but instead of using channel curvature to create a secondary flow uses microstructures placed within a straight-walled channel as pictured in Fig. 8. When a central stream of fluid containing focused particles pass through these engineered devices, the particles remain focused to the center while the surrounding sample fluid is cycled to a different cross-sectional location. The most efficient use of these devices occurs at approximately a Reynolds number of 100 and a low Péclet number (minimal diffusion as compared to fluid flow). While this method does require a sheath flow and prefocused particles the technique has been shown to remove white blood cells from lysed blood components retaining 80 % of the WBCs and removing 80 % of the total hemoglobin content at a throughput of 2700 cells/s (Amini et al. 2013; Sollier et al. 2015). The particle size resolution of this method has not been investigated but should be of a similar order as DFF as they are taking advantage of similar forces.

3.2.3 Trapping Channels

Vortex trapping is another type of dynamic inertial focusing separation method. In this case, pre-focused particles in a high aspect ratio channel are passed through a sharply expanded section of channel as pictured in Fig. 9. At sufficiently high Reynolds numbers, dependent upon the geometry but typically around 100, vortices form in the large expanded sections of the channel. This allows for a unique situation where the central flow stream does not widen or decelerate significantly retaining the shear gradient but the wall interaction force disappears. The much larger shear gradient lift forces on larger cells cause them to migrate across the seperatrix, the streamline that defines the boundary between vortex and main flow, and get trapped efficiently. The trapped cells can then be released from the vortices simply by decreasing the flow rate. While each expanded section of channel can only hold 20 cells each, both serial and parallel arrays of these channels are easily created (Hur et al. 2011c). The best resolution achieved to date with

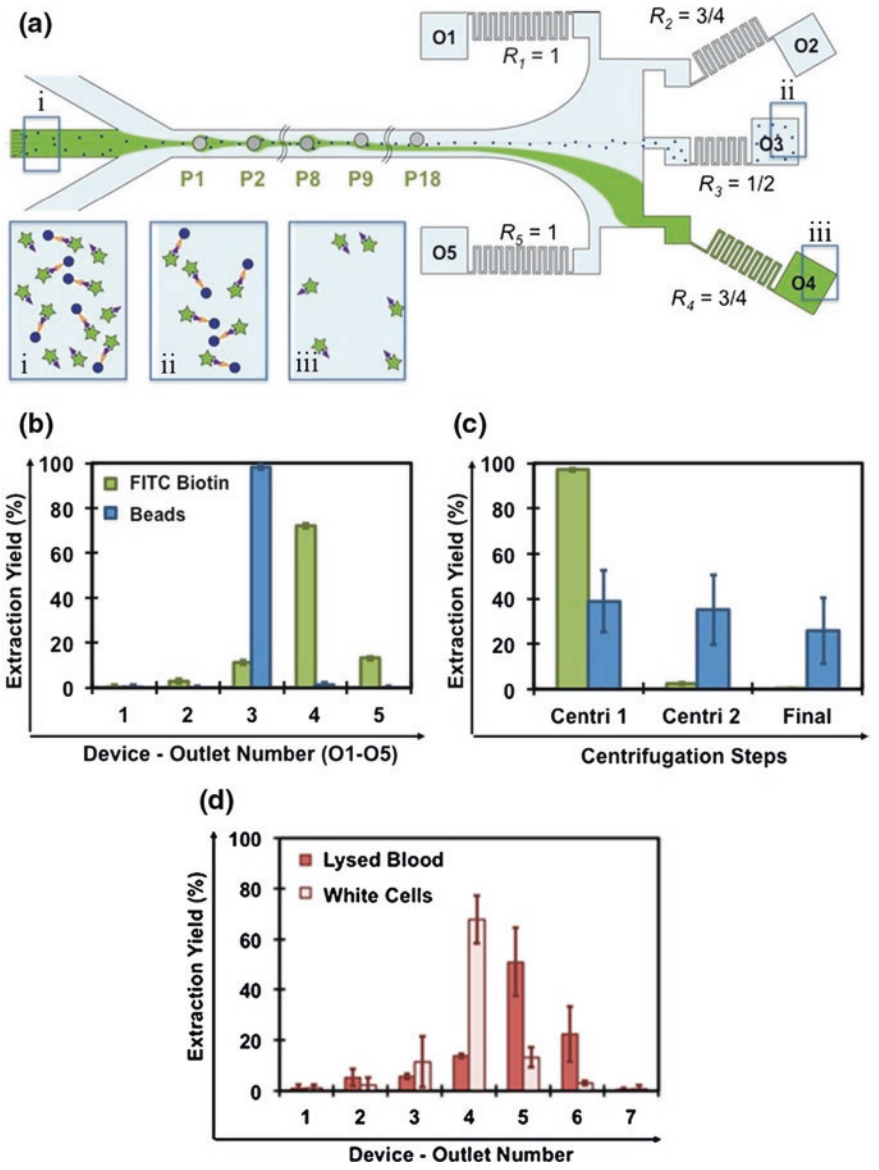

Fig. 8 **a** Post-style inertial focusing separation device schematic where a sample fluid enters at the center flanked by sheath fluid, passed through a sequence of micropillars that use secondary flow to shift smaller objects such as fluorophores across the channel while retaining large particles in the center via inertial focusing. **b** Example data separating beads from a biotinylated fluorophores as compared to centrifugation in terms of washing capabilities. **c** Example data from the same device design applied to the separation of WBCs from lysed RBC components. Reprinted from Sollier et al. (2015), with permission of Springer

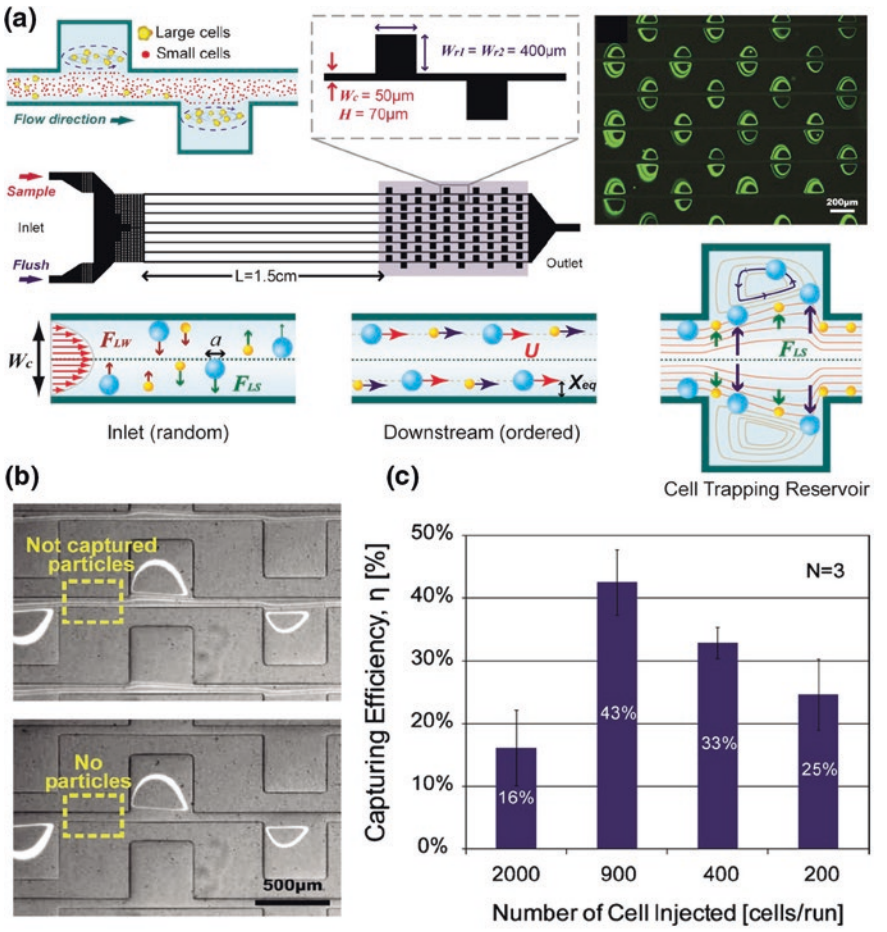

Fig. 9 **a** Device schematic and dimensions for a typical vortex trapping inertial focusing microfluidic device. **b** Example images of fluorescent particles being trapped in vortices and **c** the capture yield or efficiency as a function of the number of cells injected. Reprinted with permission from Hur et al. (2011c). Copyright 2011, AIP Publishing LLC

parallelized vortex traps was between cancer cells and blood cells (~5 μm differential) that achieved 69 % yield and 66 % purity with a throughput of ~1.25 × 10^6 cells/s with a 2.25 % hematocrit sample (18 mL/h) (Dhar et al. 2015). Vortex Biosciences Inc. is commercializing this technology for rare cell isolation. Another alternative use of this same type of separation was accomplished by focusing then separating cells using a single expansion region with a very small outflow. This produced excellent resolution between cells of ~1.5 μm or a ~9 % difference in particle diameter with the caveat that both were cell types were large, 20 and 18.5 μm (Wang et al. 2013). While a 90 % yield and 90 % purity were achieved, these experiments were completed using polystyrene microparticles rather than cells and operated at extremely low concentrations (~10^3 per mL).

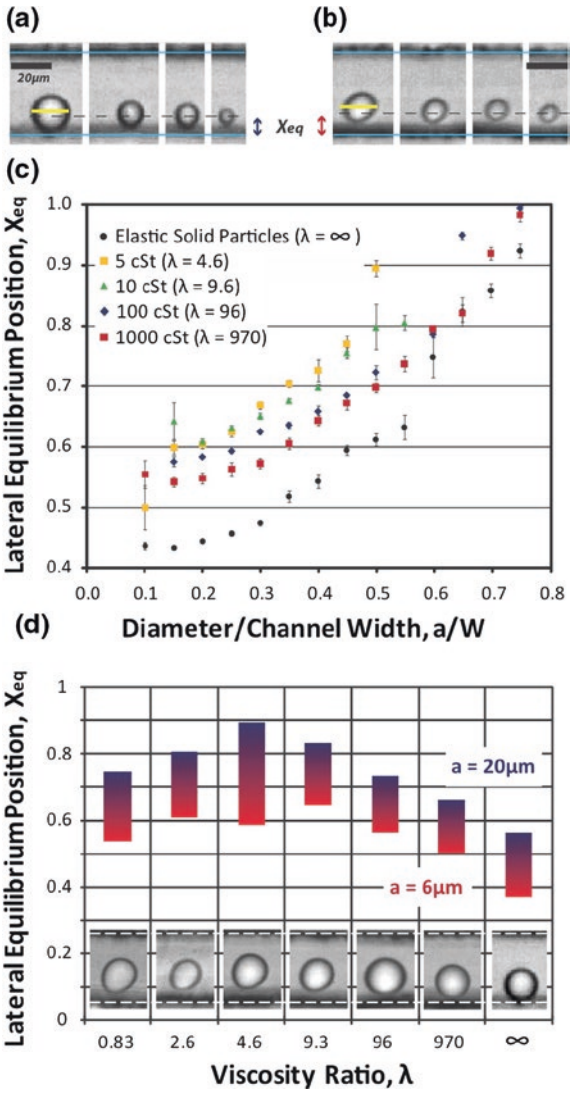

Fig. 10 Images of focused **a** rigid and **b** deformable particles highlighting the shape and equilibrium position changes. **c** Equilibrium position in terms of fraction of the channel width as a function of the interior fluid viscosity of droplets being focused. **d** Equilibrium position ranges for different sizes of droplets as a function of the internal droplet to carrier fluid viscosity ratio. Reproduced from Hur et al. (2011b) with permission of The Royal Society of Chemistry

3.3 Separation by Other Properties than Size

A unique aspect of flow dependent separation technologies such as inertial focusing is that they enable the separation of cells based upon properties other than size alone. So far, three technologies have been explored taking advantage of properties other than size in straight channels. Each different property affects how the particles equilibrate thus leading to the ability to separate them based upon those properties.

3.3.1 Deformability

The first of these properties is the deformability of cells or droplets. Deformability of single cells has been linked to metastatic potential in cancers and immunoactivation levels of WBCs (Chen et al. 2014a; Hur et al. 2011b; Kilimnik et al. 2011). The ability to separate cells in such a label-free manner enables new measurements and analyses that can be preformed downstream. This separation occurs because more deformable particles or droplets equilibrate to a position closer to the centerline of a straight rectangular cross-sectioned channel (Hur et al. 2011b). This is due to a combination of a viscoelasticity-induced lift force and shape changes associated with the shear stresses across a more deformable particle as shown in Fig. 10. This design achieved a 97 % yield of metastatic cancer cells (modified MCF7 s) from blood cells and a purity of 4 % at a throughput of 11,000 cells/s (0.167 mL/h).

3.3.2 Shape

The second property used for separation is the shape of a cell or particle. It was elucidated that the equilibrium position of a particle scales with its maximum or rotational diameter (Hur et al. 2011a; Masaeli et al. 2012). As such, in a similar manner to particle deformability, separation can be achieved based upon shapes with different maximum diameters (Hur et al. 2011a). This difference in equilibrium position difference is partially due to the rotation of nonspherical particles. Using stretched polymeric particles separation between spheres and rods with 3:1 and 5:1 aspect ratios have been shown with yields and purities around 90 % in addition to the separation of yeast cells based upon the number of buds formed on a single cell as

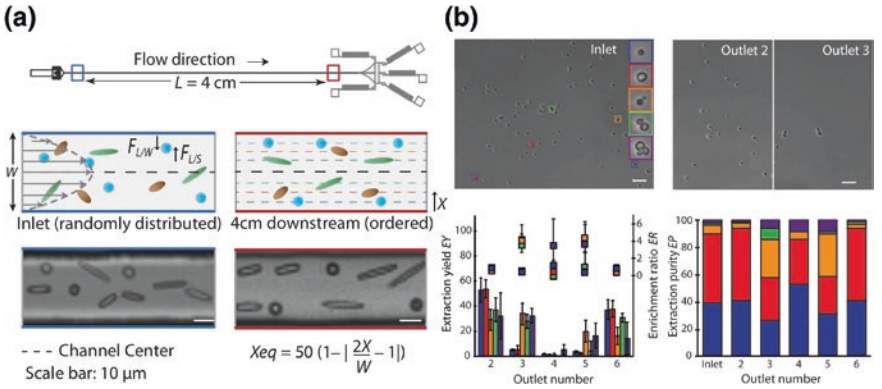

Fig. 11 **a** Device schematic and a comparison of unfocused (*left*) to focused (*right*) particles of equivalent volume but different aspect ratios. **b** Data from the separation of yeast (*Saccharomyces cerevisae*) based upon their shape or number of buds including values of yield and purity of different populations as highlighted in the inlet image (*top left*) (Masaeli et al. 2012)

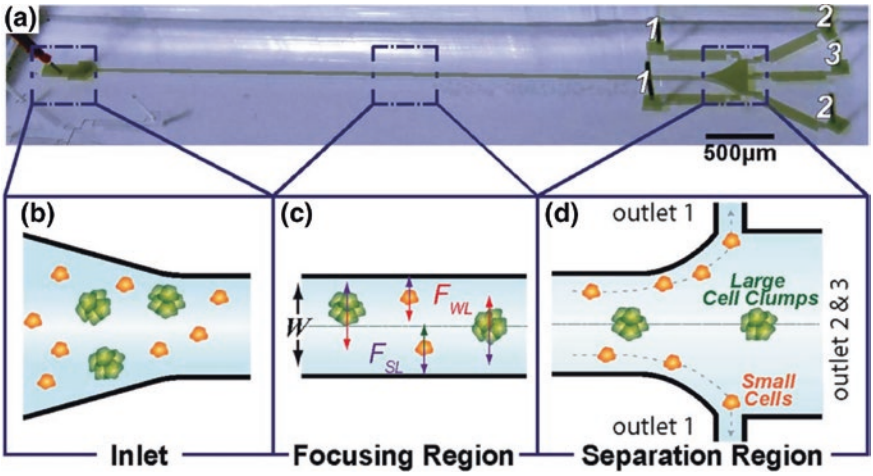

Fig. 12 **a** Device schematic for separation of clusters of cells from single cells. **b** Initially unfocused cells and clusters **c** become focused to different equilibrium positions based upon size allowing for **d** separation (Hur et al. 2012)

shown in Fig. 11. In this experiment, yeast cells (*Saccharomyces cerevisae*) undergoing budding could be separated from non-budding yeast with a yield of 54 % and a purity of 31 % at a throughput of 1500 cells/s (3.6 mL/h) (Masaeli et al. 2012). Interestingly, the difference in rotational diameter of these yeast cells is approximately only a few microns indicating impressive resolution of separation.

3.3.3 Clustering

The last property, while simply a combination of size and shape, is the tendency to form clusters. In this research, a tissue digest was performed and subsequently run through an inertial focusing channel where clusters of cells were separated from single cells based upon their different sizes and shapes, as depicted in Fig. 12. In doing so, more differentiated cells in the clusters were separated from adrenal cortical progenitor single cells (Hur et al. 2012). In general, inertial focusing for separation based upon deformability, shape, and clustering allows for novel information content separate from labeling providing a unique means of continuous flow separation otherwise unavailable.

4 Beyond Separation

The utility of inertial focusing for cell sorting is also an area of active research as both the alignment of cells and the ordering of cells are key components of any cell sorting system. A both of these effects are inherently part of inertial focusing

behaviors there would be no need for high volumes of sheath flows, drastically increasing the volumetric throughput of numerous techniques with the caveat that the input cell concentration must be low (maximum ~1 v/v%) (Kahkeshani et al. 2015). Just like for separation, different channel configurations have been studied for cytometry applications. One of the earliest designs was using a spiral device whose equilibrium position was used for measuring the fluorescence signal from beads and cells achieving a coefficient of variance of 18 % at a rate of 2100 cells/s (Bhagat et al. 2010). Another design utilizing both asymmetric curves followed by a straight channel allowing for a single equilibrium position for cell concentrations around 0.1v/v% achieving 6 % coefficient of variation at a rate of 25,000 cells/s (6 mL/h) (Oakey et al. 2010). Excellent single point focusing has also been achieved in contraction/expansion channels (Chung et al. 2012). One contraction/expansion design has even been integrated with an active fluorescence sorting mechanism (pulsed laser cavitation) (Chen et al. 2014b). In this application a unique ability in inertial microfluidics is also highlighted where the spacing between cells can be adjusted with certain channel designs once the cells have been focused. This can effectively double the spacing between cells allowing for higher purity separations (Lee et al. 2010; Chen et al. 2014b).

Another area of active research is improving imaging and detection capabilities to take advantage of the possibilities of using inertial focusing for higher throughput flow cytometry. In one case, a novel imaging system (serial time encoded amplified microscopy—STEAM) capable of ~1 ps shutter times was able to image approximately 100,000 cells/s focused to a single stream (Goda et al. 2012). Other researchers have worked on developing tools for massively parallelized imaging systems looking at numerous streams of focused cells at once (Hur et al. 2010). Finally, the adaptation of inertial focusing channel fabrication onto semiconductor surfaces has been shown and will hopefully enable the direct integration of microscale sensors with the microchannels improving the signal coupling (Ciftlik et al. 2013).

The precise ordering of cells is also useful for single cell encapsulation, as shown in Fig. 13, which can then be used for sorting using electrical fields among other types of active sorting technologies. Both straight and curved inertial focusing channels have proven to provide significant improvements in encapsulation efficiency as compared to Poisson statistics (Edd et al. 2008; Kemna et al. 2012). This spacing has been shown to be dependent on Re_P and particle concentration (Kahkeshani et al. 2015). This longitudinal ordering distance can be modulated using expansions and contractions of the channel cross section (Lee et al. 2010).

Finally, inertial focusing has also been used as integral components in complex microfluidic separation and sorting platforms for rare cell isolation incorporating multiple microfluidic technologies such as deterministic lateral displacement and multistage microfluidic MACS (Karabacak et al. 2014; Ozkumur et al. 2013; Shen et al. 2014).

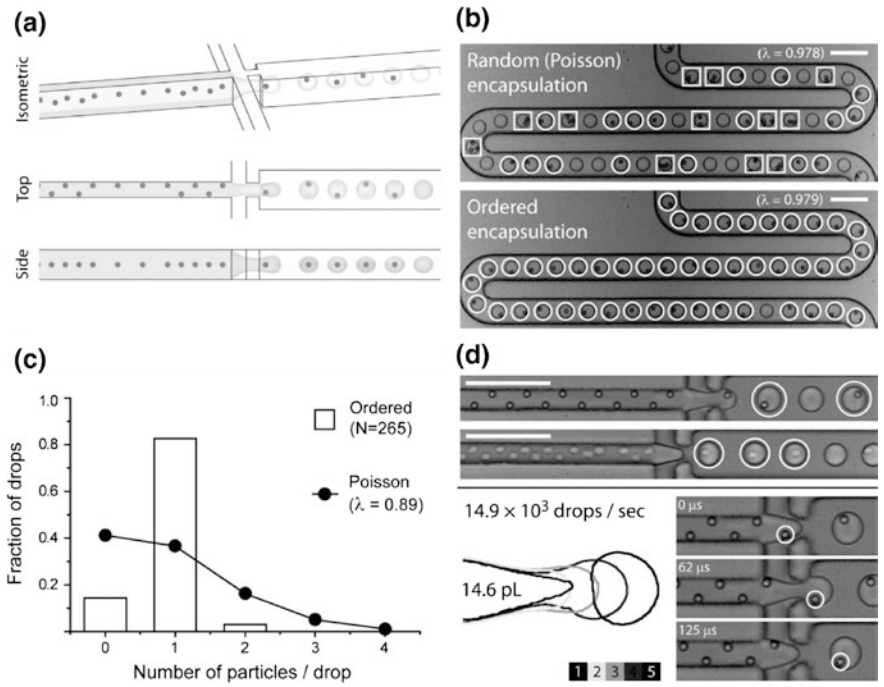

Fig. 13 Utilization of the ordering behaviors associated with inertial focusing to produce uniformly emulsion sizes with single cells in the majority of droplets. **a** Schematics of the microemulsion generating device. **b** Image-based comparison of random (not inertially focused) and ordered (focused) encapsulation. **c** Statistical comparison of encapsulation. **d** Images of droplet generation process with the average droplet size of 14.6 pL at a rate of almost 15 kHz. Reproduced from Edd et al. (2008) with permission of The Royal Society of Chemistry

5 Comparisons

In general, when investigating the performance of any inertial focusing cell separation technology there is a trade-off between the ability to handle higher volume fraction samples and the purity/yield of the technology. When accounting for all dilutions off-chip and on-chip, it appears that there is an upper limit on concentration of approximately 2.5 % volume fraction for effective operation of an inertial focusing device, which is consistent with concentration titration experiments (Martel et al. 2015). This is likely indicative of the hydrodynamic nature of inertial focusing requiring free fluid motion and minimal particle interactions in order for predictable forces to be maintained. Devices capable of operating above this limit typically do not have high yield or purity if isolating a larger cell type from one smaller. As shown in Table 1, yields and purities above 90 % are unlikely at cell concentrations above 0.5 % volume fraction, in other terms, at least a 100× dilution of blood. Despite this limitation, throughputs of inertial focusing devices are

Table 1 Table of metrics comparing all inertial focusing-based separation device performance

Channel type	Yield %	Purity %	Throughput		v/v %	Particle Sizes		Sample type	Sheath flow?	Reference
			Cells/s	mL/h		A μm	B μm			
Equilibrium										
Straight	90	ND	5.8×10^3	4.2	<0.1	10	1	WBCs from lysed blood	Yes	Gossett et al. (2012)
	100	99	7.6×10^3	2.1	<0.1	20	0.1	Exosomes on particles	Yes	Dudani et al. (2015)
	99	<0.1	2.0×10^4	13.5	<0.1	15	10	Cell lines from dilute blood	No	Zhou et al. (2014)
	85	<0.1	1.0×10^6	33.9	1.0	15	10	Cell lines from dilute blood	No	Tanaka et al. (2012)
	80	1	4.6×10^6	15	10	15	10	Cell lines from dilute blood	No	Tanaka et al. (2011)
	99	91	8.0×10^2	6	<0.1	20	10	Particles	No	Zhou et al. (2013)
	95	100	8.0×10^2	6	<0.1	10	20	Particles	No	Zhou et al. (2013)
	ND	ND	1.5×10^5	6	0.8	20	10	Particles from dilute blood	No	Zhou et al. (2013)
	95	ND	3.2×10^4	12	0.5	10	0	Particles	No	Hansson et al. (2012)
	88	62	1.9×10^6	12	0.5	6	2	Bacteria from dilute blood	No	Mach and Di Carlo (2010)
Curved/ Spiral	87	<0.1	4.6×10^4	33	0.0	15	10	Cell lines from dilute blood	No	Kim et al. (2014)
	ND	100	5.6×10^5	20	0.9	15	5	Cell lines from dilute blood	No	Sun et al. (2012)
	89	<0.1	5.6×10^5	20	0.9	15	10	Cell lines from dilute blood	No	Sun et al. (2012)
	96	99	4.6×10^3	0.6	0.0	3	2	Particles	No	Johnston et al. (2014)

(continued)

Table 1 (continued)

Channel type	Yield %	Purity %	Throughput		v/v %	Particle Sizes		Sample type	Sheath flow?	Reference
			Cells/s	mL/h		A μm	B μm			
	101	100	1.6×10^4	45	0.0	15	10	Cell lines from dilute blood	No	Burke et al. (2014)
	89	89	6.0×10^3	180	0.1	20	15	Particles	No	Kuntaegowdanahalli et al. (2009)
	83	80	1.4×10^4	180	0.1	15	10	Particles	No	Kuntaegowdanahalli et al. (2009)
	80	87	6.0×10^3	180	0.1	20	10	Particles	No	Kuntaegowdanahalli et al. (2009)
	79	75	5.0×10^4	180	0.1	15	8	Cell lines from cell lines	No	Kuntaegowdanahalli et al. (2009)
	80	16	7.1×10^4	102	<0.1	15	10	Cell lines from dilute blood	No	Warkiani et al. (2014b)
	96	96	2.2×10^3	204	1.0	26.9	18.68	Particles	No	Guan et al. (2013)
	92	ND	4.4×10^3	204	1.0	18.68	15.5	Particles	No	Guan et al. (2013)
	90	1	3.0×10^6	48	2.0	10	6	WBCs from dilute blood	No	Wu et al. (2012)
	95	2	3.0×10^5	108	0.1	10	6	WBCs from dilute blood	No	Nivedita and Papautsky (2013)
	99	93	ND	ND	ND	10	3	Particles	No	Russom et al. (2009)
	99	ND	ND	ND	ND	10.5	0	Particles	No	Seo et al. (2007)
Alternating Curves	61	99	1.5×10^6	54	0.9	3	9	Particles	No	Di Carlo et al. (2008)
	ND	99	1.5×10^6	54	0.9	2	6	Platelets from dilute blood	No	Di Carlo et al. (2008)
	98	89	9.0×10^3	36	<0.1	10	3	Particles	No	Zhang et al. (2014b)
	98	92	7.3×10^4	36	<0.1	13	5	Particles	No	Zhang et al. (2014b)

(continued)

Table 1 (continued)

Channel type	Yield %	Purity %	Throughput		v/v %	Particle Sizes		Sample type	Sheath flow?	Reference
			Cells/s	mL/h		A μm	B μm			
	ND	95	5.0×10^3	36	<0.1	12.6	5	Cell lines from dilute blood	No	Zhang et al. (2014b)
	ND	95	5.0×10^4	36	<0.1	12.6	5	Particles from dilute blood	No	Zhang et al. (2014b)
Contraction/ Expansion	85	<0.1	1.7×10^6	24	2.3	15.0	10.0	Cell lines from dilute blood	No	Bhagat et al. (2011)
	65	36	9.0×10^4	15	<0.1	15.0	7,2	Particles	No	Park and Jung (2009)
	76	32	9.0×10^4	15	<0.1	7.0	15,2	Particles	No	Park and Jung (2009)
	61	90	9.0×10^4	15	<0.1	2	7,15	Particles	No	Park and Jung (2009)
Dynamic										
Dean Flow	90	95	2.0×10^4	7.2	1	15	1	Cell lines in buffer	Yes	Yeo et al. (2015)
Fractionation	100	100	9.8×10^3	12.5	0.5	15	5	Particles	Yes	Zhang et al. (2015)
	85	100	3.3×10^4	9	5	6	0	RBCs from dilute blood	Yes	Birch et al. (2015)
	67	100	4.3×10^6	9.3	15	0.1	6	Bacteria from dilute blood	Yes	Hou et al. (2015)
	88	12	2.2×10^4	7.9	<0.1	15	10	Cell lines from dilute blood	Yes	Warkiani et al. (2014a)
	85	19	1.9×10^6	3	20	15	8	Cell lines from dilute blood	Yes	Hou et al. (2013)
	100	100	4.0×10^2	0.6	<0.1	7.32	1.9	Particles	Yes	Bhagat et al. (2008)
Posts	80	ND	2.7×10^3	2	<0.1	10	0	WBCs from lysed blood	Yes	Sollier et al. (2015)
	95	90	ND	ND	ND	10	0	Particles	Yes	Amini et al. (2013)

(continued)

Table 1 (continued)

Channel type	Yield %	Purity %	Throughput		v/v %	Particle Sizes		Sample type	Sheath flow?	Reference
			Cells/s	mL/h		A μm	B μm			
Trapping	30	85	1.8×10^4	33.8	0.1	10	5	Particles	No	Hur et al. (2011c)
	23	85	1.0×10^6	33.8	1	15	10	Cell lines from dilute blood	No	Hur et al. (2011c)
	20	40	5.1×10^6	33	5	15	10	Cell lines from dilute blood	No	Mach et al. (2011)
	20	80	2.1×10^6	30	2.25	15	10	Cell lines from dilute blood	No	Sollier et al. (2014)
	69	66	1.3×10^6	18	2.25	15	10	Cell lines from dilute blood	No	Dhar et al. (2015)
	90	90	4.0×10^2	30	0.1	20	18.5	Particles	No	Wang et al. (2013)
	86	50	4.0×10^2	30	0.1	20	10	Particles from dilute blood	No	Wang et al. (2013)

ND not determined

still high with an average of 517,000 cells/s including smaller sized items such as RBCs or an average of 13,650 cells/s considering only large cells (WBCs or cell lines).

One trend that is apparent is that the highest volumetric throughput of any device type is the curved/spiral type indicating that this type of channel is very effective at focusing across large channel dimensions. While perhaps inefficient in terms of device area compared to most straight channels, recent developments of stacking these devices makes parallelization achievable thus evening the playing field with facile parallelization of straight channels (Warkiani et al. 2014a). In terms of cellular throughput, there were no clear outliers as several devices, especially those that were able to handle higher concentrations of RBCs, achieved separation rates on the order of millions per second. It was surprising to see that the highest separation resolution channel type was also using equilibrium focusing within a spiral microchannel (Johnston et al. 2014). While at reduced throughput, due to the smaller cross section, this type of resolution may be able to compete with deterministic lateral displacement for small particles with continued device development. Finally, it should be highlighted that the versatility of DFF across different applications with minimal design changes is an impressive technological feat despite not having the highest performance in any one application (Birch et al. 2015; Hou et al. 2015; Yeo et al. 2015; Zhang et al. 2014a).

It is unclear whether or not dynamic or equilibrium separation holds a significant advantage in terms of cell separation. Theoretically, single dynamic interactions allow for more precise separations limiting chances of particle–particle interactions, however, it does require very precise prepositioning of particles. It is also clear that recently dynamic separation methods have become more prevalent, but a clear reason for this change is not yet illuminated. Another emerging trend is the use of sequential removal of fluid as focusing occurs leading to a more efficient focusing device (Burke et al. 2014; Kim et al. 2014; Martel et al. 2015).

6 Future

Inertial focusing is an important tool in microfluidics as well as a phenomenon of scientific intrigue pushing the speed limits of microfluidics. From a basic science perspective, the complex challenge of predicting and optimizing inertial focusing devices is a substantial task. With many researchers now working on technology development some amount of standardization in measurements would be helpful in order to directly compare these technologies. Focusing quality or the ability for a given design to achieve a narrow focused stream is one helpful measurement for equilibrium separation technologies that can be widely applied. Similar means of comparing dynamic systems have yet to be developed other than from the perspective of separation performance and even these metrics of throughput and purity can be presented with different definitions. Also, a very small number of scientific publications on inertial focusing use rigid microchannels (Martel et al. 2015;

Ciftlik et al. 2013). As such, the majority of data on inertial focusing is from channels that more likely than not have a different cross-sectional shape than stated. This complicates understanding the forces at play and makes it even more difficult to relate different scientific results. Without standardization of measurements or fabrication of these rigid channels it is not possible to relate all different works together impeding progress.

In most microfluidic technologies, one of the most important elements for achieving separation does not perhaps receive nearly as much attention as it should: outlet design. While some designs use a percent width of an outlet to determine its output fraction, it is actually the balance of hydraulic resistance that determines the splits. Even a change in wall angle can cause shifts in results (Mach and Di Carlo 2010). This deserves some attention and perhaps standardization.

From a theoretical perspective, inertial focusing alone cannot be a replacement for other types of cell sorting but can easily have a meaningful impact upon sample preparations and novel types of cell isolation as highlighted herein.

References

Amini H, Lee W, Di Carlo D (2014) Inertial microfluidic physics. Lab Chip. doi:10.1039/c4lc00128a

Amini H, Sollier E, Masaeli M, Xie Y, Ganapathysubramanian B, Stone HA, Di Carlo D (2013) Engineering fluid flow using sequenced microstructures. Nat Commun 4:1–8. doi:10.1038/ncomms2841

Asmolov E (1999) The inertial lift on a spherical particle in a plane Poiseuille flow at large channel Reynolds number. J Fluid Mech 381:63–87

Bhagat A, Hou H, Li L, Lim C, Han J (2011) Pinched flow coupled shear-modulated inertial microfluidics for high-throughput rare blood cell separation. Lab Chip 11(11):1870–1878

Bhagat A, Kuntaegowdanahalli S, Papautsky I (2008) Continuous particle separation in spiral microchannels using dean flows and differential migration. Lab Chip 8(11):1906–1914

Bhagat AAS, Kuntaegowdanahalli SS, Kaval N, Seliskar CJ, Papautsky I (2010) Inertial microfluidics for sheath-less high-throughput flow cytometry. Biomed Microdevices 12(2):187–195. doi:10.1007/s10544-009-9374-9

Birch CM, Hou HW, Han J, Niles JC (2015) Identification of malaria parasite-infected red blood cell surface aptamers by inertial microfluidic SELEX (I-SELEX). Sci Rep. doi:10.1038/srep11347

Burke JM, Zubajlo RE, Smela E, White IM (2014) High-throughput particle separation and concentration using spiral inertial filtration. Biomicrofluidics 8(2):024105. doi:10.1063/1.4870399

Chen X, Xue C, Zhang L, Hu G, Jiang X, Sun J (2014a) Inertial migration of deformable droplets in a microchannel. Phys Fluids 26(11):112003. doi:10.1063/1.4901884

Chen Y, Chung AJ, Wu T-H, Teitell MA, Di Carlo D, Chiou P-Y (2014b) Pulsed laser activated cell sorting with three dimensional sheathless inertial focusing. Small. doi:10.1002/smll.201302885

Chung AJ, Gossett DR, Di Carlo D (2012) Three dimensional, sheathless, and high-throughput microparticle inertial focusing through geometry-induced secondary flows. Small 9(5):685–690. doi:10.1002/smll.201202413

Ciftlik A, Ettori M, Gijs M (2013) High throughput-per-footprint inertial focusing. Small

Dhar M, Wong J, Karimi A, Che J, Renier C, Matsumoto M, Triboulet M, Garon EB, Goldman JW, Rettig MB, Jeffrey SS, Kulkarni RP, Sollier E, Di Carlo D (2015) High efficiency vortex trapping of circulating tumor cells. Biomicrofluidics 9(6):064116. doi:10.1063/1.4937895

Di Carlo D (2009) Inertial microfluidics. Lab Chip 9(21):3038. doi:10.1039/b912547g

Di Carlo D, Edd J, Irimia D, Tompkins R, Toner M (2008) Equilibrium separation and filtration of particles using differential inertial focusing. Anal Chem 80(6):2204

Di Carlo D, Irimia D, Tompkins R, Toner M (2007) Continuous inertial focusing, ordering, and separation of particles in microchannels. Proc Natl Acad Sci 104(48):18892

Dudani JS, Gossett DR, Tse HTK, Lamm RJ, Kulkarni RP, Di Carlo D (2015) Rapid inertial solution exchange for enrichment and flow cytometric detection of microvesicles. Biomicrofluidics 9(1):014112. doi:10.1063/1.4907807

Edd J, Di Carlo D, Humphry K, Köster S, Irimia D, Weitz D, Toner M (2008) Controlled encapsulation of single cells into monodisperse picoliter drops. Lab Chip 8(8):1262

Feng J, Hu H, Joseph D (1994a) Direct simulation of initial value problems for the motion of solid bodies in a Newtonian fluid. Part 1. Sedimentation. J Fluid Mech 261:95–134

Feng J, Hu H, Joseph D (1994b) Direct simulation of initial value problems for the motion of solid bodies in a Newtonian fluid. Part 2. Couette and Poiseuille flows. J Fluid Mech 277:271–301

Goda K, Ayazi A, Gossett D, Sadasivam J, Lonappan C, Sollier E, Fard A, Hur S, Adam J, Murray C (2012) High-throughput single-microparticle imaging flow analyzer. Proc Natl Acad Sci 109(29):11630–11635

Gossett DR, Di Carlo D (2009) Particle focusing mechanisms in curving confined flows. Anal Chem 81(20):8459–8465. doi:10.1021/ac901306y

Gossett DR, Tse HTK, Dudani JS, Goda K, Woods TA, Graves SW, Di Carlo D (2012) Inertial manipulation and transfer of microparticles across laminar fluid streams. Small. doi:10.1002/smll.201200588

Guan G, Wu L, Bhagat AA, Li Z, Chen PCY, Chao S, Ong CJ, Han J (2013) Spiral microchannel with rectangular and trapezoidal cross-sections for size based particle separation. Sci Rep 3:1–9. doi:10.1038/srep01475

Hansson J, Karlsson MJ, Haraldsson T, Brismar H, Van Der Wijngaart W, Russom A (2012) Inertial microfluidics in parallel channels for high-throughput applications. Lab Chip. doi:10.1039/c2lc40241f

Hasni A, Göbbels K, Thiebes A, Bräunig P, Mokwa W, Schnakenberg U (2011) Focusing and sorting of particles in spiral microfluidic channels. Procedia Eng 25:1197–1200

Ho B, Leal L (1974) Inertial migration of rigid spheres in two-dimensional unidirectional flows. J Fluid Mech 65:365–400

Hosic S, Murthy SK, Koppes AN (2015) Microfluidic sample preparation for single cell analysis. Anal Chem:acs.analchem.5b04077. doi:10.1021/acs.analchem.5b04077

Hou HW, Bhattacharyya RP, Hung DT, Han J (2015) Direct detection and drug-resistance profiling of bacteremias using inertial microfluidics. Lab Chip. doi:10.1039/C5LC00311C

Hou HW, Warkiani ME, Khoo BL, Li ZR, Soo RA, Tan DS-W, Lim W-T, Han J, Bhagat AAS, Lim CT (2013) Isolation and retrieval of circulating tumor cells using centrifugal forces. Sci Rep 3:1–8. doi:10.1038/srep01259

Humphry KJ, Kulkarni PM, Weitz DA, Morris JF, Stone HA (2010) Axial and lateral particle ordering in finite Reynolds number channel flows. Phys Fluids 22(8):081703. doi:10.1063/1.3478311

Hur S, Choi S, Kwon S, Di Carlo D (2011a) Inertial focusing of non-spherical microparticles. Appl Phys Lett 99:044101

Hur SC, Brinckerhoff TZ, Walthers CM, Dunn JCY, Di Carlo D (2012) Label-free enrichment of adrenal cortical progenitor cells using inertial microfluidics. PLoS One 7(10):e46550. doi:10.1371/journal.pone.0046550.g004

Hur SC, Henderson-Maclennan NK, Mccabe ERB, Di Carlo D (2011b) Deformability-based cell classification and enrichment using inertial microfluidics. Lab Chip. doi:10.1039/c0lc00595a

Hur SC, Mach AJ, Di Carlo D (2011c) High-throughput size-based rare cell enrichment using microscale vortices. Biomicrofluidics. doi:10.1063/1.3576780.1
Hur SC, Tse HTK, Di Carlo D (2010) Sheathless inertial cell ordering for extreme throughput flow cytometry. Lab Chip 10(3):274. doi:10.1039/b919495a
Johnston ID, Mcdonnell MB, Tan CKL, Mccluskey DK, Davies MJ, Tracey MC (2014) Dean flow focusing and separation of small microspheres within a narrow size range. Microfluid Nanofluid. doi:10.1007/s10404-013-1322-6
Kahkeshani S, Haddadi H, Di Carlo D (2015) Preferred interparticle spacings in trains of particles in inertial microchannel flows. J Fluid Mech 786:R3. doi:10.1017/jfm.2015.678
Karabacak NM, Spuhler PS, Fachin F, Lim EJ, Pai V, Ozkumur E, Martel JM, Kojic N, Smith K, P-i Chen, Yang J, Hwang H, Morgan B, Trautwein J, Barber TA, Stott SL, Maheswaran S, Kapur R, Haber DA, Toner M (2014) Microfluidic, marker-free isolation of circulating tumor cells from blood samples. Nat Protoc 9(3):694–710. doi:10.1038/nprot.2014.044
Kemna E, Schoeman R, Wolbers F, Vermes I, Weitz DA, Van Den Berg A (2012) High-yield cell ordering and deterministic cell-in-droplet encapsulation using Dean flow in a curved microchannel. Lab Chip. doi:10.1039/c2lc00013j
Khoo BL, Warkiani ME, Tan DS-W, Bhagat AAS, Irwin D, Lau DP, Lim AST, Lim KH, Krisna SS, Lim W-T, Yap YS, Lee SC, Soo RA, Han J, Lim CT (2014) Clinical validation of an ultra high-throughput spiral microfluidics for the detection and enrichment of viable circulating tumor cells. PLoS One 9(7):e99409. doi:10.1371/journal.pone.0099409.s001
Khoo BL, Wu L, Tay AKP, Bhagat AAS, Warkiani ME, Han J, Lim CT (2015) Ultra-fast, label-free isolation of circulating tumor cells from blood using spiral microfluidics. Nat Protoc 11(1):134–148. doi:10.1038/nprot.2016.003
Kilimnik A, Mao W, Alexeev A (2011) Inertial migration of deformable capsules in channel flow. Physics of Fluids 23(12):123302–123306
Kim TH, Yoon HJ, Stella P, Nagrath S (2014) Cascaded spiral microfluidic device for deterministic and high purity continuous separation of circulating tumor cells. Biomicrofluidics 8(6):064117. doi:10.1063/1.4903501
Kuntaegowdanahalli SS, Bhagat AAS, Kumar G, Papautsky I (2009) Inertial microfluidics for continuous particle separation in spiral microchannels. Lab Chip 9(20):2973. doi:10.1039/b908271a
Lee W, Amini H, Stone H, Di Carlo D (2010) Dynamic self-assembly and control of microfluidic particle crystals. Proc Natl Acad Sci 107(52):22413–22418
Lee WC, Bhagat AAS, Huang S, Van Vliet KJ, Han J, Lim CT (2011) High-throughput cell cycle synchronization using inertial forces in spiral microchannels. Lab Chip 11(7):1359–1367. doi:10.1039/c0lc00579g
Mach AJ, Di Carlo D (2010) Continuous scalable blood filtration device using inertial microfluidics. Biotechnol Bioeng 107(2):302–311. doi:10.1002/bit.22833
Mach AJ, Kim JH, Arshi A, Hur SC, Di Carlo D (2011) Automated cellular sample preparation using a Centrifuge-on-a-Chip. Lab Chip. doi:10.1039/c1lc20330d
Martel J, Toner M (2014) Inertial Focusing in Microfluidics. Annu Rev Biomed Eng 16:371–396. doi:10.1146/annurev-bioeng-121813-120704
Martel JM, Smith KC, Dlamini M, Pletcher K, Yang J (2015) Continuous flow microfluidic bioparticle concentrator. Sci Rep. doi:10.1038/srep11300
Martel JM, Toner M (2012) Inertial focusing dynamics in spiral microchannels. Phys Fluids 24(3):032001. doi:10.1063/1.3681228
Martel JM, Toner M (2013) Particle focusing in curved microfluidic channels. Sci Rep. doi:10.1038/srep03340
Masaeli M, Sollier E, Amini H, Mao W, Camacho K, Doshi N, Mitragotri S, Alexeev A, Di Carlo D (2012) Continuous inertial focusing and separation of particles by shape. Phys Rev X 2(3):031017. doi:10.1103/PhysRevX.2.031017
Matas J-P, Morris J, Guazzelli É (2009) Lateral force on a rigid sphere in large-inertia laminar pipe flow. J Fluid Mech 621(1):59–67

Matas J-P, Morris JF, Guazzelli É (2004) Inertial migration of rigid spherical particles in Poiseuille flow. J Fluid Mech 515:171–195. doi:10.1017/S0022112004000254
Miltenyi S, Müller W, Weichel W, Radbruch A (1990) High gradient magnetic cell separation with MACS. Cytometry Part A 11(2):231–238
Nieuwstadt HA, Seda R, Li DS, Fowlkes JB, Bull JL (2010) Microfluidic particle sorting utilizing inertial lift force. Biomed Microdevices. doi:10.1007/s10544-010-9474-6
Nivedita N, Papautsky I (2013) Continuous separation of blood cells in spiral microfluidic devices. Biomicrofluidics 7(5):054101. doi:10.1063/1.4819275
Oakey J, Applegate J, R, Arellano E, Di Carlo D (2010) Particle focusing in staged inertial microfluidic devices for flow cytometry. Anal Chem 82(9):3862–3867
Ozkumur E, Shah AM, Ciciliano JC, Emmink BL, Miyamoto DT, Brachtel E, Yu M, Chen P-I, Morgan B, Trautwein J, Kimura A, Sengupta S, Stott SL, Karabacak NM, Barber TA, Walsh JR, Smith K, Spuhler PS, Sullivan JP, Lee RJ, Ting DT, Luo X, Shaw AT, Bardia A, Sequist LV, Louis DN, Maheswaran S, Kapur R, Haber DA, Toner M (2013) Inertial focusing for tumor antigen-dependent and -independent sorting of rare circulating tumor cells. Sci Trans Med 5(179):179ra147–179ra147. doi:10.1126/scitranslmed.3005616
Park J, Jung H (2009) Multiorifice flow fractionation: continuous size-based separation of microspheres using a series of contraction/expansion microchannels. Anal Chem 81(20):8280–8288
Park J, Song S, Jung H (2009) Continuous focusing of microparticles using inertial lift force and vorticity via multi-orifice microfluidic channels. Lab Chip 9(7):939–948
Russom A, Gupta A, Nagrath S, Carlo D, Edd J, Toner M (2009) Differential inertial focusing of particles in curved low-aspect-ratio microchannels. New J Phys 11:075025
Saffman P (1965) The lift on a small sphere in a slow shear flow. J Fluid Mech 22(02):385–400
Segre G, Silberberg A (1961) Behavior of macroscopic rigid spheres in Poiseuille flow. J Fluid Mech 14:115–135
Segre G, Silberberg A (1962) Behaviour of macroscopic rigid spheres in Poiseuille flow Part 1. Determination of local concentration by statistical analysis of particle passages through crossed light beams. J Fluid Mech 14(01):115–135
Segré G, Silberberg A (1961) Radial particle displacements in Poiseuille flow of suspensions. Nature 189:209–210
Seo J, Lean M, Kole A (2007) Membrane-free microfiltration by asymmetric inertial migration. Appl Phys Lett 91:033901
Shen S, Ma C, Zhao L, Wang Y, Wang J, Xu J, Li T, Pang L, Wang J (2014) High-throughput rare cell separation from blood samples using steric hindrance and inertial microuidics. Lab Chip. doi:10.1039/c3lc51384j
Sollier E, Amini H, Go DE, Sandoz PA, Owsley K, Di Carlo D (2015) Inertial microfluidic programming of microparticle-laden flows for solution transfer around cells and particles. Microfluid Nanofluid. doi:10.1007/s10404-015-1547-7
Sollier E, Go DE, Che J, Gossett DR, O'byrne S, Weaver WM, Kummer N, Rettig M, Goldman J, Nickols N, Mccloskey S, Kulkarni RP, Di Carlo D (2014) Size-selective collection of circulating tumor cells using Vortex technology. Lab Chip. doi:10.1039/c3lc50689d
Sun J, Li M, Liu C, Zhang Y, Liu D, Liu W, Hu G, Jiang X (2012) Double spiral microchannel for label-free tumor cell separation and enrichment. Lab Chip. doi:10.1039/c2lc40679a
Tanaka T, Ishikawa T, Numayama-Tsuruta K, Imai Y, Ueno H, Matsuki N, Yamaguchi T (2012) Separation of cancer cells from a red blood cell suspension using inertial force. Lab Chip. doi:10.1039/c2lc40354d
Tanaka T, Ishikawa T, Numayama-Tsuruta K, Imai Y, Ueno H, Yoshimoto T, Matsuki N, Yamaguchi T (2011) Inertial migration of cancer cells in blood flow in microchannels. Biomed Microdevices. doi:10.1007/s10544-011-9582-y
Vasseur P, Cox R (1976) The lateral migration of a spherical particle in two-dimensional shear flows. J Fluid Mech 78(02):385–413

Wang X, Zhou J, Papautsky I (2013) Vortex-aided inertial microfluidic device for continuous particle separation with high size-selectivity, efficiency, and purity. Biomicrofluidics 7(4):044119. doi:10.1063/1.4818906

Warkiani M, Khoo B, Tan D, Bhagat A, Lim W-T, Yap Y, Lee S, Soo R, Han J, Lim C (2014a) An ultra-high-throughput spiral microfluidic biochip for the enrichment of circulating tumor cells. Analyst 139(13):3245–3255

Warkiani ME, Guan G, Luan KB, Lee WC, Bhagat A (2014b) Slanted spiral microfluidics for the ultra-fast, label-free isolation of circulating tumor cells. Lab Chip. doi:10.1039/c3lc50617g

Wu L, Guan G, Hou H, Bhagat A, Han J (2012) Separation of leukocytes from blood using spiral channel with trapezoid cross-section. Anal Chem

Xiang N, Chen K, Dai Q, Jiang D, Sun D, Ni Z (2014) Inertia-induced focusing dynamics of microparticles throughout a curved microfluidic channel. Microfluid Nanofluid. doi:10.1007/s10404-014-1395-x

Xiang N, Chen K, Sun D, Wang S, Yi H, Ni Z (2012) Quantitative characterization of the focusing process and dynamic behavior of differently sized microparticles in a spiral microchannel. Microfluidics and Nanofluidics. doi:10.1007/s10404-012-1025-4

Xiang N, Shi Z, Tang W, Huang D, Zhang X, Ni Z (2015) Improved understanding of particle migration modes in spiral inertial microfluidic devices. RSC Adv 5:77264–77273. doi:10.1039/C5RA13292D

Xiang N, Yi H, Chen K, Sun D, Jiang D, Dai Q, Ni Z (2013) High-throughput inertial particle focusing in a curved microchannel: insights into the flow-rate regulation mechanism and process model. Biomicrofluidics

Yeo DC, Wiraja C, Zhou Y, Tay HM, Xu C, Hou HW (2015) Interference-free micro/nanoparticle cell engineering by use of high-throughput microfluidic separation. ACS Appl Mater Interfaces 7(37):20855–20864. doi:10.1021/acsami.5b06167

Zhang J, Li W, Li M, Alici G, Nguyen N-T (2013) Particle inertial focusing and its mechanism in a serpentine microchannel. Microfluid Nanofluid. doi:10.1007/s10404-013-1306-6

Zhang J, Yan S, Li W, Alici G, Nguyen N-T (2014a) High throughput extraction of plasma using a secondary flow-aided inertial microfluidic device. RSC Adv. doi:10.1039/C4RA06513A

Zhang J, Yan S, Sluyter R, Li W, Alici G, Nguyen N-T (2014b) Inertial particle separation by differential equilibrium positions in a symmetrical serpentine micro-channel. Sci Rep 4:1–9. doi:10.1038/srep04527

Zhang X, Xiang N, Tang W, Huang D, Wang X, Yi H, Ni Z (2015) A passive flow regulator with low threshold pressure for high-throughput inertial isolation of microbeads. Lab Chip 15:3473–3480. doi:10.1039/C5LC00647C

Zhou J, Giridhar PV, Kasper S, Papautsky I (2013) Modulation of aspect ratio for complete separation in an inertial microfluidic channel. Lab Chip. doi:10.1039/c3lc50101a

Zhou J, Giridhar PV, Kasper S, Papautsky I (2014) Modulation of rotation-induced lift force for cell filtration in a low aspect ratio microchannel. Biomicrofluidics 8(4):044112. doi:10.1063/1.4891599

Microfluidic Technologies for Deformability-Based Cell Sorting

Quan Guo, Simon P. Duffy and Hongshen Ma

Abstract There are many situations in medicine and biology where it is desirable to distinguish specific cells within a population based on their mechanical deformability, which can potentially serve as a proxy for morphology or pathology. This biophysical characteristic is particularly relevant for cells in the circulatory system because deformability determines the capacity for these cells to transit through the microvasculature. These circulating cells include the abundant hematological cells such as erythrocytes (red blood cells, RBCs) and leukocytes (white blood cells, WBCs), as well as rare cells, such as circulating tumor cells (CTCs). Since deformability is such a fundamental characteristic of blood cells, deviations in normal cell deformability can contribute to a range of pathological conditions and potentially serve as a biomarker to evaluate them during treatment. In this chapter, we first discuss the role of deformability in circulating cells, including erythrocytes, leukocytes, and CTCs. We then briefly introduce our recent efforts in measuring cell deformability, and then compare the deformability of various circulating cells. Subsequently, we review the principles and applications of established strategies for deformability-based cell separation, including hydrodynamic chromatography and microfiltration. Finally, we will describe a recently developed method to sort cells based on deformability using the microfluidic ratchet mechanism, as well as its application in deformability-based separation of CTCs and deformability-based sorting of RBC infected with *P. falciparum*, the parasite that causes malaria.

Q. Guo · S.P. Duffy · H. Ma (✉)
Department of Mechanical Engineering, University of British Columbia (UBC),
2054-6250 Applied Science Lane, Vancouver, BC V6T 1Z4, Canada
e-mail: hongma@mech.ubc.ca

Q. Guo
e-mail: tomgqparker@gmail.com

S.P. Duffy
e-mail: simon.p.duffy@gmail.com

W. Lee et al. (eds.), *Microtechnology for Cell Manipulation and Sorting*,
Microsystems and Nanosystems, DOI 10.1007/978-3-319-44139-9_8

Keywords Hematological cells · Erythrocyte · Red blood cell · Malaria · *Plasmodium falciparum* · Leukocyte · White blood cell · Cell deformability · Cell sorting · Hydrodynamic chromatography · Microfiltration · Microfluidic ratchet · Microfluidics · Circulating tumor cells

1 Cell Deformability as a Physical Biomarker for Circulating Cells

This section will first describe circulatory cells for which deformability plays an important role and where deviations from normal deformability are a potential physical biomarker for pathology. Specific examples will be provided for red blood cells, white blood cells, and circulating tumor cells. Subsequently, experimental validation of such biomarkers is discussed to provide a quantitative comparison of the deformabilities of various circulating cells.

1.1 Red Blood Cell Deformability

Red blood cells, or erythrocytes, perform the critical function of circulating throughout the body to transport oxygen and carbon dioxide between tissues. Along its circulatory path, these cells must transit through pores that are much smaller than their diameter, such as in the micro-capillaries of the lung and the inter-endothelial clefts of the spleen (Fig. 1a). Consequently, normal RBCs must be able to undergo repeated and extensive deformation (Crosby 1959; Chen and Weiss 1973). The ability for RBCs to deform may be lost as a consequence of senescence (Bosch et al. 1994; Sutera et al. 1985), or as a result of hereditary disorders such as sickle cell disease (Clark et al. 1980; Nash et al. 1984), spherocytosis (Perrotta et al. 2008), thalassemia (Schrier 1994), immune hemolytic anemia (Alaarg et al. 2013), as well as some infectious diseases like malaria (Paulitschke and Nash 1993; Cranston et al. 1984). The loss of RBC deformability is medically significant as rigid cells can be sequestered in tissues causing microvascular obstruction, ultimately resulting in necrosis and tissue death (Fig. 1b).

One of the key diseases associated with alterations in RBC deformability is malaria, which results from mosquito-borne transmission of protozoan parasites of the genus *Plasmodium*. *Plasmodium falciparum* is the most prevalent and deadliest species of the parasites that cause malaria. A central aspect of infection by *P. falciparum* is the invasion of host RBCs where the parasite develops and asexually reproduces over a ~48-h period. The growth and development of parasites during this intra-erythrocytic stage has been characterized as a series of morphologically distinct stages starting from ring, progressing to trophozoite, and then to the mature schizont stage. Interestingly, the maturation of the parasite within a host RBC coincides with a progressive decrease in the deformability of that cell

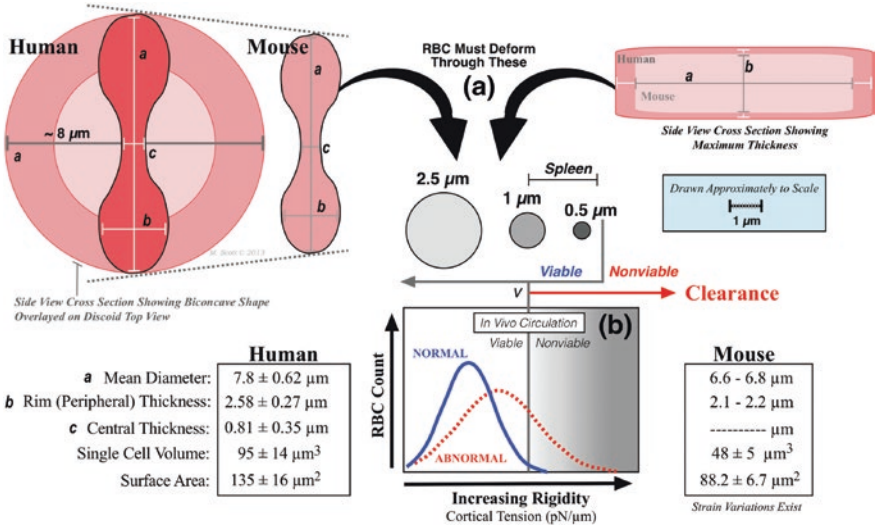

Fig. 1 **a** Schematic illustration of human and mouse RBCs in proportion to the diameters of capillary and inter-endothelial splenic pore; **b** abnormal RBCs, either from aging or caused by certain pathology, become less deformable and more susceptible to sequestration. Line v represents a threshold at which clearance from circulation is likely to occur via spleen entrapment or by other mechanism [Reproduced with permission from Kwan et al. (2013). Copyright 2012, American Journal of Hematology]

(Cranston et al. 1984; Nash et al. 1989). Consequently, RBC deformability can potentially be used to determine the stage of parasite maturation at the single cell level (Guo et al. 2012).

Multiple factors contribute to the reduction of RBC deformability over the course of the intra-erythrocytic part of the lifecycle of *P. falciparum*: (1) the byproducts of hemoglobin metabolism induce oxidative stress within the host RBC that contributes to membrane rigidification by cytoskeletal cross linking and lipid peroxidation (Mohanty et al. 2014); (2) the parasite expresses proteins that are inserted as neoantigens on the surface membrane of the host RBC and contribute to reduced host cell deformability (Mills et al. 2007; Moxon et al. 2011; Diez-Silva et al. 2012); and (3) at later stages of the parasite lifecycle, the presence of solid parasites may also impair the deformation of the host cell (Hosseini and Feng 2012). Parasitized cells ultimately rupture to release daughter merozoites and the release of heme products may contribute to rigidification of bystander uninfected RBCs (uiRBCs) (Omodeo-Salè et al. 2005). However, it is important to note that the rigidification of iRBCs increases exponentially during the asexual parasite lifecycle and parasitized cells are clearly distinguishable from bystander cells (Guo et al. 2012).

A significant challenge to the control and eventual eradication of malaria is that this disease is largely endemic to resource-poor regions, where advanced laboratory facilities may not be available. Microscopic analysis of blood smear

has been established as the standard for diagnosis because it is a sensitive method that requires only basic laboratory facilities. However, such diagnosis requires specialized training that may not be readily available. Microfluidic technologies have a potentially important role to play as these methods pave the way for novel low-cost and portable approaches to perform diagnosis and scientific research in malaria endemic regions. The development of sensitive deformability-based diagnostic systems offers the advantage of providing objective and quantitative assessment of infection. Furthermore, since deformability is a biophysical parameter, there is no need for immunological and other reagents that could limit the shelf-life of the system or impose a need for refrigeration. For these reasons, emerging microfluidic technologies have a tremendous potential to enable more accurate and earlier diagnosis of malaria, even in remote regions endemic to the infection.

Deformability-based analysis and sorting of *Plasmodium falciparum* infected RBCs (*Pf*-iRBCs) are also important tools for malaria research. Since reduction in *Pf*-iRBC deformability directly correlates with parasite intra-erythrocyte maturation, these cells can be fractionated based on the developmental stage of the intracellular parasite. This capability facilitates the discovery of biomarkers associated with parasite growth and drug metabolism, using genomic and proteomic methods. These advantages of deformability-based microfluidic sorting technologies can also extend to other hematological disorders, like sickle cell disease, or RBC senescence, to reveal how alteration of deformability contributes to RBC pathology.

1.2 White Blood Cell Deformability

White blood cells, or leukocytes, are the immune cells that protect the body from infectious disease and foreign substances. Leukocytes are classified into a range of phenotypes and sub-phenotypes that vary widely in morphology. For example, based on nuclear morphology, leukocytes can be classified into granulocytes and agranulocytes. The first group includes neutrophils, eosinophils and basophils, which have a multi-lobed nucleus and numerous cytoplasmic granules. The second group includes lymphocytes and monocytes, which have a large round nucleus.

While circulating in the blood stream, leukocytes are significantly less deformable than erythrocytes and have been reported to cause capillary obstruction (Guo et al. 2012, 2014). Leukocytes in passive circulation typically assume a spherical shape that vary in diameter from 6 to 8 μm, including lymphocytes (6.2 μm), neutrophils (7.0 μm), eosinophils (7.3 μm), and monocytes (7.5 μm) (Schmid-Schönbein et al. 1980). While the average size of these subpopulations of circulating leukocytes differs slightly, the size distribution overlaps significantly (Schmid-Schönbein et al. 1980), making it difficult to discriminate these cells based solely on size. When activated, leukocytes can undergo dramatic morphological changes that allow these cells to migrate through the endothelial wall of the blood vessels. Such transendothelial migration has been best characterized in the most abundant circulating leukocytes, including neutrophils (Yap and Kamm 2005) and lymphocytes (Brown et al. 2001; Anderson and Anderson 1976;

Miyasaka and Tanaka 2004), and involves rapid cytoskeletal remodeling from a semi-rigid spherical state into a flattened and highly deformable state. This morphological change is part of leukocyte extravasation, which enables these cells to penetrate small gaps between endothelial cells. Following extravasation, leukocytes may also further adopt other morphological conformations in the tissue. When stimulated by chemoattractants, produced during acute inflammation of the lung, neutrophils rigidify, and sequester within the tissue (Worthen et al. 1989).

The studies of leukocytes have traditionally emphasized their central role in infectious or immune hypersensitivity diseases. Currently, flow cytometry is the primary means to phenotype leukocytes and to evaluate their state. However, due to the large variety of leukocyte phenotypes and limited molecular biomarkers to indicate their status, existing approaches are unable to completely resolve leukocyte phenotype or their activation state. In some cases, these properties can potentially be resolved using biophysical properties as a proxy for differences in their morphology. Deformability-based cell separation can then leverage these properties to isolate leukocytes of specific subtypes or states for further study.

1.3 Circulating Tumor Cells

Circulating tumor cells (CTCs) are believed to be the precursors to the formation of secondary tumors during metastasis (Comen et al. 2011). CTCs are of strong prognostic value (Allard et al. 2004) and can serve as a biomarker for monitoring treatment efficacy. Therefore, detection, enumeration, capture, and characterization of CTCs has the tremendous potential to advance cancer research, diagnostics, and treatment. The long-standing challenge of CTC capture has been the extreme rarity of these cells, occurring at a density as low as 1 in 10^9 erythrocytes or 1 in 10^7 leukocytes (Miller et al. 2010). CTC capture and enumeration is typically achieved by immunoaffinity capture but this method has come under question, as the target epithelial antigens may not be expressed on the most relevant CTCs (Punnoose et al. 2010). Cell sorting by deformability represents a compelling alternative to immunoaffinity capture because a key discriminating feature of tumor cells is that they typically originate from non-hematological tissues, such as epithelium, and these cells are larger and significantly more rigid than RBCs and leukocytes.

The distinct morphology of tumor cells was first used to enrich CTCs from blood by filtration of the cells on clear plastic tape (Seal 1964). More recently, polycarbonate membrane microfiltration systems have been developed with far more precise pore size and permit rapid enrichment of CTCs (Vona et al. 2000; Desitter et al. 2011). However, an important limitation to CTC microfiltration is that these filters may clog due to the high density of cells in blood. As a consequence, microfiltration typically requires a debulking step prior to sorting, such as RBC lysis, a process that may contribute to target cell loss. Also, CTCs are typically chemically fixed so that they can be filtered under pressures that would normally lyse the cells. This cell fixation partially addresses the clogging of the filter but also rigidifies the cells such that they are sorted on the basis of size alone, but not cell deformability.

By overcoming the limitations imposed by device fouling due to clogging, it would be possible to enrich CTCs on the combined basis of cell size and deformability. Not only would this filtration system be more sensitive and selective than conventional microfilters, the added capability to sort cells by deformability would allow separation of CTCs and leukocytes of similar size. For these reasons, size- and deformability-based CTC enrichment represents a compelling label-free alternative to immunoaffinity capture of CTCs that may improve the accuracy of prognosis based on CTC enumeration.

1.4 Deformability Measurement Using Microfluidic Micropipette Aspiration

In order to establish cell deformation as a physical biomarker for cell morphology or pathology, it is important to develop robust methods to measure cell deformability. One prominent technique for measuring individual cell deformability is micropipette aspiration developed by Evans and La Celle (1975). The classic form of this technique involves the complete or partial suction of single cells into the orifice of a glass micropipette using a minute negative pressure. The intrinsic mechanical properties of aspirated cells can then be determined using various models (Hochmuth 2000) based on measured relationship between suction pressure, the diameter of the orifice, the diameter of the resting cells and the protrusion length of the cell in the pipette. So far, micropipette aspiration has presented itself as a highly effective technique for measuring the deformability of individual living cells in research settings.

Our group has applied the principle of micropipette aspiration and developed the microfluidic version of this prominent technique, as shown in Fig. 2a. Specifically, the deformability of an individual cell was investigated by pressurizing cell through micron-scale constrictions. The microstructure was designed such

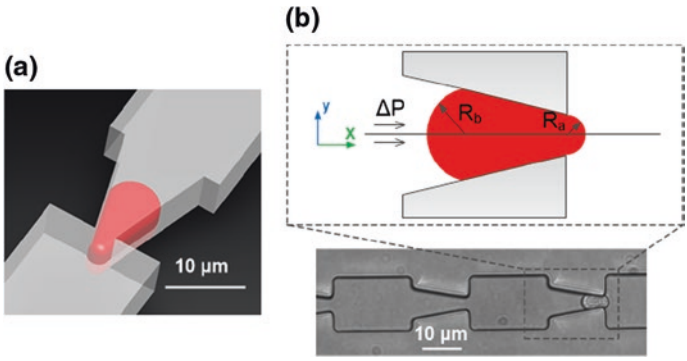

Fig. 2 Microfluidic micropipette aspiration of individual cells. **a** Schematic illustration of an individual cell passing through a 3-D micron-scale tapered constriction. **b** Deformation of a single cell through funnel constriction at the instability with leading and trailing radii edge (R_a and R_b)

that the entrance of the funnel is larger than the diameter of the cells, while the exit is smaller. The tapered funnel shape provides test cells with a smooth transition through which to deform. The funnel openings are sized to create a temporary seal with each cell as it passes through; and therefore the force applied across the funnel infers the forces required to squeeze individual cells through the constriction. To derive an intrinsic property of cells from the force measurement, an individual cell may be modeled using a simple liquid drop model (Hochmuth 2000) which considers a cell as a liquid drop with a constant cortical tension, T_c. From observation, as a cell transits the constriction, the pressure required to advance the cell increases until a point of instability, known as the Haines' jump (2009), after which the cell is rapidly pulled through the constriction. The threshold pressure for Haines' jump depends on the rigidity of the deformed cells and deformation geometry, including the radius of the leading cell surface and the radius of the trailing cell surface, which are in turn determined by the geometrical constraint provided by the funnel (Fig. 2b). The relationship can be modeled using Young–Laplace law

$$\Delta P = T_c \left(\frac{1}{R_a} - \frac{1}{R_b} \right) \tag{1}$$

In this model, R_a and R_b are the leading and trailing radii and T_c is the intrinsic cortical tension (pN/μm), representing the deformability of the test cell. Originally, the technique was developed to only process one cell at a time, which can be laborious and time-consuming. Recently, we have been able to multiplex this mechanism to enable deformability measurement of multiple cells in one run (Myrand-Lapierre et al. 2014). We have also greatly simplified the data analysis by adapting this system such that cell deformability can be measured based on transit rate of cells through a chain of microscale funnels (Santoso et al. 2015).

Using this mechanism, we have measured the cortical tension of various cells types, including hematological cells, such as erythrocytes, lymphocytes and granulocytes, cultured cancer cells (L1210 mouse lymphoma cells and RT4 bladder cancer cells) (Guo et al. 2012) and malaria *Pf*-iRBCs at different intra-erythrocytic stages (0–16 h: ring stage; 16–24 h: early trophozoite; 24–40 h: late trophozoite; 40–48 h: schizont) (Guo et al. 2012). Figure 3 illustrates the deformability spectrum of these cell types. Each cell is accompanied by images from microscopy Giemsa or Wright stain as shown in the inset images. Here, the deformability derived from measured cortical tension is normalized to 1 for healthy RBCs. RBCs parasitized by *P. falciparum* are observed to progressively become up to tenfold more rigid, within 40 h, and over 100-fold more rigid than healthy RBCs thereafter. Overall, we observed that the rigidity of parasitized RBCs increases exponentially as the parasite matures (Guo et al. 2012).

By measuring deformability, we can also discriminate between different cell types. Lymphocytes and neutrophils are the two abundant subtypes of leukocytes in circulation but they differ markedly in their cell deformability profiles (Fig. 3c). Furthermore, tumor cells of both epithelial and hematological origin were significantly more rigid than either erythrocytes or leukocyte. The sensitivity of these

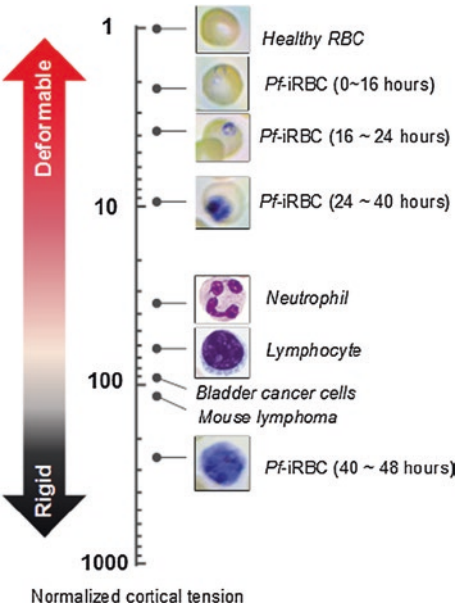

Fig. 3 Deformability spectrum of circulating cells including erythrocytes (RBCs), malaria *Plasmodium falciparum* infected RBCs (*Pf*-iRBCs), leukocytes (neutrophils, lymphocytes) as well as cultured tumor cells such as bladder cancer cells, and mouse lymphoma. Giemsa images of the *Pf*-iRBCs at different development stages over the 48-h life cycle are inserted, including early ring stage (0–16 h), early Trophozoite (16–24 h), late Trophozoite (24–40 h) and Schizont (40–48 h). Wright stain images of neutrophils and lymphocytes are also included

techniques also provides the opportunity to rapidly assess leukocyte activation, based on changes in cell deformability. Furthermore, the clear distinction between the biomechanical properties of these cells suggests that deformability-based sorting would offer an effective means to sort erythrocyte, leukocytes, and tumor cells from blood.

2 Hydrodynamic Chromatography

This section describes the first of three classes of physical cell separation approaches relevant to deformability-based cell sorting. This first approach could be broadly described as hydrodynamic chromatography where the flow path of certain cells is altered based on the physical properties of the cell via hydrodynamic effects when the heterogeneous population of cells flows through a fluidic microchannel. Specifically, deterministic lateral displacement and cell margination using non-inertial lift forces will be discussed.

2.1 Deterministic Lateral Displacement

Deterministic lateral displacement (DLD), first described by Huang et al. (2004), is a microfluidic technique for separating particles based on their sizes using a regular array of pillars. This technique has also recently has demonstrated its

potential to sort biological cells based on deformability (Beech et al. 2012; Krueger et al. 2014; Holmes et al. 2014). The principle of DLD can be explained by considering streamlines taken by infinitesimally small fluid particles in a microfluidic device where Reynolds number <<1, and thus fluid flow is entirely laminar. In this scenario, the streamlines are entirely independent of each other and do not cross or merge. Therefore, infinitesimally small fluid particles following one streamline will not move into another streamline. Particles of finite size, however, can be shifted onto a different streamline because of size exclusion, which occurs when the size of the particle exceeds the available space between the streamline and the edge of a boundary. In this case, the particle will be shifted onto a different streamline, where the amount of shift depends on particle size, and is therefore the basis of size-based separation using this mechanism (Fig. 4a).

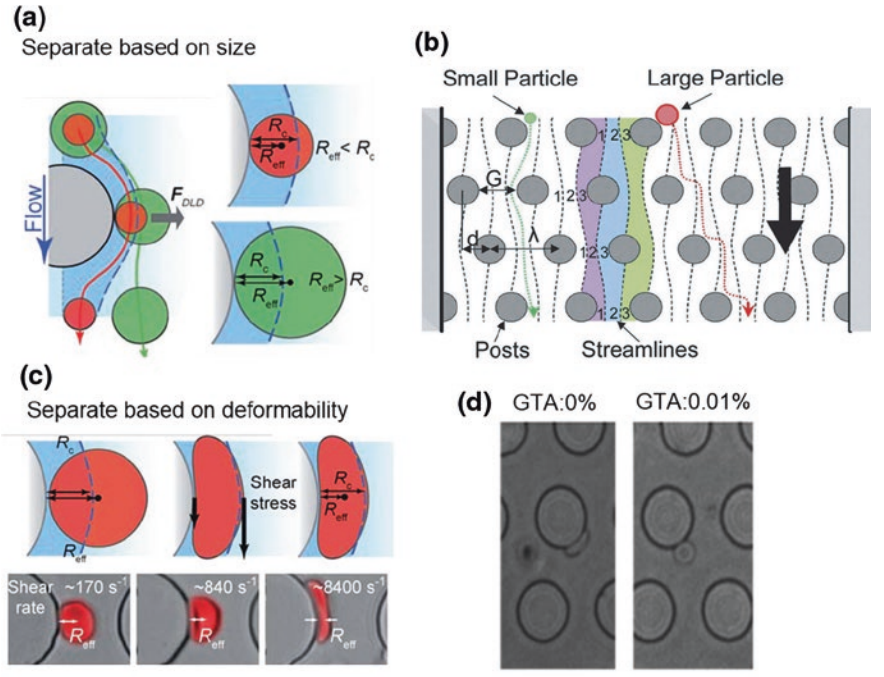

Fig. 4 Principle of deterministic lateral displacement for size and deformability-based separation. **a** *Red* particle with effective size (R_{eff}) smaller than the width of the streamline family (R_c) is confined by the streamline and follow the fluid flow; while *green* particle bigger than the streamline family width is bumped out of the streamline and therefore separated from the smaller particle. **b** Conceptual design and principle of the deterministic lateral displacement separation. **c** Effect of shear stress induced particle deformation on R_{eff}; **d** images of GTA treated RBCs interactions with the pillar at certain shear stresses; untreated RBCs is able to deform, leading to $R_{eff} < R_c$, which results in no lateral displacement; GTA-degraded RBCs retain the discoid shape ($R_{eff} > R_c$), causing lateral displacement of these cells way from the original flow direction [**a** and **c** Reproduced with permission from Beech et al. (2012). Copyright 2009, Applied Physics Letter; **b** reproduced with permission from Inglis (2009). Copyright 2012, lab on a chip; **d** reproduced with permission from Holmes et al. (2014). Copyright 2014, Interface Focus]

A separation system can be constructed by arranging the pillar array in such a way to continuously provide a shift of the particles based on size. As shown in Fig. 4b, the DLD device comprises a periodic array of micrometer-scale obstacles of either rectangular (Huang et al. 2004) or round pillars (Davis et al. 2006). Each row of the pillars is shifted horizontally to the right with respect to the previous row. For example, by shifting each row $d = 1/3\ \lambda$ (λ: center to center distance between pillars), we can consider a pillar array where fluid flow between the gap of the pillars can be divided into 3 family of streamlines, identified using purple, blue, and green colors. The three streamline families exiting the gap between first row of pillars are separated due to the lateral shift of the pillars in the next row. In this case, the purple streamline family leaving the first gap flows to the left of the pillar in the next row, while the blue and green family of streamlines flows to the right. As this process repeats, the streamlines return to their original relative positions within a single gap after three rows. Consequently, small particles within the confine of the purple streamline family will travel downwards through the array parallel to the sidewall. In contrast, particles of sizes larger than the width of the streamline family will be shifted by each row of pillars and proceed in a diagonal path through the pillar array. This process repeats at each row, resulting in distinct trajectories for larger particles along an angle through the pillar array.

DLD can also be extended to sort cells based on deformability by taking advantage of the fact that fluid flow near an obstacle could apply significant shear stress to compress nearby cells in transit. Specifically, flow near an obstacle boundary take on a parabolic velocity profile starting from zero velocity at the boundary. The velocity difference across the cell ranging from zero velocity at the boundary to the velocity at the opposing side of the cell, results in a shear stress that deforms the cell and modifies its shape. Figure 4c explains the dependence of RBC deformation near the pillar on flow rates, which can potentially influence the separation angle of the RBCs trajectory through the DLD (Beech et al. 2012). Experimentally, it has been also validated by Holmes et al. (2014). Specifically, they demonstrated the successful separation of untreated RBCs from 0.01 % glutaraldehyde (GTA) treated RBCs based on deformability. GTA is a fixative agent that induces cross linking and stabilization of RBC membrane proteins to reduce deformability in a concentration dependent manner, while the RBCs shape and size remain unchanged. Figure 4d clearly shows that GTA treated RBCs retain their discoid shape and do not deform, compared with untreated RBCs which deformed significantly under the flow shear stress. The ability of DLD to separate RBCs based on deformability further demonstrates the potential to separate diseased RBCs such as malaria *Pf*-iRBCs from uiRBCs.

In summary, DLD is a hydrodynamic method for manipulating and separating particles and cells in the laminar flow regime using pillar arrays to alter the flow paths of certain cells. The technique performs extremely well for size-based particle separation. Deformability-based cell sorting is possible in principle, but existing studies have been limited to chemically degraded RBCs and have not been extended to medically relevant scenarios.

2.2 Cell Margination Using the Non-Inertial Lift Force

Another form of cell separation using hydrodynamic chromatography is cell margination, which relies on the non-inertial lift force experienced by deformable cells near the wall of a microfluidic channel. As discussed earlier in DLD, in a microfluidic channel without any obstacles, rigid spherical particles typically do not cross streamlines in the laminar flow regime ($Re \ll 1$) where inertial fails and viscous effects dominate. However, softer cells can deform and reorient themselves under shear flow stress; and are able to experience the non-inertial lift force that can help them to cross streamlines. Originally discovered by Goldsmith and Mason in 1961, this force arises from shear stress experienced by deformable cells near the boundary of a microfluidic channel that can stretch deformable cells, such as RBCs, which produces a characteristic tank-treading motion (Goldsmith and Mason 1962; Olla 1997; Zhou et al. 2006). Tank treading motion, of RBC for example, refers to the rotation of the RBC membrane, in a similar motion to a treadmill, while cell is stretched axially. Consequently, RBCs remain a constant inclination with respect to the flow streamline which causes the non-inertial lift. As a result of this hydrodynamic lift, RBCs are pushed perpendicularly across streamlines away from the wall. Olla (1997) provided a quantitative theoretical calculation of the non-inertial lift force on objects experiencing tank tread motion, which predicted that (1) spherical objects experienced no such lift forces at $Re \ll 1$; (2) the lift force relied on the ability of the objects to deform to the ellipsoid shape. This theoretical prediction was later proved to be in good agreement to the experimental results for vesicles (Callens et al. 2008) as well as RBCs and platelets (Geislinger and Eggart 2012). Specifically, Geislinger and Eggart (2012) investigated the potential to separate RBCs, blood platelets, and solid microspheres from each other using the non-inertial hydrodynamic lift at various flow rate and fluid viscosity. A version of the cell margination effect observed for blood flow in capillaries is known as the Fåhræus–Lindqvist effect (1931). Here the highly deformable RBCs are pushed towards the center of the blood vessel because of the non-inertial lift force, while the less deformable leukocytes and platelets experience less lift force and are marginalized near the capillary walls. The phenomenon typically occurs at high hematocrit level as the accumulated RBCs collide and push the non-RBCs away from the centerline towards the side walls.

The margination effect has been used in microfluidic devices (Shevkoplyas et al. 2005) to isolate subpopulation of cells based on deformability. For example, Fåhræus–Lindqvist phenomenon was directly implemented using a biomimetic bifurcation design to isolate leukocytes from whole blood. As shown in Fig. 5a, this particular device was able to enrich leukocyte concentration over RBCs by 34-fold. Hou et al. presented another realization of the cell margination microfluidic device for deformability-based separation of RBCs infected with *Plasmodium falciparum*. As described in Sect. 1, RBCs infected with *P. falciparum* experience a dramatic reduction in their deformability as the parasite grows inside. As a result, deformable uiRBCs experienced greater lift forces, which concentrated

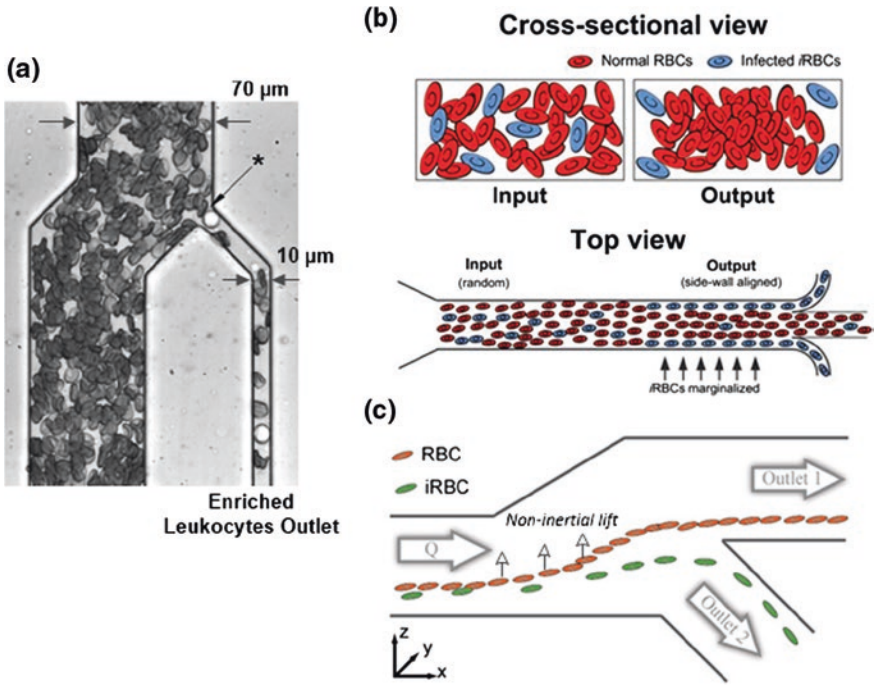

Fig. 5 **a** Biomimetic margination design of the bifurcated microfluidic channel for the concentration of leukocytes, a direct implementation of Fåhræus–Lindqvist effect; **b** schematic illustration of a microfluidic margination to perform deformability induced, margination-based separation of *Pf*-iRBCs at high hematocrits; **c** conceptual design for the separation of ring stage *Pf*-iRBCs using non-inertial lift forces. **a** Reproduced with permission from Shevkoplyas et al. (2005). Copyright 2005, Analytical chemistry; **b** reproduced with permission from Hou et al. (2010). Copyright 2010, Lab on a chip; **c** reproduced with permission from Geislinger et al. (2014). Copyright 2014, Malaria journal.

in the channel center while sterically displacing malaria iRBCs (late stages) toward the wall. After flowing through a long separation channel (~3 cm), iRBCs were enriched and collected through both the top and bottom side-channel outlets, shown in Fig. 5b. The group was able to capture iRBCs with a yield ~75 % for ring stages and >90 % for late stages with twofold enrichment of parasitemia. A significant shortcoming of the approach is the low sample (iRBCs) purity due to the requirement of high hematocrits (~40 %) input sample and high flow rate (0.2–5 μL/min). More recently (2014), Geislinger et al. (2014) demonstrated the separation of malaria iRBCs using only the hydrodynamic lift force at low flow rate and sample hematocrit. The schematic illustration of the concept is shown in Fig. 5c. The cells injected were focused to be near the lower wall using the sheath flow (not shown in the figure) before they flew through the separation channel (20 mm long) where they experienced the non-inertial lift effect. The bifurcation between Outlet 1 and 2 occurs at a distance 50 μm above the lower wall with outlet 2 connected at an angle 49° with Outlet 1 (Fig. 5c). The group was able to

achieve higher enrichment (4.3 fold) than Hou et al. (twofold) at the expense of low throughput (~12,000 cells/h).

In summary, cell margination enables deformability-based cell separation using the non-inertial lift force to selectively transport deformable cells towards the center of a microfluidic channel, while transporting rigid cells toward the channel walls. This mechanism has been adapted to separate leukocytes from RBCs (Shevkoplyas et al. 2005), as well as malaria iRBCs from normal RBCs (Hou et al. 2010). A key challenge in current studies is the need for high-density cell samples, which dramatically limits enrichment of target cells over background cells. Consequently, the cell margination mechanism is perhaps best utilized as an initial preprocessing step, before refining target cell selection through secondary and tertiary selection steps.

3 Microfiltration

Microfiltration is the process of flowing a cell sample through an array of microscale constrictions in order to capture target cells based on their sizes and deformability. Microfiltration techniques have been widely used extensively for biophysical cell separation, including the separation of leukocytes and CTCs from whole blood, where the size of the constriction opening determines the cut-off between cells captured and cells transited through the filter. This section describes current strategies for deformability-based cell separation using microfiltration. These strategies can be classified into three basic filter geometries (pore, weir, and pillar) and two filter schemes (dead-end and cross-flow filtration). Finally, this section describes challenges inherent to the selectivity of filtration-based cell separation schemes.

3.1 Filter Geometries

There are three different types of filter geometries, including pores, weirs, and pillars, as shown in Fig. 6. The pore filter microstructure consists of a membrane perforated with a 2-D array of holes. The diameter of the hole defines the critical cut-off dimension for capturing target cells of certain size and deformability. The weir filter microstructure consists of microchannels containing a sudden decrease in the channel cross section, which creates a barrier in the flow path to trap larger and more rigid cells while allowing the passage of smaller and softer cells. The size of the gap between the top of the obtrusion barrier and the top of the fluidic channel defines the critical cut-off dimension. The pillar filter microstructure consists of an array of micro-posts spaced appropriately to form constrictions to capture target cells. The narrowest distance, or gap, between each pair of pillars defines the critical cut-off dimension.

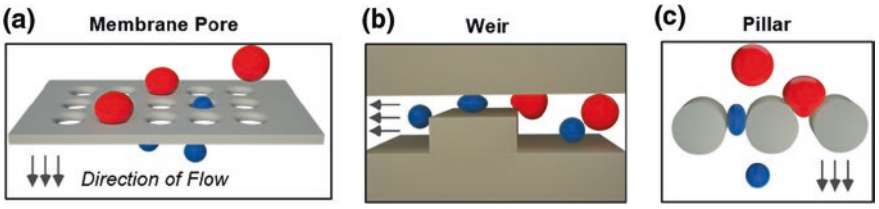

Fig. 6 Three basic filter geometries including **a** membrane pore; **b** weir; **c** pillar [This figure is reproduced with permission from Jin et al. (2014). Copyright 2014, Lab on a Chip]

3.2 Filtration Schemes

3.2.1 Dead-End Filtration

There are two types of filtration schemes (Ji et al. 2008): dead-end and cross-flow filtration, as shown in Fig. 7. In dead-end filtration, cells are simply infused into the filter microstructure using a pressure-driven flow. The process is extremely simple to perform, but a key challenge is cell clogging, which can reduce the selectivity of the process and limit the ability to extract the segregated cells for subsequent analysis. Specifically, as target cells are captured in the filter, they close off the available constrictions which increase the hydrodynamic resistance of the filters. If the sample infusion pressure is kept constant, the sample flow rate will be reduced as a result. Eventually, the sample flow comes to a complete stop, hence the name dead-end. In some cases, the increased hydrodynamic resistance is compensated by increasing the filtration pressure. However, since clogging is an unpredictable process, rising the filtration pressure greatly increases the potential to rupture the cells. Consequently, this approach necessitates fixing the cells to preserve their integrity, which greatly limit the available molecular analysis that could be applied to the captured cells (Lin et al. 2010; Zheng et al. 2007). A related issue to clogging is fouling, which occurs because captured cells remain in contact with the filter microstructure for a significant period of time during dead-end filtration. The prolonged contact between the cell and the filter microstructure

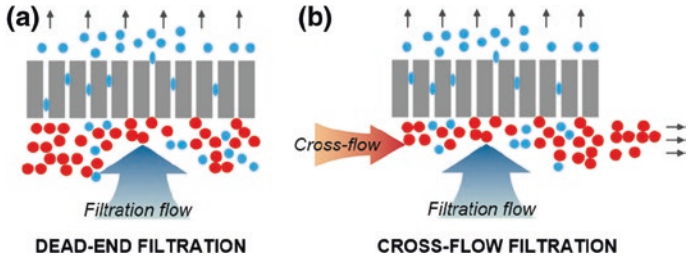

Fig. 7 Two common microfiltration schemes including **a** dead-end filtration and **b** cross-flow filtration

promotes the adsorption, which significantly limits the ability to extract the captured cells after separation.

3.2.2 Cross-Flow Filtration

To overcome clogging and enable continuous cell sorting, improved filtration techniques using cross-flow have been developed. Figure 7b is a typical cross-flow filtration scheme, in which a flow tangential to the filter surfaces is applied to remove the captured cells. This process is known as cross-flow or tangential-flow filtration. The cross-flow filtration scheme diverts most of the flow and cells stuck at the filters away and hence the filters are less prone to clogging. Since the cross-flow scheme aims to allow the less deformable cells to be stopped in a suspended state instead of being trapped in the filter permanently, this filtration process could be performed continuously.

Recent literature provides examples of using cross-flow filtration to separate leukocytes from whole blood in several cases. The design of a cross-flow filtration device typically consists of (1) two inlets (one to feed cell sample, the other to provide the cross flow), (2) a separation network consisting of an array of filter barriers and (3) two outlets (RBCs and leukocytes). Depending on the filter types, there are cross-flows using pillar (Ji et al. 2008; Chen et al. 2008; Sethu et al. 2006), weir (Chen et al. 2008; VanDelinder and Groisman 2007) or membrane pore (Li et al. 2014). For example, pillar type filters were constructed by Ji et al. by etching on silicone substrate; and by Chen et al. (2008) using silicone elastomer polydimethylsiloxane (PDMS). Both approaches were able to capture up to 90 % of all leukocytes. VanDelinder and Groisman (2007) fabricated an array of microchannels with a deep main channel, flanked by a large number of orthogonal, shallow side channels (weir type filter) to separate leukocytes from RBCs with capture efficiency of 98 % and leukocytes purity of 72 %. Despite the superior performances, the device did require diluted whole blood (1:1000) and had limited throughput of 3.6 μL/h. More recently, Li et al. (2014) also leveraged cross-filtration scheme in conjunction with a surface micro-machined PDMS membrane pore type filters to achieve leukocytes separation. The device is able to deplete majority of RBCs (purity of leukocytes ~98 %), and capture ~27 % of all leukocytes at a throughput of 17 μL/min.

Although cross-flow can significantly reduce cell clogging and adsorption, the selectivity of the approach is limited because the cross-flow action disrupts the filtration process. Previous studies on the separation of leukocytes from RBCs have found that when the cross-flow is too strong, RBCs were not given sufficient opportunity to come in contact with the filters before they were carried away by the cross-flow to leukocytes outlet. Consequently, the purity of the separated leukocytes was typically quite low in existing examples of cross-flow microfiltration device (refer to Table 1 for comparison of previous studies) (Ji et al. 2008; Chen et al. 2008; Sethu et al. 2006). When the cross-flow is set to be slow to avoid the contamination of RBCs, it typically results in poor declogging, which can result

Table 1 Performances specifications of recent research in deformability-based cell separation using microfiltration

Filtration type and method	Target cells	Performance metrics					References
		Efficiency or yield (%)	Purity (%)	Enrichment over WBCs	Enrichment over RBCs	Capacity/throughput	
Dead-end; pore	LNCaP prostate; MCF-7 breast	86.5	–	10^3	–	–/>120 ml h^{-1}	Zheng et al. (2011)
Dead-end; pillar	Mixture of cancer cells	80	90	–	–	–	Tan et al. (2009)
Dead-end; pillar	PC-3 prostate cancer	>90	–	60–200	–	1 ml whole blood/0.2 ml min^{-1}	Lu et al. (2010)
Dead-end; pillar	Leukocytes	18–25	<1	–	5–10	1.5 µL whole blood/–	Alvankarian et al. (2013)
Dead-end; weir	Leukocytes	71	~10	–	210	Diluted blood/4000 cells s^{-1}	Choi et al. (2007)
Dead-end; weir	Leukocytes	60	–	–	–	Whole blood/3–15 µL h^{-1}	Chen et al. (2013)
Dead-end; pore	Leukocytes	>90	–	–	–	1.5 µL whole blood/–	Hosokawa et al. (2012)
Dead-end; pore	Leukocytes	72–85	–	–	1	200 µL whole blood/10 µL min^{-1}	Ji et al. (2008)
Dead-end; weir	Leukocytes	~70	–	–	1.1–1.7	<50 µL whole blood/10–50 µL min^{-1}	Ji et al. (2008)
Dead-end; pillar	Leukocytes	70–95	–	–	1.25–2	300 µL whole blood/20 µL min^{-1}	Ji et al. (2008)
Cross-flow; weir	Leukocytes	98	72	–	–	Diluted whole blood/3.6 µL h^{-1}	VanDelinder and Groisman (2007)
Cross-flow; pillar and weir	Leukocytes	20–90	<1		2–10	Diluted blood/10 µL min^{-1}	Chen et al. (2008)

(continued)

Table 1 (continued)

Filtration type and method	Target cells	Performance metrics					References
		Efficiency or yield (%)	Purity (%)	Enrichment over WBCs	Enrichment over RBCs	Capacity/throughput	
Cross-flow; pore	Leukocytes	27.4 ± 4.9	93.5 ± 0.5	–	–	Whole blood/~17 μL min^{-1}	Li et al. (2014)
Cross-flow; pillar	Leukocytes	97	<1	–	2	–/5 μL min^{-1}	Sethu et al. (2006)
Cross-flow; pillar	Leukocytes	70–95 %	–	–	2.5–20	Whole blood/20 μL min^{-1}	Ji et al. (2008)

in low capture efficiency in some cases (Li et al. 2014). The potential underlying issue for the sub-optimal selectivity of cross-flow schemes arises from the fact that the cross-flow is not applied directly against the filtration but at a 90° angle to filtration flow. This issue suggests the idea of developing a declogging flow in the direction against the filtration flow to achieve more efficient declogging effect. This strategy will be discussed in detail in Sect. 4.

3.3 Applications of Microfiltration for Deformability-Based Cell Sorting

Despite the issues of cell clogging and adsorption associated with microfiltration, this approach is attractive to many researchers as a simple and economic way of sorting cells based on their mechanical deformability. Table 1 summaries some of microfiltration techniques developed so far for deformability-based cell sorting. Typical applications using microfiltration include: (1) separating culture cancer cells from whole blood as a model for patient-derived CTCs; (2) leukocytes separation from RBCs; and (3) pathological RBCs separation such as malaria *Pf*-iRBCs from uiRBCs. Table 1 identifies the filter types and filtration schemes employed by each paper and summarizes their performance specifications, including capture efficiency, purity or enrichment, capacity, and throughput.

In general, for dead-end filtration, the device can either only process limited amount of blood (up to 1 mL) or requires diluted whole blood. Techniques utilizing cross-flow schemes can perform continuous separation but also requires diluted whole blood in many cases. The performances of cross-flow microfiltration for leukocyte separation from RBCs are generally better than those of dead-end microfiltration. Specifically, Ji et al. (2008) compared the performances of cross-flow and dead-end microfiltration with the same cut-off size (~3.5 μm) for isolating leukocytes from human whole blood samples. The results confirm that cross-flow filtration scheme with pillar filter geometry has better performances in terms of leukocytes capture efficiency, purity, and blood handling capacity than those of dead-end filtrations using either pillar, weir or pores.

Studies of CTCs separation typically involved experiments of separating cultured cancer cells spiked in whole blood as a model to predict the performances of CTCs enrichment from patient sample blood. In early studies using cultured cancer cells, the samples were typically fixed before filtration by various cross-linking agents such as glutaraldehyde and paraformaldehyde (Desitter et al. 2011; Lin et al. 2010; Zheng et al. 2007; Hosokawa et al. 2010), because the deformability of cancer cells was considered to be detrimental to capture efficiency. Recent studies by Zheng et al. (2011) have been able to capture viable CTCs (without fixation) based on the combination of size and deformability without compromising the capture efficiency.

In summary, microfiltration is a simple and economical strategy to separate biological cells based on deformability despite issues associated with cell clogging

and adsorption. Although microfiltration using cross-flow scheme can reduce the likelihood of clogging and adsorption, the cross-flow cannot solve the clogging issue completely without disrupting the filtration process. This limitation suggests the idea of developing alternative microfiltration strategy that can completely liberate all cells from filters and reduce the duration of contact of cells with the filters to avoid adsorption.

4 Deformability-Based Cell Sorting Using Microfluidic Ratchet

This section introduces an improved microfiltration scheme utilizing the microfluidic ratchet mechanism developed by our group. We describe the underlying principle of the microfluidic ratchets and how this mechanism permits continuous deformability-based sorting of complex samples, such as whole blood, without clogging or adsorption. Finally, thus enabling continuous deformability-based separation of CTCs, as well as sorting of RBCs to enrich for cells infected with *P. falciparum*.

4.1 Microfluidic Ratchet Mechanism

The principle of the microfluidic ratchet mechanism relies on the deformation of individual cells through tapered constrictions with openings smaller than their diameter. Deforming cells along the direction of the funnel taper requires less pressure than against the direction of the funnel taper. Oscillatory flow of an appropriate magnitude coupled with this physical asymmetry, allow some cells to transport through the funnel unidirectionally in a ratcheting manner, while other cells are blocked by the funnel and released on the subsequent flow reversal. The outcome of this transport process depends on the ability of single cells to deform or squeeze through micrometer-scale size constrictions when subjected to a precisely controlled pressure, and thereby enabling deformability-based cell separation. The oscillatory flow plays the additional role of minimizing contact between cells and the funnel constrictions to prevent cell clogging and adsorption.

Microstructures forming individual microfluidic ratchets are designed as a 2-D tapered constriction, where the opening at the entrance side is larger than the typical cell diameter, while the opening at the exit side is smaller than the typical cell diameter (Fig. 8). Key geometrical parameters of this microstructure includes (1) the pore size W_0, defined as minimum opening of the funnel, (2) the thickness of the funnel microstructure, and (3) the shape of the funnel taper (θ). The tapered constrictions are sized such as a cell is laterally constrained and must deform in order to transit, but is vertically unconstrained to provide stress relief. Under these conditions, the deformation force required to transit cells through such a

constriction can be modeled using Young Laplace's Law (Eq. 1) and liquid drop model described in Sect. 1.4.

$$\Delta P = T_c \left(\frac{1}{R_a} - \frac{1}{R_b} \right) \tag{1}$$

From this model, the pressure (ΔP) required to squeeze a cell through the funnel constriction is a function of membrane cortical tension (T_0), as well as the leading and trailing radii (R_a and R_b) of the cells. Because of their confinement in an asymmetric taper, the cell requires a different deformation pressure to transit through the taper along the direction of the taper versus against the direction of the taper (Fig. 8b, c) (Guo et al. 2011). Specifically, when a cell is squeezed along the direction of the taper (Fig. 8a), both the leading and trailing radii are constrained, which reduces the difference between R_a and R_b, resulting in smaller transiting pressure. Conversely, when a cell is squeezed against the direction of the taper (Fig. 8b), only the leading edge (R_a) is constrained while the trailing edge (R_b) is unconstrained, which results in larger differences between R_a and R_b, leading to larger transiting pressure.

The existence of the deformation pressure asymmetry has been experimentally confirmed by deforming L1210 mouse lymphoma cells (~10 μm diameter) through funnel constrictions with a range of pore sizes (6–9 μm) and shapes ($\theta = 0°$, 5°, and 10°) (Guo et al. 2011). A microfluidic device was specifically designed to measure the deformation pressure required to transit L1210 cells both along the direction of the funnel taper (Fig. 8a) and against the direction of the funnel taper (Fig. 8b). The expected deformation pressure asymmetry was observed, and the deformation pressure increased with decreasing pore size. Furthermore, the pressure asymmetry increased as the taper angle (θ) decreased from 10° to 5°, but

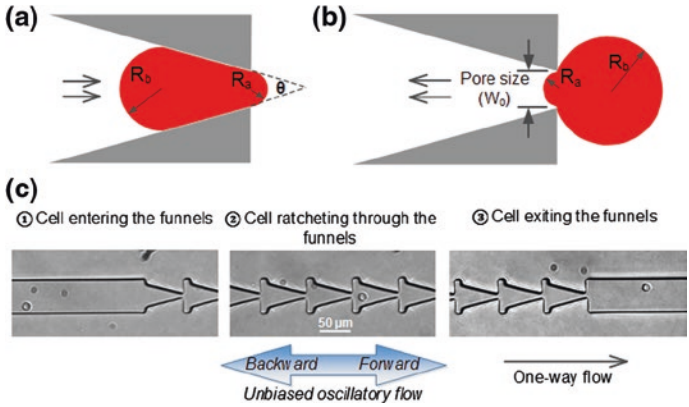

Fig. 8 Microfluidic ratchet with asymmetry shape funnel constriction. **a**, **b** asymmetry deformation of individual cells leading to different transiting pressures required to squeeze cell through either direction; **c** images of the individual cell ratchet through a series of funnels of the same size under a certain oscillatory pressure and frequency

disappeared as the angle was reduced to 0°. These results agreed with the theoretical predictions obtained using Young–Laplace Law (Eq. 1) and form the basis of the microfluidic ratchet to allow ratchet transport of cells using oscillatory flow.

To confirm oscillatory flow through tapered constrictions can indeed transport single cells in a ratcheting manner, a separate microfluidic device, containing 37 funnels constrictions with a 6 μm pore size (W_0) arranged in series at a pitch of 60 μm, was designed to track the movement of single cells through a series of funnel constrictions (Fig. 8c) (Guo et al. 2011). A negative control was performed by placing L1210 mouse lymphoma cell under unbiased oscillatory flow in a microfluidic channel without microstructures (region in Fig. 8c①). Expectedly, these cells showed no net motion confirming the reversibility of low Reynolds number flow. When the same cell was then placed within a series of funnels, the same unbiased oscillatory flow caused the cells to ratchet along the direction of the funnel taper. Specifically, the cell was able to squeeze through the tapered constriction in the forward phase of the oscillation flow, but is prevented from return to its starting point during the backward phase of the oscillation flow. Parameters influencing the ratchet effect, including pore size, oscillation frequency, and magnitude of the oscillation flow were further investigated. Specifically, ratcheting was found to only occur when the pressure exceeds the threshold deformation pressure for the cell to transit along the direction of taper, confirming the transport process is selective based on cell deformability, or more precisely, cell squeezability.

Based on the microfluidic ratchet effect, deformability-based cell sorting can be achieved when deformable cells ratchet through the funnels while rigid cells are blocked by the constrictions and subsequently released under the reverse flow (Fig. 9a, b). To process a large number of cells, a microfluidic device containing a 2-D array of micrometer-scale funnel constrictions was designed as shown in Fig. 9c. Specifically, the pore size remains the same at each row of the funnels, while gradually decreases from bottom to top rows. Microchannels lining the top and bottom array provide an oscillatory flow biased towards upward direction, while the microchannels lining the left of the funnel array provide a constant cross flow. Cells are infused from the bottom-left corner of the sorting region and transported through the array by vertical oscillatory flows and constant horizontal cross-flow. As shown in Fig. 9c, the upward phase of the oscillatory flow works to discriminate the cells based on deformability, the downward phase of the oscillatory works to release the cells to prevent clogging and fouling, and the simultaneous cross-flow works to extract the sorted cells. These three flows combine to propel the cells in a zigzag diagonal path through the constriction array. As cells reach a limiting pore size that prevents their transit, they proceed horizontally between funnel rows towards the outlet reservoirs. Since cells with different deformability will be blocked by different pore sizes, the cell population is sorted based on deformability in this manner.

The microfluidic ratchet cell sorting process presents several advantages over traditional microfiltration (Sect. 3). First, during the ratchet sorting process, within the funnel microstructures, the cells do not experience significant deformation until nearing their blocking funnel row. As a result, the integrity and viability of

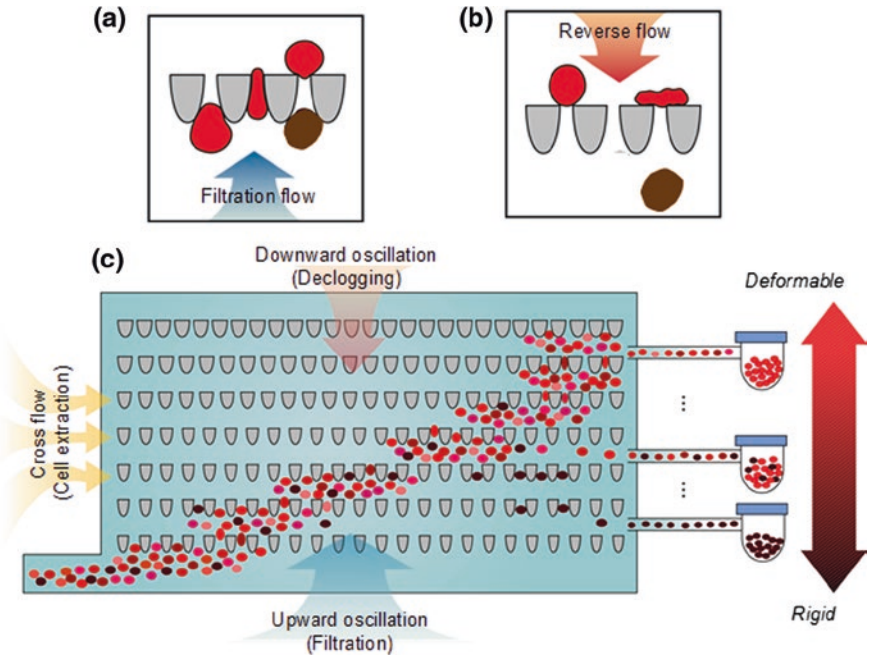

Fig. 9 **a**, **b** Tapered funnel constrictions enable unidirectional flow of cells (ratchet behavior) under oscillation excitation consisting of upward filtration flow and downward reverse flow; **c** conceptual design of the ratchet cell sorting [This figure was reproduced with permission from Guo et al. (2016). Copyright 2016, Lab on a Chip]

the cells are maintained throughout the sorting process. Second, because this oscillatory flow ensures that cells are not trapped within the funnel microstructure, the hydrodynamic resistance of the filter remains constant, which ensures that all incoming cells to experience a constant filtration force. Third, the oscillatory flow ensures that cells come into contact with the filtration microstructures only momentarily (1–2 s at the most), which prevent cell adsorption and enable processing of high-density samples, such as whole blood. Finally, the funnel array design is capable of sorting a cell sample into multiple outlets, which provide significant greater ability to analyze heterogeneous samples compared to binary cell separation schemes.

4.2 Deformability-Based Sorting of RBCs Using Microfluidic Ratchets

As discussed in Sect. 1.1, the function of RBCs centrally depends on its ability to deform and deviation from normal deformability is often associated with pathology. An important example of this type of pathology is in malaria caused by *P.*

falciparum, where development and maturation of the intra-erythrocytic stage of the parasite is directly associated with reduced deformability of infected RBCs. We developed a version of the microfluidic ratchet device to sort RBCs based on deformability in order to enrich for iRBCs to improve diagnostic sensitivity. A secondary objective is to extract iRBCs from different development stages in order to elucidate the molecular processes of development and to discover targets for new drugs.

The microfluidic ratchet device developed to sort RBCs is shown in Fig. 10a (Guo et al. 2016). The central part of the device is a 2-D array of funnel constrictions (Fig. 10b). The funnel array is connected by a left cross-flow inlet (CFI) and sample inlet (SI), to nine outlet collectors (O1–9) on the rightmost edge of the device (Fig. 10a). Oscillation inlet 1 and 2 (Osc1 and Osc2) line the top and bottom of the sorting matrix. These flows combine to propel the cell population to form a characteristic diagonal trajectory through the funnel array, as shown in Fig. 10b. As RBCs reach their blocking pore size (Fig. 10c), they were released under the downward oscillation and subsequently they proceeded horizontally in between the funnel rows to their designated outlets under the cross flow.

In this design, the sorting region used to sort RBCs is composed of 35 rows and 630 columns of funnels. The thickness of the funnel is designed to be ~4.5 μm to provide stress relief in the vertical direction while the RBCs are deformed laterally through the funnel pore. The pore size remains the same in each row while decreases every four rows from the bottom row. In total, the 35 rows of constrictions consist of 9 different sizes (1.5, 1.75, 2, 2.25, 2.5, 3, 3.5, 6, and 7.5 μm) and therefore, sort the input sample based on deformability into 9 fractions in outlets O1–O9. The most deformable RBCs are collected in O1 while least deformable ones are collected in O9.

Deformability-based sorting of RBCs was validated by sorting RBCs treated with glutaraldehyde (GTA), which chemically degrades RBC deformability in a dose-dependent manner. RBC samples from healthy donors were treated with 0, 0.01, 0.015, 0.025 and 0.05 % GTA. Compared to untreated RBCs, GTA-treated RBCs take on a distinct trajectory through the matrix of funnel constrictions that direct them into different outlets in a concentration dependent manner (Fig. 10d). To investigate the potential for sorting iRBCs containing *P. falciparum* parasites, malaria iRBCs at ring, early trophozoite, late trophozoite and schizont stages were obtained through synchronized culture and sorted through the microfluidic ratchet. The *Pf*-iRBCs were collected into different outlets that reflected the rigidification of these cells during parasite maturation.

Furthermore, we investigated the ability to improve malaria diagnostic sensitivity through a step of enrichment using the microfluidic ratchet. Specifically, clinically relevant samples, which contains only ring stage iRBCs at concentration <0.01 %, were prepared and sorted through the device. The majority of the RBCs were collected in O1–3 while the iRBCs were enriched in O4–9. Giemsa microscopy is recognized as the gold standard for malaria diagnosis and it was found that *Pf*-iRBC enrichment could enable Giemsa parasite detection well below the current detection limit (Fig. 10e).

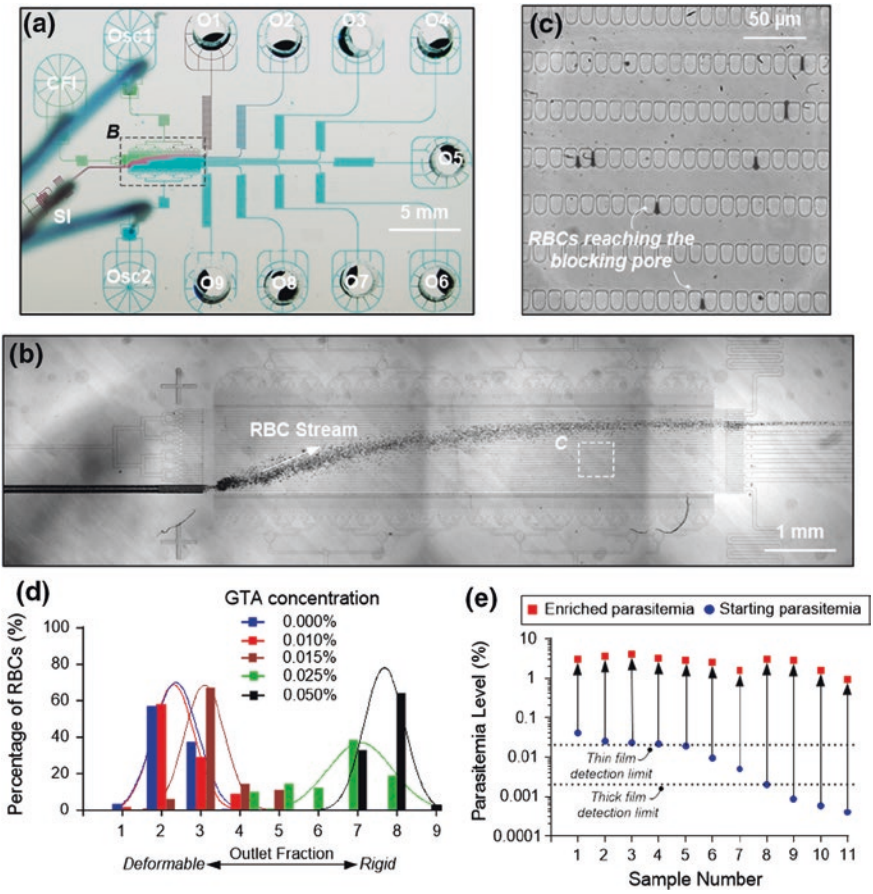

Fig. 10 Images of the ratchet cell sorting device. **a** Image of the overall design of a typical ratchet sorting device; **b** RBCs follow a diagonal trajectory in response to the sample inlet (SI) flow, cross-flow inlet (CFI) flow and biased oscillation flows (Osc1 and Osc2); RBCs introduced through the SI transit the funnel matrix until reaching the blocking pore sizes (**c**). **d** Distributions of RBCs population treated with varying concentrations of GTA show a monotonic rightwards shift, consistent with the loss of RBCs deformability; **e** enrichment of ring stage iRBCs from ultra-low parasitemia (<0.01 %) improves the sensitivity limit of gold standard Giemsa microscopy [This figure is reproduced with permission from Guo et al. (2016). Copyright 2016, Lab on a Chip]

4.3 Deformability-Based Separation of CTCs Using Microfluidic Ratchets

Separating circulating tumor cells (CTCs) from patient blood sample offers tremendous potential for the detection and characterization of cancer. The key challenge in separation and analysis of CTCs from patient blood is their extreme

rarity, where there are only a few CTCs in each ml of whole blood. Significant interest in label-free CTCs enrichment strategies based on morphological differences between CTCs and hematological cells has arisen since the immunoaffinity method has been under questions for its reliability. While tumor cells are generally larger, CTCs may sometimes significantly overlap in size with leukocytes. This situation is particularly relevant in cases of prostate and colorectal cancer where CTCs from patients are known to be smaller and have significant overlap in size with leukocytes (Coumans et al. 2013; Ligthart et al. 2013; Park et al. 2014). In this circumstance, combined size and deformability sorting, by microfluidic ratchet, is particularly advantageous. The ability for the microfluidic ratchet to sort blood perpetually, without clogging, as well as the capacity to isolate viable CTCs are also important advantages to the characterization of these cells.

The CTC sorting device (Jin et al. 2016) is similar, in principle and design, to the malaria sorting device, with some notable exceptions. Like the malaria sorting device, the CTC sorting device consisted of sample (SI) and cross-flow (CFI) input channels, a sorting region, oscillatory channels lining the top and bottom (Osc1 and Osc2) and outlet channels (Fig. 11a). However, the sorting region consisted of 32 rows and 2047 columns and the funnel pore sized ranged from 18 to 2 μm, with a constant thickness of 30 μm. This geometry was designed to clearly separate CTC and contaminating leukocyte populations, and these two cell populations were collected into two distinct outlets. Another difference between the sorting devices was that the CTC sorting device permitted RBCs to transit vertically through the sorting region and drain into Osc1 (Fig. 11b). This ensured that these cells did not accumulate within and foul the sorting region.

The CTC sorting device was initially validated using whole blood spiked with cultured cancer cells (UM-UC13 bladder cells). Experimental result indicated that leukocytes and the bladder cancer cells were clearly separated by the 6 μm pore. Accordingly, the device was designed to have only two outlets: leukocyte outlet and tumor cells outlet, divided by the cut-off 6 μm pore funnel row. The spiking experiment indicated that the microfluidic ratchet cell sorting process can enrich tumor cells by 10^4-fold with a capture efficiency of >90 % and viability of 99.1 %. The capacity to sort CTC from whole blood of patients with metastatic castrate-resistant prostate cancer (mCRPC) was subsequently evaluated. Label-free biophysical enrichment of CTCs from mCRPC patients represents a particular challenge because there is a significant overlap between the diameters of CTCs and leukocytes in these patient samples. This underscores the importance of deformability-based sorting of these CTCs. Following analysis of 20 mCRPC patient blood samples and 4 healthy control donor samples, we established that the microfluidic ratchet enabled detection of significantly more CTCs than the conventional CellSearch system (Fig. 11c, d).

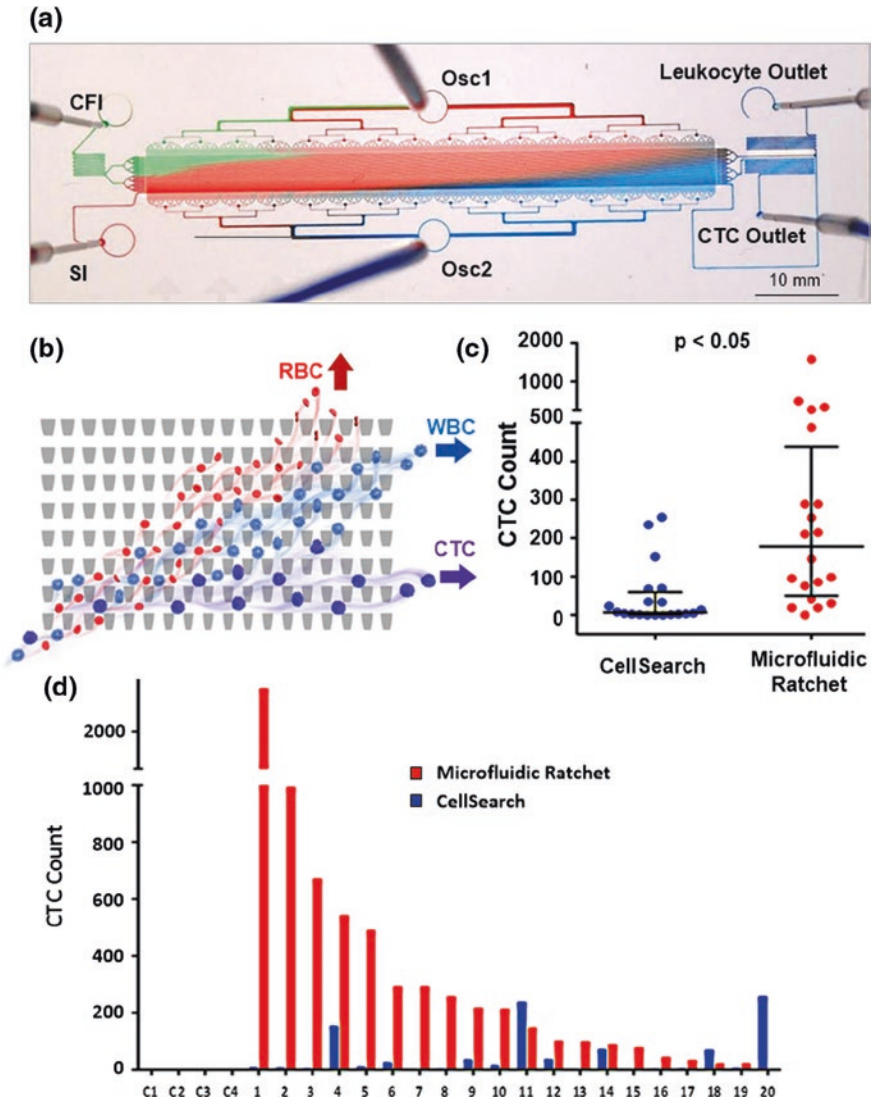

Fig. 11 **a** Image of the overall design of CTCs separation; **b** schematic illustration of the sorting process which drains RBCs into the upward oscillation channels, and separates CTCs from contaminant leukocytes through the ratchet sorting region. **C** and **D** Comparison of CTCs enumeration using both microfluidic ratchet and CellSearch for patients with mCRPC; the *p* value indicates a significant difference by Wilcoxon-ranked sum [This figure is reproduced with permission from Jin et al. (2016). Copyright 2016, Small]

5 Summary

This chapter first described the potential for cell deformability to serve as a physical biomarker for circulatory cells where the ability to deform is essential. Specific instances relating to red blood cells, leukocytes, and circulating tumor cells are explored. Subsequently, we reviewed existing approaches for deformability-based cell sorting including hydrodynamic chromatography and microfiltration. Hydrodynamic chromatography relies on interactions between particles and obstacles in flow to route cells into different paths based on differences in size and deformability. This approach includes the techniques of deterministic lateral displacement and cell margination. Microfiltration separate cells by flowing the cell sample through an array of microscale constrictions. Despite significant development, however, this approach lacks selectivity because of clogging and fouling. The final part of this chapter describes a recent advance to potentially address the challenges in microfiltration by sorting cells based on deformability using the microfluidic ratchet mechanism. This mechanism leverages the asymmetrical pressure required to squeeze single cells through tapered constriction to selectively transport single cells based on deformability using oscillatory flow. This approach has been applied to separate RBCs infected with *P. falciparum* in order to isolate infected cells to improve the sensitivity of malaria diagnosis. The microfluidic ratchet mechanism has also been applied to the separation of viable CTCs directly from whole blood and demonstrated significant improvements in yield compared to conventional methods.

References

Alaarg A, Schiffelers RM, van Solinge WW, van Wijk R (2013) Red blood cell vesiculation in hereditary hemolytic anemia. Front Physiol 4:1–15. doi:10.3389/fphys.2013.00365

Allard WJ, Matera J, Miller MC et al (2004) Tumor cells circulate in the peripheral blood of all major carcinomas but not in healthy subjects or patients with nonmalignant diseases. Clin Cancer Res 10:6897–6904. doi:10.1158/1078-0432.CCR-04-0378

Alvankarian J, Bahadorimehr A, Yeop Majlis B (2013) A pillar-based microfilter for isolation of white blood cells on elastomeric substrate. Biomicrofluidics 7:14102. doi:10.1063/1.4774068

Anderson AO, Anderson ND (1976) Lymphocyte emigration from high endothelial venules in rat lymph nodes. Immunology 31:731–748

Beech JP, Holm SH, Adolfsson K, Tegenfeldt JO (2012) Sorting cells by size, shape and deformability. Lab Chip 12:1048. doi:10.1039/c2lc21083e

Bosch FH, Werre JM, Schipper L et al (1994) Determinants of red blood cell deformability in relation to cell age. Eur J Haematol 52:35–41. doi:10.1111/j.1600-0609.1994.tb01282.x

Brown MJ, Hallam JA, Colucci-Guyon E, Shaw S (2001) Rigidity of circulating lymphocytes is primarily conferred by vimentin intermediate filaments. J Immunol 166:6640–6646. doi:10.4049/jimmunol.166.11.6640

Callens N, Minetti C, Mader M-A et al (2008) Hydrodynamic lift of vesicles under shear flow in microgravity. Europhys Lett 83:6. doi:10.1209/0295-5075/83/24002

Chen LT, Weiss L (1973) The role of the sinus wall in the passage of erythrocytes through the spleen. Blood 41:529–537

Chen X, Cui D, Liu C, Li H (2008) Microfluidic chip for blood cell separation and collection based on crossflow filtration. Sens Actuators B Chem 130:216–221. doi:10.1016/j.snb.2007.07.126
Chen J, Chen D, Yuan T et al (2013) A microfluidic chip for direct and rapid trapping of white blood cells from whole blood. Biomicrofluidics 7:34106. doi:10.1063/1.4808179
Choi S, Song S, Choi C, Park J-K (2007) Continuous blood cell separation by hydrophoretic filtration. Lab Chip 7:1532–1538. doi:10.1039/b705203k
Clark MR, Mohandas N, Shohet SB (1980) Deformability of oxygenated irreversibly sickled cells. J Clin Invest 65:189–196. doi:10.1172/JCI109650
Comen E, Norton L, Massagué J (2011) Clinical implications of cancer self-seeding. Nat Rev Clin Oncol 8:369–377. doi:10.1038/nrclinonc.2011.64
Coumans FAW, van Dalum G, Beck M, Terstappen LWMM (2013) Filtration parameters influencing circulating tumor cell enrichment from whole blood. PLoS ONE. doi:10.1371/journal.pone.0061774
Cranston HA, Boylan CW, Carroll GL et al (1984) *Plasmodium falciparum* maturation abolishes physiologic red cell deformability. Science 223(80):400–403. doi:10.1126/science.6362007
Crosby W (1959) Normal functions of the spleen relative to red blood cells—a review. Blood 14:399–408
Davis JA, Inglis DW, Morton KJ et al (2006) Deterministic hydrodynamics: taking blood apart. Proc Natl Acad Sci USA 103:14779–14784. doi:10.1073/pnas.0605967103
Desitter I, Guerrouahen BS, Benali-Furet N et al (2011) A new device for rapid isolation by size and characterization of rare circulating tumor cells. Anticancer Res 31:427–441
Diez-Silva M, Park Y, Huang S et al (2012) Pf155/RESA protein influences the dynamic microcirculatory behavior of ring-stage *Plasmodium falciparum* infected red blood cells. Sci Rep 2:614. doi:10.1038/srep00614
Evans EA, La Celle PL (1975) Intrinsic material properties of the erythrocyte membrane indicated by mechanical analysis of deformation. Blood 45:29–43
Fåhræus R, Lindqvist T (1931) The viscosity of the blood in narrow capillary tubes. Am J Physiol Hear Circ Physiol 96:562–568
Geislinger T, Eggart B (2012) Separation of blood cells using hydrodynamic lift. Appl Phys Lett 100:183701. doi:10.1063/1.4709614
Geislinger TM, Chan S, Moll K et al (2014) Label-free microfluidic enrichment of ring-stage *Plasmodium falciparum*-infected red blood cells using non-inertial hydrodynamic lift. Malar J 13:375. doi:10.1186/1475-2875-13-375
Goldsmith H, Mason S (1962) The flow of suspensions through tubes. I. Single spheres, rods, and discs. J Colloid Sci 17:448–476. doi:10.1016/0095-8522(62)90056-9
Guo Q, McFaul S, Ma H (2011) Deterministic microfluidic ratchet based on the deformation of individual cells. Phys Rev E 83:051910. doi:10.1103/PhysRevE.83.051910
Guo Q, Reiling SJ, Rohrbach P, Ma H (2012a) Microfluidic biomechanical assay for red blood cells parasitized by *Plasmodium falciparum*. Lab Chip 12:1143–1150. doi:10.1039/c2lc20857a
Guo Q, Park S, Ma H (2012b) Microfluidic micropipette aspiration for measuring the deformability of single cells. Lab Chip 12:2687–2695. doi:10.1039/c2lc40205j
Guo Q, Duffy SP, Matthews K et al (2014) Microfluidic analysis of red blood cell deformability. J Biomech 47:1767–1776. doi:10.1016/j.jbiomech.2014.03.038
Guo Q, Duffy SP, Matthews K et al (2016) Deformability based sorting of red blood cells improves diagnostic sensitivity for malaria caused by *Plasmodium falciparum*. Lab Chip. doi:10.1039/C5LC01248A
Haines WB (2009) Studies in the physical properties of soil. V. The hysteresis effect in capillary properties, and the modes of moisture distribution associated therewith. J Agric Sci 20:97. doi:10.1017/S002185960008864X
Hochmuth RM (2000) Micropipette aspiration of living cells. J Biomech 33:15–22
Holmes D, Whyte G, Bailey J et al (2014) Separation of blood cells with differing deformability using deterministic lateral displacement. Interface Focus 4:20140011. doi:10.1098/rsfs.2014.0011

Hosokawa M, Hayata T, Fukuda Y et al (2010) Size-selective microcavity array for rapid and efficient detection of circulating tumor cells. Anal Chem 82:6629–6635. doi:10.1021/ac101222x

Hosokawa M, Asami M, Nakamura S et al (2012) Leukocyte counting from a small amount of whole blood using a size-controlled microcavity array. Biotechnol Bioeng 109:2017–2024. doi:10.1002/bit.24471

Hosseini SM, Feng JJ (2012) How malaria parasites reduce the deformability of infected red blood cells. Biophys J 103:1–10. doi:10.1016/j.bpj.2012.05.026

Hou HW, Bhagat AAS, Chong AGL et al (2010) Deformability based cell margination–a simple microfluidic design for malaria-infected erythrocyte separation. Lab Chip 10:2605–2613. doi:10.1039/c003873c

Huang LR, Cox EC, Austin RH, Sturm JC (2004) Continuous particle separation through deterministic lateral displacement. Science 304:987–990. doi:10.1126/science.1094567

Inglis DW (2009) Efficient microfluidic particle separation arrays. Appl Phys Lett 94:2007–2010. doi:10.1063/1.3068750

Ji HM, Samper V, Chen Y et al (2008) Silicon-based microfilters for whole blood cell separation. Biomed Microdevices 10:251–257. doi:10.1007/s10544-007-9131-x

Jin C, McFaul SM, Duffy SP et al (2014) Technologies for label-free separation of circulating tumor cells: from historical foundations to recent developments. Lab Chip 14:32–44. doi:10.1039/C3LC50625H

Jin C, Park ES, Guo Q et al (2016) Continuous flow deformability-based separation of circulating tumor cells using microfluidic ratchets. Small 12:1909–1919

Krueger T, Holmes D, Coveney P (2014) Deformability-based red blood cell separation in deterministic lateral displacement devices—a simulation study. Biomicrofluidics 8:1–10. doi:10.1039/b000000x

Kwan JM, Guo Q, Kyluik-Price DL et al (2013) Microfluidic analysis of cellular deformability of normal and oxidatively damaged red blood cells. Am J Hematol 88:682–689. doi:10.1002/ajh.23476

Li X, Chen W, Liu G et al (2014) Continuous-flow microfluidic blood cell sorting for unprocessed whole blood using surface-micromachined microfiltration membranes. Lab Chip 14:2565–2575. doi:10.1039/c4lc00350k

Ligthart ST, Coumans FAW, Bidard FC et al (2013) Circulating tumor cells count and morphological features in breast, colorectal and prostate cancer. PLoS ONE 8:e67148. doi:10.1371/journal.pone.0067148

Lin HK, Zheng S, Williams AJ et al (2010) Portable filter-based microdevice for detection and characterization of circulating tumor cells. Clin Cancer Res 16:5011–5018

Lu B, Xu T, Zheng S et al (2010) Parylene membrane slot filter for the capture, analysis and culture of viable circulating tumor cells. In: IEEE international conference on micro electro mechanical systems, pp 935–938. doi:10.1109/MEMSYS.2010.5442361

Miller MC, Doyle GV, Terstappen LWMM (2010) Significance of circulating tumor cells detected by the cell search system in patients with metastatic breast colorectal and prostate cancer. J Oncol 2010:617421. doi:10.1155/2010/617421

Mills JP, Diez-Silva M, Quinn DJ et al (2007) Effect of plasmodial RESA protein on deformability of human red blood cells harboring *Plasmodium falciparum*. Proc Natl Acad Sci USA 104:9213–9217. doi:10.1073/pnas.0703433104

Miyasaka M, Tanaka T (2004) Lymphocyte trafficking across high endothelial venules: dogmas and enigmas. Nat Rev Immunol 4:360–370. doi:10.1038/nri1354

Mohanty JG, Nagababu E, Rifkind JM (2014) Red blood cell oxidative stress impairs oxygen delivery and induces red blood cell aging. Front Physiol 5:1–6. doi:10.3389/fphys.2014.00084

Moxon CA, Grau GE, Craig AG (2011) Malaria: modification of the red blood cell and consequences in the human host. Br J Haematol. doi:10.1111/j.1365-2141.2011.08755.x

Myrand-Lapierre M-E, Deng X, Ang RR et al (2014) Multiplexed fluidic plunger mechanism for the measurement of red blood cell deformability. Lab Chip. doi:10.1039/c4lc01100g

Nash GB, Johnson CS, Meiselman HJ (1984) Mechanical properties of oxygenated red blood cells in sickle cell (HbSS) disease. Blood 63:73–82

Nash GB, O'Brien E, Gordon-Smith EC, Dormandy JA (1989) Abnormalities in the mechanical properties of red blood cells caused by *Plasmodium falciparum*. Blood 74:855–861

Olla P (1997) The lift on a tank-treading ellipsoidal cell in a bounded shear flow. J Phys II 7:1533–1540. doi:10.1051/jp2:1997201

Omodeo-Salè F, Motti A, Dondorp A et al (2005) Destabilisation and subsequent lysis of human erythrocytes induced by *Plasmodium falciparum* haem products. Eur J Haematol 74:324–332. doi:10.1111/j.1600-0609.2004.00352.x

Park S, Ang RR, Duffy SP et al (2014) Morphological differences between circulating tumor cells from prostate cancer patients and cultured prostate cancer cells. PLoS ONE. doi:10.1371/journal.pone.0085264

Paulitschke M, Nash GB (1993) Membrane rigidity of red blood cells parasitized by different strains of *Plasmodium falciparum*. J Lab Clin Med 122:581–589

Perrotta S, Gallagher PG, Mohandas N (2008) Hereditary spherocytosis. Lancet 372:1411–1426. doi:10.1016/S0140-6736(08)61588-3

Punnoose EA, Atwal SK, Spoerke JM et al (2010) Molecular biomarker analyses using circulating tumor cells. PLoS ONE 5:1–12. doi:10.1371/journal.pone.0012517

Santoso AT, Deng X, Lee J-H et al (2015) Microfluidic cell-phoresis enabling high-throughput analysis of red blood cell deformability and biophysical screening of antimalarial drugs. Lab Chip. doi:10.1039/C5LC00945F

Schmid-Schönbein GW, Shih YY, Chien S (1980) Morphometry of human leukocytes. *Blood,* 56(5):866–875, Nov. 1980

Schrier SL (1994) Thalassemia: pathophysiology of red cell changes. Annu Rev Med 45:211–218. doi:10.1146/annurev.med.45.1.211

Seal SH (1964) A sieve for the isolation of cancer cells and other large cells from the blood. Cancer 17:637–642. doi:10.1002/1097-0142(196405)17:5<637:AID-CNCR2820170512>3.0.CO;2-I

Sethu P, Sin A, Toner M (2006) Microfluidic diffusive filter for apheresis (leukapheresis). Lab Chip 6:83–89. doi:10.1039/b512049g

Shevkoplyas SS, Yoshida T, Munn LL, Bitensky MW (2005) Biomimetic autoseparation of leukocytes from whole blood in a microfluidic device. Anal Chem 77:933–937. doi:10.1021/ac049037i

Sutera SP, Gardner RA, Boylan CW et al (1985) Age-related changes in deformability of human erythrocytes. Blood 65:275–282

Tan SJ, Yobas L, Lee GYH et al (2009) Microdevice for the isolation and enumeration of cancer cells from blood. Biomed Microdevices 11:883–892. doi:10.1007/s10544-009-9305-9

VanDelinder V, Groisman A (2007) Perfusion in microfluidic cross-flow: separation of white blood cells from whole blood and exchange of medium in a continuous flow. Anal Chem 79:2023–2030. doi:10.1021/ac061659b

Vona G, Sabile A, Louha M et al (2000) Isolation by size of epithelial tumor cells. Am J Pathol 156:57–63. doi:10.1016/S0002-9440(10)64706-2

Worthen GS, Schwab B, Elson EL, Downey GP (1989) Mechanics of stimulated neutrophils: cell stiffening induces retention in capillaries. Science 245:183–186. doi:10.1126/science.2749255

Yap B, Kamm RD (2005) Mechanical deformation of neutrophils into narrow channels induces pseudopod projection and changes in biomechanical properties. J Appl Physiol 98:1930–1939. doi:10.1152/japplphysiol.01226.2004

Zheng S, Lin H, Liu J-Q et al (2007) Membrane microfilter device for selective capture, electrolysis and genomic analysis of human circulating tumor cells. J Chromatogr A 1162:154–161. doi:10.1016/j.chroma.2007.05.064

Zheng S, Lin HK, Lu B et al (2011) 3D microfilter device for viable circulating tumor cell (CTC) enrichment from blood. Biomed Microdevices 13:203–213

Zhou R, Gordon J, Palmer AF, Chang H-C (2006) Role of erythrocyte deformability during capillary wetting. Biotechnol Bioeng 93:201–211. doi:10.1002/bit.20672

Microfluidic Aqueous Two-Phase Systems

Glenn M. Walker

Abstract Aqueous Two-Phase Systems (ATPS) are an established technology that have been used to separate out biologically important particles such as biomolecules, organelles, and whole cells. ATPS are formed by mixing polymers such as polyethylene glycol (PEG) and dextran (Dex) at sufficiently high concentrations such that two immiscible phases are formed. Traditional macroscale ATPS are performed in test tubes and require relatively large reagent volumes and are limited to a vertical configuration where the interface lies perpendicular to the direction of gravity. Settling becomes problematic for larger particles and the long diffusion distances mean that separations require significant time. Recent advances in microfluidics systems allow novel configurations of ATPS that are impossible with traditional techniques. Examples are nanoliter ATPS droplets or parallel streams of ATPS which enable new applications and improvements over traditional separations. Microscale ATPS can separate particles in seconds instead of hours using only microliters of reagent.

Keywords Amino acids · Aqueous two-phase systems (ATPS) · Bacteriorhodopsin (BR) · Bovine serum albumin (BSA) · Carbonic anhydrase · Chinese hamster ovary (CHO) · Dextran · DNA · Droplets · Glutathione S-transferase · Green fluorescent protein acgfp1 · Human erythrocytes (RBC) · Human leukocytes (WBC) · Human T lymphoma (Jurkat) · Immunoglobulin G (IgG) · Microfluidic · Mycotoxin ochratoxin A (OTA) · Ovalbumin · Partition coefficient · Partitioning · Plant aggregates (strawberry) · Polyethylene glycol · Separation · α-Amylase · β-Galactosidase

G.M. Walker (✉)
Department of Biomedical Engineering, North Carolina State University,
911 Oval Drive, Box 7115, Raleigh, NC 27695-7115, USA
e-mail: gmwalker@ncsu.edu

W. Lee et al. (eds.), *Microtechnology for Cell Manipulation and Sorting*,
Microsystems and Nanosystems, DOI 10.1007/978-3-319-44139-9_9

1 Introduction

This chapter explores aqueous two-phase systems (ATPS)—mixtures of polymers in solution that separate into two phases—and their application to microfluidic systems. A two-phase system results from mixing two immiscible liquids and allowing the mixture to settle. The differences in density between the phases results in a denser phase on the bottom and the less dense phase on the top. A common example of a two-phase system is oil and water. If a mixture of oil and water is shaken, tiny droplets of oil will become dispersed throughout the water. Over time, the droplets will coalesce to form a top layer, while the heavier water sinks to the bottom. The phase separation that occurs in this type of system, called a water–organic system, results from the hydrophobic and hydrophilic properties of the liquids in the system.

An ATPS differs from a water–organic system (e.g., water and oil) because it comprises two immiscible solutions of polymers dissolved in water. In contrast to the oil and water system, both phases of the ATPS consist of water, typically between 85 and 99 % by weight (Albertsson 1986). The high water content makes an ATPS ideal for analyzing biomolecules because it will not denature proteins, unlike solvents used in water–organic systems. Furthermore, the interfacial tension between phases is much lower in an ATPS, with typical values of 0.0001–0.1 dyne/cm, compared to solvent-based systems which typically have interfacial tensions 10–100 times larger (Albertsson 1986). The most common ATPS uses the polymers polyethylene glycol (PEG) and dextran (Dex), although many other combinations of polymers can be used as well. In addition to polymer–polymer ATPS, a polymer and salt solution can also be used to create an ATPS useful for biological separations. One example is a mixture of PEG and a polyelectrolyte such as sodium dextran sulfate. Examples of biologically incompatible ATPS are numerous in the literature and have been explored in detail elsewhere. In this chapter, we focus only on ATPS systems that are compatible with biological cells and molecules.

The term ATPS implies solutions containing two polymers or one polymer and one salt. However, another class of biologically compatible two-phase systems has been demonstrated. These two-phase systems are created with micelles and are called aqueous two-phase micellar systems (ATPMS). ATPMS are formed by generating a homogenous mixture of micelles and then adjusting solution conditions to create two phases, each containing a different concentration and average size of micelles (Liu et al. 1996). The difference in concentration of micelles endows the ATPMS with the ability to preferentially partition molecules, similar to ATPS.

While ATPS contain only two phases, the general concept of mixing incompatible polymer solutions can be used to create systems with three, four, or more phases (i.e., polyphase systems). Eighteen phase systems have even been demonstrated (Albertsson 1986). A key advantage to polyphase systems is that they are capable of rapidly partitioning a solution into multiple fractions. Multiple phases

can be screened at once to determine which has the best affinity for a specific biomolecule. Alternatively, many biomolecules in a sample can be separated into specific fractions in a single step using a polyphase system.

ATPS have been adopted by industry as a key separation technology (Walter et al. 1985). ATPS are used to separate and purify target molecules, organelles, and even cells (Benavides et al. 2011). ATPS are especially useful for separating biological samples because the final polymer mixtures are typically at least 90 % water by weight. The interfacial tension between phases is low, which minimizes damage to cells and denaturation of molecules. The polymers that constitute the two phases are nontoxic. In contrast, ATPS made from organic solvents cannot be used to partition biological samples. Many biological samples denature upon contact with solvents and lose their structure and functionality. In a traditional ATPS workflow, a sample is diluted into one of the phases and then allowed to equilibrate within the ATPS. Alternatively, the ATPS may be mixed which forms droplets of one phase suspended in the other. The droplets greatly increase the surface area of the phase boundary exposed to the sample. Greater surface area and shorter diffusion distance between phases accelerates the distribution of sample among phases. The molecule(s) of interest will then partition into the different phases depending on their affinity for each phase.

1.1 History

The first documented instance of aqueous two-phase systems was by Beijerinck in 1896 (Beijerinck 1896). He reported that mixtures of agar and starch or agar and gelatin would separate into two phases. Approximately 50 years later, other groups began studying the behavior of two-phase systems (Dobry and Boyer-Kawenoki 1947; Bungenberg de Jong 1949). Albertsson was the first to begin popularizing ATPS in 1958 (Albertsson 1958) and then published a book on the topic that remains a standard text today (Albertsson 1986). The work by Albertsson was the first to systematically explore the use of ATPS for separating particles that could not withstand the harsh chemicals present in solvent-based systems.

1.2 ATPS Formation

The result of mixing immiscible polymers in solution depends on the interaction between the polymer molecules (i.e., attraction or repulsion) and on the concentration of the polymers. Mixing two polymers results in an increase in entropy, however, the high molecular weight of polymers typically used in ATPS increases the number of interactions between molecules; intermolecular forces become more significant. As a result, intermolecular forces dictate the final phase composition of the system. When two polymer solutions, or a polymer solution and

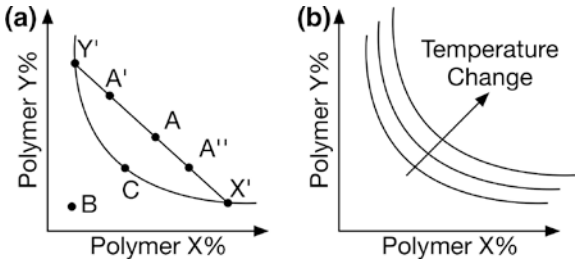

Fig. 1 **a** Example ATPS phase diagram showing the binodal curve and tie lines. Polymer X is denser than Polymer Y. Polymer concentrations shown for A result in two phase systems. Polymer concentrations for B result in one phase systems. A′ and A″ lay on the same tie line as A and will yield an equilibrated ATPS with the same polymer concentrations in the bottom and top phases. Point C the critical point. **b** Temperature changes slightly shift the binodal curve such that higher polymer concentrations are needed to create stable ATPS

polyelectrolyte, are mixed together there are three possible outcomes (Albertsson 1986):

1. **Incompatibility:** The polymers separate into two separate phases.
2. **Complex coacervation:** The polymers separate within one phase and the other phase consists mainly of solvent.
3. **Complete miscibility:** The polymers do not separate.

A phase diagram is used to identify the outcome of mixing two polymer solutions, or a polymer and polyelectrolyte solution. In the phase diagram, the concentration of the more dense polymer is plotted on the horizontal axis and the concentration of the less dense polymer is plotted on the vertical axis, as shown in Fig. 1. The binodal curve shows the phase boundary of the system. In Fig. 1a, mixing polymer X and Y at concentrations that yield point A will result in a two-phase system. Using a quarter of polymer X and Y concentrations will create a system at point B, which only yields a one-phase system.

All two-phase systems will ultimately equilibrate to points on the binodal curve. If polymers X and Y are mixed to form an initial concentration at A, after equilibration the bottom phase will contain a high concentration of polymer X and a low concentration of polymer Y (point X′). Conversely, the top phase will contain a high concentration of polymer Y and a low concentration of polymer X (point Y′). A tie line can be drawn between points Y′, A, and X′, as shown in Fig. 1a. Tie lines show what the final concentrations of the ATPS will be after equilibration. Any initial concentration of polymers that lie on a specific tie line will always result in a final concentration given by the two end points that lie on the binodal curve. For example, systems in which polymer X and Y concentrations are initially at A′ will equilibrate to X′ and Y′. Similarly for systems initially at A″, the final equilibrium concentrations will for the bottom and top phases will be X′ and Y′, respectively. For each of these systems, A, A′, and A″, the final volumes of the bottom and top phases will be slightly different, due to the conservation of

mass. There is a point, called the critical point, at which the initial polymer concentrations are the same as the equilibrated concentrations (Fig. 1a). ATPS should not be created near the critical point because environmental factors that affect the position of the binodal curve can cause the system to shift from a two-phase system to a one-phase system. The position of the binodal curve can be affected by temperature, as shown in Fig. 1b, however its effect is often small.

1.3 ATPS Partitioning

A small particle, such as a biomolecule, inserted into an ATPS will seek one of three locations to minimize its interfacial free energy: the top phase, the bottom phase, or at the interface between phases. For a sufficiently small particle, gravity can be neglected and random thermal motion (i.e., Brownian motion) drives the particle to its equilibrium location. However, for a larger particle, such as a microbead or a biological cell, gravity will also play a role in determining the final location. In this second case, a particle denser than the top phase will settle to the interface. If the downward force on the particle generated by gravity exceeds the upward force created by the interfacial tension between the phases, then the particle will continue settling through the bottom phase if its density is greater than the bottom phase. If the upward force at the interface is greater than gravitational force, then the particle will remain trapped at the interface. Microfluidic systems provide one way to overcome settling because they can be used to create ATPS with a vertical interface, so cells will settle within a single phase instead of through the interface. Both large and small particles can be attracted or repulsed by electrochemical potentials within the phases of the ATPS and at the double layer that forms at the interface between phases.

The partition coefficient is used to quantify the relative concentrations of a particle within both phases of an ATPS. The equation used to calculate the partition coefficient, K, is

$$K = \frac{C_t}{C_b}, \tag{1}$$

where C_t and C_b are the equilibrium particle concentrations in the top and bottom phases, respectively. In the microfluidic ATPS literature, phases are rarely separated into top and bottom configurations because gravity does not play a significant role. The phases lay parallel to one another or are arranged in concentric spheres (i.e., droplets). Therefore, partition coefficients are more often defined as the ratio of particle concentration in PEG to Dex, or in terms of live cells versus dead cells. Careful attention should be paid to the partition coefficient definition being used, as the variety of partition coefficients found in the literature can make it difficult to compare performance among different ATPS systems.

Ignoring gravity, the surface properties of the particle play the most significant role in determining the partition coefficient. The mechanisms behind partitioning

are complex and interrelated and are beyond the scope of this chapter. Broadly speaking, there are six factors that can influence the partition coefficient: (1) size, (2) electrochemical potential, (3) hydrophobic affinity, (4) biospecific affinity, (5) molecular conformation, and (6) chiral affinity. The most commonly explored to date in the literature are size, potential, and hydrophobic affinity. The reader is referred to Albertsson for a more detailed discussion of each of these mechanisms (Albertsson 1986).

2 Microfluidic Approaches for Creating ATPS

Several strategies for ATPS separation have been developed for laboratory use: single-step partition, repeated batch extractions, countercurrent distribution, liquid–liquid columns, and partition chromatography (Albertsson 1986). The single-step partition is the most common approach for creating lab-scale ATPS and is most often implemented in a test tube containing the two phases and the sample that is to be separated.

In contrast to standard macroscale approaches, microfluidic systems have intrinsic advantages that can enhance the performance of ATPS (Hardt and Hahn 2012). Microfluidic systems can easily manage microliters to picoliters of fluid volumes, in contrast with the milliliters required in macroscale setups. Therefore, sample volumes and reagent costs are minimized. Microfluidic systems also leverage the physics of the microscale to make ATPS separations more efficient. Short diffusion distances translate into faster separation times and no mixing is necessary. In macroscale systems, an ATPS separation may take hours and stirring is sometimes required. At the microscale, separations can occur in seconds. Novel phase boundaries can be formed using the laminar flow characteristic of the microscale. In macroscale systems, the separated phases of ATPS are stacked vertically, like playing cards in a deck. In a microfluidic device ATPS can be formed using droplets or with horizontal phase boundaries using parallel streams of each phase. Lastly, microfluidic systems contain surface area-to-volume ratios 100–1000 times larger than those found in macroscale systems. The increased surface area of the phase boundary accelerates the separation of samples compared to macroscale systems.

2.1 Continuous Flow

The phases within a macroscale ATPS remain static and diffusion is the driving force for sample separation between them. Macroscale laminar flow is difficult to achieve and the low interfacial tension between ATPS phases makes disruption of the interface inevitable. As a result, macroscale ATPS that use flow are uncommon. In contrast, it is easy to generate laminar flow within microfluidic devices

and with careful balancing one can maintain a stable interface between the phases of an ATPS. The ability to flow streams parallel to one another allows more precise analysis of the separation of particles and enables the study of the factors affecting ATPS separation efficiency.

2.1.1 Single Interface Systems

Yamada et al. were the first to demonstrate a microfluidic ATPS (Yamada et al. 2004). Their microfluidic system used laminar flow in a microfluidic device to generate a stable vertical interface between a PEG phase and a Dex phase as shown in Fig. 2a. Their device design consisted of two inlets and two outlets and they used the device study the migration of plant cells from strawberry tissue in the PEG phase to the Dex phase. They studied the effects of a pinched separation region (i.e., a temporary reduction in microchannel width) to improve extraction efficiency. The authors also explored how salt concentration within the phases could be changed to reverse the trend.

A second example of a single interface microfluidic ATPS was demonstrated by Nam and coworkers (Nam et al. 2005). They used a three inlet/three outlet device in which the outer two streams were PEG and Dex and the middle stream contained a mixture of sample, buffer, and Chinese Hamster Ovary (CHO) cells, as shown in Fig. 2b. They investigated the effect of pH and flow rate on interface stability. A key disadvantage to their approach is that excessive buffer stream flow rates dilute the PEG and Dex streams to concentrations below the binodal curve, resulting in a single phase system within the microchannel. In other words, their setup was particularly susceptible to oscillating between one and two phases. Tsukamoto et al. also used a middle buffer stream, but they did not investigate the effect of dilution on device performance (Tsukamoto et al. 2009). One way to minimize the effects of excessive dilution would be to use initial PEG and Dex concentrations further away from the binodal curve; this would minimize the dilution caused by the middle buffer stream. The strategy of using the middle stream to dilute a single interface ATPS has been used by Silva et al. to generate binodal curves for ATPS and is discussed later in the chapter (Silva et al. 2014).

A three inlet/two outlet device was used by Meagher et al. to isolate proteins (Meagher et al. 2008). The device had three inlet channels that contained a PEG-rich phase and monobasic and dibasic potassium phosphate on the two outer streams to form a PEG-salt ATPS as shown in Fig. 2c. The middle inlet contained the sample. The two outlet streams contained PEG in one and the interface and salt in the other. Because of the large difference in viscosity between the PEG and salt phases, this system has a large flow imbalance and the salt stream requires eight times as much volume over the course of the experiment as the PEG stream. The collection efficiency is also highly dependent on the flow balance because the interface (i.e., part of the PEG stream) is routed into the waste; if too much of the PEG stream is routed to the waste, collection efficiency suffers.

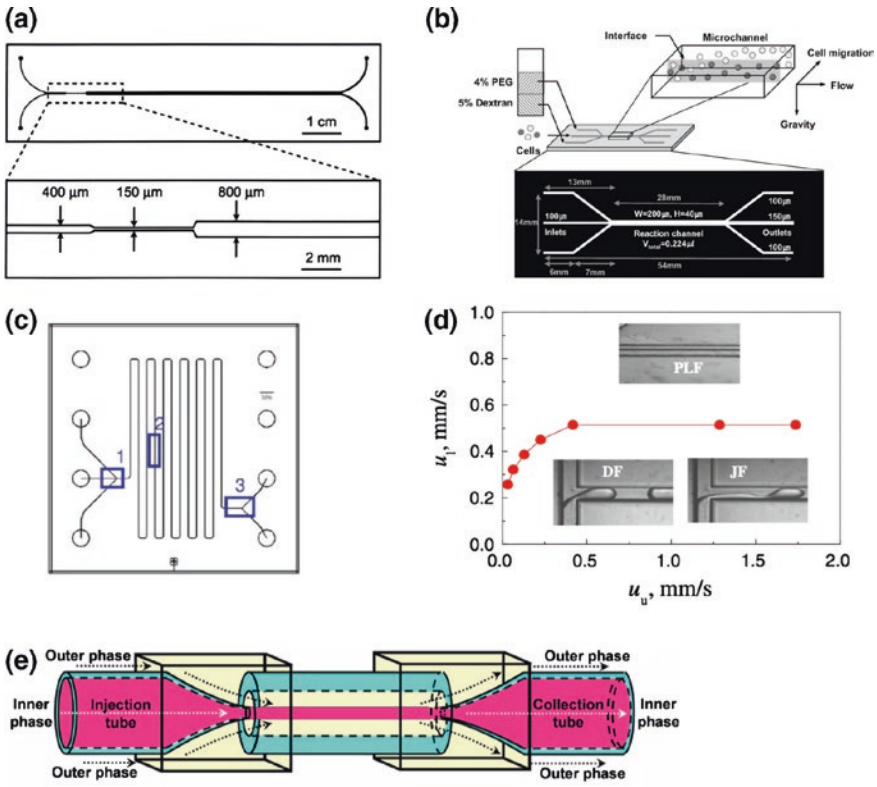

Fig. 2 **a** Yamada et al. were the first to demonstrate a microfluidic ATPS using a two inlet/two outlet design (Yamada et al. 2004). Reprinted with permission from John Wiley & Sons. **b** Nam et al. used a three inlet/three outlet microfluidic ATPS to sort cells (Nam et al. 2005). Reprinted with permission from Springer. **c** A three inlet/two outlet device was used by Meagher and coworkers to separate proteins (Meagher et al. 2008). Reprinted with permission from Royal Society of Chemistry. **d** Lu et al. used a simple T-junction (two inlet/one outlet) device to merge the two phases (Lu et al. 2010). Reprinted with permission from Springer. **e** A coaxial system has been tested that maximizes the interfacial surface area between two phases (Huang et al. 2013). Reprinted with permission from Springer

Huh et al. used a three inlet/three outlet PEG and potassium phosphate microfluidic ATPS with the sample injected into a middle inlet (Huh et al. 2010). Their system is not a typical ATPS, however, because the middle stream appears to create a distinct third phase, instead of diluting the phases as in the work by others (Nam et al. 2005; Tsukamoto et al. 2009). The middle stream used by Huh et al. contained sample isolated from a sucrose gradient, so it is possible that the authors inadvertently created a three phase system within their device.

Lu et al. further explored single interface ATPS behavior using a PEG and sodium sulfate system in a simple T-junction microfluidic device, as shown in Fig. 2d (Lu et al. 2010). They mapped out system behavior as a function of stream

flow rates and divided behavior into three regimes: (1) continuous two-phase flow with a smooth boundary, (2) slugs of sodium sulfate within a PEG continuous phase, or (3) "jetting flow" where slugs leave thin trails as they move down the channel.

Huang et al. used coaxial flow to create an outer stream of PEG that contained an inner stream of ammonium sulfate as shown in Fig. 2e (Huang et al. 2013). This setup is novel because it is a single interface configuration but maximizes the interfacial surface area between streams. In a configuration where two laminar streams are flowing side by side, only one quarter of each stream is exposed to the interface (i.e., the sides of the streams in contact with one another). However, by using coaxial flow, Huang et al. were able to expose the entire surface of the salt phase to the PEG phase, which results in greater flux of sample between phases.

2.1.2 Double Interface Systems

One interface exists between the phases in macroscale ATPS. Microfluidic systems allow the creation of ATPS that contain more than one interface between two phases (e.g., a Dex stream with a PEG stream on either side) by using multiple microchannels that contain alternating polymer solutions. Munchow et al. demonstrated the first double interface ATPS in a microfluidic system (Münchow et al. 2007). They constructed a three inlet/one outlet device which contained proteins suspended in a Dex stream injected into the middle inlet while PEG streams were injected into the two outer inlets as shown in Fig. 3a. In these experiments, PEG streams on either side were important because an electric field perpendicular to the microchannel was used to separate the proteins out of the Dex stream. Since the proteins could migrate toward either electrode, PEG was needed on both sides. In a different application, Soo Hoo and Walker demonstrated a three inlet/three outlet double interface system of two outer Dex streams and a middle PEG stream to enrich leukocytes (Soo Hoo and Walker 2009). Cells were loaded into PEG and depending on their type (i.e., leukocyte or erythrocyte) migrated out of the middle stream to one of the outer Dex streams as shown in Fig. 3b. Two interfaces were used by the authors because it increased leukocyte enrichment.

Two-interface polymer and salt systems have been implemented as well. Silva et al. created a three inlet/three outlet device with sodium chloride solution in the middle stream and PEG in the outer streams (Silva et al. 2012). Novak et al. also used a PEG and salt system (potassium phosphate) to create a two interface system (Novak et al. 2015). In this latter work, the middle stream contained the potassium phosphate and the outer streams were PEG.

2.1.3 Triple Interface Systems

As with macroscale ATPS, there is no limit to the number of interfaces or phases that can be created within a microfluidic system. A microfluidic system with six

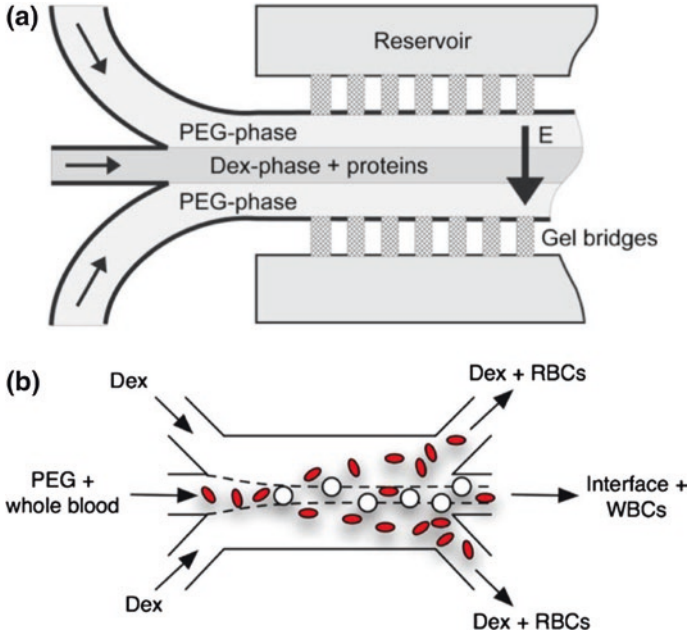

Fig. 3 **a** The first example of a microfluidic double interface ATPS comprising an inner Dex stream exposed to two outer PEG streams was by Münchow et al. (2007). Reprinted with permission from the Royal Society of Chemistry. **b** A three inlet/three outlet system can be used to collect particles from either phase or from the interface (Soo Hoo and Walker 2009). Reprinted with permission from Springer

interfaces of alternating PEG and Dex phases has been demonstrated by Frampton and coworkers (Frampton et al. 2011). This device was used to deliver reagents to specific lanes within a microchannel containing adhered cells. This application of ATPS in particular is a good demonstration of the unique techniques that become available when ATPS are implemented at the microscale.

2.2 Droplets

In addition to the continuous flow ATPS discussed in the previous section, the ability to create droplets constituting ATPS is another example of the inherent advantage of the microscale. The contents within droplets can be rapidly mixed via chaotic advection, which accelerates sample partitioning between the phases. Sample volumes are minimized because droplet volumes typically range from nanoliters to picoliters. Lastly, droplets can be routed within the device so that only droplets of interest are collected at the output for further analysis. However,

despite the many advantages of droplet ATPS, the low interfacial tension between phases (0.1–0.001 N m^{-1}) makes droplet formation challenging and novel methods are required to create droplets at the microscale. The various methods for forming droplets include fluid shear, mechanical actuation, and electrical actuation, and are discussed below.

2.2.1 Continuous Flow

Vijayakumar and coworkers were the first to demonstrate ATPS droplets within a microfluidic device (Vijayakumar et al. 2010). The group created ATPS droplets by using oil as a continuous phase and dispensing a mixture of PEG and DEX into droplets that then self-organized into a PEG outer phase and Dex inner phase. The droplet generation region of the device was a simple T-junction, as shown in Fig. 4a. The group's device included a narrow region halfway down the length of the main channel to induce intradroplet mixing via chaotic advection. The width of the narrow region was less than the droplet diameter, so as the droplet passed through the region intradroplet convection was induced. After the droplet exits the mixing region, the channel widens to allow the PEG outer phase and Dex inner phase to reform. Typical droplet diameters were 93 μm for the entire droplet and 41 μm for the inner Dex droplet and could be controlled by controlling the flow rates for PEG and Dex. The authors found that complete mixing of the droplet contents takes ~200 ms and re-equilibration ~650 ms. The temporary mixing disrupted the separate phases and if molecules or cells were present within the droplet, would greatly accelerate partitioning into separate phases. The demonstrate the efficacy of their mixing strategy, they introduced a Jurkat cell labeled with antibodies that possessed an affinity for PEG into the Dex phase, where it stayed until after mixing.

Choi et al. used electric fields to pinch off droplets of ammonium sulfate in a continuous phase of tetrabutylammonium bromide (TBAB) as shown in Fig. 4b (Choi et al. 2010). Then they used electric fields to direct droplets to a variety of locations downstream. The use of electric fields gives precise control over droplet size and the rate of droplet formation because both can be controlled by the duration of electrical pulses, which are easily computer-controlled. The ability to sort and direct droplets downstream could also find use in ATPS applications. The one drawback to the system that Choi et al. demonstrated is that it is not compatible with biological systems because of their choice of ATPS. However, a biologically compatible ATPS should be adaptable to their system.

Another actuation-based approach to droplet formation was demonstrated by Ziemecka and coworkers who integrated a piezoelectric actuator into a microchannel to induce instabilities in laminar streams of PEG and Dex to promote droplet formation, as shown in Fig. 4c (Ziemecka et al. 2011a). Their approach is unique not only because of the use of an off-the-shelf piezoelectric actuator, but because they were also the first to demonstrate two-interface droplets that consisted of a PEG droplet encapsulated by a Dex droplet which was encapsulated by a PEG

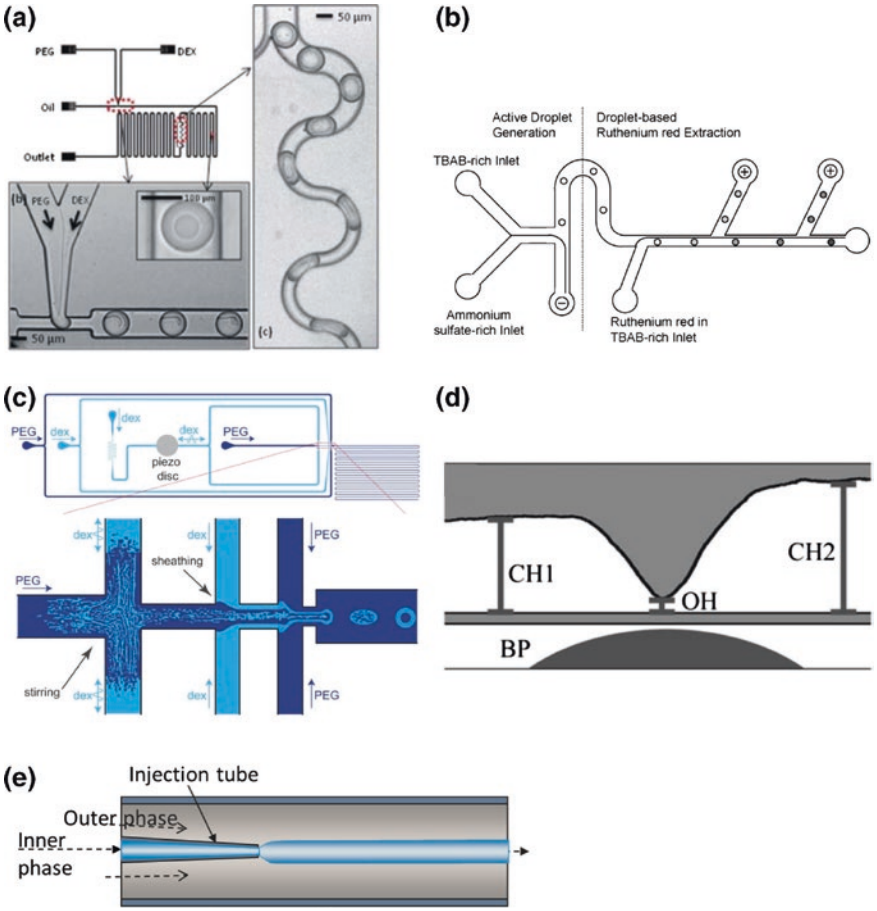

Fig. 4 **a** The first demonstration of ATPS droplet formation used a simple T-junction to create droplets containing PEG and Dex in a continuous oil phase (Vijayakumar et al. 2010). Reprinted with permission from the Royal Society of Chemistry. **b** Electrical pulses have been used to pinch off droplets of a polyelectrolyte phase into a continuous phase of a different polyelectrolyte (Choi et al. 2010). Reprinted with permission from Elsevier. **c** A piezoelectric actuator has been used to disrupt the phase boundary and create droplets (Ziemecka et al. 2011a). Reprinted with permission from the Royal Society of Chemistry. **d** An inexpensive solenoid (Braille pin; BP) was used by Lai et al. to periodically stop flow of the Dex stream from CH1 to CH2 which closed the gap OH (Lai et al. 2011). Reprinted with permission from the Royal Society of Chemistry. **e** Mechanical agitation of tubing connected via an orbital shaker has been used to create PEG droplets in a continuous phase (Shum et al. 2012). Reprinted with permission from AIP Publishing LLC

droplet. The piezoelectric actuator modulated the flow rate of an inlet Dex stream which created a droplet containing a mixture of PEG and Dex not separated into phases. This mixed droplet then flowed into a continuous PEG stream where the droplets equilibrate into a Dex outer and PEG inner droplet. The droplets are not

stable indefinitely, because the PEG inner core will eventually migrate out of the droplet and into the continuous PEG phase. However, this re-equilibration took approximately 20 min, which is longer than the duration of the droplet within the device (5 min). Even though the droplets have a short lifetime they remain intact long enough to perform useful analyses within the device.

Ziemecka and others extended their initial work to create polymerized Dex droplets within a PEG continuous phase (Ziemecka et al. 2011b). They found that the frequency of their actuator controlled the poly/monodispersity of droplets, and that the rate of droplet formation is approximately equal to the frequency of the actuator. They explored frequencies from 0 to 50 Hz and found that droplet diameters were fairly uniform at 40–50 μm in diameter for frequencies ranging from 25 to 50 Hz.

Another type of mechanical actuator for droplet creation was presented by Lai et al., who used backside exposure photolithography to create multilevel rounded channels that were actuated via an off-chip solenoid (i.e., a Braille pin) and generated Dex droplets within a PEG continuous phase ATPS (Lai et al. 2011). The computer-controlled Braille pin was used to mechanically deform a narrow region within a polydimethylsiloxane (PDMS) device and acted as an on/off valve for the Dex stream as shown in Fig. 4d. They explored the effect of the pin frequency on Dex droplet volume and spacing. Frequencies ranged from 2.5 to 0.83 Hz.

Shown in Fig. 4e is another approach to making droplets was presented by Shum et al. who used an orbital shaker to mechanically oscillate the tubing connecting a syringe containing the dispersed phase, PEG, to its inlet channel (Cheung Shum et al. 2012). The group used concentric glass capillary tubes instead of molded polymer microchannels to simplify device fabrication. The authors investigated droplet formation in four different ATPS: (1) PEG/Dex, (2) PEG-diacrylate(DA)/Dex, (3) PEG/potassium phosphate, and (4) PEG-DA/potassium phosphate. They found that an orbital shaker frequency of 6–8 Hz was necessary to make droplets. Frequencies above or below this range resulted in two-phase flow within the larger glass capillary. The group explored several ways to increase droplet stability by creating an outer shell on the droplets. The approaches they tried were: (1) photocross-linking the PEG-DA via UV light, (2) loading PEG droplets with calcium chloride and the continuous phase with sodium carbonate, and (3) loading PEG droplets with calcium chloride and the continuous phase with alginic acid. The first two methods successfully created droplets while the third resulted in continuous threads.

Lee et al. explored the formation of ATPS "slugs"—droplets that span the width of the microchannel—and the regimes within these droplets as a function of flow rate and relative concentration of PEG and Dex phases (Lee et al. 2012). The authors used oil as the continuous phase and sheared off PEG and Dex streams into slugs using a simple T-junction. The group discovered three regimes of flow that generate distinct morphologies within the slugs: (1) lobe, where Dex remains in a separate phase within the PEG droplet, (2) heterogeneous fragments, in which Dex begins to break up into smaller droplets within the larger PEG droplet, and (3) reticulate, in which the phases appear very well mixed. The amount of interfacial

surface area between the phases is greatest in the reticulate regime and least in the lobe regime. The authors proposed that one could induce flow to generate increased surface area (e.g., to promote separation of suspended particles or molecules) and then stop flow to induce re-separation of the phases. The ability to control the interfacial surface area via flow rate is not possible with other microfluidic ATPS configurations and offers some exciting possibilities. The phases could be rapidly alternated between well mixed and separated to improve separation efficiency or to allow the addition of more particles for separation. This experimental setup also allows the fundamental processes driving ATPS formation to be studied with greater precision.

Instead of using an actuator to create droplets, Geschiere et al. explored the breakup of Dex cylindrical jets into droplets within a PEG continuous phase due to Rayleigh–Plateau instability (Geschiere et al. 2012). The authors constructed a model two-phase system with similar viscosities to a PEG/Dex system using water, glycerol, hexadecane, and surfactants and compared the breakup behavior of this system to a PEG/Dex system. They found that the PEG/Dex system required 20 times the distance to break up into droplets compared to the water/glycerol system. Their results demonstrate that PEG/Dex systems are not accurately predicted by Rayleigh-Plateau theory because the their breakup time is much longer than anticipated. They also captured confocal images of the Dex stream within the PEG background and found that gravity plays a role in breakup behavior. If the Dex stream settles to the bottom of the channel before breaking up, it will remain a stream due to interactions with the bottom surface of the microchannel. They conclude that flow rates and channel lengths must be sufficient to promote breakup of the Dex stream before it can settle.

Moon and coworkers created ATPS droplets in a three inlet device by oscillating the pressure driving the Dex stream which caused the Dex to form droplets in a continuous PEG stream (Moon et al. 2015). They used compressed air, a regulator, and a computer-controlled solenoid valve to pressurize the head space of a pipette tip containing Dex. Pressure pulses were applied from 10 to 150 ms followed by no pressure ranging from 750 to 4000 ms. PEG flow rate was constant and controlled by a syringe pump. The group developed an empirical relationship showing that Dex droplet volume is proportional to Dex flow rate and pressure duration and inversely proportional to PEG flow rate and absence of pressure.

2.2.2 Static

While the bulk of ATPS droplet work has been performed in microfluidic systems under continuous flow, Boreyko and colleagues presented a novel approach to creating stationary droplets (Boreyko et al. 2013). In their setup a main microchannel is filled with oil and contains smaller perpendicular microchannels on either side as shown in Fig. 5. These smaller microchannels are used to inject PEG and Dex which forms droplets attached to the wall. Once the PEG and Dex droplets grow past a certain size, they interact and merge into a single two-phase droplet.

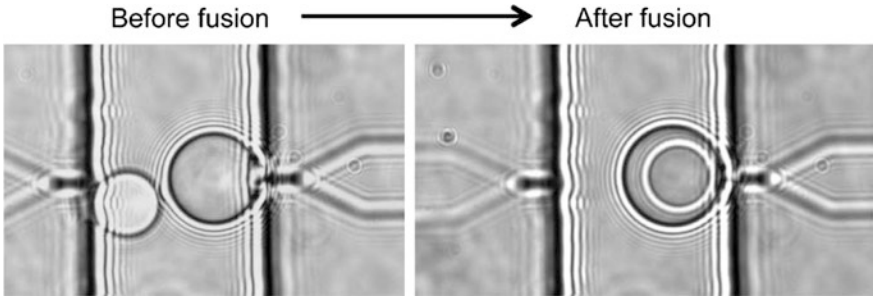

Fig. 5 ATPS droplets have been created without flow by precisely injecting small quantities of PEG and Dex via side channels within a larger microchannel (Boreyko et al. 2013). Reprinted with permission from the Royal Society of Chemistry

The authors used this setup to determine the binodal curve of a PEG and Dex ATPS, which is normally a tedious and time-consuming process. They were able to create single phase droplets, two-phase droplets, and via evaporation a Dex droplet with a thin PEG shell. This setup is ideal for determining the phase diagram of ATPS, but it is not suitable for high throughput sorting or screening applications.

3 Microfluidic Applications

3.1 Biomolecule Sorting

ATPS have a track record of being used in the biotechnology industry to separate various biological molecules (Benavides et al. 2011). However, the exact mechanisms of separation remain elusive and it can be difficult and time-consuming to develop the best ATPS for an application. Microfluidic ATPS allow continuous operation and monitoring of the separation and can accelerate the process of identifying the appropriate mixtures to create a two-phase solution (i.e., to generate a binodal curve). Microscale systems are also able to partition biomolecules and reach equilibrium in seconds compared to hours in traditional macroscale ATPS. These advantages have been recognized by researchers who have used microfluidic ATPS to purify a variety of biomolecules, as summarized in Table 1.

Munchow et al. were the first to separate biomolecules using a microfluidic ATPS (Münchow et al. 2007). They suspended proteins in a stream of Dex situated between two outer PEG streams and then used an electric field perpendicular to the streams to separate the proteins. They used bovine serum albumin (BSA), which prefers Dex, to test their system and found that BSA could be transported from PEG to Dex using any applied voltage, but that a voltage greater than 2.5 V was needed to move the BSA through the phase boundary from Dex into PEG. Munchow and coworkers followed up their original work with another study that

Table 1 Summary of biomolecules sorted with microfluidic ATPS

Biomolecule	Reference(s)
α-amylase	Novak et al. (2015)
Amino acids (Glu, Lys, Trp)	Campos et al. (2014)
Bacteriorhodopsin (BR)	Huh et al. (2010)
β-galactosidase	Hahn et al. (2011)
Bovine serum albumin (BSA)	Münchow et al. (2007), Münchow et al. (2008), Huang et al. (2013), Hahn et al. (2011)
Carbonic anhydrase	Hahn et al. (2011)
DNA	Hahn et al. (2011)
Glutathione S-transferase	Meagher et al. (2008)
Green fluorescent protein AcGFP1	Meagher et al. (2008)
Immunoglobulin G (IgG)	Silva et al. (2012)
Mycotoxin ochratoxin A (OTA)	Soares et al. (2014)
Ovalbumin	Münchow et al. (2008)

looked at the effect of interfacial effects on the transport of molecules between phases (Münchow et al. 2008). They used BSA and ovalbumin and reported partition coefficients of 2.53 and 1.42, respectively.

Meagher et al. demonstrated the separation of proteins containing genetically engineered hydrophobic tags, 4–8 amino acids long, to increase protein affinity for PEG (Meagher et al. 2008). The authors loaded their sample into a salt stream and molecules of interest were collected in the PEG stream. They demonstrated a threefold increase in recovery of cell lysate containing the monomeric green fluorescent protein AcGFP1 and a 40 % recovery of the enzyme glutathione S-transferase (compared to 0 % without a tag). The authors also separated BSA and beta-galactosidase within their systems as a proof of concept. Unlike the system demonstrated by Munchow et al., this system did not use an electric field for separation. They demonstrated partition coefficients of 2–10 depending on the hydrophobic tag used.

Huh and coworkers separated bacteriorhodopsin (BR) using a PEG and potassium phosphate microfluidic ATPS (Huh et al. 2010). Bacteriorhodopsin is a light sensitive protein in the membrane of the bacteria *Halobacterium salinarium*. The molecule has attractive properties for photonics applications, but it is difficult to isolate. The BR protein is embedded in the lipid membrane of the bacteria and must be isolated from a sample containing membrane fragments in addition to BR protein. In this device, the authors injected sample into a middle stream and on either side there was a PEG and a potassium phosphate stream. Lipids (i.e., membrane fragments) prefer the PEG phase due to their hydrophobicity but BR remains in the original sample stream. The authors were able to achieve 100 % purity and 81 % recovery rate by running the sample through the ATPS for three cycles.

Silva et al. used a microfluidic ATPS to partition a monoclonal antibody, FITC immunoglobulin G (IgG) from a salt-rich phase to a PEG-rich phase (Silva et al. 2012). They measured a partition coefficient of 2.15 and achieved a recovery of 54 % with the microfluidic system, which is comparable to the 60 % recovery common in a macroscale setup.

Huang and coworkers used a microfluidic PEG/Dex ATPS consisting of coaxial streams to recover bovine serum albumin (BSA) (Huang et al. 2013). In their setup, BSA was loaded into the outer PEG phase and was collected in the inner Dex phase. A key advantage to the coaxial streams is the that Dex surface area exposed to PEG is maximized, compared to side-by-side laminar flow streams. They achieved the same extraction efficiency (71 %) as in a beaker, but the separation only took 3.6 s to complete compared to hours for the beaker.

Soares et al. developed a polymer/salt microfluidic ATPS comprising PEG and a mixture of sodium phosphate and potassium phosphate to extract the mycotoxin ocratoxin A (OTA) from red wine samples (Soares et al. 2014). The ATPS serves as a sample preconditioning step to extract and concentrate OTA before it flows downstream to an on-chip detection region where an immunoassay is performed to quantify OTA levels. In their setup, the wine sample is diluted into the salt stream and the OTA is extracted into the PEG stream. The group found that the ATPS lowered the limit of detection of their assay. The authors did not investigate multiple flow rates to optimize their ATPS, but they noted that the relative positions of the PEG and salt streams changed down the length of the channel and that the PEG stream bifurcates to flow on both sides of the salt stream.

Campos and coworkers used a PEG-caseinate ATPS to differentially extract lysine from a mixture that also contained glutamate and tryptophan (Campos et al. 2014). The amino acids were mixed with buffer and then injected into the middle stream of a five inlet device. PEG was flowed on either side of the inlet stream followed by caseinate on either side of the PEG streams. The authors applied voltages of 0, 7.4, and 14.7 kV m^{-1} and found that only voltages above 7.4 kV m^{-1} successfully removed lysine from the mixture. Without the electric field, 0 % of the lysine was removed. With the electric field above the threshold value, 53 % of lysine was removed while only 30 % of the tryptophan and glutamate were removed.

Novak et al. used a three-stream ATPS with PEG in the outer streams and potassium phosphate in the middle stream to extract the enzyme α-amylase (Novak et al. 2015). They demonstrated a significant improvement in time at the expense of a lower collection efficiency. A macroscale ATPS extracted α-amylase from the potassium phosphate phase with an efficiency of 74 % in 2.5 h. The microfluidic system performed extraction in 10 s, a two orders of magnitude improvement, but only achieved an efficiency of 52 %. Extraction efficiency was defined as the difference in concentration between the inlet and outlet of the microchannel of α-amylase.

3.2 Cell Sorting

Sorting cells with an ATPS at the can be challenging. If gravity dominates, these particles cannot be separated by solution affinity (via ATPS) alone because settling affects ATPS performance (Yamada et al. 2004). Settling causes the cells to accumulate at the interface between phases (if they are loaded into the top phase and prefer the top phase) or at the bottom of the bottom phase. Cells must be exposed to the interface for separation to occur, unlike biomolecules, which can be driven by a concentration gradient. The large surface area-to-volume ratio present in microfluidic systems enhances the separation of cells via ATPS. These systems are more efficient in microfluidic devices than at the macroscale. Also, gravity no longer affects system performance because it is not in the direction of the interface; settling is no longer an issue, overcoming one of the main drawbacks to using ATPS for cell separation at the macroscale. Low interfacial tension is also an advantage of ATPS for cell sorting because cells can pass between phases without injury caused by surface tension. Finally, mixing may be required at the macroscale, which can induce shear damage in cells. Table 2 shows a summary of cell types that have been sorted using microfluidic ATPS.

Yamada et al. were the first to sort cells using a microfluidic ATPS (Yamada et al. 2004). They used a two inlet/two outlet device to enrich cells isolated from strawberry tissue. One stream contained the cells suspended in PEG while the other contained Dex. The two phases were forced to flow through a narrow channel region slightly wider than the cells so that the cells would be exposed to both phases. The channel then widened and the cells remained in the energetically favored phase. The authors explored how salt concentration within the phases affected cell enrichment efficiency. With the optimal configuration, approximately 70 % of the cells migrated from the PEG stream to the Dex stream.

The first mammalian cells were sorted by Nam et al. who used Chinese Hamster Ovary (CHO) cells in a microfluidic ATPS comprising PEG and Dex (Nam et al. 2005). The cells were injected at the interface of the two phases and the authors found that live cells preferred PEG while dead cells remained at the interface. By adjusting system pH they could control the hydrophobicity of the PEG stream and in turn increase or decrease the affinity of the CHO for the PEG stream. They reported 100 % recovery of live cells using their device.

The first use of human cells in a microfluidic ATPS was by Soo Hoo and Walker who used PEG and Dex streams to separate leukocytes from whole blood

Table 2 Summary of cells sorted with microfluidic ATPS

Cell type	Reference(s)
Chinese Hamster Ovary (CHO)	Nam et al. (2005)
Human Erythrocytes (RBC)	Soo Hoo and Walker (2009), Tsukamoto et al. (2009)
Human Leukocytes (WBC)	Soo Hoo and Walker (2009), Tsukamoto et al. (2009)
Human T Lymphoma (Jurkat)	Tsukamoto et al. (2009), Vijayakumar et al. (2010)
Plant Aggregates (strawberry)	Yamada et al. (2004)

(Soo Hoo and Walker 2009). They mixed blood into a PEG solution and injected it into the middle stream of a three inlet/three outlet device under two different ATPS configurations: parallel streams of PEG/PEG/Dex and Dex/PEG/Dex. They observed that red blood cells prefer the Dex phase but that leukocytes prefer the interface. By collecting the cells trapped at the interface in a middle outlet channel, they were able to achieve a ninefold increase in leukocyte concentration. Approximately one year later, Tsukamoto et al. also demonstrated a three inlet/three outlet whole blood cell separation device using PEG and Dex ATPS (Tsukamoto et al. 2009). They were able to achieve 96 % isolation efficiency of Jurkat cells in the PEG stream and 99 % isolation efficiency of erythrocytes in the Dex stream. The authors found that erythrocytes prefer the hydrophilic Dex phase while leukocytes (Jurkat cells) prefer the hydrophobic PEG phase.

Vijayakumar and coworkers demonstrated that hydrophobic antibodies could be used to change the preferred phase for Jurkat cells (Vijayakumar et al. 2010). They mixed Jurkat cells in Dex and then created ATPS droplets with an inner Dex phase and outer PEG phase. Without the antibody, 98 % of the Jurkat cells remained in the Dex phase. With the antibody 93 % of the cells migrated to PEG. This approach could dramatically broaden the number of cells that can be isolated using ATPS. Antibodies can be raised that are specific to single cell types, and using the strategy of Vijayakumar et al. any cell type could be targeted in a heterogeneous sample and be isolated with high purity.

3.3 Cell Patterning

The phase separation characteristic of ATPS makes preferential partitioning of cells and biomolecules possible. However, phase separation can be used to enable a new type of application, namely, to create unique cell culture environments suitable for high throughput screening. The affinity specific classes of molecules have for the phases of ATPS can be harnessed to confine the molecules necessary for cell growth or for delivering genetic material via transfection reagents.

The first report of patterning cells via ATPS was by Tavana et al., who deposited nanoliter sized droplets of Dex on the bottom of wells filled with PEG (Tavana et al. 2009). The Dex droplets remained distinguishable on the bottom of the well because the phases are immiscible and because Dex is denser than PEG. The group demonstrated how droplets of Dex loaded with transfection complexes could be precisely patterned to transfect specific regions of a monolayer of human embryonic kidney (HEK293H) cells in the bottom of a 1536 well plate. There are several advantages to using ATPS for targeted transfection of cells: (1) ATPS are biocompatible, (2) nanoliter scale droplets are used, minimizing reagent consumption, and (3) transfection complexes preferentially stay in the Dex phase, and do not diffuse away, further minimizing reagent use and accelerating transfection. Plasmid DNA and lentivirus are expensive and can be a limiting factor for high

throughput screening, so the ability to minimize transfection reagent use for high throughput screening makes this application of ATPS particularly attractive.

Even though laminar flow in microfluidic channels allows one to selectively deposit cells and control the location of small molecules, ATPS provide even more precise control because the small molecules and cells preferentially prefer one phase. Frampton et al. exploit this selective affinity by demonstrating ATPS for cell patterning and selective cell removal within microchannels (Frampton et al. 2011). The authors used streams of Dex to carry cells into a microchannel and then stopped the streams to allow the cells to settle and attach. By separating multiple Dex streams with thin streams of PEG in a seven inlet device, the authors were able to pattern four cell types simultaneously. The authors also used a Braille pin valving technique to generate droplets of Dex containing cells and then used these droplets to pattern islands of cell cultures within the microchannel. Lastly, the authors demonstrated selective trypsinization of attached cells by loading trypsin into a Dex stream which minimized its diffusion into neighboring parallel streams.

Leung et al. used ATPS to create 3D collagen microgels containing embedded breast cancer cells (231-LUC) (Leung et al. 2015). The authors took advantage of collagen's preference for Dex over PEG to robotically pipette submillimeter diameter droplets of collagen and Dex on the bottom of wells filled with PEG. After the droplets gelled, the PEG was thoroughly washed out of the wells because it can be toxic to cells after long-term exposure. The authors demonstrated the superiority of 3D culture to 2D culture in predicting the cytotoxicity of the popular chemotherapeutics cisplatin, paclitaxel, and doxorubicin. An advantage of this approach is that the collagen microgels equilibrate more rapidly to a bolus of drug added to the well than larger gels made by traditional methods. Their microgel equilibrated in 5 min, compared to 6 h for a larger traditional collagen gel construct.

3.4 Protein Microgels

PEG and Dex ATPS can also be used to create environments for the patterning of proteins, enabling new types of experiments to elucidate the mechanisms of protein nanofibril formation. As an example, Shimanovich and coworkers used droplets of PEG and Dex to study the formation of protein nanofibrils by carefully controlling the microscale localization of lysozyme monomer proteins (Shimanovich et al. 2015). The authors mixed egg white lysozyme in PEG and Dex and then formed single and two-phase droplets in an oil continuous phase. Heat for 24 h was used to promote nanofibril formation. The authors characterized fibril formation in single phase droplets, two-phase PEG/Dex (outer/inner), and Dex/PEG droplets. They found that lysozyme monomers migrate preferentially to the Dex phase and form amyloid fibrils there; they also form fibers at the PEG/Dex and oil interfaces. The authors found that the fibril network stabilizes the droplet compared to droplets without protein.

3.5 ATPS Characterization

While microfluidic ATPS have been applied to the sorting and separation of cells and biomolecules, these systems have also been used to study the behavior of two-phase systems. In particular, microfluidic ATPS allow one to study the mechanisms of phase formation and the forces that drive particle separation between the phases. Such studies are possible with traditional macroscale ATPS, but they are more tedious and they do not allow precise control of the ATPS components. It is also much more challenging to visualize the phase boundary and the migration of particles as they separate in macroscale ATPS.

In the first microfluidic study of particle separation within an ATPS, Munchow and coworkers used a microfluidic ATPS consisting of PEG and Dex to elucidate the role the interface plays in diffusive transport of proteins between phases of an ATPS (Münchow et al. 2008). This type of study is not feasible at the macroscale because the phases must be positioned vertically, one on top of the other, and measurements of molecular concentration at the interface are difficult to make. In contrast, a microfluidic system with parallel streams of PEG and Dex allows easy observation of fluorescent protein concentration at the interface. Using their microfluidic system, the authors were able to create a one-dimensional mathematical model that predicted the time-dependent concentration of proteins within the phases of the ATPS. They used ovalbumin and BSA and experimental results agreed well with their model. Of particular note, the authors did not take into account the electric field created by the double layer at the phase interface (~1–3 mV). Previous work with macroscale ATPS suggested that this electric field may inhibit protein transport across the phase boundary. However, Munchow et al. did not incorporate the electric field into their model, which still predicted accurately the experimental results. Therefore, they suggest that the electric field is only important if the molecules are smaller than the thickness of the double layer (typically 10 s of nm).

PEG and Dex ATPS have been further characterized by Hahn et al., who used a similar setup to Munchow et al. (Hahn et al. 2011). The group investigated the mass transfer resistance of the liquid/liquid interface of their ATPS using proteins and stained DNA as probes. The authors used electrophoresis perpendicular to the three flow streams (Dex in the middle and PEG on either side) to probe the underlying physics affecting the separation of molecules. They identified three factors that impact the transport between phases: (1) electrophoretic mobilities of proteins in each phase, (2) the partition coefficient of the molecules, and (3) the mass transfer resistance at the phase interface due to adsorption. They found that for proteins, the separation into phases is governed solely by electrophoretic mobility and the partition coefficient (i.e., the intrinsic preference of the protein for each phase). Proteins do not adsorb to the interface but DNA does.

Lai et al. took advantage of the phase separation of Dex droplets in a PEG continuous phase to explore the kinetics of dextranase (Lai et al. 2014). They observed the phase boundary of Dex as it was degraded by dextranase and were

able to extrapolate the kinetics from the gradual disappearance of the two phases. Their approach provides a new label-free method for estimating Michaelis constants for dextranase that agree with previously determined values in the literature.

Silva et al. used microfluidic ATPS to rapidly generate binodal curves for ATPS comprising PEG, Dex, and potassium phosphate (Silva et al. 2014). This study leverages the power of microfluidics because the system allows one to generate the many data points required for creating a binodal curve using only 1 mL of each solution. The authors flowed streams of different polymer or salt concentration next to each other with a DI water stream in the middle and monitored the outlet of the microchannel for an interface. Polymer and salt concentrations were altered via flow rate. If an interface was present, then the concentrations resided above the binodal curve. If an interface was not present, then the concentrations were below the binodal curve. Concentrations on the binodal curve resulted in an interface that was transient. Each point on the binodal curve required 4 min to generate and there were approximately 48 points per curve. Generate a binodal curve using the microfluidic method required approximately 3–3.5 h, much shorter than with traditional methods.

4 Summary

ATPS are an old technology that have been adapted to microfluidic formats within the past ten years. The traditional applications of ATPS were limited to separating biological particles such as biomolecules, organelles, or whole cells. Migrating the technology to microscale dimensions has enabled new applications. The phase interface in microfluidic system is not limited to a horizontal orientation. Multiple phases can easily be created and manipulated using microfluidic devices with multiple inlets. Laminar flow ensures that the streams remain stable and the interface undisturbed. Reagent use is minimized in microfluidic systems and diffusion distances are orders of magnitude shorter, resulting in more rapid separations. The separation efficiency is improved compared to macroscale ATPS, in some cases. New techniques to pattern and experimentally probe cells have been demonstrated using the immiscible phases of ATPS. Undoubtedly, as more researchers experiment with microfluidic ATPS new applications will continue to be realized that enable novel experimental approaches currently unavailable.

References

Albertsson P-A (1986) Partition of cell particles and macromolecules. Wiley, Hoboken

Albertsson P-A (1958) Partition of proteins in liquid polymer-polymer two-phase systems. Nature 182:709–711

Beijerinck MW (1896) Über eine Eigentümlichkeit der löslichen Stärke. Centralblatt fur Bakteriologie 2:697–699

Benavides J, Rito-Palomares M, Asenjo JA (2011) Downstream processing and product recovery-aqueous two-phase systems. In: MooYoung M (ed) Comprehensive biotechnology, 2nd edn, vol 2. Elsevier, Amsterdam, pp 697–713

Boreyko JB, Mruetusatorn P, Retterer ST, Collier CP (2013) Aqueous two-phase microdroplets with reversible phase transitions. Lab Chip 13:1295–1301. doi:10.1039/c3lc41122b

Bungenberg de Jong HG (1949) In: Kruyt HR (ed) Colloid science, vol 2: Reversible Systems Elsevier, Amsterdam, pp 280–297

Campos C, Park JK, Neuzil P et al (2014) Membrane-free electroextraction using an aqueous two-phase system. RSC Adv 4:49485–49490. doi:10.1039/C4RA09246E

Choi YH, Song YS, Kim D-H (2010) Droplet-based microextraction in the aqueous two-phase system. J Chromatogr A 1217:3723–3728. doi:10.1016/j.chroma.2010.04.015

Dobry A, Boyer-Kawenoki F (1947) Phase separation in polymer solution. J Polym Sci Part B Polym Chem 2:90–100. doi:10.1002/pol.1947.120020111

Frampton JP, Lai D, Sriram H, Takayama S (2011) Precisely targeted delivery of cells and biomolecules within microchannels using aqueous two-phase systems. Biomed Microdevices 13:1043–1051. doi:10.1007/s10544-011-9574-y

Geschiere SD, Ziemecka I, van Steijn V et al (2012) Slow growth of the Rayleigh–Plateau instability in aqueous two phase systems. Biomicrofluidics 6:22007–22007–22007–22011. doi:10.1063/1.3700117

Hahn T, Münchow G, Hardt S (2011) Electrophoretic transport of biomolecules across liquid–liquid interfaces. J Phys Condens Matter 23:279502–279509. doi:10.1088/0953-8984/23/27/279502

Hardt S, Hahn T (2012) Microfluidics with aqueous two-phase systems. Lab Chip 12:434–442. doi:10.1039/C1LC20569B

Huang Y, Meng T, Guo T et al (2013) Aqueous two-phase extraction for bovine serum albumin (BSA) with co-laminar flow in a simple coaxial capillary microfluidic device. Microfluid Nanofluid 16:483–491. doi:10.1007/s10404-013-1245-2

Huh YS, Jeong C-M, Chang HN et al (2010) Rapid separation of bacteriorhodopsin using a laminar-flow extraction system in a microfluidic device. Biomicrofluidics 4:14103. doi:10.1063/1.3298608

Lai D, Frampton JP, Sriram H, Takayama S (2011) Rounded multi-level microchannels with orifices made in one exposure enable aqueous two-phase system droplet microfluidics. Lab Chip 11:3551–3554. doi:10.1039/c1lc20560a

Lai D, Frampton JP, Tsuei M et al (2014) Label-free direct visual analysis of hydrolytic enzyme activity using aqueous two-phase system droplet phase transitions. Anal Chem 86:4052–4057. doi:10.1021/ac500657k

Lee S, Wang P, Kun Yap S et al (2012) Tunable spatial heterogeneity in structure and composition within aqueous microfluidic droplets. Biomicrofluidics 6:22005–220058. doi:10.1063/1.3694841

Leung BM, Moraes C, Cavnar SP et al (2015) Microscale 3D collagen cell culture assays in conventional flat-bottom 384-well plates. J Lab Autom 20:138–145. doi:10.1177/2211068214563793

Liu CL, Nikas YJ, Blankschtein D (1996) Novel bioseparations using two-phase aqueous micellar systems. Biotechnol Bioeng 52:185–192

Lu Y, Xia Y, Luo G (2010) Phase separation of parallel laminar flow for aqueous two phase systems in branched microchannel. Microfluid Nanofluid 10:1079–1086. doi:10.1007/s10404-010-0736-7

Meagher RJ, Light YK, Singh AK (2008) Rapid, continuous purification of proteins in a microfluidic device using genetically-engineered partition tags. Lab Chip 8:527–532. doi:10.1039/b716462a

Moon B-U, Jones SG, Hwang DK, Tsai SSH (2015) Microfluidic generation of aqueous two-phase system (ATPS) droplets by controlled pulsating inlet pressures. Lab Chip 15:2437–2444. doi:10.1039/C5LC00217F

Münchow G, Hardt S, Kutter JP, Drese KS (2007) Electrophoretic partitioning of proteins in two-phase microflows. Lab Chip 7:98–102. doi:10.1039/b612669n

Münchow G, Schönfeld F, Hardt S, Graf K (2008) Protein diffusion across the interface in aqueous two-phase systems. Langmuir 24:8547–8553. doi:10.1021/la800956j

Nam K-H, Chang W-J, Hong H et al (2005) Continuous-flow fractionation of animal cells in microfluidic device using aqueous two-phase extraction. Biomed Microdevices 7:189–195. doi:10.1007/s10544-005-3025-6

Novak U, Lakner M, Plazl I, Znidarsic-Plazl P (2015) Experimental studies and modeling of α-amylase aqueous two-phase extraction within a microfluidic device. Microfluid Nanofluid. doi:10.1007/s10404-015-1550-z

Shimanovich U, Song Y, Brujic J et al (2015) Multiphase protein microgels. Macromol Biosci 15:501–508. doi:10.1002/mabi.201400366

Silva DFC, Azevedo AM, Fernandes P et al (2014) Determination of aqueous two phase system binodal curves using a microfluidic device. J Chromatogr A 1370:115–120. doi:10.1016/j.chroma.2014.10.035

Silva DFC, Azevedo AM, Fernandes P et al (2012) Design of a microfluidic platform for monoclonal antibody extraction using an aqueous two-phase system. J Chromatogr A 1249:1–7. doi:10.1016/j.chroma.2012.05.089

Shum H, Varnell J, Weitz DA (2012) Microfluidic fabrication of water-in-water (w/w) jets and emulsions. Biomicrofluidics 6:12808–128089. doi:10.1063/1.3670365

Soares RRG, Novo P, Azevedo AM et al (2014) On-chip sample preparation and analyte quantification using a microfluidic aqueous two-phase extraction coupled with an immunoassay. Lab Chip 14:4284–4294. doi:10.1039/c4lc00695j

Soo Hoo JR, Walker GM (2009) Microfluidic aqueous two phase system for leukocyte concentration from whole blood. Biomed Microdevices 11:323–329. doi:10.1007/s10544-008-9238-8

Tavana H, Jovic A, Mosadegh B et al (2009) Nanolitre liquid patterning in aqueous environments for spatially defined reagent delivery to mammalian cells. Nat Mater 8:736–741. doi:10.1038/nmat2515

Tsukamoto M, Taira S, Yamamura S et al (2009) Cell separation by an aqueous two-phase system in a microfluidic device. Analyst 134:1994–1998. doi:10.1039/b909597g

Vijayakumar K, Gulati S, deMello AJ, Edel JB (2010) Rapid cell extraction in aqueous two-phase microdroplet systems. Chem Sci 1:447–452. doi:10.1039/c0sc00229a

Walter H, Brooks D, Fisher D (eds) (1985) Partitioning in aqueous two-phase system: theory, methods, uses, and applications to biotechnology. Academic Press, New York

Yamada M, Kasim V, Nakashima M et al (2004) Continuous cell partitioning using an aqueous two-phase flow system in microfluidic devices. Biotechnol Bioeng 88:489–494. doi:10.1002/bit.20276

Ziemecka I, van Steijn V, Koper GJM et al (2011a) All-aqueous core–shell droplets produced in a microfluidic device. Soft Matter 7:9878–9880. doi:10.1039/c1sm06517c

Ziemecka I, van Steijn V, Koper GJM et al (2011b) Monodisperse hydrogel microspheres by forced droplet formation in aqueous two-phase systems. Lab Chip 11:620–624. doi:10.1039/c0lc00375a

Index

W. Lee et al. (eds.), *Microtechnology for Cell Manipulation and Sorting*,
Microsystems and Nanosystems, DOI 10.1007/978-3-319-44139-9